ABSTRACT

Title of Dissertation: GLOBAL ANALYSIS OF TRANSITIONAL HYPERSONIC FLOW OVER CONE AND CONE-FLARE GEOMETRIES

Cole E. Sousa
Doctor of Philosophy, 2024

Dissertation Directed by: Professor Stuart Laurence
Department of Aerospace Engineering

Accurately predicting the laminar-to-turbulent boundary-layer transition on hypersonic vehicles remains one of the principal challenges in characterizing the expected heat loads and skin friction the vehicle will experience in flight. Ground facilities, while incapable of replicating the complete set of flow conditions found at hypersonic flight, play a critical role in providing physical measurements of the transition process. The experimental characterization of hypersonic boundary-layer disturbances, however, has traditionally faced limitations in its ability to provide spatiotemporally dense data sets comparable to those of computational fluid dynamics (CFD) investigations. The present work aims to provide global off-body measurements of hypersonic boundary-layer disturbances at frequencies much greater than that of the fundamental instability, enabling the exploration of nonlinear phenomena and more extensive comparisons between experimental and computational studies.

The current methodology utilizes the fact that hypersonic-boundary layer disturbances have

been observed to propagate at measurable and statistically predictable velocities. Particularly for the second-mode instability, the density gradient fields acquired by a calibrated schlieren system provide an avenue for resolving dense high-frequency spatiotemporal data. Disturbance propagation velocities extracted from the schlieren images are used to conduct a time-interpolation of the disturbances, which transforms spatially-available descriptions of the travelling waveforms into up-sampled temporal signals at specific pixel locations. When performed across the entire schlieren field of view, the resulting time-resolved signals have a new sampling frequency much greater than the original camera frame rate and a spatial density equal to the camera resolution. This enables the spectral analysis of high-frequency disturbances, including superharmonics of the fundamental instability, which are not originally resolvable from raw time series of the video data.

The methodology is employed here in three different experimental data sets, comprising a 7° half-angle sharp cone at zero incidence in Mach 6 flow, a 7° half-angle sharp cone at variable incidence in Mach 14 flow, and a cone-flare geometry composed of a 5° frustum with compression angles of +5°, +10°, and +15° at zero incidence in Mach 14 flow. A comprehensive global analysis is conducted on the linear and nonlinear development of the second-mode instability waves in each case. Pointwise measures of the autobicoherence are used to identify specific triadic interactions and the locations of their highest levels of quadratic phase coupling. Significant resonance interactions between the second-mode fundamental and harmonic instabilities are found along with interactions between these and the mean flow. Bispectral mode decomposition is employed to educe the flow structures associated with these interactions. A similar analysis is performed for the power spectrum, with power spectral densities computed for each pixel's time-series and spectral proper orthogonal decomposition employed to derive the modal structure and

energy of the flow at specific frequencies.

The instability measurements taken on the cone-flare geometry are the first of their kind at Mach 14. The analysis reveals that incoming second-mode waves undergo extended interactions with the shock waves present at the corner, consistently leading to amplification of the waves and accelerating their nonlinear activity. The disturbance energy is also found to strongly radiate along the shock waves, a behavior that appears to be intensified at high Mach numbers. In the case of separated flow at the corner, additional low-frequency disturbances arise along the shear layer. Self-resonance of these disturbances leads to the radiation of elongated structures upstream of reattachment, which extend outward from the shear layer and terminate at the separation shock. This shear-layer disturbance is determined to be dominantly unstable between separation and reattachment but is significantly damped after reattachment.

GLOBAL ANALYSIS OF TRANSITIONAL HYPERSONIC FLOW OVER ON CONE AND CONE-FLARE GEOMETRIES

by

Cole E. Sousa

Dissertation submitted to the Faculty of the Graduate School of the
University of Maryland, College Park in partial fulfillment
of the requirements for the degree of
Doctor of Philosophy
2024

Advisory Committee:
Professor Stuart Laurence, Chair/Advisor
Professor Kenneth Yu
Professor Christopher Cadou
Professor James Baeder
Professor Johan Larsson

Acknowledgments

I would first like to extend my deepest gratitude to my advisor, Professor Stuart Laurence, for entrusting me with the remarkable opportunity to delve into the realm of hypersonics. His unfaltering encouragement for my academic journey commenced over eight years ago during my undergraduate years at the University of Maryland. Professor Laurence's extensive expertise and esteemed reputation in the field of hypersonics have facilitated invaluable research collaborations, affording me unparalleled experiences conducting experiments at renowned facilities worldwide.

Additionally, I am tremendously thankful to Professors Kenneth Yu and Christopher Cadou for generously sharing their insights and research acumen with me throughout my academic pursuits, both within the confines of structured coursework and during program examinations. I am also grateful to Professors James Baeder and Johan Larsson for their invaluable guidance and perspective, which greatly contributed to the completion of this dissertation.

I extend my heartfelt appreciation to all my colleagues in the High-Speed Aerodynamics and Propulsion Lab. During my time here, I have never encountered a solitary experiment. Each member of our team has extended a helping hand, nurturing a culture of camaraderie and co-operation. I am immensely fortunate to have been surrounded by such altruistic and inspiring individuals, and wish each of you abundant success and fulfillment in your future pursuits.

Lastly, I wish to express my profound gratitude to my cherished family. None of my achievements would have been possible without your endless support and dedication. I am indebted to my wife, Alessandra, whose boundless love, care, and laughter sustained not only me but also our two children throughout the duration of my studies. Above all, I am eternally grateful to my parents, Todd and Kim. Words fail to encapsulate the depth of my gratitude for the countless opportunities you have bestowed upon me. Your unwavering presence has been a constant source of strength and inspiration. Every sense of pride and accomplishment, every triumphant "Huzzah!" — I wholeheartedly share them with you.

This project was funded by the United States Air Force Office of Scientific Research (Dr. Brett Pokines) through grant FA9550-17-1-0085.

Table of Contents

List of Tables

List of Figures

Nomenclature

Acronyms

AEDC	Arnold Engineering Development Complex
BAM6QT	Boeing/Air Force Office of Scientific Research Mach 6 Quiet Tunnel
BMD	Bispectral Mode Decomposition
CPSD	Cross Power Spectral Density
DNS	Direct Numerical Simulation
FLDI	Focused Laser Differential Interferometry
FR	Frame Rate
FSD	Focused Schlieren Deflectometry
HEG	High-Enthalpy Shock Tunnel Göttingen (HEG)
HWA	Hot-Wire-Anemometry
LST	Linear Stability Theory
M6QT	Texas A&M University Mach 6 Quiet Tunnel
MSC	Magnitude Squared Coherence
NPSE	Nonlinear Parabolic Stability Equations
POD	Proper Orthogonal Decomposition
PSD	Power Spectral Density
PSE	Parabolic Stability Equations
RMS	Root Mean Square
SNR	Signal-to-Noise Ratio
SPOD	Spectral Proper Orthogonal Decomposition
SVD	Singular Value Decomposition
SWBLI	Shock-wave/boundary-layer interaction
TSP	Temperature-sensitive paint
TTL	Transistor-Transistor Logic
T-S	Tollmien-Schlichting

Variables

α	streamwise component of the complex disturbance wavenumber κ
b	Width of point light source
β	lateral component of the complex disturbance wavenumber κ
C	Contrast
d	Displacement of knife-edge away from 50% cut-off
δ	Boundary-layer thickness
ϵ	Light ray deflection angle
ϵ_y	Light ray deflection angle in the direction normal to the knife-edge cut-off

f	Frequency
f_0	Second-mode fundamental frequency
F	Nondimensionalized frequency
F_1	Focal length of first parabolic mirror
F_2	Focal length of second parabolic mirror
F_{lens}	Focal length of calibration lens
F_s	Sampling frequency
h_0	Freestream stagnation enthalpy
I	Illuminance at camera viewing plane with a cut-off
I_0	Illuminance at camera viewing plane without a cut-off
ΔI	Change in illuminance due to light ray deflection
κ	Disturbance complex wavenumber
K	Gladstone-Dale constant
L	Width of refractive index disturbance
λ	Numerical range of a bispectral density matrix
M	Total number of blocks/realizations
M_c	Convective Mach number across a free shear layer
n	Total number of pixels in a schlieren image
N	Number of temporal samples in each block subdivision
N_a	Number of images used to create an average flow-on image
N_f	Number of frequency triads contributing to the summed mode spectrum
n_t	Total number of temporal samples
η	Refractive index
ρ	Test gas density
r	Radial distance from the lens optical center
Re	Reynolds number
$Re_s^{1/2}$	Local stability Reynolds number
s	Spatial coordinate in the streamwise direction
U_e	Boundary-layer-edge velocity
ω	Disturbance frequency
X	Horizontal spatial coordinate in schlieren image
x	Direction orthogonal to the light-ray direction
Y	Vertical spatial coordinate in schlieren image
y	Spatial coordinate in the direction normal to the model wall
Z	Light-ray direction

Chapter 1: Introduction

1.1 Motivation

In today's geopolitical climate, the United States finds itself heavily motivated in the development of hypersonic missile capabilities. This is largely because the United States' greatest global adversaries, Russia and China, have exhibited many successive technological advances in this area, with Russia commissioning the very first hypersonic missile during its recent invasion of Ukraine. In the last few years, the United States Pentagon has continued to increase its budget requests for hypersonic research, with efforts being focused on the development of hypersonic boost-glide missiles, in which a maneuverable missile is deployed from a rocket booster upon reaching hypersonic speeds, and hypersonic cruise missiles, which utilize onboard air-breathing propulsion during flight. Both systems experience extended flight times within the stratosphere at hypersonic speeds, in stark contrast to long-range missiles following a ballistic trajectory, which reach hypersonic speeds but spend most of their flight time outside of the atmosphere.

Sustained hypersonic flight in the high-density gas of the stratosphere exposes the vehicle surface to extreme aerothermal loading. Thermal management is therefore one of the most critical design considerations for these vehicles. Unfortunately, despite now multiple decades of research effort into prediction methods for hypersonic vehicle skin friction and heat flux, large uncertainty remains in the characterization of these flow quantities. This is, in part, because of the complexity

associated with the laminar-to-turbulent transition of the boundary layer on the vehicle surface. The local heat flux and skin friction are highly influenced by the state of the boundary layer, with laminar-to-turbulent transition typically accompanied by an increase in these quantities by a factor of 5 or greater. Without adequate modeling capabilities of the transition process, safety factors applied to the turbulent heating rates are adopted. This results in a suboptimal design of the thermal protection system, leading to detrimental increases in vehicle mass and volume.

1.2 Hypersonic Boundary-Layer Stability

Turbulence is ubiquitous in fluid flows and its transition from an initially laminar state has fascinated the minds of investigators for many generations. Much of the theoretical framework began with the papers of Lord Rayleigh in the late 1800s and early 1900s, which described an intrinsic linear instability of many inviscid laminar base flows to superposed fluctuating disturbances of infinitesimal amplitude. A viscous theory was soon after investigated by Ludwig Prandtl and two of his students, Walter Tollmien and Hermann Schlichting, who predicted the existence of growing waves of vorticity in wall-bounded shear flows. The linear theory in general was rejected by a majority of those within the community for multiple decades until the experimental discovery of the predicted instability waves, now termed Tollmien-Schlichting (T-S) waves, by Schubauer and Skramstad in 1947. The discovery quickly led to global optimism regarding the linear theory and extensive theoretical, experimental, and computational investigations have since been conducted to further our understanding of the transition process under its scope.

The linear stability theory is based upon a dimensionless expression of the Navier-Stokes

equations, where each flow variable is divided into a steady mean-flow term and an unsteady small disturbance term. The equations are then linearized by dropping the terms which are quadratic in the disturbances. In the case of wall-bounded flows, the equations are further simplified by adopting a parrallel-flow assumption. The result is a set of separable equations, permitting normal mode solutions of the form

$$\mathbf{q}(x, y, z, t) = \bar{\mathbf{q}}(y)\exp\left[i(\alpha x + \beta z + \omega t)\right], \tag{1.1}$$

where $\mathbf{q}$ is the state vector containing the flow variables, $\bar{\mathbf{q}}(y)$ is the complex eigenfunction describing the structure of the wave through the boundary layer, α and β are the x and z components of the complex wavenumber k, and ω is the disturbance frequency. Only specific combinations of α, β, and ω are permitted for any given set of boundary conditions, Reynolds number, and boundary-layer profile. This relationship is called the dispersion relation,

$$\omega = \Omega(\alpha, \beta), \tag{1.2}$$

and its solution determines the eigenvalues of the normal modes, and thus whether they are stable or unstable.

Boundary-layer transition on flat plates, axisymmetric bodies, and airfoils at subsonic and low-supersonic speeds is heavily dominated by the growth of T-S waves. In each of these cases, all other modes are stable and do not substantially interact with the T-S waves, resulting in a relatively simple single-mode system that can be effectively predicted with linear theory. Leslie Mack, however, discovered that the disturbance spectrum for hypersonic boundary layers is con-

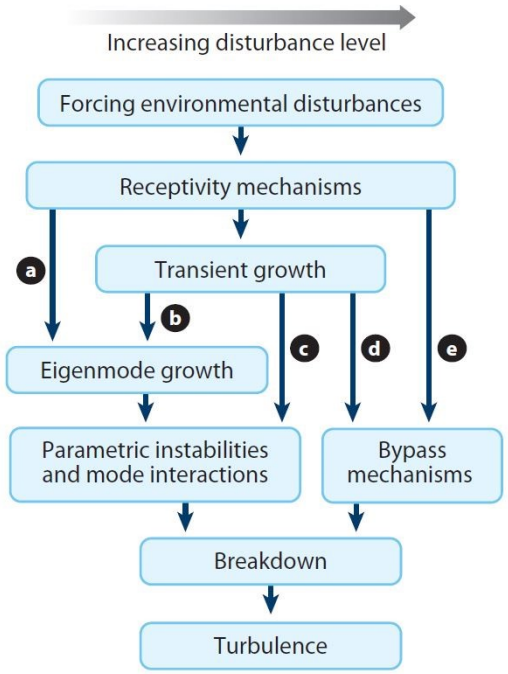

Figure 1.1: Paths to turbulence in boundary-layer flows. Image courtesy of Fedorov (2011).

siderably more complex, owing to a region of the mean flow that is now supersonic relative to the phase speed of modal fluctuations. According to Mack's framework, there are first, second, and higher modes present in hypersonic boundary layers that may simultaneously be unstable, with T-S waves belonging to the first mode and the second and higher modes characterized by trapped acoustic waves reflecting between the wall and the generalized sonic line within the boundary layer.

For slender, axisymmetric bodies at low incidence, upon the boundary-layer-edge Mach number reaching a sufficiently high value ($\gtrsim 4$), the transition to turbulence is dominated by the growth of second-mode-instability disturbances (Mack 1975) rather than the first mode (i.e., the growth rate of the second mode surpasses that of the first mode). The second mode is an inviscid instability with a maximum amplification rate for two-dimensional disturbances (i.e., $\beta = 0$). Mack predicted that the most-amplified second-mode frequencies would be tuned to

the boundary-layer thickness, scaling with U_e/δ, where U_e is the boundary-layer-edge velocity and δ the boundary-layer thickness. Experimental evidence of the existence of the second mode was first provided by Kendall in 1967 (Kendall 1967) in the Jet Propulsion Laboratory supersonic wind tunnel at Mach 4.5. Both unstable first-mode and second-mode waves were measured with hot-wire anemometry and the second-mode growth rates and frequencies were in good agreement with Mack's predictions. In subsequent experiments, Demetriades (Demetriades 1977 and Demetriades 1978), Kendall (Kendall 1975), Stetson (Stetson et al. 1983), and Stetson and Kimmel (Stetson and Kimmel 1992) all observed the second-mode instability and performed parametric studies characterizing the effects of wall temperature, nose bluntness, angle of attack, freestream Reynolds number, and Mach number on the second-mode stability.

1.3 Second-Mode Measurement Techniques

The proportionality of the most-amplified second-mode frequencies to U_e/δ results in dominant frequencies in the range of approximately 100 kHz to over 1 MHz, with the upper extent occurring in hypervelocity facilities. This initially made acquiring instability measurements a significant challenge due to the lack of sensors with adequate frequency responses in the early years of hypersonic boundary-layer transition investigations. There has been a long history of using surface pressure taps and thermocouples within this field of research (e.g., Lachowicz et al. 1996), however these are useful only for identifying transition locations. As noted by Schneider (2004), transition location is heavily influenced by freestream noise, which varies considerably between ground facilities, and thus a direct measurement of instability-wave growth is needed for code validation. The earliest investigations into second-mode instability mechanisms were

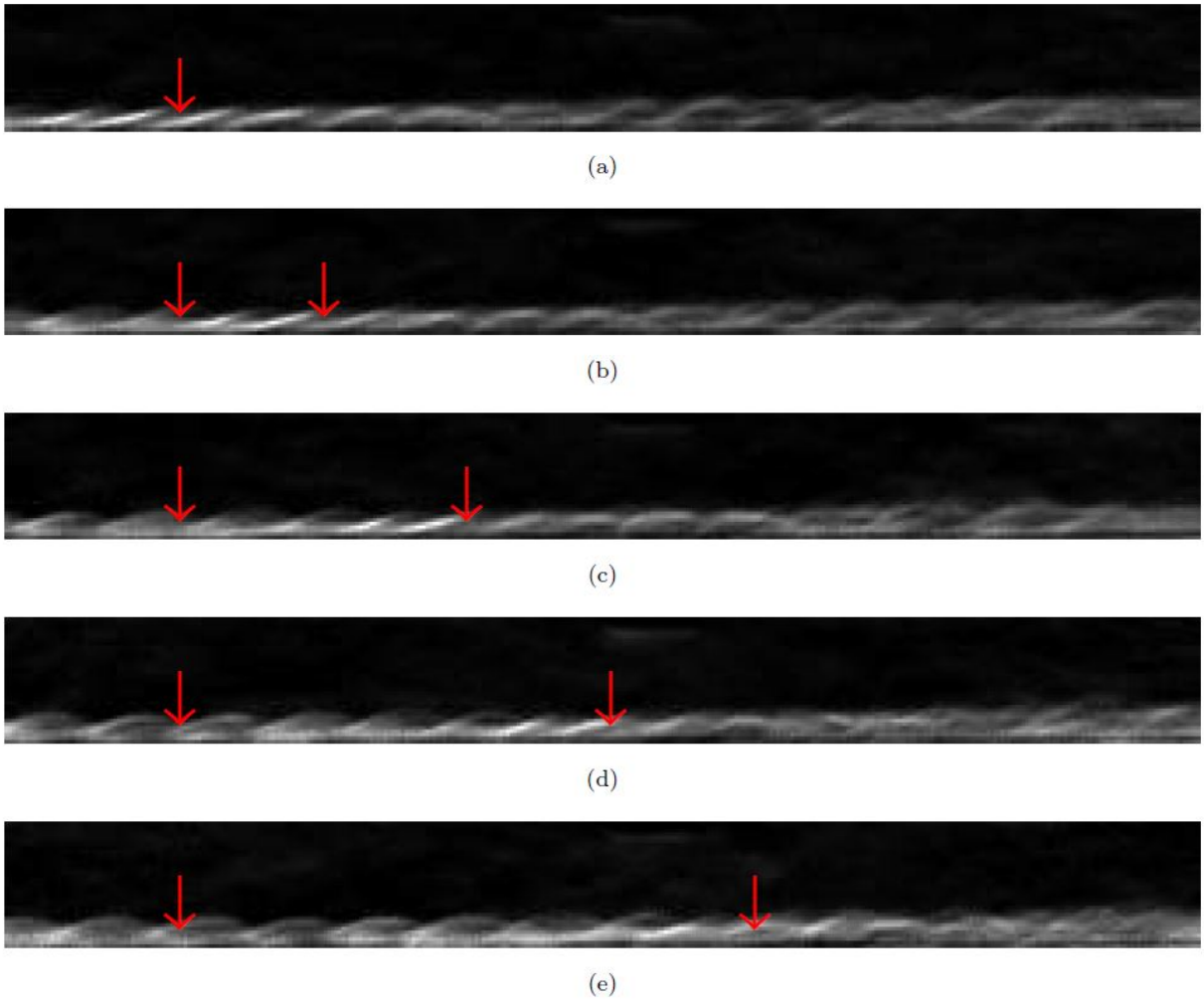

Figure 1.2: Propagation of second-mode waves, captured with schlieren imagery (Casper et al. 2013).

all performed using hot-wire anemometry (e.g., Kendall 1967; Demetriades 1977, 1978; Kendall 1975; Stetson et al. 1983; Stetson and Kimmel 1992). Although this technique has been shown to be able to resolve second-mode content, a hot-wire system with a sufficient frequency response often requires the use of extremely thin hot wires (Li 2004). This places significant mechanical limitations on the system, and thus imposes constraints on the test facility Reynolds number and enthalpy (Estorf et al. 2008), such that, for example, a shock tunnel would produce test conditions that are too harsh. Additionally, the hot-wire anemometry is intrusive, which pre-

cludes simultaneous measurement in multiple streamwise locations. Acquiring a dense spatial matrix of data within the boundary layer, while possible, requires either the use of mechanical systems to translate the probe during the experiment or a larger test matrix to incorporate various discrete-point measurements. Stetson et al. (1983) used both continuous-traverse and discrete-point surveys to analyze boundary-layer stability on a sharp cone at Mach 8. Similarly, Chokani (1999) made discrete-point hot-wire anemometer measurements taken 6.35 mm apart along the cone surface at the maximum root mean square (rms) disturbance height within the boundary layer. A continuous-traverse mechanism would require a sufficiently long test duration, thus adding further constraints on the test facility. The numerous limitations of hot-wire anemometry led researchers to search for other non-intrusive measurement techniques.

Such an instrument was provided with the introduction of the PCB® piezoelectric pressure sensor (e.g., PCB® model 132). This sensor was originally designed for detecting the arrival of a propagating shock wave. However, it was shown by Fuji (2006) in 2006 that the PCB® 132 sensors, with a resonant frequency of over 1 MHz and a pressure resolution of 7 Pa, could be effectively used to measure the second mode on a cone in a hypersonic ground facility. This spurred further investigations using the sensors, (e.g., Estorf et al. (2008); Fuji et al. (2011); Casper et al. (2009, 2013, 2014)), which confirmed their accuracy based on excellent agreement with LST predictions of second-mode frequencies and amplification rates. The study of Casper et al. (2013) noted that spectral broadening occurred in the PCB® spectra at the streamwise position of transition to turbulence (the transitional state of the boundary layer was confirmed with schlieren imagery) with a simultaneous decrease in the amplitude of the second mode, likely caused by averaging with intermittent turbulent bursts. Recently, Marineau et al. (2019) compiled and analyzed the PCB® data collected in 11 different hypersonic wind tunnels across Germany, Belgium,

Japan, and the United States measured on similar sharp cone models. The results identified trends in the second-mode growth rates, including a decreasing growth rate with increasing Mach number over 6, a weak increase in the maximum second-mode amplitudes with increasing Mach number over 6, and a strong decrease in the maximum second-mode amplitudes found at Mach 5 compared to those at Mach 6. Good agreement of measured growth rates with predictions from the Parabolic Stability Equations (PSE) provided confidence that the stability equations could be used effectively across multiple facilities (note that the PSE solutions are an improvement upon eigensolutions found with LST as they account for the history of the disturbance and the streamwise variation of the base flow; see Herbert 1997). Perhaps most significantly, the data revealed a consistent increase in the maximum integrated growth rate (i.e., N-Factor) with increasing freestream unit Reynolds number for all Mach numbers. It was concluded that increasing the unit Reynolds number resulted in an increase in the most-amplified second-mode frequencies (due to the change in the boundary-layer thickness). Tunnel noise, which provides the initial amplitudes of second-mode disturbances, has lower spectral amplitudes at higher frequencies (see Duan et al. 2018) and this leads to an increase in the N-factor at transition. Consequently, it was demonstrated that transition N-factors could not accurately be used for transition prediction without close consideration of the disturbance environment (i.e., Pate's correlation should be avoided).

In addition to hot-wire anemometry, measurement techniques that capture off-surface disturbances include schlieren imagery and focused laser differential interferometry (FLDI). Early experiments were able to use schlieren to capture images of second-mode waves (e.g., Potter and Whitfield 1965; Fischer and Wagner 1972; Demetriades 1974), allowing investigators to confirm the structure of the second-mode density fluctuations and wavelengths. However, the frame rates

of these initial schlieren images were much too low to obtain additional quantitative information regarding the second-mode frequency spectra. It was VanDercreek et al. (2010) who integrated deflectometry with a focused schlieren system, allowing the first non-intrusive off-body measurements of a hypersonic boundary-layer at samplings rates sufficient to analyze the second mode. Their setup consisted of an optical fiber placed at the imaging plane of the schlieren system, followed by a photomultiplier tube, preamplifier, and oscilloscope. Changes in the light intensity at the optical fiber head, which correspond to fluctuations in the refractive index at a specific point in the schlieren focal plane, were recorded at a sampling rate governed by the oscilloscope and preamplifier – here, approximately 1 MHz. Their experiments were conducted on a 7° half-angle cone at Mach 10. Excellent agreement was observed in the second-mode frequencies compared to measurements from PCB® sensors embedded on the model surface, though the focused schlieren deflectometry (FSD) had low signal-to noise at frequencies above approximately 300 kHz. The work inspired further investigations using the FSD system by Hofferth et al. (2013), who conducted a similar set of experiments on a flared-cone in the Texas A&M University Mach 6 Quiet Tunnel (M6QT). A modified system, which coupled a photodetector directly to the fiber optic cable of the FSD, allowed for much better signal-to-noise at high frequencies, enabling the analysis of second-mode harmonics up to the 3rd harmonic (i.e., $3f_0$). The obvious shortcoming of FSD is that each fiber optic cable is only capable of capturing data from a single point in the field of view for each test. Similarly, FLDI has high signal-to-noise ratios and bandwidth, resulting in high fidelity measurements of second-mode power spectral densities by providing pointwise measurements of density disturbances. Notably, in the experiments of Parziale et al. (2013), FLDI was shown to be capable of exceptional temporal and spatial resolution, reaching sampling rates upwards of 20 MHz and beam focal diameters in the test section less than 100 μm

(for comparison, the focal diameter of the FSD in VanDercreek et al. 2010 was on the order of the boundary-layer thickness). The high temporal resolution makes FLDI particularly useful in boundary-layer transition studies conducted in hypervelocity facilities, where the second-mode frequencies may exceed 1 MHz. Although there are significant advantages to FLDI, the system requires precise installation and its pointwise nature limits its usefulness in providing a full picture of the transition process (despite recent advances in multipoint and linear-array systems (e.g., Gragston et al. 2021; Weisberger et al. 2020, 2022; Hameed et al. 2020).

Advancements in ultrahigh-speed cameras over the last 10-20 years have made direct measurement of second-mode wave packets possible with schlieren cinematography. This approach was popularized with the work of Laurence et al. (2012), which derived the structural and propagation characteristics of the second mode using schlieren taken at a frame rate of 500 kHz in the high-enthalpy shock tunnel Göttingen (HEG). As mentioned previously, hot-wire anemometry is not conducive to the harsh conditions of shock tunnels and thus alternative methods must be utilized to measure off-body characteristics of boundary-layer disturbances in these facilities. The propagation speeds of wave packets were measured using two-dimensional image correlation and power spectral densities of the wave packets were calculated along individual rows of pixels in the images. The work of Laurence et al. (2012) was expanded upon by Laurence et al. (2014a, 2016), which incorporated the additional schlieren techniques of a non-uniformly-pulsed laser light source and two-point deflectometry. The application of a multi-phased laser burst enabled the improved characterization of second-mode propagation speeds, such that both the fundamental and first harmonic propagation speeds were calculated on a cone in HEG and found to be identical. The two-point deflectometry additionally enabled the calculation of disturbance growth rates between two off-body streamwise locations. The schlieren-based methods

also identified wall-normal variations of second-mode power spectral densities. At low-enthalpy conditions ($h_0 \approx 3.3$ MJ kg^{-1}), the fundamental and first-harmonic second mode have energy maxima initially close to the wall and near $y/\delta = 0.70 - 0.75$ and develop an additional peak at the boundary-layer edge closer to transition. At high-enthalpy conditions ($h_0 \approx 12$ MJ kg^{-1}), the disturbance energy is much more concentrated at the wall, owing to a significantly higher edge-to-wall temperature ratio.

The characterization of second-mode propagation speeds by Laurence et al. (2012, 2014b, 2016) motivated the development of spatial-to-temporal pixel signal reconstruction techniques by Kennedy et al. (2017, 2018b). These studies demonstrated that, given the near constant propagation speed of the fundamental and harmonic second-mode waves, a pixelwise temporal signal could be reconstructed between the time stamps of two successive schlieren images by utilizing the second-mode waveform present in the images and the propagation speed of that waveform. If the schlieren frame rate was sufficiently large ($\sim 1/2$ the fundamental second-mode frequency), such that wall-normal (vertical) displacement of the second-mode wave packets between two images was negligible, the streamwise (horizontal) row of pixel intensities upstream of any particular pixel could be horizontally scanned over that pixel at the second-mode propagation speed to estimate the temporal signal at that pixel between successive images. The reconstructed temporal signals thus had their effective sampling rates significantly increased, enabling the characterization of second-mode harmonics (even if the relevant frequencies lay above the Nyquist frequency of the camera frame rate). Studies on hypersonic boundary layers over slender cones by Kennedy (2019) utilized this technique for discrete locations in the schlieren image along the maximum rms disturbance streamline. Good agreement was observed between the experimental growth rates of the fundamental second mode and PSE predictions within the linear regime. This

reconstruction technique is adopted for the analysis of schlieren data conducted in the present dissertation. Modifications to the technique are fulfilled to facilitate global reconstruction of the schlieren videos (rather than at discrete points), as well as to generalize the technique to two-dimensional flow fields with spatially varying disturbance propagation velocities. Details of these algorithms are discussed in Chapter 2.

1.3.1 Nonlinear Wave-Packet Development

In general, the transition to turbulence may follow any of the paths depicted in Figure 1.1, with the low-disturbance environments typically found in flight resulting in path "a". The growth of second-mode disturbances is initially governed by eigenmode growth, which is well predicted by linear stability theory. However, upon reaching a sufficient amplitude, nonlinear interactions involving the primary instability become important, which thereby transfer energy into harmonically-related waves via the quadratic terms of the Navier-Stokes equations. Despite substantial research efforts in the area of hypersonic-boundary-layer transition, a complete understanding of the nonlinear and secondary instability regimes has yet to be reached. The high characteristic frequencies of the second mode (ranging from 100 kHz to over 1 MHz) have created significant barriers to thorough experimental study of second-mode disturbance development, particularly concerning the nonlinear regime, which necessarily involves second-mode superharmonics at even higher frequencies. High-fidelity computational tools have been developed, including the Nonlinear Parabolized Stability Equations (NPSE) and Direct Numerical Simulations (DNS), that can simulate nonlinear breakdown of wave packets (see, for example, Sivasubramanian and Fasel 2014, 2015; Unnikrishnan and Gaitonde 2020). These tools offer perhaps the most

detailed descriptions of the viable pathways to transition; however, the chief nonlinear mechanisms involved are dependent on the choice of forcing used to initiate disturbances. Experimental data are required to compare with and validate computational results, particularly concerning the nonlinear mechanisms.

Experimental investigation of nonlinear disturbances in a hypersonic boundary layer originated with Kimmel and Kendall's (Kimmell and Kendall 1991) analysis of data obtained by Stetson et al. (Stetson et al. 1983) in a conventional Mach 8 tunnel. The key result of their analysis was the identification of a first-harmonic peak that appeared in the spectra at approximately twice the frequency of the fundamental second mode, which was not predicted by linear stability theory. A bispectral analysis on the signals revealed quadratic phase-locking between the fundamental and first-harmonic second-mode frequencies, strongly indicating nonlinear wave propagation. Their results showed a deviation of the fundamental growth rate from that predicted by linear stability theory when the first harmonic became amplified, suggesting that nonlinear theories may be required for accurate prediction of wave growth in this region. Other notable early works in the field include those by Chokani (Chokani 2005, 1999), which analyzed the nonlinear regime of transition on a cooled flared cone in a Mach 6 quiet tunnel, and Bountin et al. (2008), which analyzed nonlinear breakdown on a sharp cone in a conventional Mach 6 tunnel using artificial excitation of boundary-layer disturbances via a unidirectional pulse at the second-mode fundamental frequency. In the case of artificial excitation, subharmonic resonance was observed to be the dominant nonlinear interaction, whereas in the cases of natural transition the dominant interaction was the fundamental self-interaction. This is somewhat contrary to analogous cases in low-speed experiments utilizing artificial disturbance excitation (see Kachanov and Levchenko 1984) but may be attributed to the significantly higher presence of the first mode in

the experiments of Bountin et al. (2008), which provided larger amplitude priming oscillations for the second-mode subharmonic resonance interaction. Note that, while the freestream Mach numbers of Chokani (2005, 1999) and Bountin et al. (2008) were similar, the higher amplitudes of the first mode in the experiments of Bountin et al. (2008) were likely a result of the unidirectional pulse being placed in a streamwise location on the model that was receptive to first-mode type disturbances (for an analogous CFD demonstration of this effect, see Novikov et al. 2016). More recent experimental studies include those by Craig et al. (2019), which utilized a schlieren-based measurement technique and identified second-mode fundamental self-interaction as the dominant nonlinear interaction.

The role of superharmonics in hypersonic-boundary-layer transition remains uncertain. Their amplification is the earliest indication of nonlinear significance in second-mode dominated flows. However, like the fundamental disturbance, they are primarily two-dimensional waves whereas turbulence is inherently three-dimensional. In addition, they reach amplitudes prior to breakdown that are only fractions of the fundamental instability, indicating they are not directly responsible for breakdown. There is significant evidence in low-speed transition studies, however, that superharmonics play a vital role in initially exciting three-dimensionality in two-dimensional boundary-layer flows. The process, first theorized by Craik (1971) and further supported by Nayfeh and Bozatli (1971) and Kachanov and Levchenko (1984), involves two simultaneous three-wave resonance interactions: (a) the self-interaction of the fundamental two-dimensional disturbance (1,0) to produce a two-dimensional first harmonic (2,0), and (b) the interaction between the first harmonic (2,0) and a pair of its oblique subharmonic waves (1,$\pm$1). The process thereby transfers energy from the two-dimensional primary instability into three-dimensional waves of the same family. Although this theory was originally developed with

regards to K-type breakdown (also commonly referred to as fundamental resonance) of the first mode, an analogous mechanism was identified for the second mode in hypersonic cone boundary layers in the computational investigations of Sivasubramanian and Fasel (2014) and Sivasubramanian and Fasel (2015) using DNS. In the first, broadband disturbance forcing was applied to simulate a "natural transition" scenario and fundamental resonance was identified as the dominant nonlinear mechanism. Subsequently, the latter investigation perturbed the flow using only a limited number of waves to investigate the fundamental resonance mechanism in isolation. Fundamental breakdown of the second mode was observed to lead to a fully developed turbulent boundary layer and was thus determined to be a viable pathway for transition to turbulence on sharp hypersonic cones.

1.3.2 Shock-Wave/Boundary-Layer Interactions

Slender straight cones at zero and low-nonzero incidence have served as the canonical geometry of initial hypersonic boundary-layer transition studies because the transition process is dominated by the growth of the second mode without significant competition or interaction with other unstable modes. Given the extensive research outlined above, the wave-packet development of the second mode on this geometry is by now well characterized, especially within the linear regime. There is therefore progressive interest among the community in studying the boundary-layer transition on more complex model configurations that involve multi-mode transition. One such geometry is a model with a straight conical forebody followed by a secondary conical frustum of increased half-angle, such that an axisymmetric compression corner is generated at their junction. This geometry has been referred to with multiple names, including a

double-cone, bicone, and cone-flare. Here, we will refer to it as a cone-flare. The outer mold line of true hypersonic vehicles occasionally exhibit sudden angle changes (e.g., on a control surface or engine intake); the cone-flare is intended to replicate the flow deflection experienced at these compression corners while also ensuring the dominant incoming instability encountering the flow deflection is well-known (e.g., either the first or second modes, depending on the freestream conditions).

When a supersonic flow encounters a positive flow deflection (i.e., compression corner), an oblique shock wave will be generated at the corner, introducing a shock-wave/boundary layer interaction (SWBLI). For low turning angles, the oblique shock wave will remain attached to the wall at the point of deflection and a weakly positive (adverse) pressure gradient will exist across the shock. The pressure gradient will increase in strength with increasing turning angle and, upon reaching a sufficiently strong pressure gradient, cause the incoming boundary layer to separate, thus generating a region of separated flow at the corner known as a separation bubble. The SWBLI will not only affect incoming disturbances propagating from the upstream boundary layer but can also give rise to new instability mechanisms. This is particularly true in the separated case due to (1) the emergence of a shear layer between the slow recirculating flow of the separation bubble and the fast flow traversing above the bubble, creating unstable shear-layer disturbances, and (2) streamline curvature in the SWBLI region, leading to a centrifugal instability in the form of Görtler vortices.

The stability of compressible free shear layers was originally investigated by Lees and Lin (1946), who provided the basic formulation of the mathematical theory. The stability characteristics of shear-layer disturbances were later investigated with respect to variations in Mach number, Reynolds number, and the velocity and temperature ratios across the shear layer (e.g.,

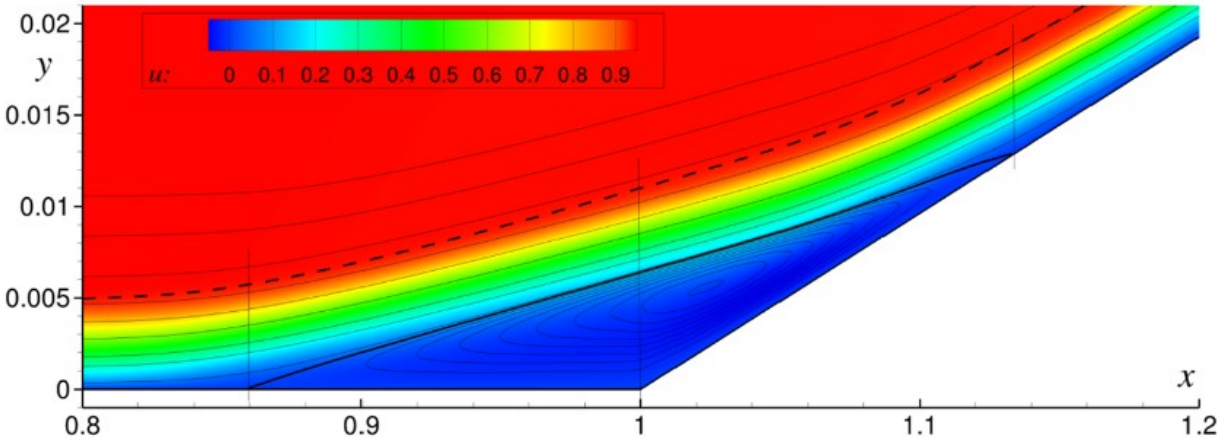

Figure 1.3: Field of u velocity and streamlines near the separation region: zero streamline (bold) and mixing layer (dashed line). Taken from Novikov et al. (2016).

Zhuang et al. 1990; Jackson and Grosch 1989, 1990) in the context of compressible mixing layers found in scramjet engines. Two groups of unstable modes were identified (referred to as the slow and fast modes), both of the vortical type, whose stability was heavily dependent on the convective Mach number, M_c, of the fast-moving gas relative to the slow-moving gas. The maximum instability growth rate sharply decreased with increasing convective Mach number for $M_c < M_*$, where M_* is a critical Mach number at which the disturbance phase speeds are both sonic, and decreased more slowly thereafter until reaching a reversal point, after which the growth rate began to increase again. Increasing the temperature of the slow-moving gas relative to the fast-moving gas led to an overall decrease in the growth rate of the instabilities and delayed the reversal to higher convective Mach numbers. Although the characteristics of the second-mode and shear-layer instabilities are reasonably well understood in isolation, only recently have researchers begun to investigate how they might interact and compete in leading transition in hypersonic compression corner flows. Providing insight into this multi-mode competition is of practical importance as it will guide vehicle designers in deciding which instability is more important to control.

There is a considerable quantity of prior research on cone-flare geometries at hypersonic

conditions, as well as for similar geometries that induce two-dimensional SWBLIs, such as the double-wedge and cylinder-flare. Much of this work has been focused on the effects of boundary-layer transition on the flow topology and aerothermal loading (e.g., Miller et al. 1964; Zakkay et al. 1967; Heffner et al. 1993; Running et al. 2019, 2020; Roghelia et al. 2017). Part of the motivation for ongoing research into the flow topology on these geometries is the presence of spanwise heat-flux variations aft of the compression corner. While this is an interesting phenomenon, of greater relevance to the present study are the more limited studies that elucidate the dominant transition mechanisms. Balakumar et al. (2002, 2005) numerically investigated a 5.5° compression ramp encountering a freestream Mach number of 5.373, performing a stability analysis of the flow field using PSE and DNS for the case of separated flow at the corner. They studied the stability of two-dimensional, fixed-frequency disturbances traversing the corner and identified multiple unstable modes. The second mode, which was the dominant instability approaching the corner, was found to be unstable upstream of separation and downstream of reattachment but was neutrally stable while traversing the separation region. In its place, a lower-frequency mode at approximately 38% of the second-mode dominant frequency was found to be the most unstable within the separation region. However, upon investigating the density eigenfunctions for each of these disturbances, they noticed the low-frequency eigenfunction changed from a first-mode type distribution upstream of the corner to a second-mode type distribution within the separation region. Similarly, the eigenfunction for second-mode dominant frequencies changed from a second-mode type distribution to a third-mode (i.e., the second of the higher acoustic modes, according to Mack's terminology) type distribution within the separation region. This suggests that the most unstable mode within the separated region remains as an acoustic mode, with a relatively thick supersonic region inside the separated region boundary layer leading to larger

wavelengths, and hence lower frequencies.

The work of Novikov et al. (2016) extended the simulations of Balakumar et al. (2002, 2005) to investigate three-dimensional disturbances on the same configuration and flow conditions. They monitored the streamwise development of broad-spectrum wave packets generated with a localized pulse at the wall boundary. The transition process was dependent on the wave packet structure entering the corner, which was controlled by locating the pulse in a streamwise position that was dominantly receptive to either the first mode or second mode. For a wave packet that was dominated by the second-mode instability, as will be most relevant here, the process was in general agreement with that of Balakumar et al. (2002, 2005). High-frequency second-mode disturbances were unstable upstream of separation and downstream of reattachment but neutrally stable while traversing the corner. Planar mid-frequency disturbances were amplified throughout the separation region, as well as oblique low-frequency disturbances, which were most-amplified just upstream of the reattachment point. These low-frequency disturbances disappear quickly after reattachment. Notably, in the case of a first-mode dominated wave packet entering the separation region, only oblique modes are unstable within the separated region, with minor amplification of low-frequency planar acoustic disturbances only at the separation point.

The transition process on a cylinder-flare with a 15° axisymmetric compression corner at Mach 5 was studied numerically by Lugrin et al. (2021) using quasi-DNS, with the computational domain encompassing 60° in the azimuthal direction. Three-dimensional disturbances were excited using white noise forcing. It was found that the upstream boundary layer was first-mode dominated with a weakly unstable second mode. Through the separated region at the compression corner, the second mode was immediately damped and found to be inconsequential during the transition process. Instead, the proposed transition mechanism was first-mode oblique break-

down, which is a nonlinear process by which stationary streamwise streaks are excited by the nonlinear difference interaction of a pair of oblique first-mode waves of equal frequency and opposite spanwise wavenumber. These nonlinearly-generated streaks were linearly amplified after the reattachment point, leading to the eventual breakdown to turbulence.

Benitez et al. (2020) obtained FLDI and PCB measurements on a cone-cylinder-flare in the Boeing/AFOSR Mach 6 Quiet Tunnel (BAM6QT) at Purdue University, offering rare off-body disturbance measurements near the shear layer at the compression corner and within the downstream flare boundary layer. At sufficiently high Reynolds numbers, the second mode was found within both the separation region and on the flare and found to grow in amplitude downstream of the corner. Additional lower frequency disturbances were identified in the range of 50-170 kHz, which possessed a distinctly different propagation speed than the second-mode propagation speed. These disturbances were not seen in the FLDI measurements taken at the shear layer at the corner but were found to begin growing in amplitude in the FLDI and PCB stations located downstream of the corner. It was concluded that these disturbances were generated by the shear layer, as they were only present with flare angles sufficiently high to cause separation at the corner.

More recently, Butler and Laurence (2021) performed experimental investigations of boundary-layer transition on a 5° half-angle cone-flare at Mach 6 with various compression angles of +5°, +10°, and +15°, intended to induce both fully attached and separated corner flows. They used ultra-high speed calibrated schlieren with frame rates up to 822 kHz, enabling direct measurement of the second-mode disturbances from pixelwise intensity signals. For an attached-shock case (corresponding to the +5° configuration), they observed second-mode dominated flow through the corner. The weakly separated case (corresponding to the +10° configuration) exhibited combined second-mode and low-frequency shear-layer disturbances, with the former unstable before

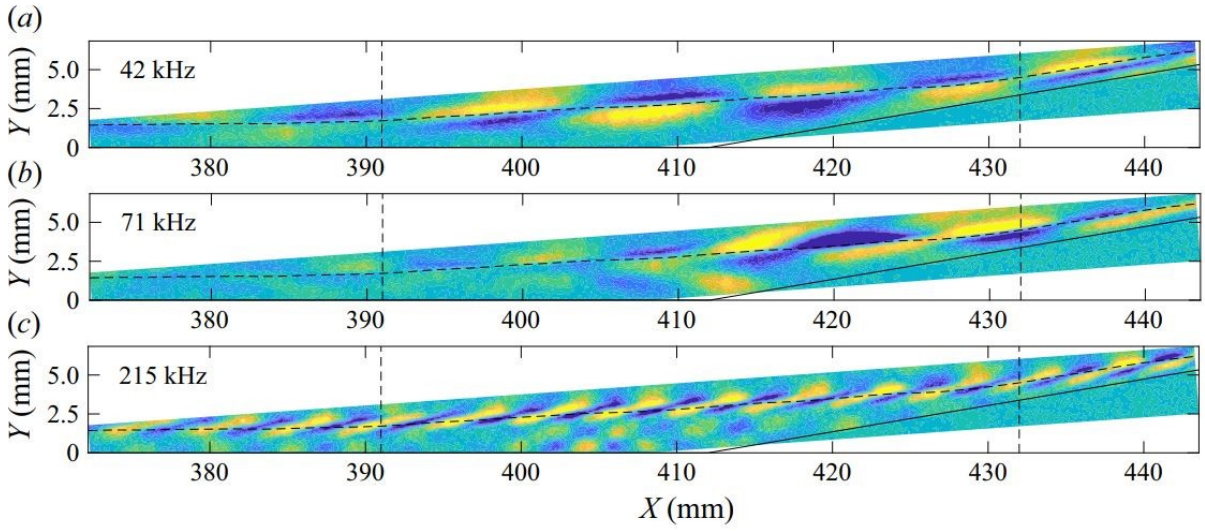

Figure 1.4: (Top to bottom) SPOD mode shapes corresponding to shear-layer disturbances at 42 kHz and 71 kHz; SPOD mode shape corresponding to second-mode disturbance at 215 kHz. Taken from Butler and Laurence (2021).

separation and after reattachment and neutrally stable in-between and the latter amplified within the separation region. By increasing the compression to +15°, the shear-layer instability became dominant, reaching N-factors significantly higher than those of the second-mode. In every configuration, significant disturbance energy, both of second-mode and shear-layer origin, was seen to be radiated along the shocks present at the corner. The precise mechanism ultimately responsible for breakdown, however, was not deduced.

1.4 Scope of Current Work

The goal of the present study is to address some of the current gaps in our understanding of the transition process over slender cone and cone-flare geometries. In particular, we are interested in improving and utilizing the reconstruction technique developed by Kennedy et al. (2017, 2018b), as this technique enables quantification of high-frequency content from calibrated schlieren cinematography without sacrificing the field of view of the image. The methodology

is first applied to two sets of experiments performed on a sharp 7° half-angle cone, one at zero angle of attack at Mach 6, conducted in the NASA Langley 20-inch Mach 6 wind tunnel, and the other at nonzero angle of attack at Mach 14, conducted in AEDC Tunnel 9. The reconstruction technique is applied globally, such that analysis of the second-mode development across the entire field of view is facilitated. The focus is to ensure that the expected behavior of the second-mode fundamental instability is observed in the linear regime, and then to proceed with a more novel global analysis of the nonlinear regime, including a characterization of the second-mode harmonics. Flush-mounted PCB® sensors are included in the model to compare with and validate the second-mode frequencies resolved from the schlieren analysis. Spectral proper orthogonal decomposition and a bispectral analysis, incorporating both pointwise autobicoherence investigations and bispectral mode decomposition, are utilized to elucidate the dominate instability structures and their nonlinear interactions with each other.

Once the usefulness of the global reconstruction technique has been demonstrated on the more canonical straight-cone boundary layer, we progress to its application on a cone-flare geometry. As outlined in the previous section, while multiple instabilities have been identified in the corner region, there is not yet a clear consensus on the dominant instability mechanisms leading to breakdown. In addition, it remains to be answered what influence the Mach number has on the development and interplay of the present instabilities. To date, the studies investigating the transition process on these geometries have been limited to freestream Mach numbers of 6 and below (although, there are a small number of older studies focused on the characterization of the mean flow at higher Mach numbers, e.g., Miller et al. 1964; Zakkay et al. 1967). This motivated us to conduct a set of experiments at Mach 14 in the Mach 10-20 Longshot Hypersonic Gun Tunnel, using an identical geometry to that used in Butler and Laurence (2021). With a substantially

higher Mach number, the shock waves present in the corner region will lie significantly closer to the body, leading to an extended interaction with the incoming second-mode disturbances. Additionally, the temperature ratio across the mixing layer of the separated region will be skewed towards higher temperatures within the separation bubble, which is expected to have an effect on the stability of shear-layer disturbances. Utilizing the aforementioned analytical methods, these effects will be addressed in the present study.

Chapter 2: Diagnostic and Analytical Techniques

2.1 Calibrated Schlieren

Schlieren flow visualization is an optical technique that records the density fluctuations within a transparent medium by transforming these fluctuations into regions of light and dark in a greyscale image. The method relies upon the principles of refraction, whereby local changes in the gas density result in deflections in the path of a passing light ray. Various schlieren systems have been developed over the years; in the present work, one experimental campaign utilizes a basic inline two-lens schlieren setup and the other two campaigns utilize the conventional Z-type schlieren. The Z-type system is schematically shown in Figure 2.1. Here, light emitted from a circular source is collimated by a parabolic mirror of focal length F_1 and passed through a test section that possesses some field of varying refractive index of width L. The light rays exiting the test section are re-focused by a second parabolic mirror with focal length F_2, typically identical to the first, and a camera is placed behind the focal point to capture the resulting image. As the light ray encounters changes in the refractive index over the course of the distance L, its path will be deflected by an angle, ϵ, given by

$$\epsilon = \frac{1}{\eta_\infty} \int_0^L \frac{\partial \eta}{\partial x} \partial Z, \tag{2.1}$$

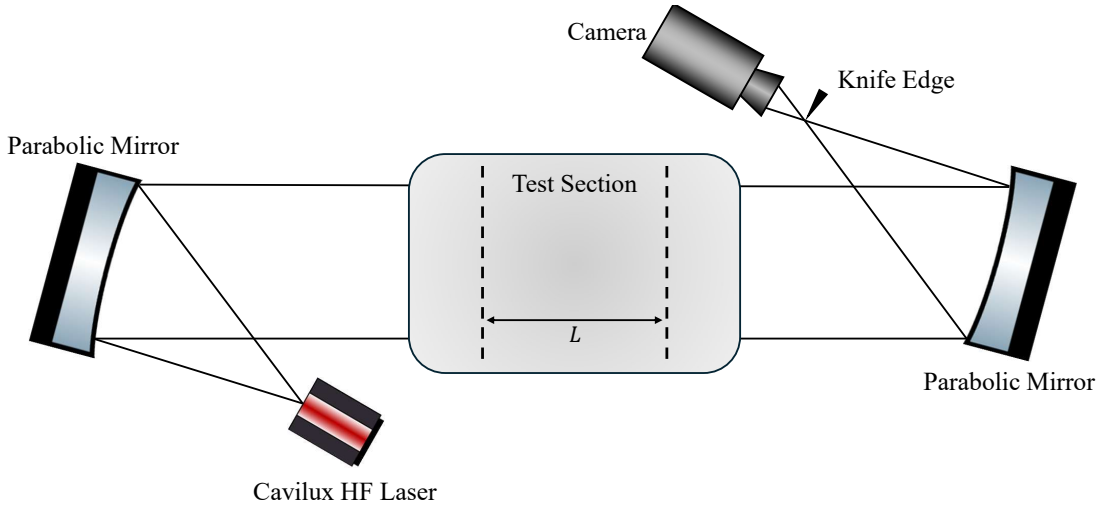

Figure 2.1: Z-type schlieren utilizing synchronized laser as the light source

where x represents the direction orthogonal to the light-ray direction, Z. A linear relationship between the refractive index, η, and the gas density, ρ, can be expressed with the Gladstone-Dale relation:

$$\eta = K\rho + 1, \tag{2.2}$$

where K is the Gladstone-Dale constant of the test gas.

In a schlieren system, a knife edge, referred to as the "cut-off", is placed at the focal point of the second mirror. Note that the circular light source is typically generated using an aperture of width b, which, in the current system, will create a focal "point" of the same size on the opposite end of the system. Partially inserting the knife edge at the focal point will uniformly decrease the intensity of undeflected light rays. Following from the principles described in Settles (2001) and Speak and Walters (1954), the illuminance at the camera is equal to

$$I = I_0 \frac{b/2 - d}{b}, \tag{2.3}$$

where I_0 is the illuminance without a cut-off and d is the displacement of the knife edge away from 50% cut-off. Light rays deflected by an angle ϵ_y, where now y denotes the portion of the deflection normal to the knife edge, will have their focal points shifted by a distance of approximately $F_2\epsilon_y$ and will experience a different amount of cut-off. The deviation in illuminance at the camera is then equal to

$$\Delta I = I_0 \frac{F_2 \epsilon_y}{b}. \tag{2.4}$$

The contrast observed in the schlieren image as a result of a varying refractive index will therefore be

$$C = \frac{\Delta I}{I} = \frac{F_2}{b/2 - d}\epsilon_y, \tag{2.5}$$

with the quantity

$$\frac{F_2}{b/2 - d} \tag{2.6}$$

often being referred to as the overall sensitivity of the schlieren system. The sensitivity for a given system with fixed mirrors is then maximized by driving the cut-off into the focal point as much as possible. This, however, simultaneously lowers the overall illuminance of the image according to equation 2.3. A highly-sensitive schlieren system thus necessitates a high-powered light source.

It is clear from equation 2.4 that there is an injective relation between the light ray deflection angle, ϵ_y, and the resulting change in illuminance, ΔI, so long as the light source, mirrors, and knife-edge position remain fixed. For a circular light source and focal point (as is commonly the case), this relationship is nonlinear and may be difficult to accurately characterize analytically due to uncertainties within the system (e.g., imperfections in the mirrors, misalignment of

optical components, etc.). A simple method of mapping this relationship, described in Schardin (1942) and Hargather and Settles (2012), involves instead placing a weak converging lens into the schlieren field of view. Collimated light rays passing through the calibration lens are focused to a point such that they are deflected by an angle that is dependent on the radial location of the passing light ray (see Figure 2.2). For a weak lens, we can approximate this as

$$\frac{r}{F_{lens}} = \tan\epsilon \approx \epsilon, \tag{2.7}$$

where r is the radial distance from the lens center and F_{lens} the focal length. Since the deflection angle varies with radial position on the lens, the passing light rays will experience a different level of cut-off by the knife edge and a pixel-intensity gradient that is normal to the knife edge will be imaged inside of the calibration lens. This effect is shown in Figure 2.3 for the calibration lens used in the current experiments at two different sensitivity settings. The deflection angles that span the intensity gradient within the calibration lens determine the angles that may be measured by the schlieren system. A high-sensitivity system enables better signal-to-noise for small deflection angles at the expense of restricting the range of observable angles. The pixel intensity located at the lens' optical center corresponds to undeflected light rays; however, since there is never 100% light transmission through the lens, this intensity will be slightly less than the background intensity observed outside of the lens. In the present experiments, a plano-convex spherical lens of N-BK7 glass with a focal length of 10 m, a diameter of 25.4 mm, and a light transmission rate of 92% was used for calibration.

The intensity profiles observed in Figure 2.3 provide the necessary information for the transformation of pixel intensities in a schlieren image to deflection angles via equation 2.8,

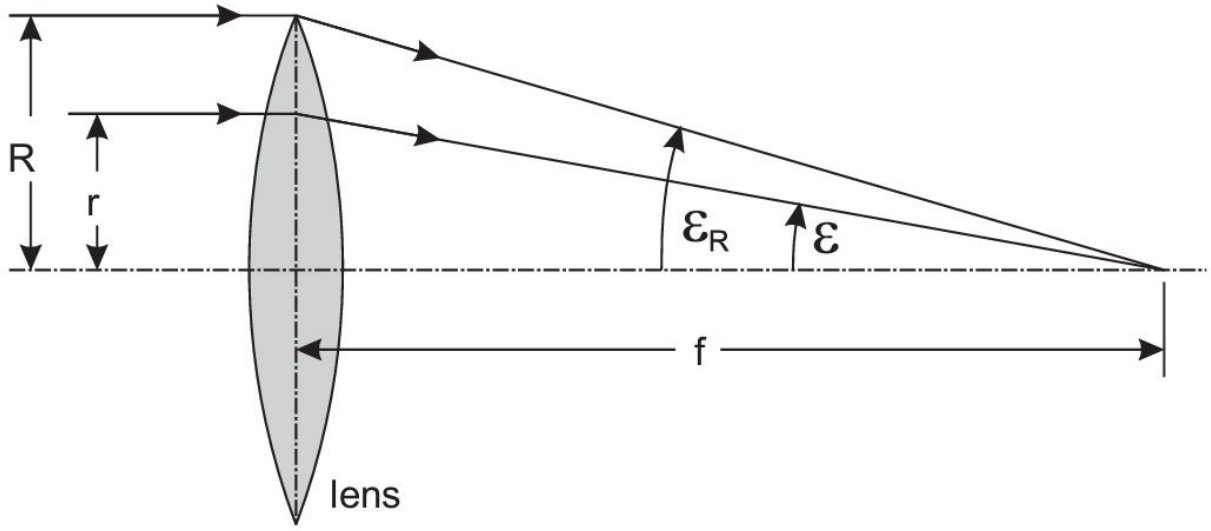

Figure 2.2: Collimated light rays passing through a converging lens. Image courtesy of Hargather and Settles (2012).

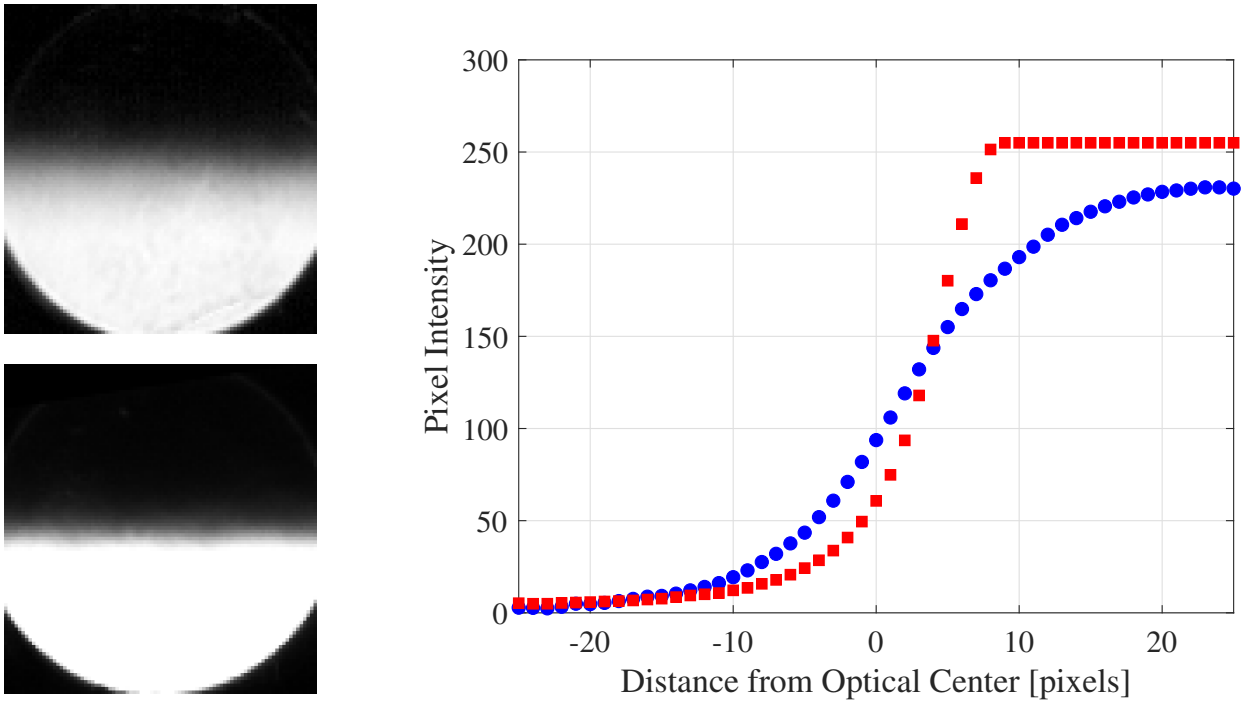

Figure 2.3: (Top Left) Calibration lens at low sensitivity. (Bottom Left) Calibration lens at high sensitivity. (Right) Calibration curves for low-sensitivity (blue ○) and high-sensitivity (red □) lenses.

where now ϵ is equal to ϵ_y since only deflections normal to the knife edge are observed by the system. Inserting equation 2.2 into 2.1 we are left with

$$\epsilon_y = \frac{K}{\eta_\infty} \int_0^L \frac{\partial \rho}{\partial y} \partial Z. \tag{2.8}$$

Given that the base flow and disturbances under investigation are approximately two-dimensional, equation (1.8) can suitably be approximated as

$$\epsilon_y = \frac{KL}{\eta_\infty} \frac{\partial \rho}{\partial y}, \tag{2.9}$$

with L representing the width of the refractive index disturbance.

Note that the light source depicted in Figure 2.1 is a Cavilux HF Laser. This is a high-powered (280 Watt) pulsed-diode light source that generates low-coherence light at 640 nanometers. In high-speed mode, the laser operates for 10 seconds at a 2% duty cycle with an adjustable pulse-width from 10 ns up to 200 μs at 10 ns increments, yielding a maximum operating frequency of 2 MHz. The laser also accepts external TTL (transistor-transistor-logic) signals for frame synchronization purposes. These capabilities make it ideal for use in a schlieren investigation of hypersonic boundary-layer disturbances, providing high-powered short-duration light pulses that enable sufficient illumination at high frame rates that effectively freeze the flow.

2.2 Time-Resolved Signal Reconstruction Technique

2.2.1 Straight Cone Algorithm

If each camera pixel were to be used as an independent sensor, the Nyquist criterion would dictate a frame rate of many times the second-mode frequency to obtain frequency-resolved measurements of instability power and growth rates, including harmonics, from the raw pixel intensity time-series (e.g., as was done in Butler and Laurence 2021). To bypass this requirement, time-resolved pixel intensity signals are reconstructed using neighboring spatial data to increase the effective frame rate, taking advantage of the near constant propagation speed of the second-mode wave-packets and associated harmonic content (Laurence et al. 2016). Such a technique was employed by Kennedy et al. (2018b) for select interrogation locations; here we extend it to every pixel within the visualized boundary layer to allow global analysis techniques to be employed. A high camera frame rate (on the order of half the fundamental disturbance frequency) is still recommended to ensure wave-packets do not evolve significantly between images (e.g., such that flow movement in the direction normal to the wall is negligible), as this would render the interpolation employed inaccurate.

Although this reconstruction technique has already been described in Kennedy et al. (2017), given its importance in the present analysis, it is outlined again here. The first step in the reconstruction is the calculation of the average propagation speed of the second-mode wave-packets; further details of this procedure are provided in section 3.4. The signal reconstruction procedure, outlined in Figure 2.4, is then conducted as follows. Consider a wave-packet propagating downstream at speed U_p. The pixel intensity at a specific streamwise location, X_0, is known exactly

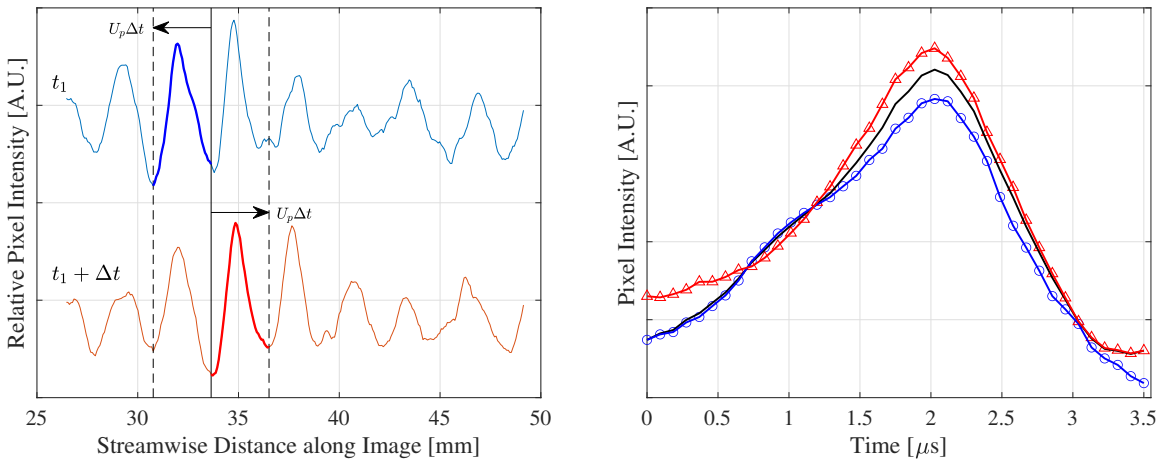

(a) (b)

Figure 2.4: (a) Pixel intensity signals along a single row in successive images. (b) Reconstructed signal (black −) using a linearly-weighted average of the bolded portions of the signals at t_1 (blue ○) and $t_1 + \Delta t$ (red △).

“

from the two schlieren images at times t_1 and $t_1 + \Delta t$, where Δt is equal to $1/FR$ and FR is the camera frame rate. We wish to reconstruct the signal between these two known points in time. Since we know the propagation speed, we have two possibilities for generating such a reconstruction: (a) the pixel intensities between $X_0 - U_p\Delta t$ and X_0 in the first image (which represents information that is about to pass over X_0); or (b) the pixel intensities between X_0 and $X_0 + U_p\Delta t$ in the second image (representing information that has just passed over X_0). The fidelity of either option degrades as we consider pixels further from X_0. Therefore, we use a linearly-weighted average of the two such that the reconstructed signal is exact at t_1 and $t_1 + \Delta t$. Figure 2.4 exemplifies this process, where the blue and red signals represent the rowwise pixel intensity signals of a single row in the boundary layer at times t_1 and $t_1 + \Delta t$. This process is repeated for all images of interest and all linearly-weighted-averaged signals are concatenated into a single temporal signal. The resulting effective sampling frequency is $U_p/\Delta x$, where Δx is the pixel spacing in the imaging plane. Clearly, the assumption of a constant propagation speed for all disturbances is implicit in

this technique; effects of a deviation from this assumption are examined in Appendix A.

2.2.2 Cone-Flare Algorithm

The technique as described thus far is limited to analyses of fundamental and harmonic second-mode content on straight cones, such that the assumptions of a constant propagation speed and quasi-parallel disturbance streamlines remain valid. Boundary-layer disturbances passing through a compression corner, as in the current study, will violate these assumptions; therefore, a modified reconstruction procedure, capable of handling disturbances with spatially-variant velocities, has been developed and will be outlined in the following section.

2.2.2.1 Disturbance Propagation Velocities

The first task in either reconstruction algorithm is the calculation of the disturbance velocities. On straight cones in hypersonic flow conditions, it is sufficient to compute the average streamwise phase speed of the fundamental second mode. Here, we must compute the average disturbance phase speed and direction at every point in the image field of view. Note that, because the reconstruction requires a unique propagation velocity for the determination of the locally-relevant waveform along the distance $U_p \Delta t$, the technique cannot consider multiple disturbances of different types (e.g., first mode, second mode, shear-layer disturbances) simultaneously as their phase velocities may differ substantially. The following description of the reconstruction procedure will be outlined and illustrated for the calculation of second-mode velocities.

To improve the accuracy of the disturbance velocimetry, each schlieren image first undergoes a series of manipulations to accentuate the desired features. This image processing sequence

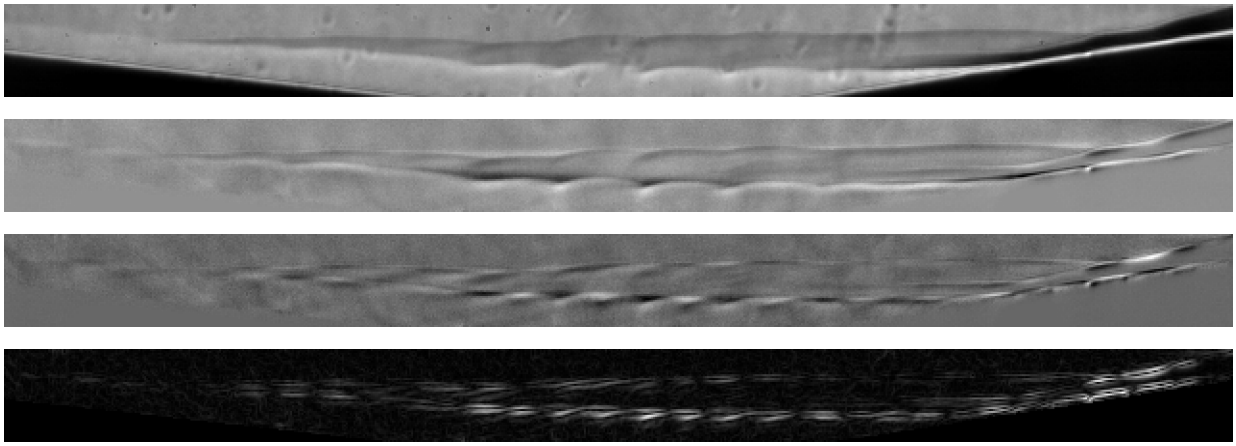

Figure 2.5: Image processing sequence from top to bottom: original image, reference-subtracted image, high-pass-filtered image, and image gradient magnitude.

is exemplified in Figure 2.5. Consider an image of interest, I_n, taken during the useful test time. To begin, the image I_n is reference-subtracted using an average of ~100 sequential images centered at I_n. Once all images I_1 through I_{n_t}, where n_t is the total number of images in the useful test time, have been reference-subtracted, each pixel-intensity time-series (taken from images I_1 through I_{n_t}) is filtered using a zero-phase filter to attenuate all frequencies outside the second-mode band. In the current experiments (see Chapter 5), the fundamental second mode is found between 130-350 kHz (estimated with flush-mounted PCB® sensors). For the case of shot 1874, which has a Nyquist frequency of 125 kHz (determined by the camera frame rate), the second mode is aliased to approximately all resolvable frequencies; therefore, a low-pass filter with a cutoff frequency of 50 kHz is chosen to accentuate the strongest second-mode content while attenuating shear-layer disturbances that may be present in the range of 50-125 kHz. For the cases of shots 1877 and 1878, which have Nyquist frequencies of 250 kHz, a high-pass filter with a cutoff frequency of 130 kHz is used. The images are then reconstructed using the filtered pixel time-series signals. Finally, a Sobel filter is applied to each image to estimate the magnitude of the image gradient. This step is motivated by the Sobel operator's usefulness in edge-detection

algorithms. The computation of disturbance propagation speeds relies on the ability to track the translation of individual wave packets in image pairs; emphasizing the wave-packet edges was found to improve tracking accuracy.

Once the image processing is complete, the algorithm proceeds with computing the disturbance displacements throughout the field of view for every image pair, as follows. Consider two successive images, as shown in Figure 2.6, taken from shot 1877. At every pixel, a correlation window is extracted around said pixel from the first image of the pair, depicted as a white box in the top image of Figure 2.6. In the subsequent image, a collection of windows of the same dimensions are also extracted; to help prevent unrealistic results, these secondary windows are only chosen in a region of the image where it is suspected the feature windowed in the first image could have moved. Cross-correlation coefficients are then computed between the window of the first image and all secondary windows of the subsequent image. The result is a matrix of coefficients, shown for example as the colored region in the bottom image of Figure 2.6, where each colored pixel represents the coefficient value (blue corresponding to a low correlation and red a high correlation) for the window boxed around that pixel. A two-dimensional Gaussian filter is convolved with the matrix of correlation coefficients to apply smoothing, and the location of the maximum provides the displacement of the feature windowed in the first image. This sequence is repeated for every pixel in the first image. In order to handle points close to the image boundaries and the cone surface, the images are padded with NaN (i.e., "Not a Number") values and the pixel values corresponding to the cone-flare surface are replaced with NaN. In this manner, when performing the cross correlation for windows which contain NaN values, the NaN indices are omitted. Once displacements for each pixel in the first image of the pair have been computed, the process is repeated for all other image pairs and the average displacements are recorded. Note

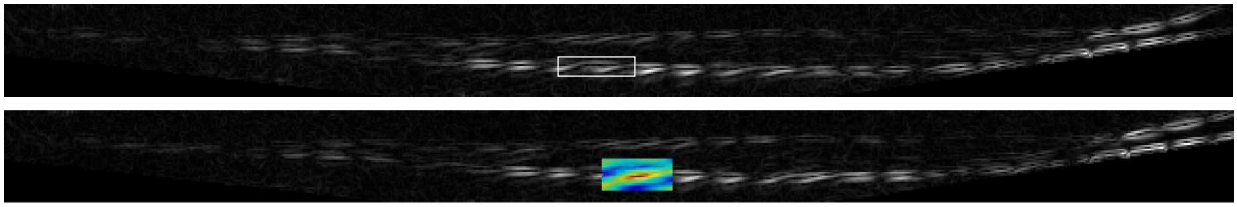

Figure 2.6: Cross correlation window in first image (top) and matrix of cross correlation coefficients in subsequent image (bottom)

that the methodology thus far is akin to an upwind numerical discretization scheme, where the displacement of the feature between two images is represented at the most upstream point. To improve the order of accuracy, this is modified such that the averaged displacements are instead represented at the midpoints, i.e.,

$$\begin{aligned} \tilde{U}(X + \frac{U(X,Y)}{2}, y + \frac{V(X,Y)}{2}) &= U(X,Y), \\ \tilde{V}(X + \frac{U(X,Y)}{2}, y + \frac{V(X,Y)}{2}) &= V(X,Y), \end{aligned} \tag{2.10}$$

where $\tilde{U}$ and $\tilde{V}$ represent the modified horizontal and vertical displacements in pixels, U and V the original displacements, and X and Y the horizontal and vertical coordinates in pixels. This operation creates a nonuniform spatial grid that is different from the original uniform grid of the images; therefore the gridded data of $\tilde{U}$ and $\tilde{V}$ is interpolated back onto the original grid.

2.2.2.2 Temporal Signal Reconstruction

As stated previously, the temporal signal reconstruction technique performed at a certain pixel involves the concatenation of spatial signals around that pixel, with the propagation velocities providing the necessary information to determine the disturbance streamline through the

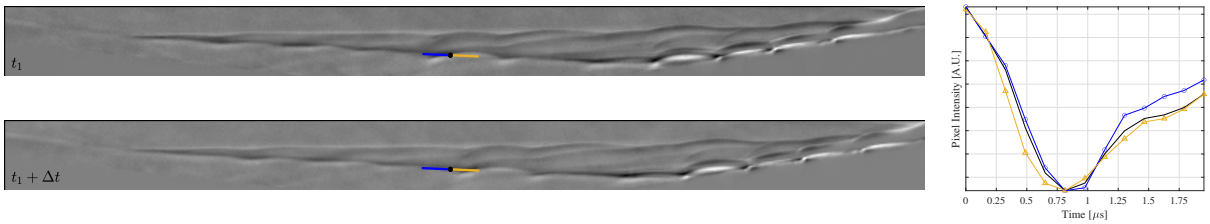

Figure 2.7: Local disturbance streamline through pixel undergoing temporal reconstruction. Two sequential images are shown (left). Reconstructed signal (black −) using a linearly-weighted average of the backward spatial signal at t_1 (blue ○) and forward spatial signal at $t_1 + \Delta t$ (yellow △).

pixel as well as to transform spatial units into temporal ones. The procedure here in general follows closely to that described in section 2.2.1, with modifications to address the now spatially variant disturbance velocity grid. Note that there are two equally valid choices for the spatial signals to be used to reconstruct a temporal signal over a particular pixel located at (X_0,Y_0): (1) the upstream portion of the streamline passing through (X_0,Y_0), now of length $\int_t^{t-\Delta t} \boldsymbol{u}(X(\tau), Y(\tau))\, \mathrm{d}\tau$, where $\boldsymbol{u}(X, Y)$ is the disturbance velocity vector at (X, Y), or (2) the downstream portion of the streamline, of length $\int_t^{t+\Delta t} \boldsymbol{u}(X(\tau), Y(\tau))\, \mathrm{d}\tau$. The validity of either option degrades as the distance away from (X_0,Y_0) increases, as the waveform in the spatial signal has a longer time to deform from its true value at (X_0,Y_0). Option (1) better represents the leading half of the waveform and option (2) better represents the trailing half; therefore, a linearly-weighted averaging of the two spatial signals is chosen for the reconstruction.

Figure 2.7 exemplifies the procedure using two sequential reference-subtracted images, where the reconstruction technique is performed at a given pixel located at (X_0,Y_0), denoted as a black marker. Blue and yellow lines in either image represent the backward and forward streamlines through (X_0,Y_0), each spanning a time equal to Δt. The temporal signal at times between t_1 and $t_1 + \Delta t$ are constructed from a linearly-weighted averaging of the backward spatial signal

obtained from the image taken at time t and the forward spatial signal obtained at time $t + \Delta t$, as shown in Figure 2.7. The signal is exact at both t_1 and $t_1 + \Delta t$, ensuring the concatenation of each spatial signal does not produce a discrete error in the reconstructed signal (as would be the case if performing the reconstruction using either the backward or forward signals alone). Note that, if one were to use all of the available pixels in the spatial signals to reconstruct the temporal ones, a nonuniform magnitude of the disturbance velocity (i.e., $\|\boldsymbol{u}(X, Y)\| \neq c$, where c is a constant) would produce a spatially-variant temporal resolution, as the distances $\int_t^{t-\Delta t} \boldsymbol{u}(X(\tau), Y(\tau))\, \mathrm{d}\tau$ and $\int_t^{t+\Delta t} \boldsymbol{u}(X(\tau), Y(\tau))\, \mathrm{d}\tau$ depend on the position. To prevent this, the number of pixels spanned by the distance $\|\boldsymbol{u}(X, Y)\|_{min}\Delta t$, where $\|\boldsymbol{u}(X, Y)\|_{min}$ is the minimum measured velocity magnitude in the field of view, dictates the temporal resolution for all reconstructed signals. At locations where the backward or forward streamlines span more than this limit, the distance is evenly divided by the minimum; if the division results in non-integer pixel locations, the values are estimated using a bicubic interpolation.

2.3 Model Reduction Techniques

Improvements in computational and experimental diagnostic techniques have dramatically increased the quantity of obtainable data from fluid dynamic investigations in the last couple of decades. This is, of course, desirable; however, it presents the modern challenge of how to effectively analyze such large caches of information. One of the most popular approaches has been the use of model reduction techniques (see, for example, Towne et al. 2018; Taira et al. 2017; Hill et al. 2023; Theofilis 2011; Butler and Laurence 2021), which attempt to reduce the dimensionality of the available data by decomposing a complex flow field into its fundamental features, or

modes, and retaining only those which contribute the largest percentages of the total energy (variance). Given these benefits, this field of mathematics has experienced incredible growth in recent years and various techniques have been developed. In the current work, two model reduction techniques are utilized: the spectral proper orthogonal decomposition (SPOD) and the bispectral mode decomposition (BMD). A brief mathematical outline of these methods is provided in the following subsections; however, the complete theoretical and algorithmic descriptions can be found in Towne et al. (2018); Schmidt and Colonius (2020) (SPOD) and Schmidt (2020) (BMD).

2.3.1 Spectral Proper Orthogonal Decomposition

Spectral proper orthogonal decomposition seeks to identify a set of spatiotemporal orthogonal modes that best estimate the cross-spectral density (CSD) tensor of the time-resolved pixel intensity data. The technique is a modern alternative to the traditional "space-only" POD, which extracts spatially-coherent structures in the data set by obtaining a basis that is orthogonal under a spatial inner product and optimally represents the spatial variance within the flow field. Conceptually, "space-only" POD can be equated to performing a singular value decomposition on a non-square data matrix that is constructed directly from the flow field data. These resulting modes are energy-ranked in a hierarchical fashion such that the leading modes capture a greater portion of the underlying dynamical processes. While these POD modes optimally represent the variance present in the flow, each mode is likely to contain contributions from multiple frequencies, and for this reason, it is not possible to represent a travelling structure with a single mode (i.e., the modes are not temporally-coherent). The spectral POD algorithm addresses this issue by performing the decomposition in the frequency domain of the data set, thereby extract-

ing sets of energy-ranked modes that oscillate at a single frequency and optimally represent the spatiotemporal flow statistics. The algorithm is constructed as follows.

Consider a state vector, $\mathbf{q}$, that is measured by either a computational or experimental diagnostic tool. This vector may contain multiple flow field variables and spatial dimensions (e.g., density, velocity, and/or pressure measurements in a three-dimensional spatial field). In the current work, $\mathbf{q} \in \mathbb{R}^n$, where n is the total number of pixels in each image, contains the pixel intensity values (to be calibrated into density gradients) within the two-dimensional field of view of the camera. Each "snapshot" of the state vector is then $\mathbf{q}_t$ and represents a reshaped column vector containing the pixel intensity values for each schlieren image (to be precise, since we will be conducting a time-interpolation of the pixel intensity signals, $\mathbf{q}_t$ contains the entire field of pixel intensity values at a specific time in the temporally-reconstructed signals). The process then involves concatenating all state vectors into a single data matrix, $\mathbf{Q}$, i.e.,

$$\mathbf{Q} = [\mathbf{q}_1 \quad \mathbf{q}_2 \quad \mathbf{q}_3 \quad \cdots \quad \mathbf{q}_{n_t}] \tag{2.11}$$

where n_t is the total number of temporal samples. Note that performing a singular value decomposition on $\mathbf{Q}$ would get you the "space-only" POD modes (note, also, the distinction that singular value decomposition is merely a method for acquiring the POD modes, which is useful for conceptual understanding but is generally not the most computationally efficient approach). However, for SPOD we continue by employing Welch's method to estimate the cross-spectral density tensor. The matrix $\mathbf{Q}$ is divided into M total blocks, which may be overlapping, and a

discrete Fourier transform is conducted on each block.

$$\begin{aligned}
\mathbf{Q}^{(1)} \rightarrow DFT \rightarrow \hat{\mathbf{Q}}^{(1)} &= \begin{bmatrix} \hat{\mathbf{q}}_1^{(1)} & \hat{\mathbf{q}}_2^{(1)} & \hat{\mathbf{q}}_3^{(1)} & \cdots & \hat{\mathbf{q}}_N^{(1)} \end{bmatrix} \\
\mathbf{Q}^{(2)} \rightarrow DFT \rightarrow \hat{\mathbf{Q}}^{(2)} &= \begin{bmatrix} \hat{\mathbf{q}}_1^{(2)} & \hat{\mathbf{q}}_2^{(2)} & \hat{\mathbf{q}}_3^{(2)} & \cdots & \hat{\mathbf{q}}_N^{(2)} \end{bmatrix} \\
&\vdots \\
\mathbf{Q}^{(M)} \rightarrow DFT \rightarrow \hat{\mathbf{Q}}^{(M)} &= \begin{bmatrix} \hat{\mathbf{q}}_1^{(M)} & \hat{\mathbf{q}}_2^{(M)} & \hat{\mathbf{q}}_3^{(M)} & \cdots & \hat{\mathbf{q}}_N^{(M)} \end{bmatrix},
\end{aligned} \tag{2.12}$$

In equation 2.12, N is the number of temporal samples in each block and $\hat{\mathbf{q}}_k^{(i)}$ denotes the vector comprising the k^{th} Fourier coefficient of each pixel's temporal signal from the i^{th} block. The Fourier coefficients for a given frequency, f_k, are collected from all available blocks to construct a new matrix

$$\hat{\mathbf{Q}}_{f_k} = \begin{bmatrix} \hat{\mathbf{q}}_{f_k}^{(1)} & \hat{\mathbf{q}}_{f_k}^{(2)} & \hat{\mathbf{q}}_{f_k}^{(3)} & \cdots & \hat{\mathbf{q}}_{f_k}^{(M)} \end{bmatrix}, \tag{2.13}$$

which, when multiplied with its Hermitian transpose, estimates the cross-spectral density matrix

$$\hat{\mathbf{C}}_{f_k} = \frac{1}{n} \hat{\mathbf{Q}}_{f_k} \hat{\mathbf{Q}}_{f_k}^H. \tag{2.14}$$

An orthogonal set of SPOD modes is extracted for each frequency bin by solving one of two eigenvalue decomposition problems, namely

$$\hat{\mathbf{C}}_{f_k} \mathbf{W} \hat{\mathbf{\Phi}}_{f_k} = \hat{\mathbf{\Phi}}_{f_k} \hat{\mathbf{\Lambda}}_{f_k}, \tag{2.15}$$

or

$$\hat{\mathbf{Q}}_{f_k}^H \mathbf{W} \hat{\mathbf{Q}}_{f_k} = \hat{\mathbf{\Psi}}_{f_k} \hat{\mathbf{\Lambda}}_{f_k}, \tag{2.16}$$

where $\mathbf{W}$ is a weighting function (equal to the identity matrix in the current application) and $\hat{\mathbf{\Phi}}_{f_k} = \hat{\mathbf{Q}}_{f_k}\hat{\mathbf{\Psi}}_{f_k}$. The latter option is referred to as the method of snapshots and, assuming $M < n$ (which is typically the case), requires less computation since $\hat{\mathbf{C}}_{f_k}$ is $rank(M)$. The SPOD eigenvalues are located in the diagonal matrix $\hat{\mathbf{\Lambda}}_{f_k}$ and their associated eigenvectors, representing the SPOD modes, are located in $\hat{\mathbf{\Phi}}_{f_k}$.

As the SPOD algorithm is based upon Welch's method of spectral density estimation, there is a trade-off between frequency resolution and variance. Large block sizes are desirable for greater frequency resolution, enabling accurate distinction between dynamical features operating at different frequencies. However, the variance (i.e., uncertainty) of the estimate can only be reduced by averaging over a greater number of blocks, or realizations. The SPOD thus converges as the number of blocks and the number of snapshots in each block both increase. This requirement is often the limitation in effectively employing SPOD for fluid flows as many experimental diagnostic tools do not provide the volume of data needed to create a sufficiently large ensemble of realizations.

2.3.2 Bispectral Mode Decomposition

While SPOD is generally applicable in nonlinear flows and reveals the energy contributions of the dominant flow structures, it does not grant any insights into the existence of nonlinearity. Triadic nonlinear interactions are of particular interest here as these are the result of the quadratic nonlinearity of the Navier-Stokes equations and are the primary mechanism of energy transfer between frequency components. The bispectrum is a classical technique that can detect quadratic phase coupling in one-dimensional signals. The bispectral mode decomposition is the extension

of the classical bispectrum to multidimensional data sets, revealing the coherent flow structures associated with triadic interactions and their regions of highest activity in the flow field.

The aspect of BMD which distinguishes it from the traditional bispectrum is the incorporation of spatial integration of the pointwise bispectral density:

$$\bar{b}(f_1, f_2) = E\left[\int_\Omega \hat{\mathbf{q}}(\mathbf{x}, f_1) \circ \hat{\mathbf{q}}(\mathbf{x}, f_2) \circ \hat{\mathbf{q}}^*(\mathbf{x}, f_1 + f_2)\, \mathrm{d}\mathbf{x}\right], \tag{2.17}$$

Here, $\bar{b}$ is used to refer to the integral measure of the bispectrum, $\mathbf{x}$ is the vector of spatial coordinates, Ω is the spatial region of integration, $\hat{\mathbf{q}}$ is the Fourier transform of state vector $\mathbf{q}$, * denotes the complex conjugate, and $\circ$ denotes element-wise multiplication. As a shorthand notation, $\hat{\mathbf{q}}_{f_1 \circ f_2}$ will be used to represent the Hadamard product between $\hat{\mathbf{q}}(\mathbf{x}, f_1)$ and $\hat{\mathbf{q}}(\mathbf{x}, f_2)$, and $\hat{\mathbf{q}}_{f_1+f_2}$ will be used to represent $\hat{\mathbf{q}}(\mathbf{x}, f_1 + f_2)$. The principles of Welch's method, traditionally used as a power spectral density estimator, are adapted to estimate the bispectral density matrix. As in SPOD, temporal data is separated into a series of blocks, representing different realizations of the flow. Discrete Fourier transforms are computed for each block of data and the bispectral density matrix, $\mathbf{B}$, is formulated as

$$\hat{\mathbf{Q}}_{f_1 \circ f_2} = \begin{bmatrix} \hat{\mathbf{q}}^{(1)}_{f_1 \circ f_2} & \hat{\mathbf{q}}^{(2)}_{f_1 \circ f_2} & \hat{\mathbf{q}}^{(3)}_{f_1 \circ f_2} & \cdots & \hat{\mathbf{q}}^{(M)}_{f_1 \circ f_2} \end{bmatrix}, \tag{2.18}$$

$$\hat{\mathbf{Q}}_{f_1 + f_2} = \begin{bmatrix} \hat{\mathbf{q}}^{(1)}_{f_1 + f_2} & \hat{\mathbf{q}}^{(2)}_{f_1 + f_2} & \hat{\mathbf{q}}^{(3)}_{f_1 + f_2} & \cdots & \hat{\mathbf{q}}^{(M)}_{f_1 + f_2} \end{bmatrix}, \tag{2.19}$$

$$\mathbf{B} = \mathbf{B}(f_1, f_2) = \frac{1}{M} \hat{\mathbf{Q}}^H_{f_1 \circ f_2} \hat{\mathbf{Q}}_{f_1 + f_2}. \tag{2.20}$$

In the current use of BMD, $\mathbf{B}$ is an auto-bispectral density matrix since $\mathbf{q}$ contains only one state

variable - the pixel intensity. However, spatial cross-correlation is a consequence of the formulation of **B**. This implies the integral measure of the bispectral density and results in differentiation between sum and difference interactions. In the context of modal decomposition, **B** and BMD is at this point analogous to the cross-spectral density tensor, $\hat{\mathbf{C}}_{f_k}$, and SPOD. However, $\hat{\mathbf{C}}_{f_k}$ is a Hermitian matrix whereas **B** is not and thus the procedures diverge here. Instead of computing an orthogonal basis, the principle task of BMD is to find the unit vector, **a1**, which maximizes the Rayleigh Quotient of **B**, i.e.,

$$\mathbf{a}_1 = arg\ max\ \left|\frac{\mathbf{a}^H\mathbf{B}\mathbf{a}}{\mathbf{a}^H\mathbf{a}}\right|. \tag{2.21}$$

The outputs of BMD are then the cross-frequency fields, bispectral modes, and interaction maps, defined as

$$\mathbf{\Phi}_{f_1 \circ f_2} = \hat{\mathbf{Q}}_{f_1 \circ f_2}\mathbf{a}_1 \qquad \text{(Cross-Frequency Field)}, \tag{2.22}$$

$$\mathbf{\Phi}_{f_1 + f_2} = \hat{\mathbf{Q}}_{f_1 + f_2}\mathbf{a}_1 \qquad \text{(Bispectral Mode)}, \tag{2.23}$$

$$\mathbf{\Phi}_{f_1, f_2} = \left|\mathbf{\Phi}_{f_1 \circ f_2} \circ \mathbf{\Phi}_{f_1 + f_2}\right| \qquad \text{(Interaction Map)}. \tag{2.24}$$

The bispectral modes are linear combinations of Fourier modes and are interpreted as the physical structures resulting from the nonlinear interaction between content at frequencies f_1 and f_2. The cross-frequency fields are maps of phase alignment between content at f_1 and f_2 but do not represent physical flow structures observed in the data. The interaction maps are the Hadamard product of these and display the local bicorrelation strength among content at f_1, f_2, and $f_1 + f_2$.

Chapter 3: Straight cone at zero incidence at Mach 6

In this chapter, the second-mode instability on a 7° half-angle sharp cone at Mach 6 is analyzed using high-speed calibrated schlieren imagery. Experiments were conducted in the NASA Langley 20-Inch Mach 6 facility at unit Reynolds numbers between 6.56×10^6 and 9.71×10^6 m^{-1}. Time-resolved pixel intensity signals throughout the boundary layer are reconstructed using spatially available data in the schlieren images to recover an effective sampling rate of over 10 MHz (compared to fundamental second-mode frequencies between 200-350 kHz); these are then converted to quantitative density gradients using a thin-lens-based calibration technique. A global analysis is performed on the schlieren data to investigate the nonlinear growth of the second-mode fundamental and harmonic content.

3.1 Facility Overview

Experiments were performed in the NASA Langley 20-Inch Mach 6 Wind Tunnel. Reservoir and free-stream properties for each of the three test conditions used are outlined in Table 3.1 (test conditions were determined according to the procedure described by Hollis 1996). A complete description of the facility and its capabilities can be found in Berger et al. (2015). The model wall temperature, T_w, varied slightly for each test as tests were run sufficiently close together that the model did not cool completely in between. The average model wall temperature

was 302.5K ±6.5K, where 6.5K is the 2σ value; the wall temperature changed by approximately 2.8K during a run.

Table 3.1: Test matrix and conditions.

Condition	Re66	Re79	Re97
M	5.97	5.98	5.99
Re_∞ $[10^6/m]$	6.56	7.94	9.71
P_0 [bar]	8.00	9.62	11.82
T_0 [K]	488	486	486
U_∞ [m/s]	928	927	927
P_∞ [Pa]	531	632	770
T_∞ [K]	60.4	60.0	59.9
ρ_∞ [kg/m^3]	0.0307	0.0367	0.0449

3.2 Model and Instrumentation

A 0.52 m long 7° half-angle cone was employed as the test article for this campaign. The model consisted of a 15-5 stainless steel frustum with a base diameter of 0.127 m and an interchangeable 15-5 stainless steel nose tip. A nose tip radius of 0.152 mm was used for the current campaign. The test article was instrumented with a variety of flush mounted pressure sensors and thermocouples, including PCB® 132-B38 fast-response pressure transducers, Kulite XCS-062 pressure transducers, Type-E Chromel-Constantan coaxial thermocouples, and static pressure ports. Only data captured from the PCB® sensors that were located in the schlieren field of view are presented in this analysis: there were two such sensors, located at distances of 294.3 mm and 345.5 mm from the nose tip, measured along the cone surface. Further details about the test article design and complete instrumentation layout can be found in Leidy et al. (2021).

3.3 Schlieren Specifications

High-speed flow visualization was performed using a standard two-lens schlieren setup. The schlieren hardware was mounted on top of two 0.61 m by 0.91 m breadboards located on opposing spanwise sides of the wind-tunnel test section; these boards were suspended from an overhead beam that provided vibration isolation from the tunnel. Light emitted from a Cavilux HF laser operating at 810 nm with either 50 or 70 ns pulse-widths was collimated by a 101.6 mm diameter achromatic lens with a focal length of 500 mm before entering the test section. Light leaving the test section was focused using an identical 101.6 mm lens and captured with a Phantom v2512 high-speed camera with a 12-bit depth at a nominal frame rate of 285 kHz, approximately equal to the expected second-mode frequencies at the tested conditions (200-340 kHz). An image resolution of 1280x64 was used for all images with a scale of 0.0756 mm/pixel. The camera was angled to be aligned with the cone surface and fixed at the same location on the cone for all experiments described here, with the camera viewing plane extending from 288.0 mm to 384.7 mm from the nose tip along the cone surface. A horizontal knife-edge cutoff was used to visualize the density gradients approximately normal to the cone surface.

3.4 Propagation Speeds

As mentioned in section 2.2, average propagation speeds of the second-mode wave-packets are computed before time-resolved signals can be reconstructed. Due to the large number of images used for each reconstructed signal, an automated wave-packet identification algorithm similar to that described in Shumway and Laurence (2015) is first applied to all images: this

identifies the presence and bounds of second-mode wave-packets. For each image containing a wave-packet, the propagation speed is estimated using a two-dimensional cross-correlation between that and the following image (see Laurence et al. 2014a). The total number of images containing wave-packets for each condition together with the mean and standard deviation of the calculated propagation speeds from those images are displayed in Table 3.2. The ratio of propagation speed to boundary-layer-edge velocity, U_p/U_e, is also shown for each condition, with U_e calculated using the Taylor-Maccoll equation. The second-mode propagation speeds are equal to approximately 90% of the edge velocity, consistent with prior work on hypersonic boundary layers over slender cones (e.g., Maslov et al. 2006; Kennedy et al. 2017; Butler and Laurence 2021).

Table 3.2: Numbers of images with identified wave packets and calculated propagation speeds for all conditions.

Condition	Re66	Re79	Re97
Number of Images	11070	13159	14796
Propagation Speed U_p [m/s]	835.3	824.9	819.2
σ [m/s]	40.6	20.9	11.5
U_p/U_e	0.91	0.90	0.90

3.5 General Behavior

Example image sequences showing the propagation of second-mode waves are shown in Figures 3.1–3.3, with brackets bounding particular wave-packets observed. The horizontal axis of each image is aligned with the cone surface. While some variation is observed at a given condition (which is typical of conventional, noisy facilities), the image sequences selected are representative of the general wave-packet behavior seen at each condition. Each image has been

reference subtracted using an average flow-on image to accentuate perturbations about the mean-flow state.

At condition Re66 (Figure 3.1), second-mode waves are weak and infrequent. Variations in pixel intensity caused by the disturbances are much less pronounced than the other two conditions, indicating smaller fluctuations in density. At this condition, wave-packets are just becoming discernible in select images of the run and breakdown (characterized by the degradation of the periodic wave-packet structures prior to the onset of turbulence) is not observed. At condition Re79 (Figure 3.2), second-mode waves are frequent, but not continuous, and experience large growth. Note, for example, that as the bracketed wave-packet progresses through the image sequence in Figure 3.2, the disturbance is noticeably amplified, as seen by the larger variation in greyscale intensity associated with the disturbance. Breakdown is occasionally observed near the end of the camera viewing plane, but this occurs intermittently (e.g., a secondary wave-packet seen to the right of the bracketed wave-packet in the first image of the sequence appears to flare out above the boundary layer and deform, possibly indicating the beginning of breakdown). At condition Re97 (Figure 3.3), near continuous waves propagate through the image plane, many of which are mature as they enter the field of view. The downstream portion of the visible boundary layer at this condition, though not continuously turbulent, often experiences turbulent bursts. The wave-packet bracketed in Figure 3.3, for example, does not appear to experience any noticeable amplification before losing much of its periodic structure and taking on a more chaotic appearance by the end of the sequence.

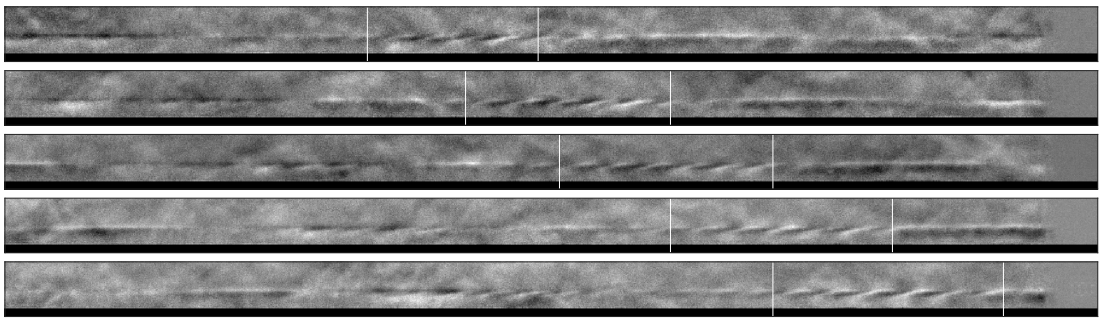

Figure 3.1: Reference-subtracted image sequence for condition Re66 at intervals of 14.0μs.

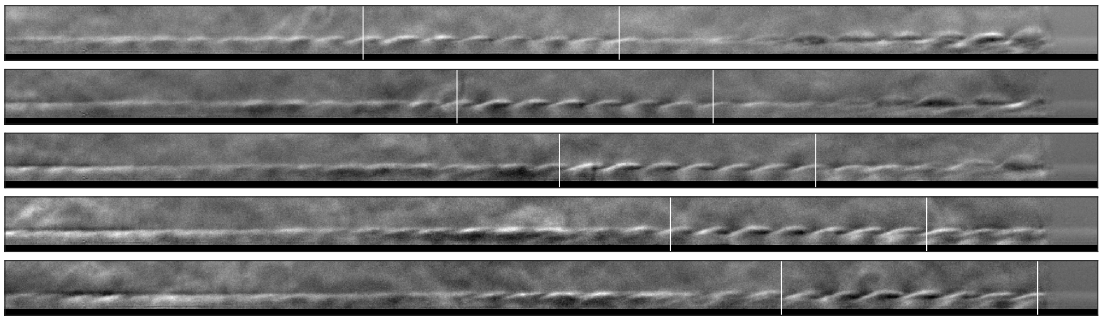

Figure 3.2: Reference-subtracted image sequence for condition Re79 at intervals of 14.0μs.

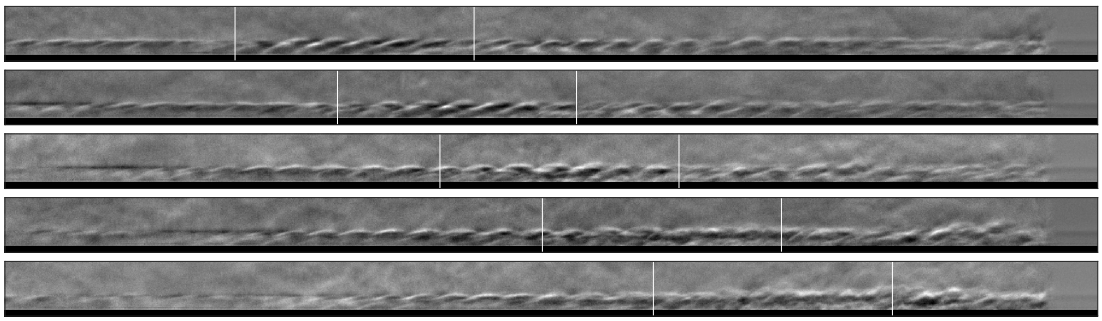

Figure 3.3: Reference-subtracted image sequence for condition Re97 at intervals of 14.0μs.

3.6 Power Spectral Density and N-Factor Analysis

A Fourier transform of the reconstructed and calibrated pixel intensities is conducted to analyze the spatial evolution of spectral content within the boundary layer. Power spectral densities

(PSD) are calculated using Welch's method with data segments of length 2375 (zero padded to a length of 4096) with 50% overlap between segments, resulting in 159 total segments. A Blackman window function is applied to each segment prior to zero-padding. This specific choice of segment size was selected to achieve an acceptable balance between frequency resolution and reduction in variance.

One problem with the reconstruction procedure described in section 2.2 is that it can produce strong artifacts in the signal: as seen in Figure 3.4 (taken from condition Re97), these take the form of narrow-band power spikes, which appear in the signal PSD at approximately integer multiples of the camera frame rate and are orders of magnitude stronger than the second-mode power (though the apparent power of the artifacts is reduced in Figure 3.4 due to spectral leakage). In the present experiments, they were determined to primarily arise due to the presence of imperfections in the test section windows that alter the intensity at specific pixel locations in every image, introducing a repeating pattern with a frequency corresponding to the camera frame rate in the reconstructed signal. Although these artifacts could be mitigated by normalization with a reference image, in some cases additional steps had to be taken. In the present analysis, multiple zero-phase band-stop filters centered at the artifact spike frequencies were thus applied to the reconstructed signals before computing the PSD. Spectral leakage that occurs during the application of Welch's method, however, causes the influence of the filter to also decrease the power of the second-mode content at nearby frequencies, resulting in divots in the PSD. The PSD data at the frequencies corresponding to each divot were thus removed and the remaining data in the second-mode frequency band were used to create a third-order polynomial fit; the removed data were then replaced with values from this curve fit at the corresponding frequencies. Figure 3.4 also displays the same PSD curve after the removal of the artifact spikes. Note that

the unaltered PSD is averaged with 59 total segments to moderately reduce the variance while preserving the narrow-banded appearance of the artifacts. The modified PSD is averaged with 159 segments – the number used in all other presentations of schlieren PSDs in this paper.

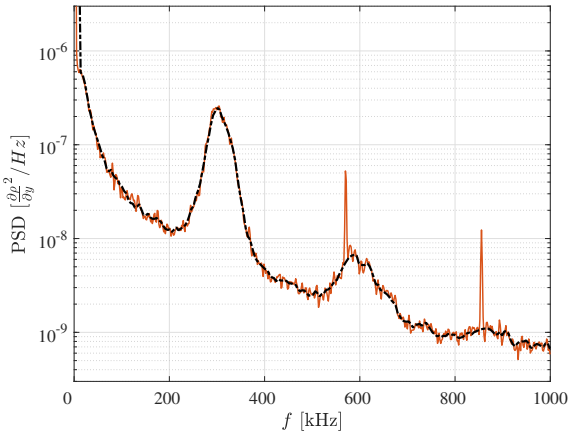

Figure 3.4: Power spectral densities of reconstructed time-resolved signal (solid red line) and after removal of artifacts (dashed black line).

Figure 3.5 compares the PSDs of pressure fluctuations captured by the two PCB® sensors in the schlieren field of view with the corresponding schlieren-derived PSDs for each condition. The pressure PSDs are normalized by the square of the static pressure on the cone surface derived from the Taylor-Maccoll solution. We first note that the frequencies of the second-mode fundamental and first harmonic are in excellent agreement between the two measurement techniques, strengthening our confidence in the reliability of the reconstruction technique to capture this content (it should be pointed out that there is a well-known resonance in the PCB® sensors at approximately 300 kHz). Clear growth in both the fundamental and first harmonic is observed between the two stations for conditions Re66 and Re79. For Re97, however, little growth takes place, indicating that the wave packets are close to saturation on average; the spectral broadening for the downstream sensor is also consistent with saturation and the onset of breakdown.

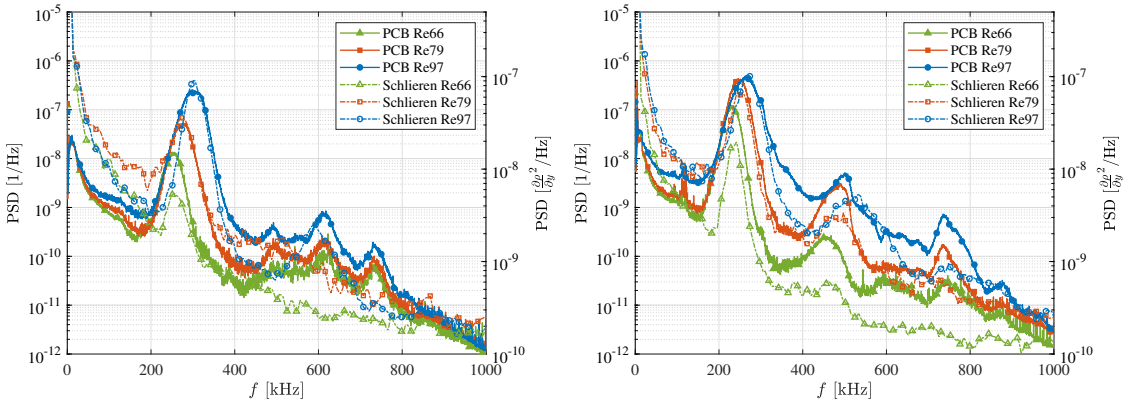

(a) (b)

Figure 3.5: Power spectral densities of pressure fluctuations, captured with PCB® 132-B38 sensors, and density gradients, captured with schlieren imagery, for all conditions at streamwise locations of (a) 294.3 mm and (b) 345.5 mm.

In the left column of Figure 3.6, contours of the PSD for each condition, showing its development in the streamwise direction, are presented. At each point downstream, the plotted PSD is taken from the wall-normal pixel exhibiting the maximum second-mode power. The change in N-factor, ΔN, for each frequency is displayed in the corresponding right-hand plot for each condition, with the most upstream location of the visualization window used as a reference point, s_0. These are computed with the equation:

$$\Delta N(f, s) = \frac{1}{2} \ln \frac{PSD(f, s)}{PSD(f, s_0)}. \tag{3.1}$$

For the N-factor plots, physical distances along the cone, s, are converted to the Stability Reynolds number, $Re_s^{1/2}$, where $Re_s = Re_\infty s$, and frequencies are nondimensionalized according to the convention used by Stetson et al. (1983), defined by

$$F = \frac{2\pi f}{U_\infty Re_\infty}. \tag{3.2}$$

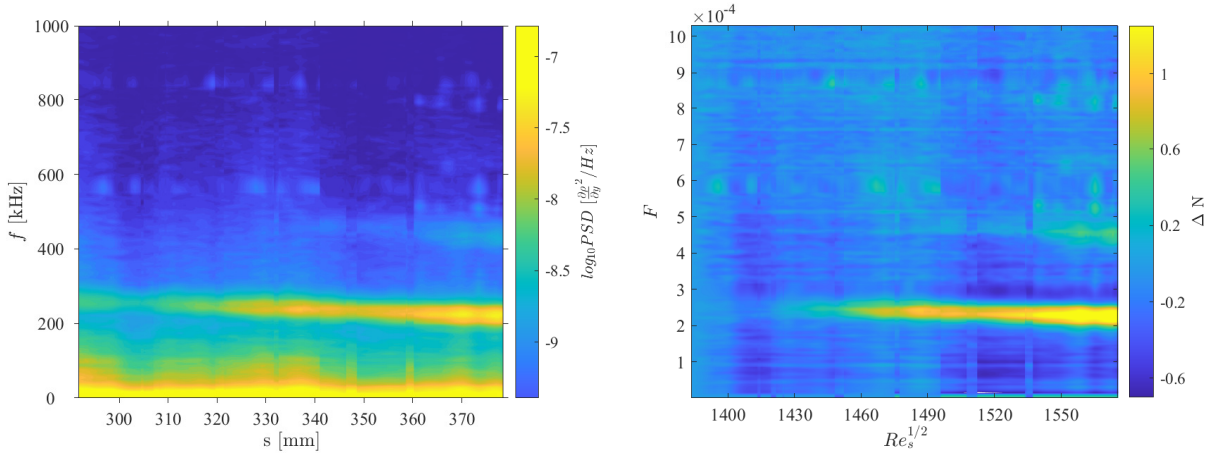

(a) Condition Re66

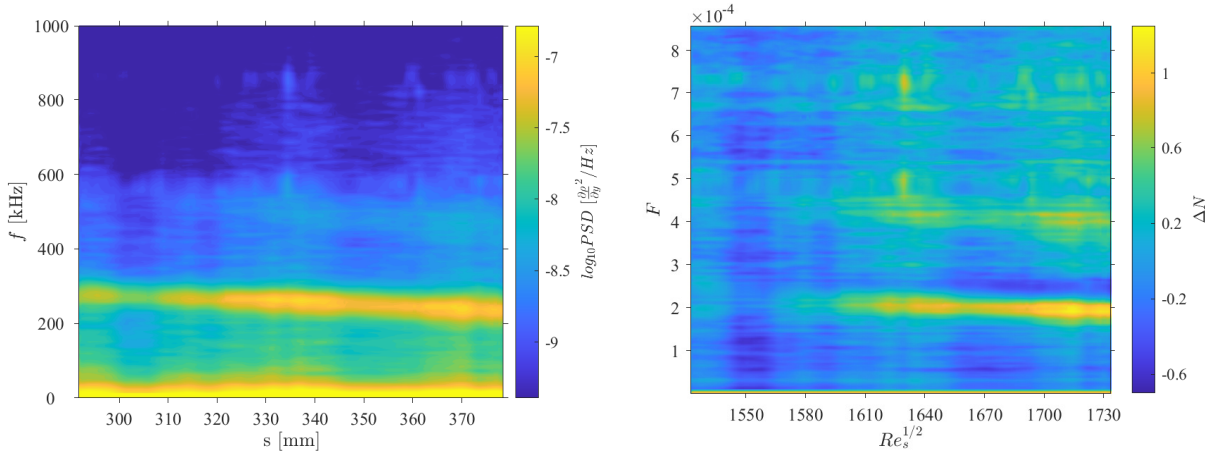

(b) Condition Re79

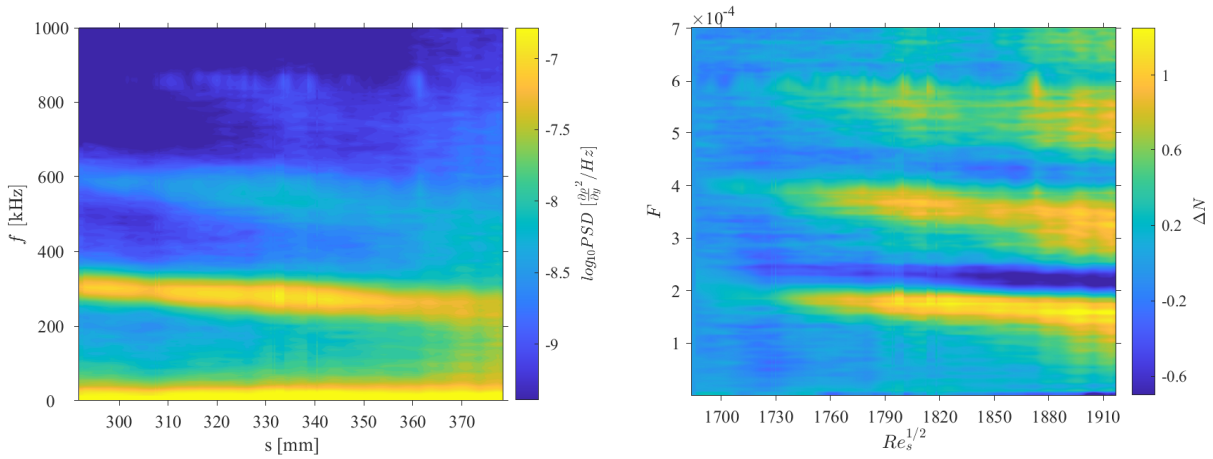

(c) Condition Re97

Figure 3.6: Power spectral density (left column) and change in N-factor (right column) along the curve of maximum second-mode strength for all conditions.

The N-factor plots provide a better picture of the local growth of disturbances across the camera field of view compared to the PSDs (which represent the entire history of amplification). Note that, because the reconstruction technique requires the use of neighboring upstream and downstream pixels, s_0 corresponds to a value of 291.8 mm and the analysis concludes at $s = 378.7$ mm rather than the true beginning and end of the camera viewing plane (288.0 mm and 384.7 mm).

The most-amplified fundamental frequencies at each streamwise location are shown in the upper plot of Figure 3.7 for each condition. The trends are consistent with prior work (e.g., Kennedy et al. 2018b; Marineau et al. 2019), with most-amplified frequencies decreasing steadily as flow progresses downstream and also being generally lower at lower unit Reynolds numbers at the same streamwise locations. Both effects are due to the changes in boundary-layer thickness. The corresponding lower figure displays these frequencies in nondimensional form plotted against the stability Reynolds number and shows good collapse of the data. The change in N-factor along the most-amplified frequencies of the fundamental, i.e.,

$$\Delta N(f, s) = \frac{1}{2} \ln \frac{PSD(f_{0,max}, s)}{PSD(f_{0,max}, s_0)}, \tag{3.3}$$

is also computed and used to compare the maximum disturbance growth among each condition. These values will be denoted as ΔN_{max} to distinguish them from those depicted in Figure 3.6.

Starting with condition Re66, we see that the initial power of the fundamental second-mode content enters the image viewing plane at approximately 260 kHz. Wave-packets at this condition experience large growth, reaching the greatest ΔN_{max} value among the fundamental peak frequencies at 1.15. The greatest ΔN value of this condition across all individual frequencies is 1.42, located at the downstream end of the image viewing plane at a frequency slightly lower than

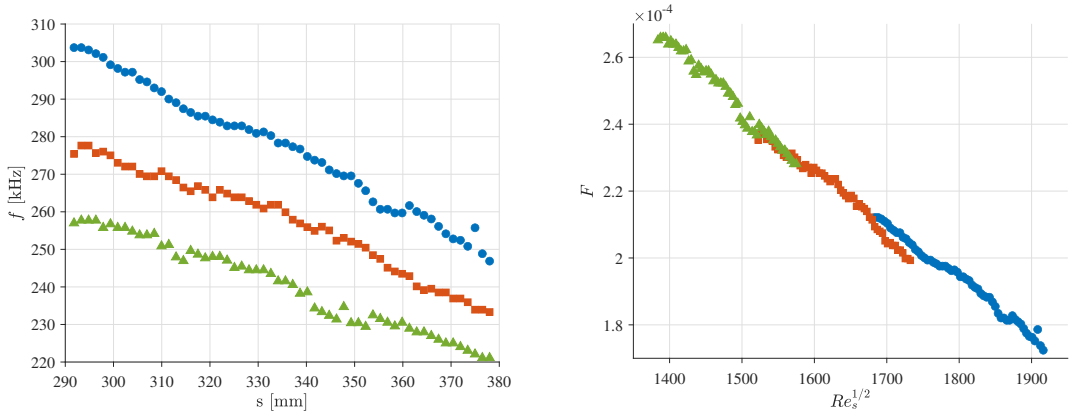

(a) (b)

Figure 3.7: Most-amplified frequencies of the fundamental second mode for conditions Re66 △, Re79 □, and Re97 ○ in (a) dimensional and (b) nondimensional form.

the local fundamental peak frequency. This, in combination with the lack of spectral broadening observed, indicates that wave-packets are still growing. Note that the ΔN values of Figure 3.6 are computed with upstream content at the same frequency used as the reference, whereas ΔN_{max} is calculated with the most-amplified fundamental frequency used as the reference. Peak ΔN values in Figure 3.6 will thus in general appear greater (because the reference power is smaller) and occur at frequencies lower than the most-amplified frequency (because lower frequencies become amplified with growing boundary-layer thickness). The only distinguishable harmonic content at Re66 is at the very end of the viewing plane, where the first-harmonic begins to emerge in the 400-460 kHz frequency band.

At condition Re79, the peak fundamental second-mode content again grows throughout the image viewing plane, though here only reaching a ΔN_{max} value of 0.56, indicating that wave-packets are approaching their saturation limit. The overall power of the second-mode content at Re79 is roughly an order of magnitude greater than in Re66 and significant energy emerges in the first-harmonic frequency band of 420-520 kHz, which reaches a peak ΔN value of 0.80.

At condition Re97, the second-mode fundamental and harmonics reach their peak power between $s = 325 - 345$ mm ($R = 1777 - 1831$). This saturation location of approximately $R = 1800$ is consistent with previous experiments in this facility (see Marineau et al. 2019) and is also supported by the PCB® data. The peak ΔN_{max} value is 0.33, the lowest of all conditions, and ΔN_{max} decreases significantly after reaching the saturation amplitude, falling to a value of -0.31 by the end of the field of view. The peak ΔN value found among all frequencies is 1.34 (which, somewhat surprisingly, exceeds the 1.23 value of condition Re79), which again occurs at the end of the viewing plane at a frequency below the local peak fundamental frequency. There is significant spectral broadening observed in Figure 3.6c, consistent with the initial breakdown to turbulence, which is precipitated by nonlinear interactions that cause energy redistribution to the second-mode side bands. The first and second harmonics experience the largest growth at this condition, reaching maximum ΔN values of 1.11 and 0.95. The spectral broadening and harmonic growth are clear evidence that the second mode is experiencing nonlinear growth for the majority of the streamwise positions observed at this condition.

3.7 Bispectral Analysis

The N-factor contour plots of Figure 3.6 indicate significant growth of the second-mode first harmonic at approximately twice the fundamental frequency with increasing Reynolds number and moderate growth of the second harmonic. The signal autobispectrum is thus computed to quantify the nature of the nonlinear interactions responsible for this harmonic content. The use of the reconstruction technique allows us to evaluate the bispectrum to high frequencies over the entire visualization region. The normalized bispectrum, or bicoherence, presented by Brillinger

(1965) is

$$b^2(f_1, f_2) = \frac{|E[\hat{X}(f_1)\hat{X}(f_2)\hat{X}^*(f_1 + f_2)]|^2}{|E[\hat{X}(f_1)]|^2|E[\hat{X}(f_2)]|^2|E[\hat{X}(f_1 + f_2)]|^2}, \tag{3.4}$$

where E is the expectation operator, $\hat{X}(f)$ is the Fourier transform of a segment of the calibrated pixel intensity time-resolved signal, and $*$ denotes the complex conjugate. For this analysis, we use the discrete formulation

$$b^2(f_1, f_2) = \frac{|\frac{1}{M}\sum_{i=1}^{M}\hat{X}(f_1)^{(i)}\hat{X}(f_2)^{(i)}\hat{X}^*(f_1 + f_2)^{(i)}|^2}{\frac{1}{M}\sum_{i=1}^{M}|\hat{X}(f_1)^{(i)}|^2|\hat{X}(f_2)^{(i)}|^2|\hat{X}(f_1 + f_2)^{(i)}|^2}, \tag{3.5}$$

where M is the number of blocks. This formula provides a statistical measure of quadratic phase coupling between frequencies f_1, f_2, and $f_1 + f_2$. Quadratic phase coupling is observed when waves at f_1 and f_2 are passed through a nonlinear quadratic system, producing a harmonic signal at $f_1 + f_2$. If the phases among the content of a signal at f_1, f_2, and $f_1 + f_2$ are random, indicating that these three waves are spontaneously independent, then b^2 will go to zero over many realizations. A b^2 value that is elevated above the noise floor is an indication that there is a fraction of the wave power at $f_1 + f_2$ that has been generated through quadratic phase coupling. For these data, segments of length 512 were used with 50% overlap, resulting in 741 total blocks.

In this subsection, we present a limited set of results for discrete pixel locations to give a picture of the range of interactions present; in the following subsection, several of these interactions will be selected for global analysis. Example bicoherence results for conditions Re66 and Re97 are displayed in Figures 3.8 and 3.9 at downstream locations of 315 mm and 365 mm, in each case at the wall-normal location exhibiting the maximum second-mode power. Note that there are multiple symmetry lines in the frequency plane of the autobicoherence; only the

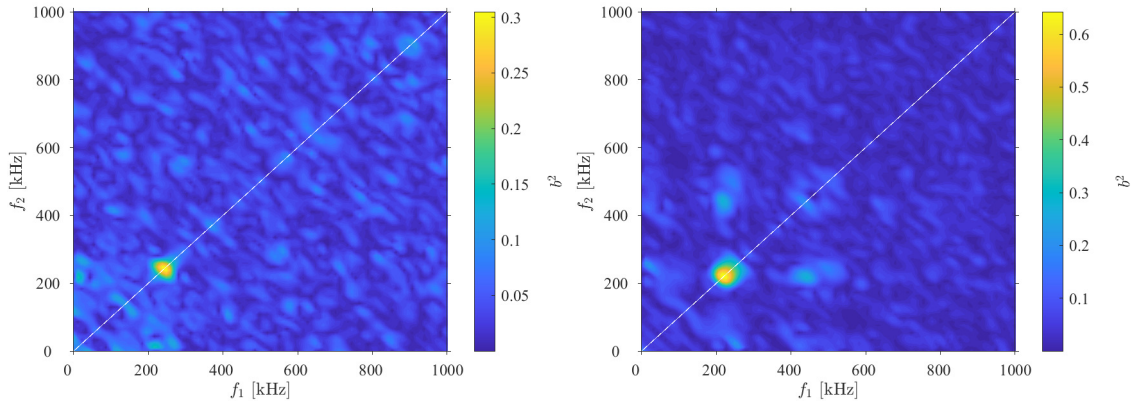

(a) (b)

Figure 3.8: Bicoherence maps for condition Re66 at (a) $s = 315$ mm, $Re_s^{1/2} = 1437$ and (b) $s = 365$ mm, $Re_s^{1/2} = 1549$.

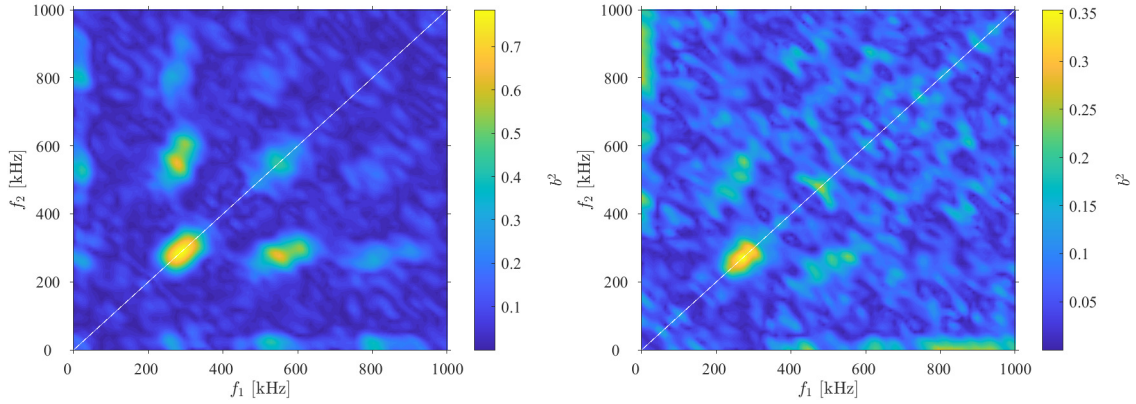

(a) (b)

Figure 3.9: Bicoherence maps for condition Re97 at (a) $s = 315$ mm, $Re_s^{1/2} = 1748$ and (b) $s = 365$ mm, $Re_s^{1/2} = 1884$.

first quadrant is plotted here (with the symmetry line $f_1 = f_2$), since difference interactions are essentially indistinguishable from the corresponding sum (first-quadrant) interactions in the autobicoherence.

The nonlinear interactions at condition Re66 are initially weak as wave-packets enter the camera viewing plane and are at their strongest in the final streamwise location used in this analysis. At the most upstream station ($Re_s^{1/2} = 1437$), the most prominent interaction is the

$f_0 + f_0 \rightarrow 2f_0$ fundamental resonance, where f_0 is the second-mode fundamental frequency (in this case 250 kHz). Note that the strength of the first harmonic increases in Figure 3.6a downstream of this location, suggesting that this resonance interaction is the source of first-harmonic growth. There are two additional interactions present, both of which are only slightly elevated from the noise floor (here $b^2 \lesssim 0.08$). One lies at $f_0 + \delta f \rightarrow f_0 + \delta f$, where δf represents low frequencies up to approximately 50 kHz, with $b^2 \approx 0.16$. Due to the symmetry of the autobicoherence, there are three possible candidates for the correct location of this triadic interaction, which could only be determined conclusively with the use of a cross-bicoherence. At similar conditions, however, both Chokani (2005) and Craig et al. (2019) came to the conclusion that, due to the presence of amplitude modulation of the fundamental second mode in their signals (as well as modulation of the second-mode harmonics in analogous interactions), such interactions were most likely of the family $f_0 + \delta f \rightarrow f_0 + \delta f$, representing the interaction between the fundamental side bands with low-frequency waves to produce spectral broadening. The second weak interaction is located at approximately $\frac{1}{2}f_0 + \frac{1}{2}f_0 \rightarrow f_0$, which represents subharmonic resonance, with $b^2 \approx 0.12$. Note that this interaction, which persists downstream at approximately the same strength (Figure 3.9b), rises only minutely above the noise floor. The interaction is not discernible at condition Re97, where the noise floor has increased. Bountin et al. (2008) suggested that the second-mode subharmonic consists of a pair of oblique first-mode waves. A light-ray passing through a subharmonic wave will therefore pass through a non-constant phase, which will reduce the signal-to-noise ratio. Craig et al. (2019) similarly used a schlieren-based measurement system to study nonlinear behavior of the second mode and did not observe the subharmonic interaction. It is therefore plausible that a subharmonic interaction is occurring but is unobservable with the current measurement system. Further downstream ($Re_s^{1/2} = 1549$), the bicoherence level

of the fundamental resonance interaction has approximately doubled (and f_0 has also decreased to 220 kHz). Weak interactions are also present at this downstream location corresponding to $2f_0 + 2f_0 \rightarrow 4f_0$ (resonance of the first harmonic) and $2f_0 + f_0 \rightarrow 3f_0$. Despite the presence of these nonlinear interactions, from Figure 3.6 we can conclude that their presence has not yet caused the fundamental growth rates to deviate substantially from linear growth.

For condition Re97, multiple significant nonlinear interactions are already present at the upstream station ($Re_s^{1/2} = 1748$, where f_0 is now 290 kHz); these are also broader in width than previously. In addition to those already mentioned for Re66, we see peaks at $3f_0 + f_0 \rightarrow 4f_0$ and $3f_0 + 2f_0 \rightarrow 5f_0$, indicating the existence of higher-frequency harmonics in the reconstructed signals. Low-frequency interactions are also present for several of the harmonics, which are analogous to the low-frequency interactions mentioned previously. The low-frequency peaks at Re97 now extend completely to the abscissa, which was not the case for Re66. Each of these interactions, $nf_0 + 0 \rightarrow nf_0$ (or possibly $nf_0 - nf_0 \rightarrow 0$), where n is an integer, corresponds to energy exchange between the relevant fundamental/harmonic and the mean flow. In general, however, we should be cautious in interpreting interactions involving lower frequencies, as there is no guarantee that low-frequency disturbances will be propagating at the same speed as the second mode, as is assumed in the reconstruction. The strength of nonlinear interactions decreases significantly at the downstream location ($Re_s^{1/2} = 1884$), where turbulent bursts are often seen. The $f_0 + f_0 \rightarrow 2f_0$ and $2f_0 + f_0 \rightarrow 3f_0$ interactions persist above the noise floor, but higher-harmonic-generating peaks are no longer visible. Low-frequency interactions are also broadened along the abscissa at this station, which is consistent with the breakdown process (e.g., Chokani 2005; Craig et al. 2019).

3.8 Spectral Proper Orthogonal Decomposition and Global Bicoherence

High-frequency reconstruction of the global schlieren data allows for further analysis of coherent flow structures by means of spectral proper orthogonal decomposition (SPOD). SPOD seeks to identify a set of spatiotemporal orthogonal modes that best estimate the cross-spectral density (CSD) tensor of the time-resolved pixel intensity data, extracting sets of energy-ranked modes that oscillate at a single frequency and optimally represent the spatiotemporal flow statistics. A brief outline of the algorithm is presented in section 2.3.1 and a complete description can be found in Towne et al. (2018). Here we compute the SPOD modes using a total of 25,000 "snapshots" of the flow, where each snapshot is represented by a single image from the time-resolved reconstructed signals. These 25,000 snapshots were segmented using Hamming windows of length 512 with 50% overlap, resulting in 98 realizations of the flow. We are primarily concerned with the SPOD modes that exhibit the highest energy since these typically contain the second-mode content. An exception to this is at the frequencies of the artifacts mentioned in section 3.6, where mode 1 is instead produced by the artifacts and possesses no coherent shape. The second mode content at these frequencies is found at mode 2.

We note at this point that it might be possible to extract SPOD modes corresponding to the fundamental and harmonics at aliased frequencies from the raw images (without reconstruction). In theory, isolating a single mode at a particular frequency when multiple modes exist is possible with SPOD if the modes are orthogonal under the space-time inner product

$$\langle \psi_1, \psi_2 \rangle = \int_{-\infty}^{\infty} \int_{\Omega} \psi_2^*(x,t)\psi_1(x,t)\mathrm{d}x\mathrm{d}t, \tag{3.6}$$

where here ψ refers to a mode shape of pixel intensities, Ω is the camera field of view, x and t are the spatial and temporal coordinates, and an asterisk denotes the Hermitian transpose. Equation 3.6 was found to be nonzero for the dominant disturbance mode shapes of the current data. Therefore, performing SPOD on the raw images resulted in significant contamination of second-mode SPOD mode shapes from both lower-wavenumber and harmonically-related content.

Select modes within the frequency bands of the fundamental and first harmonic of the second mode are shown in Figures 3.10 and 3.11 for condition Re97. Note that, for clarity of features, the vertical axis has been elongated here compared to Figures 3.1–3.3. Dashed white lines indicate the approximate boundary-layer edge, taken from a similarity solution of the compressible boundary-layer equations using the Illingworth transformation (Illingworth 1950), where we have assumed a constant wall-to-edge temperature ratio (ranging from 0.60 to 0.61, depending on the run) and a constant boundary-layer edge Mach number determined by the Taylor-Maccoll solution (ranging from 5.34 to 5.36). For these figures, only the real part of the mode shape is shown. The vibrancy of the mode at any given pixel is a metric of the pixel's contribution to the total modal energy; however, pixels between a peak and a valley contribute similar energy but have very low intensity because they are at a phase where the wave structure is at least partly imaginary. At each frequency shown, the mode shapes acquire the distinct rope-like structure of the second mode in the regions where the modal energy is highly concentrated. As we would expect, the location of highest energy concentration shifts downstream with decreasing modal frequency. This is also true of the first-harmonic mode shapes seen in Figure 3.11, which again exhibit the typical rope-like second-mode structures (though of course with a shorter wavelength). Note that the frequency resolution of the SPOD is approximately 20kHz, and the selected first-harmonic frequencies in Figure 3.11 are the closest bins to doubles of the plotted fundamental

frequencies in Figure 3.10. Both the fundamental and first-harmonic modal energies are strongest in the upper half of the boundary layer; however, the second-mode energy within the fundamental frequency range extends slightly above the boundary-layer edge and down closer to the cone surface, whereas the modal energy in the first-harmonic frequency range is more concentrated in the upper half of the boundary layer and drops off rapidly above the boundary-layer edge. The PSDs at streamwise locations of 315, 335, and 355 mm at the same conditions are plotted in Figure 3.12. These locations are chosen to match the approximate locations of peak energy seen in the fundamental SPOD modes in Figure 3.10. Vertical dashed lines in Figure 3.12 indicate the sample SPOD frequencies from Figures 3.10 and 3.11. We note that the relative power between the selected locations is consistent between the PSD and SPOD for each frequency, giving confidence that the SPOD analysis is producing physically reasonable results.

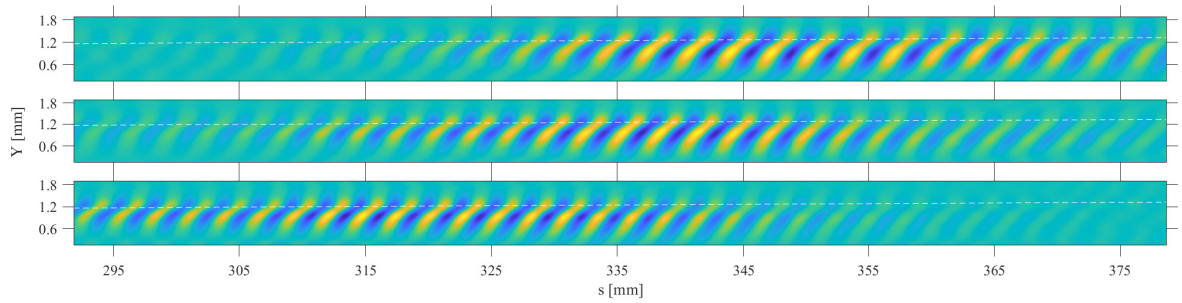

Figure 3.10: SPOD mode shapes at condition Re97 at frequencies of 249kHz (top), 275kHz (middle), and 302kHz (bottom).

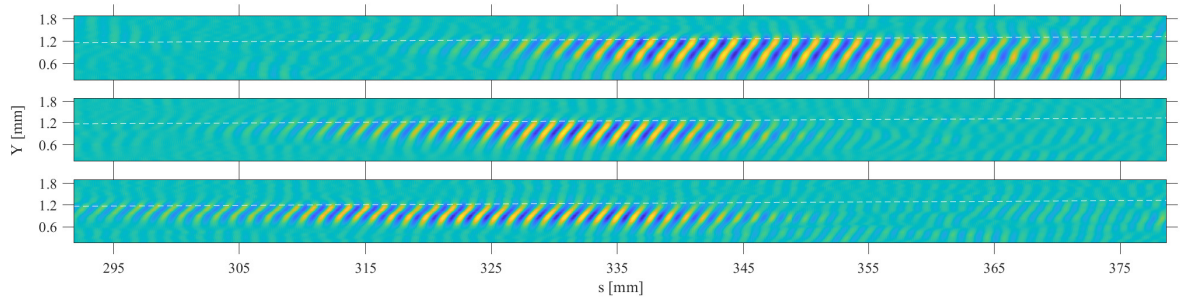

Figure 3.11: SPOD mode shapes at condition Re97 at frequencies of 497kHz (top), 550kHz (middle), and 593kHz (bottom).

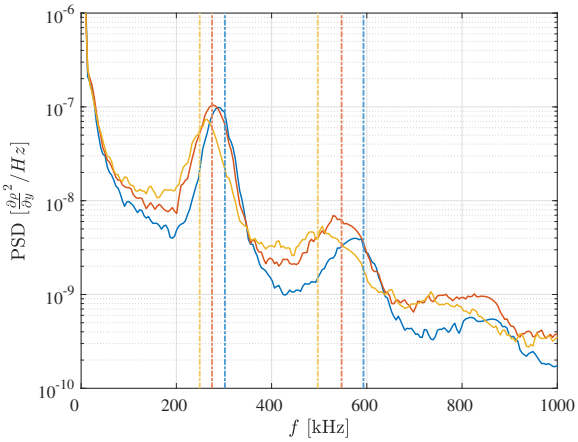

Figure 3.12: Power spectral densities at streamwise locations of 315 mm (blue), 335 mm (red), and 355 mm (yellow) for condition Re97. Dashed vertical lines are located at the SPOD frequencies shown in Figures 11 and 12.

In Figures 3.13–3.15, we compare the global results from the various analysis techniques for each condition. The top subplot in each of these figures represents the power of the most-amplified frequency in the second-mode fundamental frequency range at every pixel in the boundary layer; the second subplot shows the same for the first-harmonic content. The third and fourth subplots show the SPOD modes at the frequencies corresponding to the most-amplified second-mode fundamental and first harmonic. For conditions Re79 and Re97, a similar subplot is included showing the SPOD mode at the most-amplified second-harmonic frequency (this is omitted for condition Re66 due to the lack of coherence in the mode shapes at these higher frequencies, which is expected since the PSDs at this condition lacked any appreciable content in the second-harmonic frequency range). The remaining subplots show the bicoherence level of various nonlinear interactions throughout the boundary layer. Here, the bicoherence is calculated for each reconstructed pixel intensity signal within the boundary layer using the same algorithm outlined in section 3.7, thus generating a plot similar to those found in Figures 3.8 and 3.9 for every pixel. For each of these bicoherence plots, a 3×3 box of neighboring points is selected,

centered at the frequencies generating the highest b^2 value for the interaction in question; the plotted magnitude is the average over this box. For these figures, in addition to the dashed white lines representing the boundary-layer edge, dot-dashed lines are included to demarcate the critical layer, $U = U_p$, where U_p is equal to the calculated second-mode propagation speed.

This previous consistency seen between the PSD and SPOD modes is apparent again in Figures 3.13–3.15, with SPOD mode shapes containing the highest energy and coherency in the same regions of peak power shown in the PSD subplots. At the most-amplified fundamental frequencies, the primary peaks in the PSD and SPOD lie very close to the critical layer upstream, but then spread down toward the cone surface further downstream. A minor secondary peak also occurs for each condition at approximately the boundary-layer edge, with a noticeable valley existing between these two peaks. This dip in fundamental second-mode power between the critical layer and boundary-layer edge is more prominent at conditions Re79 and Re97 and is visible in both the PSD and SPOD subplots. The SPOD mode shapes also show that the second-mode fundamental content extends beyond the boundary-layer edge for each condition. Outside the boundary layer, the mode-shape contours appear to steepen to close to vertical, consistent with measurements of wave-packet structure angle in Kennedy et al. (2022). The most-amplified first- and second-harmonic frequencies similarly show the highest concentration of energy at vertical heights very near the critical layer; however, at these frequencies the power is more sustained between the critical layer and boundary-layer edge.

The nonlinear interaction with the highest bicoherence is consistently the fundamental resonance, $f_0 + f_0 \rightarrow 2f_0$, and this is strongest along a narrow band closely aligned with the critical layer. At condition Re66, this band appears to lie precisely on the critical layer; at conditions Re79 and Re97, it lies just above the critical layer at the most upstream locations and

migrates slightly toward the cone surface downstream. Comparing the corresponding PSD plots at each condition, we note that peaks in the second-mode harmonic power lie downstream of peaks in the global bicoherence (this is consistent with earlier observations, e.g., in Kennedy et al. 2018b) but at approximately the same wall-normal location. This finding is in accordance with the usual interpretation that the harmonic content is nonlinearly generated through fundamental self-resonance. Similar banded peaks are observed for the $2f_0 + f_0 \rightarrow 3f_0$ and $3f_0 + f_0 \rightarrow 4f_0$ interactions, though these are shifted slightly downstream and reach significantly lower peak b^2 values compared to the fundamental resonance (note, however, that no clear peaks in the $3f_0 + f_0 \rightarrow 4f_0$ interaction are observed at Re79). Chokani (1999) similarly measured higher-harmonic-generating peaks downstream of fundamental resonance, showing that the distance over which the first harmonic showed measurable growth was approximately twice the distance over which the second harmonic showed measurable growth. Both harmonics saturated at approximately the same location. This is presumably because the first harmonic must reach some threshold amplitude before the nonlinear product of its resonance with the fundamental is substantial, and similarly for subsequent interactions.

Significant $f_0 + 0 \rightarrow f_0$ and $2f_0 + 0 \rightarrow 2f_0$ interactions are also observed and seen to increase in strength with increasing unit Reynold's number. In each case, the strength of these interactions is found to be highest just outside of the boundary-layer edge, with the exception of the $2f_0 + 0 \rightarrow 2f_0$ interaction at Re66. At condition Re97, there is also an elevated band for $2f_0 + 0 \rightarrow 2f_0$ interaction along the critical layer prior to the saturation location, although this is found to be weaker than the interactions above the boundary layer seen further downstream. As stated previously, these interactions are an indication of energy exchange between the second mode and the mean flow, with the sum interaction being responsible for energy transfer from

the mean flow into the second mode, especially the second-mode side bands (Craig et al. 2019; Chokani 2005), and the difference interaction producing mean-flow distortion.

The location of these mean-flow interactions above the boundary layer motivates further investigation. The autobicoherence was inspected at four streamwise positions of s = 300, 330, 345, and 375 mm for Re97 at a vertical height of 1.59 mm, which corresponds to the height of peak b^2 for the $f_0 + 0 \rightarrow f_0$ interaction. Since the boundary layer is continuously growing, this vertical height corresponds to approximately $y/\delta = 1.35$ at the most upstream position and $y/\delta = 1.20$ at the most downstream position. Figure 3.16 displays the bicoherence plots at the s = 330 mm s = 375 mm stations; the PSD of each pixel's signal is shown above and to the side of each bicoherence plot. While the second-mode content weakens rapidly above the boundary layer, there is still clear content there at the fundamental frequencies. At these locations, only significant interactions with low frequencies and the mean flow are observed. At s = 300 mm, a peak at $f_0 + \delta f \rightarrow f_0 + \delta f$ is present at the lower-side-band frequencies of the fundamental. This peak does not extend to the abscissa, indicating that interactions with low frequencies, not the mean flow, initiate the sequence. At station s = 330 mm, this peak expands to the abscissa and a second peak emerges at $2f_0 + \delta f \rightarrow 2f_0 + \delta f$. There is very little discernible content at the first harmonic in the PSDs, but if we assume that the content is approximately centered at twice the fundamental peak frequency, then the $2f_0 + \delta f \rightarrow 2f_0 + \delta f$ interaction exists again at the lower side band. At s = 345 mm, low-frequency interactions emerge at the upper side bands of the second-mode fundamental and first harmonic. Two additional peaks also appear along the abscissa in the 800 – 1000 kHz range, indicating low-frequency and mean-flow interactions with higher harmonics. Finally, at station s = 375 mm, peak interactions with low frequencies disperse and develop into broadband interactions along the abscissa. This progression of interactions is

in very close agreement to that found in Craig et al. (2019), which they measured inside the boundary layer at approximately the location of maximum rms mass flux fluctuation.

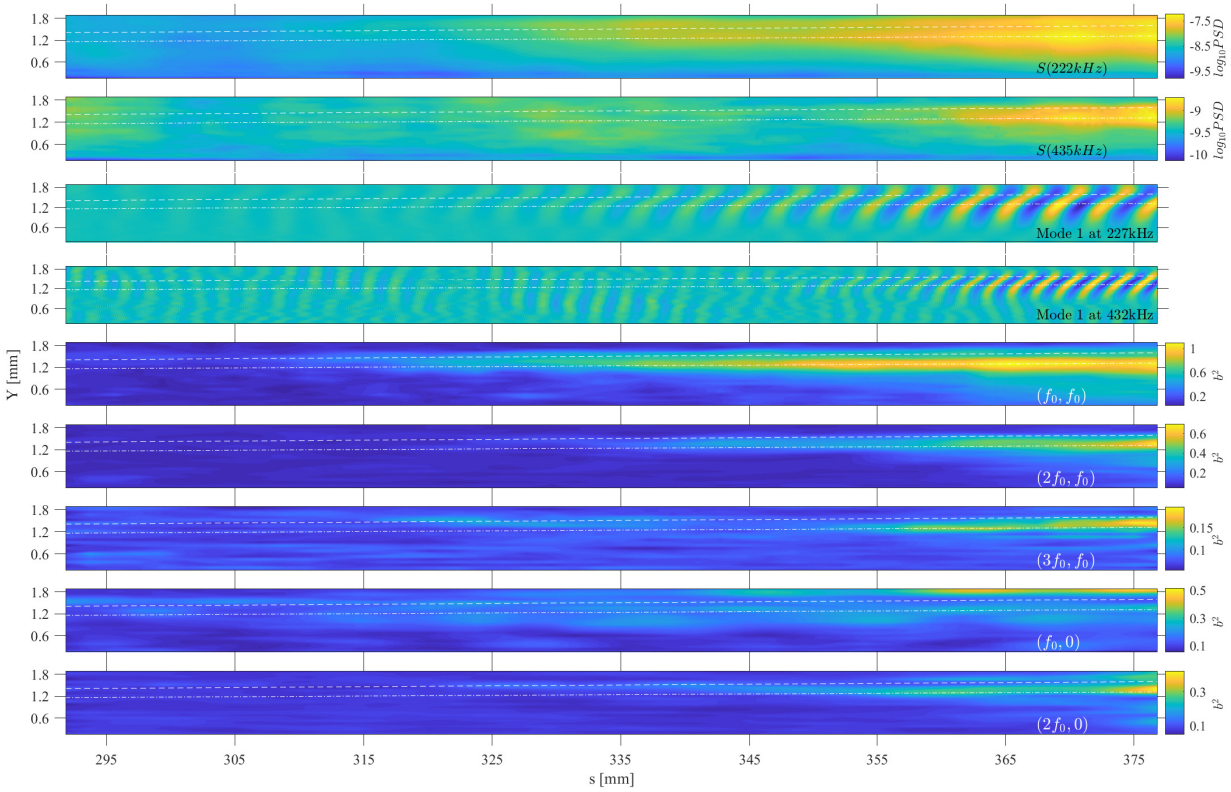

Figure 3.13: Global analysis of condition Re66: Comparison between the power of the most-amplified second-mode fundamental frequency (222kHz), the power of the most-amplified second-mode first-harmonic frequency (435kHz), the most dominant SPOD mode shapes at the second-mode fundamental and first-harmonic frequencies (227kHz and 432kHz), and multiple interactions found in the global bicoherence.

3.9 Bispectral Mode Decomposition

In the previous sections, we have used the normalized bispectrum, or bicoherence, to quantify the level of quadratic phase coupling for a number of triadic interactions seen in the boundary layer. Though the normalization used does not strictly bound the bicoherence between 0 and 1, the result can still be interpreted as being closely related to the percentage of the wave power that

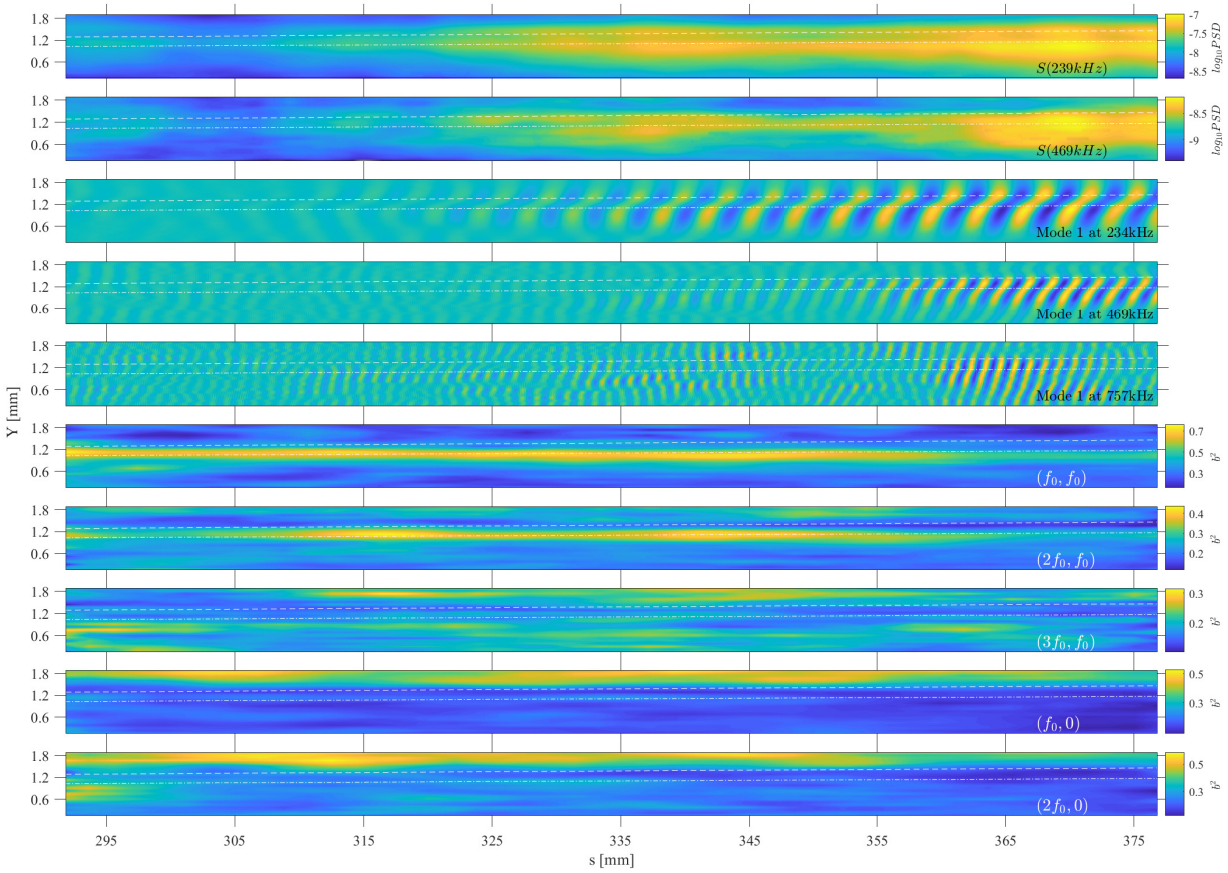

Figure 3.14: Global analysis of condition Re79: Comparison between the power of the most-amplified second-mode fundamental frequency (239kHz), the power of the most-amplified second-mode first-harmonic frequency (469kHz), the most dominant SPOD mode shapes at the second-mode fundamental, first-harmonic, and second-harmonic frequencies (234kHz, 469kHz, and 757kHz), and multiple interactions found in the global bicoherence.

is involved in the energy exchange during the interactions. In this section, we turn to a slightly different approach for analyzing the bispectrum called bispectral mode decomposition (BMD). This method seeks to educe coherent structures associated with triadic interactions and may be thought of as an extension of SPOD to higher-order spectra. However, rather than generating modes that optimally represent the cross-spectral density tensor, as in SPOD, BMD generates modes that optimally represent a bispectral density matrix. A brief outline of the methodology is provided in section 2.3.2, and a complete description can be found in Schmidt (2020).

The presentation of results found in Figures 3.17 and 3.18 display the bispectral modes and

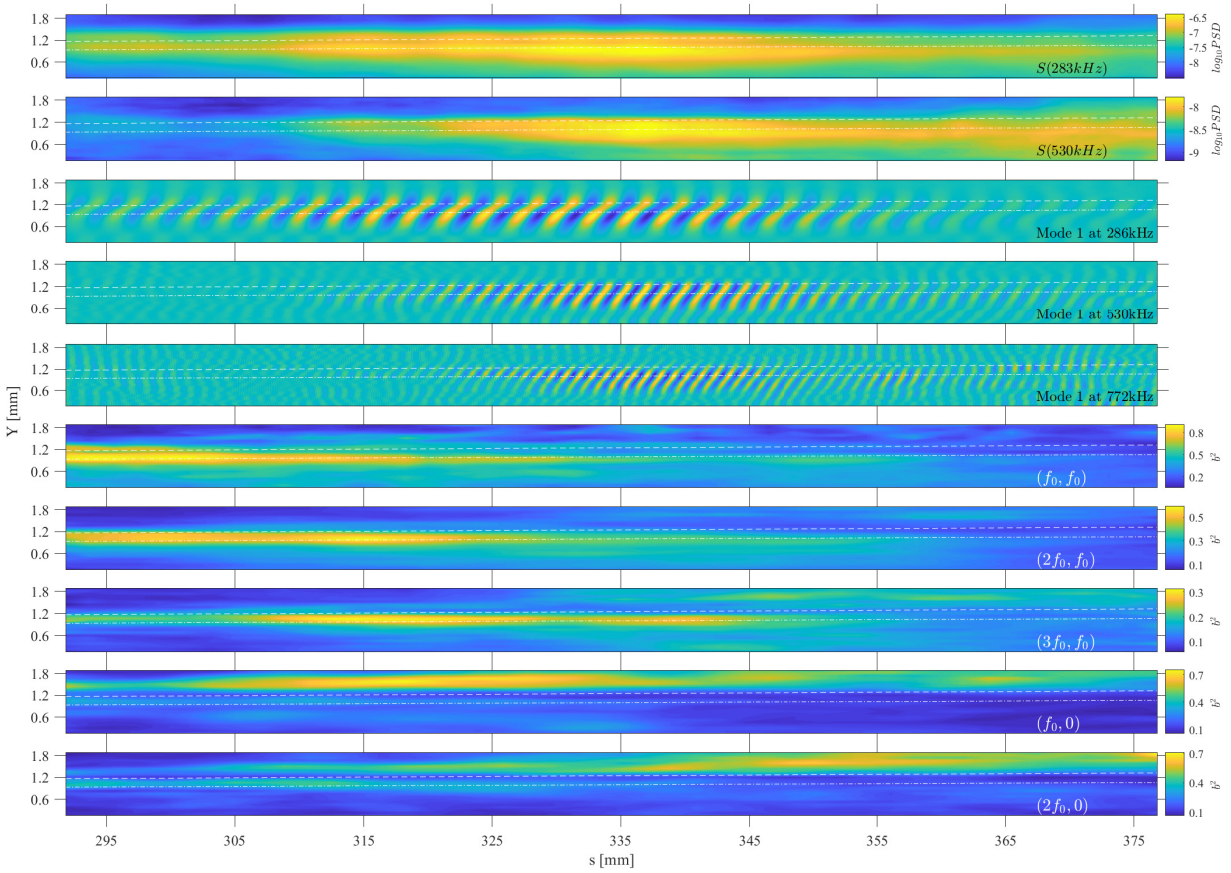

Figure 3.15: Global analysis of condition Re97: Comparison between the power of the most-amplified second-mode fundamental frequency (283kHz), the power of the most-amplified second-mode first-harmonic frequency (530kHz), the most dominant SPOD mode shapes at the second-mode fundamental, first-harmonic, and second-harmonic frequencies (286kHz, 530kHz, and 772kHz), and multiple interactions found in the global bicoherence.

interaction maps that are generated using BMD. The bispectral modes are linear combinations of Fourier modes and are interpreted as the physical structures resulting from the nonlinear interaction between f_1 and f_2. The interaction maps display the local bicorrelation strength between f_1, f_2, and $f_1 + f_2$. These maps are similar to the global bicoherence plots presented in section 3.8 with the important distinction that the current interaction maps are not normalized by the power spectrum; it is therefore the level of energy exchange involved in each triadic interaction that is quantified rather than the percentage of the wave power involved.

Figures 3.17 and 3.18 present the BMD results for the $f_0 - f_0 \rightarrow 0$, $f_0 + 0 \rightarrow f_0$, $f_0 + f_0 \rightarrow 2f_0$,

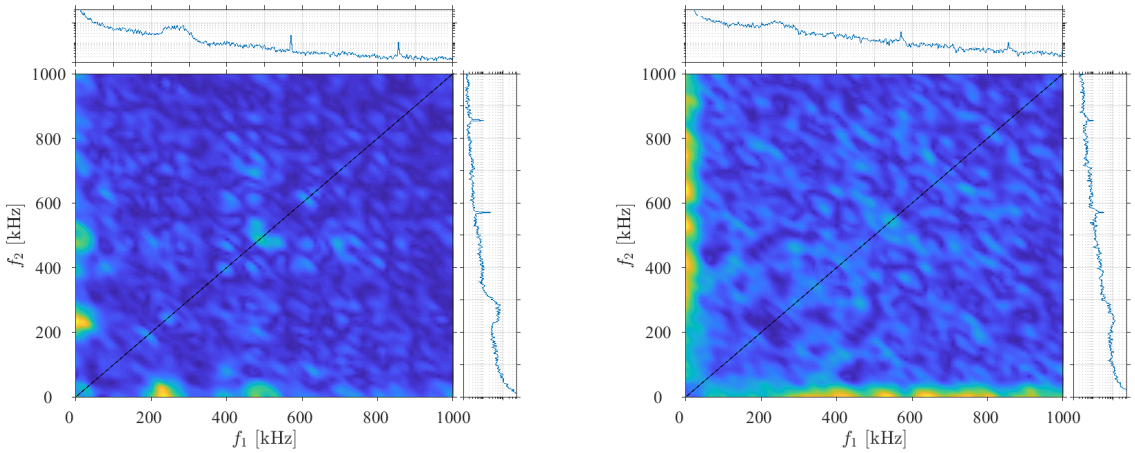

(a) s = 330 mm (b) s = 375 mm

Figure 3.16: Autobicoherence at multiple streamwise positions above the boundary-layer edge for condition Re97.

$2f_0 + f_0 \rightarrow 3f_0$, and $3f_0 + f_0 \rightarrow 4f_0$ interactions at condition Re97. Saturation of the interaction color-maps are set to the maximum value of each interaction. Lines indicating the boundary-layer edge (dashed) and critical layer (dot-dashed) have again been included for reference. The frequencies selected for f_1 and f_2 are the most-amplified second-mode fundamental and harmonic frequencies found at this condition (296 kHz, 529 kHz, and 762 kHz). Note that these slightly differ from the frequencies displayed in Figure 3.15 due to the segmentation of signals into blocks of length 256 rather than 512 – the frequencies selected here are the nearest frequency bins to those in Figure 3.15. In each case, the bispectral modes at $f_1 + f_2$ are nearly identical to the SPOD modes at the same frequencies. This agreement confirms that the second-mode harmonic flow structures identified in the most-dominant SPOD mode shapes are, in fact, generated through a triadic interaction. The BMD analysis successfully identifies coherent structures up to the third harmonic (shown in Figure 3.17 at 1058 kHz), whereas SPOD was only capable of visualizing the second harmonic. This is likely due to the ability of BMD to reject content that is not interacting nonlinearly through a triadic interaction. There are notable discrepancies,

however, between the interaction maps presented here and the previously presented global bicoherence plots. The primary locations of interaction strength for the fundamental second-mode difference self-interaction, $f_0 - f_0 \rightarrow 0$, are found inside the boundary layer approximately along the maximum rms disturbance streamline. There are slightly elevated regions in the interaction map above the boundary-layer edge that indicate nonlinear interactions may be present; however, their contribution to the integral measure of the bispectral density are much less significant than previously indicated by the global bicoherence plots. This may be because, despite having high b^2 values, the second-mode power is considerably lower above the boundary layer, and therefore the total amount of energy exchange involved in those interactions is relatively insignificant. The corresponding sum interaction, $f_0 + 0 \rightarrow f_0$, shows even lower bicorrelation strength above the boundary layer. The primary locations of interaction strength for the sum interactions that produced harmonic second-mode content are found at similar vertical heights as those in the global bicoherence plots displayed in Figure 3.15 but shifted downstream. Here, they align closely with the location of peak second-mode fundamental and first harmonic content observed in the global PSD plots of Figure 3.15. This is a somewhat unsurprising result, as BMD produces nonnormalized quantities and is therefore more heavily weighted by the PSD at the relevant frequencies.

3.10 Summary

A global approach was utilized to analyze the nonlinear development of hypersonic boundary layers using a combination of spectral techniques. These included the traditional pixelwise power spectrum and bispectrum as well as modal decomposition of the entire flow field via spectral proper orthogonal decomposition and bispectral mode decomposition. When used in con-

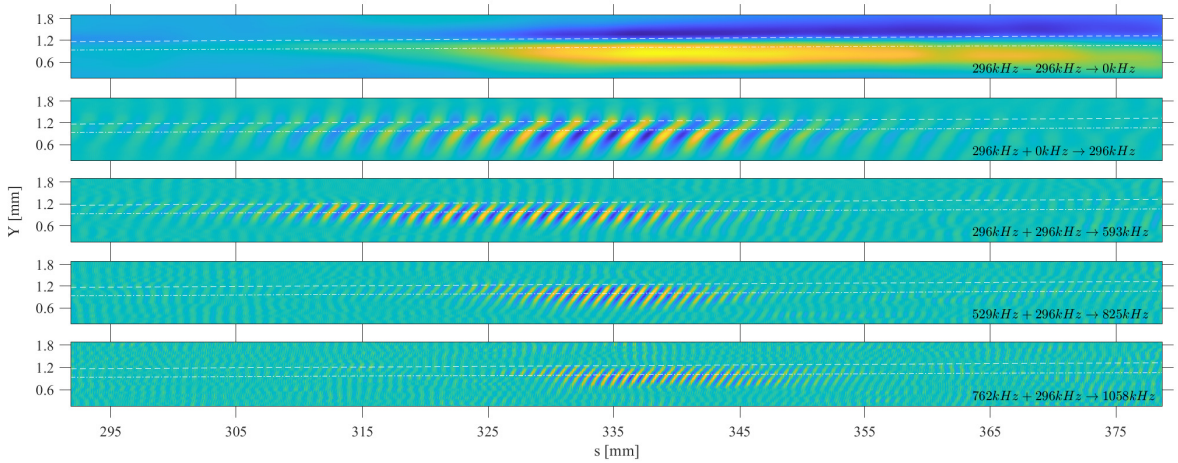

Figure 3.17: BMD analysis of condition Re97: Bispectral modes.

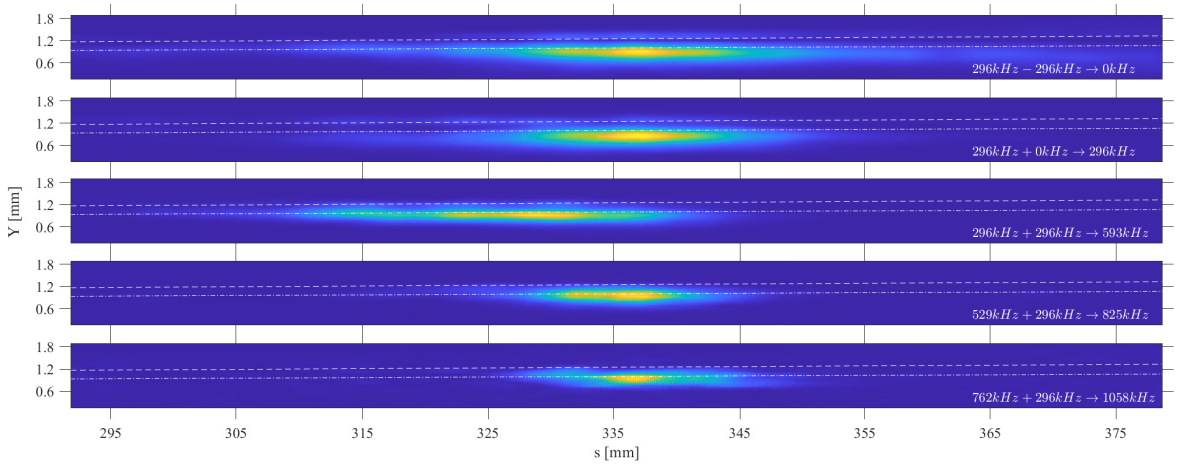

Figure 3.18: BMD analysis of condition Re97: Interaction maps.

junction, these techniques allow the visualization of the spatiotemporal evolution of fundamental and harmonic instabilities and the correlation of these with specific triadic interactions. This technique was applied to experimental data collected from a 7° half angle sharp cone at Mach 6. High-speed calibrated schlieren imagery was employed at a frame rate approximately equal to the second-mode fundamental frequency. Time-resolved pixel intensity signals were reconstructed using neighboring spatial data to achieve an effective sampling rate of above 10 MHz, allowing for higher order second-mode harmonics to be recovered. The unit Reynolds numbers studied resulted in laminar to transitional boundary layers in the camera field of view.

Global analysis was performed using spectral proper orthogonal decomposition of pixel-intensity signals. Spatial modulation of second-mode disturbances at discrete frequencies were visualized at the fundamental, first-harmonic, and second-harmonic frequencies. The most dominant SPOD modes within the second-mode frequency bands were characterized by the distinct rope-like structure of the second-mode. Good correlation was observed between regions of high energy in the SPOD modes and regions of elevated PSD at the same frequencies. Both SPOD and PSD maps identified wall-normal maxima in the second-mode fundamental and first-harmonic energy at approximately the critical layer. Minor decreases in power were observed in the fundamental energy between the critical layer and boundary-layer edge, while the harmonic energy was more sustained in this region.

Multiple nonlinear interactions were identified by first analyzing the global autobicoherence at each condition. Comparisons were then made for the highest Reynolds number condition between the global bicoherence and the bispectral mode decomposition. The nonlinear interactions found to be significant included sum interactions involving the second-mode fundamental with itself and its harmonics that produced higher harmonic content. Autobicoherence levels computed from discrete pixel signals indicated elevated nonlinear interactions involving up to the 4th harmonic ($5f_0$) at streamwise locations just prior to breakdown; second-mode harmonic structures associated with these interactions were observed with BMD up to the 3rd harmonic ($4f_0$). These sum interactions were found to have the greatest level of quadratic phase coupling along and just above the critical layer. Peak values in the first-harmonic PSDs and BMD interaction maps were always found to lag peaks in the global bicoherence for these sum interactions at the same vertical heights. Nonlinear interactions between the second-mode and the mean flow were also present in the bicoherence at transitional locations along the cone surface. These

were found to have the greatest level of quadratic phase coupling just above the boundary-layer edge; however, the BMD analysis suggested these interactions were insignificant or artifactual. In addition, BMD proved effective in confirming that the structures identified by SPOD were, in fact, harmonics, rather than some unrelated wave, and denoised the data such that even higher harmonic structures could be visualized.

Chapter 4: Straight cone at angle of attack at Mach 14

This chapter provides experimental measurements of the second-mode fundamental and superharmonics on a 7 °half-angle cone at zero and nonzero angles-of-attack (windward side only) at Mach 14. High-speed calibrated schlieren measurements are collected and a reconstruction technique of time-resolved pixel-intensity signals is employed (see section 2.2) to enable spectral analysis of second-mode fundamental and harmonic content. In Kennedy et al. (2018a), a preliminary analysis of this data set was provided at select interrogation points (i.e., a limited selection of pixels) within the boundary layer. Here, the analysis is expanded to the entire schlieren field of view to allow the application of global analysis techniques.

4.1 Experimental Methodology

4.1.1 Facility Overview

Experiments were performed in the AEDC Hypervelocity Wind Tunnel 9 facility. Only condition A, outlined in Table 4.1, was used for the present analysis. A complete description of the facility and its capabilities can be found in Marren et al. (2015). Root-mean-square freestream pressure fluctuations at this run condition are between approximately 5-6% of average pitot pressure measurements (Lafferty and Norris 2007).

Table 4.1: Test matrix and conditions.

Condition	M	Re_∞ [$10^6/m$]	U_∞ [m/s]	h_0 [MJ/kg]
A	13.50	2.49	1852	1.76

4.1.2 Model and Instrumentation

A 1.55 m long 7° half-angle cone was employed as the test article for this campaign. The model consisted of three 15-5 stainless steel sections with base diameters of 0.127 m, 0.254 m, and 0.381 m and an interchangeable 15-5 stainless steel nose tip. A nose tip radius of 0.152 mm was used for the current campaign. The test article was instrumented with a variety of flush-mounted pressure sensors and thermocouples, including PCB® 132-A31 fast-response pressure transducers, Kulite® XCS-093 pressure transducers, Micro Switch® 15-psia transducers, and Type-E Chromel-Constantan coaxial thermocouples. Further details regarding the test article design and complete instrumentation layout can be found in Marineau et al. (2017). For the current analysis, only schlieren data is utilized. Following the flow start-up period of each experiment, the model was initially held at nominally 0° angle of attack for approximately 200 milliseconds, before beginning the sweep to 10°. In the present analysis we use reconstructed signals generated from 5,000 successive images for the 0° angle-of-attack state. For nonzero angles, successive images in a range of ±0.1° from the specified angle are used for reconstruction, resulting in approximately 800-1,000 images.

4.2 Schlieren Specifications

High-speed flow visualization was performed using a standard Z-type schlieren setup. Light emitted from a Cavilux HF laser operating at 640 nm with 50 ns pulse-widths was col-

limated and refocused by two identical 762 mm diameter mirrors with focal lengths of 5000 mm. Light was captured with a Phantom v2512 high-speed camera with a 12-bit depth at a nominal frame rate of 72 kHz, approximately equal to one half of the second-mode fundamental frequency predicted by linear stability theory at 0° angle-of-attack. An image resolution of 1024x320 was used for all images with a scale of 0.62 mm/pixel. The camera viewing plane extended from approximately 730 mm to 1220 mm from the nose tip along the cone surface. A horizontal knife-edge cutoff was used to visualize the density gradients approximately normal to the cone surface.

4.3 Propagation Speeds

Propagation speeds of second-mode wave-packets are computed using the method as described in section 3.4. Results are displayed in Table 4.2, including the total number of images used at each angle-of-attack condition, the average propagation speed, and the standard deviation. Propagation speeds are shown to increase slightly at nonzero angle of attack, but all averages remain within one standard deviation. Note that the edge velocity should decrease on the windward side as the angle of attack is increased.

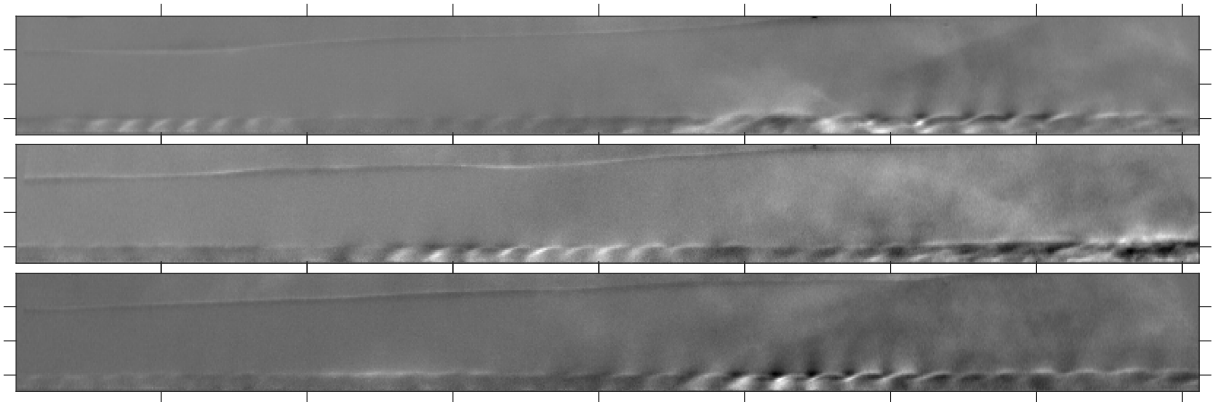

Figure 4.1: Reference-subtracted image sequence at 0° angle of attack at intervals of 97.2μs.

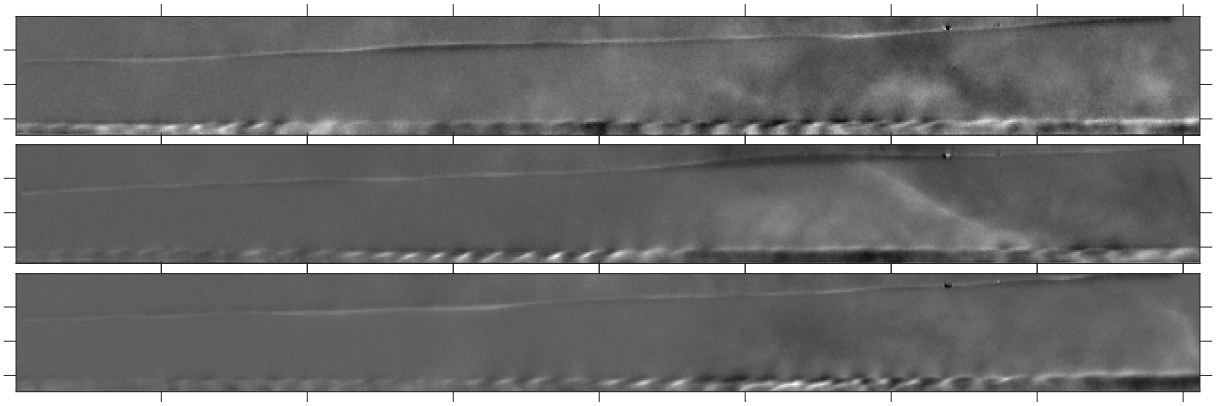

Figure 4.2: Reference-subtracted image sequence at 1° angle of attack at intervals of 97.2μs.

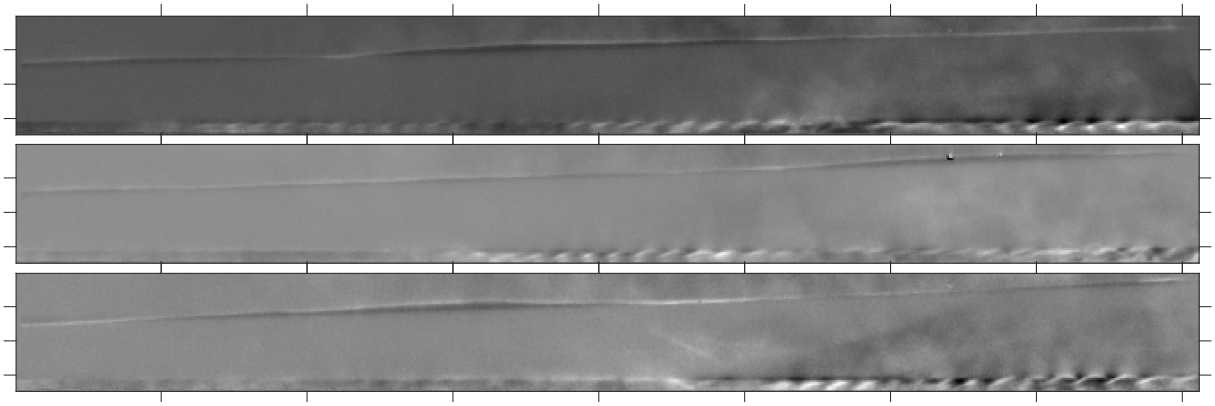

Figure 4.3: Reference-subtracted image sequence at 2° angle of attack at intervals of 97.2μs.

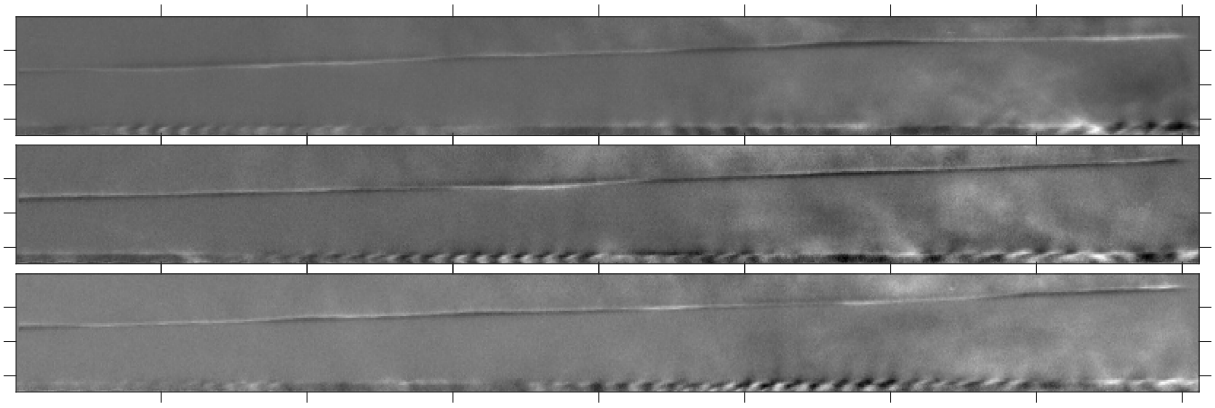

Figure 4.4: Reference-subtracted image sequence at 3° angle of attack at intervals of 97.2μs.

Example image sequences showing the propagation of second-mode waves are shown in Figures 4.1-4.4; in each sequence, every seventh image is displayed. The horizontal axis of

Table 4.2: Numbers of images with identified wave packets and calculated propagation speeds for all conditions.

AoA	0°	1°	2°	3°
Number of Images	5000	1001	771	911
Propagation Speed U_p [m/s]	1670	1692	1692	1694
σ [m/s]	32.9	30.2	35.1	33.7

each image is aligned with the cone surface. Each image has been reference subtracted using an average flow-on image as a means to accentuate perturbations about the mean-flow state. The qualitative behavior of the second-mode wave-packets is consistent for each angle-of-attack state. Particular wave-packets in each sequence can be observed to grow in intensity as they propagate downstream, evident by more pronounced variations in pixel intensity caused by the disturbances. As the angle of attack is increased, the boundary layer thickness noticeably decreases, leading to a decrease in the second-mode disturbance wavelength. The boundary-layer thickness at the midpoint of the image viewing plane started from approximately 14 pixels at 0° to 8 pixels at 3°.

4.4 Power Spectral Density and N-Factor Analysis

First, a spectral analysis of the reconstructed and calibrated pixel intensities is conducted to analyze the spatial evolution of disturbance content within the boundary layer. Power spectral densities (PSD) are calculated using Welch's method with a Blackman window function and 50% overlap between segments. The amount of segments used varied with each condition due to the varying length of the signals.

In the left column of Figure 4.5, contours of the PSD for each angle of attack are displayed, showing the spectral development in the streamwise direction. At each streamwise position, the plotted PSD is taken from the wall-normal pixel exhibiting the maximum second-mode power.

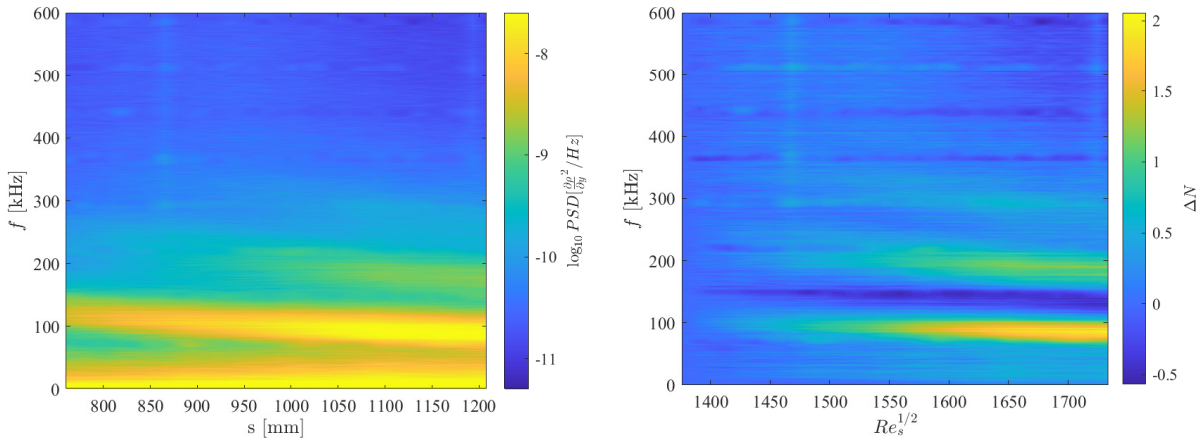

(a) 0° Angle of Attack

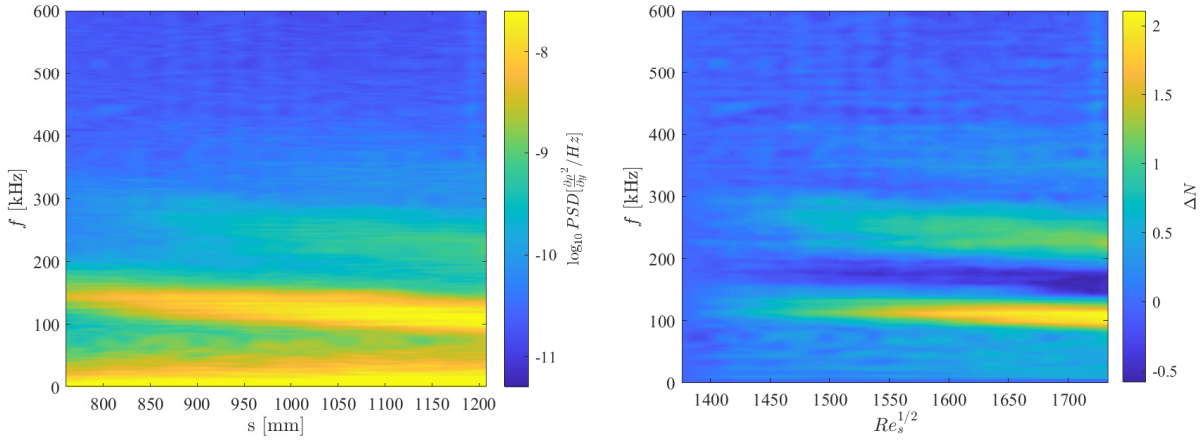

(b) 1° Angle of Attack

Figure 4.5: Power spectral density (left column) and change in N-factor (right column) along the pseudo-streamline of maximum second-mode power for all angle-of-attack states.

The change in N-factor, ΔN, for each frequency is displayed in the corresponding right-hand plot, computed with equation 3.1 (see section 3.6). In the N-factor plots, the streamwise coordinates are converted to the corresponding Stability Reynolds number, $Re_s^{1/2}$, where $Re_s = Re_\infty s$.

The most-amplified fundamental frequencies at each streamwise location are shown in Figure 4.6 for each angle-of-attack state. Due to the decreasing boundary-layer thickness with increasing angle of attack, the most-amplified frequencies increase with angle of attack.

In Figure 4.7, the N-factor growth of the most-amplified second-mode fundamental, first-

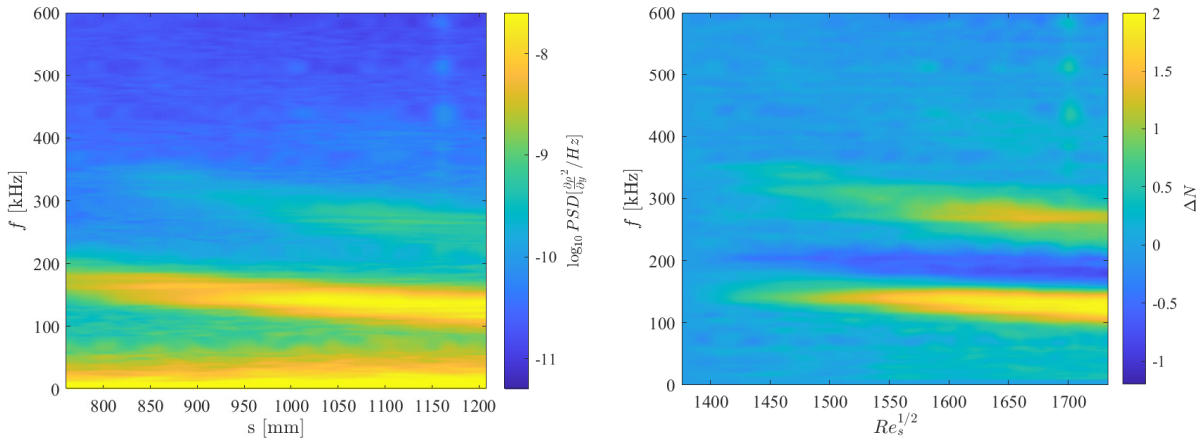

(c) 2° Angle of Attack

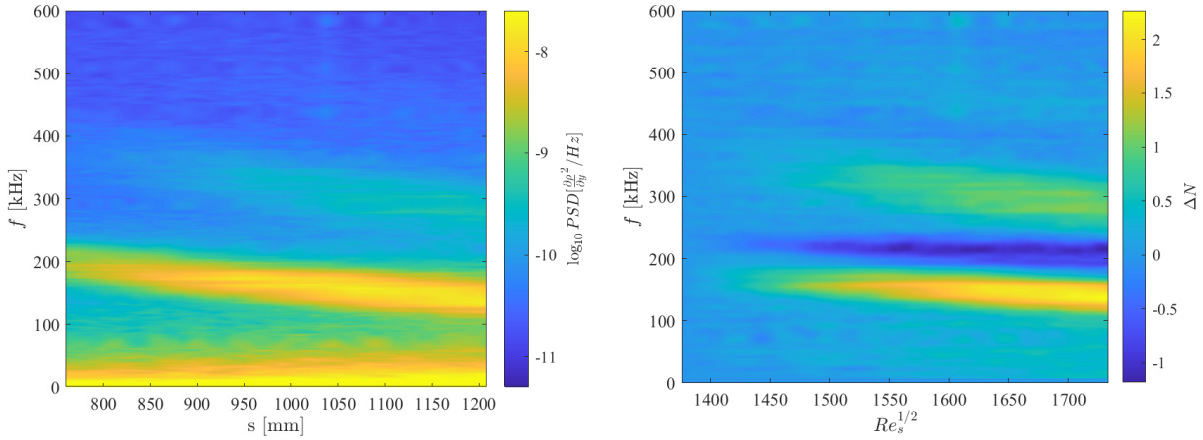

(d) 3° Angle of Attack

Figure 4.5: Power spectral density (left column) and change in N-factor (right column) along the curve of maximum second-mode strength for all angle-of-attack states.

harmonic, and second-harmonic frequencies are plotted. The growth rates of the fundamental instability are computed with the equation

$$\Delta N(f, s) = \frac{1}{2} \ln \frac{PSD(f_{0,max}, s)}{PSD(f_{0,max}, s_0)}. \tag{4.1}$$

where $f_{0,max}$ represents the most-amplified frequency in the fundamental frequency range (i.e., those displayed in Figure 4.6a). Growth rates of the first and second harmonics are computed

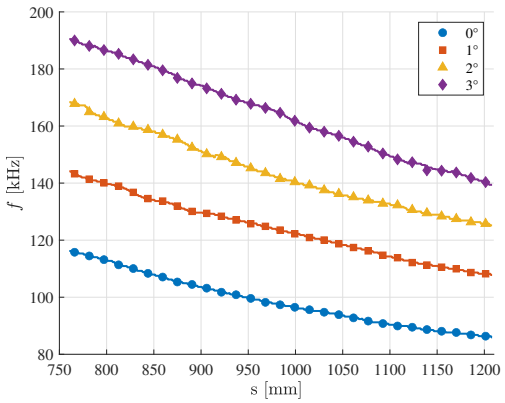

(a)

Figure 4.6: Most-amplified frequencies of the fundamental second mode for states 0° (○), 1° (□), 2° (△), and 3° (◊).

at $2f_{0,max}$ and $3f_{0,max}$, respectively. The figures show that the growth rates of the second-mode fundamental and first-harmonic do not change appreciably with angle of attack. However, there is some irregularity in the growth rates, particularly for nonzero angles-of-attack, which may be caused by the lower quantities of images available. Additionally, the growth rates of the first harmonic are consistent over the angles of attack examined, with the possible exception of the 3° angle-of-attack case, which appears to have its growth rate diminish more than the other cases for $Re_s^{1/2} > 1550$. Notably, this likeness vanishes for the second-harmonic growth rates, where the growth rate at 0° angle of attack is approximately double that of the nonzero angle-of-attack cases. This may be physical, but a plausible culprit of this discrepancy is a signal-to-noise limitation. From the contour plots of Figure 4.5, we see that the second-harmonic bands at nonzero angle-of-attack cases are discernible but only barely above the surrounding noise floor. Duan et al. (2018) showed that there is a drop-off in the PSD of freestream pressure fluctuations with increasing frequency. With the second-harmonic frequencies increasing with nonzero angle of attack, the priming oscillations may be low enough amplitude such that the weak nonlinear forcing causing

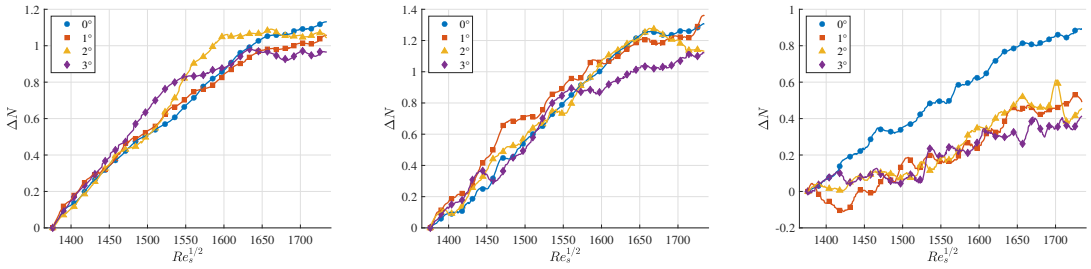

(a) (b) (c)

Figure 4.7: N-factor growth for second-mode fundamental (a), first-harmonic (b), and second-harmonic (c) instabilities.

second-harmonic growth is not sufficient to grow the second-harmonic amplitude significantly above the noise floor.

4.5 Spectral Proper Orthogonal Decomposition

In this section we employ spectral proper orthogonal decomposition (SPOD) to educe coherent flow structures associated with the second-mode fundamental and superharmonic frequencies. Once again, the algorithm employed in this analysis can be found in detail in section 2.3.1 and in Towne et al. (2018). SPOD is an eigenvalue problem and therefore the two principal outputs from the technique that will be presented are the SPOD eigenvalue spectrum and the SPOD eigenvectors (i.e., the mode shapes). We are primarily concerned with the leading SPOD modes (i.e., those that exhibit the highest energy at each frequency) since these typically contain the relevant second-mode content, and all SPOD results presented will pertain to these modes. For the case of 0° angle of attack, where more images are available for analysis, the SPOD modes are computed using a total of 50,000 "snapshots" of the flow, where each snapshot is represented by a single reconstructed image from the time-resolved reconstructed signals. These 50,000 snapshots were segmented using Hamming windows of length 256 with 50% overlap, resulting in 389

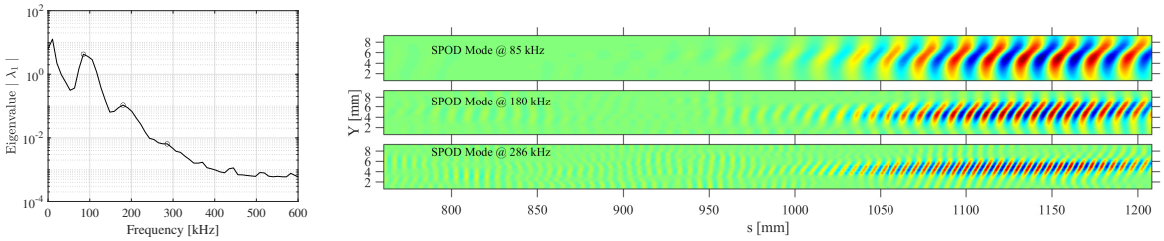

(a) (b)

Figure 4.8: (a) Energy density spectrum of leading SPOD mode at 0° angle of attack (b) SPOD mode shapes at 0° angle of attack at frequencies of 85kHz (top), 180kHz (middle), and 286kHz (bottom).

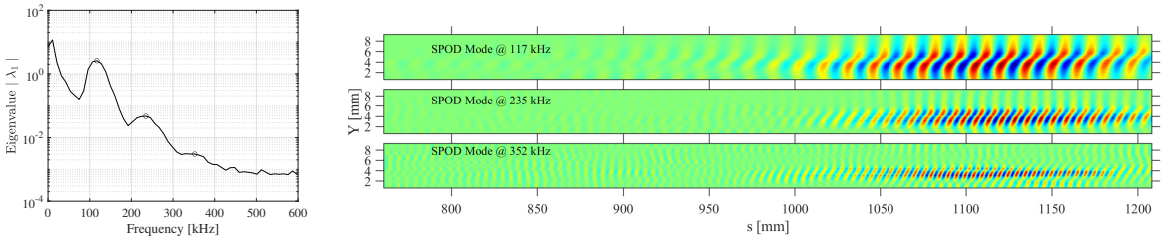

(a) (b)

Figure 4.9: (a) Energy density spectrum of leading SPOD mode at 1° angle of attack (b) SPOD mode shapes at 1° angle of attack at frequencies of 117kHz (top), 235kHz (middle), and 352kHz (bottom).

realizations of the flow and a frequency resolution of 10.6 kHz. For the cases of nonzero angle of attack, the full reconstructed signals are used for SPOD analysis and consist of 37,000, 28,490, and 33,670 total snapshots for the 1°, 2°, and 3° cases, respectively. Hamming windows of length 256 with 50% overlap are similarly used, resulting in approximately the same frequency resolution as the 0° case (slight variations exist here due to the dependency of each case's effective sampling rate on the calculated propagation speed).

Figures 4.8–4.11 display the eigenvalue spectrum of SPOD mode 1 and the leading SPOD mode shapes at the second-mode fundamental, first-harmonic, and second-harmonic peak frequencies for each angle-of-attack state. These peak frequencies correspond to the SPOD eigenvalue spectrum, not the pixelwise PSDs, and therefore represent the structures with the highest

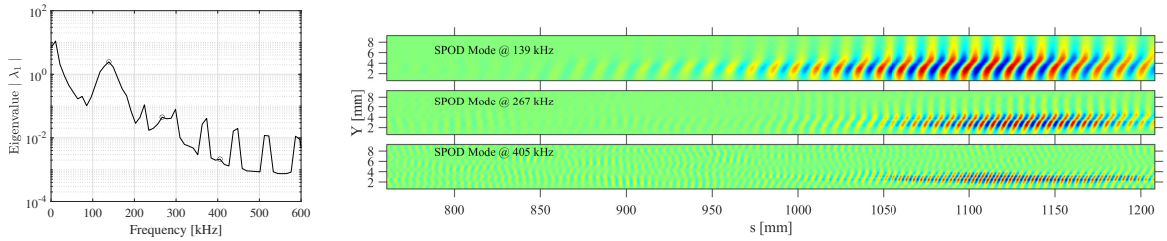

(a) (b)

Figure 4.10: (a) Energy density spectrum of leading SPOD mode at 2° angle of attack (b) SPOD mode shapes at 2° angle of attack at frequencies of 139kHz (top), 267kHz (middle), and 405kHz (bottom).

spatiotemporal energy across the entire field of view. SPOD mode shapes are plotted as contours of the real part of the eigenvectors. The peak frequencies are marked as open circles on the corresponding eigenvalue spectrum plots. Note that the vertical axis has been elongated here for clarity of features. In each case, the characteristic rope-like appearance of second-mode disturbances is the dominant coherent structure identified by SPOD. The fundamental second-mode peak increases in frequency and decreases in power with increasing angle of attack; the same trends are observed for the superharmonics. The mode shapes at 0° angle of attack are the most coherent in so far as the energy contours of each wave in the structures are uninterrupted by noise in the regions where the structures are prominent and incoherent fluctuations outside of these regions are significantly lower in power. With increasing angle of attack, the coherence of the structures decreases, particularly for the superharmonic mode shapes. More variance can be observed in the energy contours of each wave crest and background fluctuations increasingly approach the energy levels of the coherent structures.

Note that artifactual spikes arise in the SPOD eigenvalue spectrum for the 2° angle-of-attack state at integer multiples of approximately 75 kHz. These are the result of a piece of debris slowly passing through the boundary layer during this period of the test. Because the debris

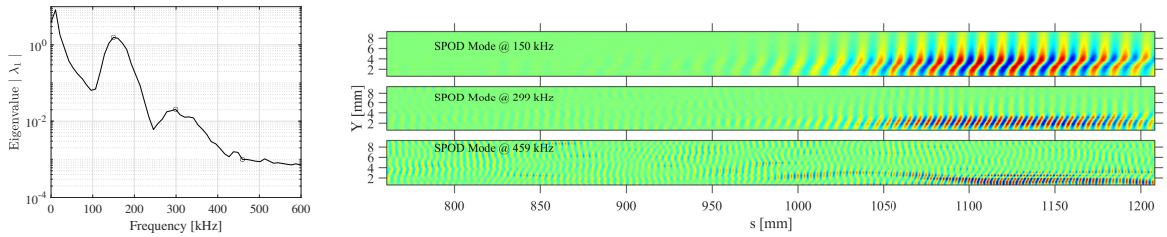

(a) (b)

Figure 4.11: (a) Energy density spectrum of leading SPOD mode at 3° angle of attack (b) SPOD mode shapes at 3° angle of attack at frequencies of 150kHz (top), 299kHz (middle), and 459kHz (bottom).

propagates at a significantly different velocity from the second-mode content, the reconstruction technique introduces periodic errors in the signal. An in-depth analysis on the spectral anomalies produced in the reconstructed signals by such errors in propagation speed can be found in Appendix A. Fortunately, the peak frequencies of the second-mode fundamental and superharmonic content are not obscured by these artifacts. Additionally, the local peak in the eigenvalue spectrum for the 3° case between approximately 430-450 kHz is noise-induced. No coherent structures exist for the SPOD mode shapes at these frequencies – instead, the mode shape at 459 kHz depicts the most coherent structure associated with the second harmonic.

In Figure 4.12 the wall-normal energy distributions are plotted for the leading SPOD modes shown in Figures 4.8–4.11. These are generated by first taking the absolute value of the complex mode shape (rather than the real part of the mode, as is done in Figures 4.8–4.11 to depict the wave structures), and then plotting the column of values at the streamwise location of maximum energy. In all cases, the wall-normal extent of the content becomes narrower with increasing harmonic. The peak harmonic energy is found at approximately the same wall-normal position as the fundamental content: At zero incidence, the first harmonic is found one pixel (0.62 mm) closer to the wall than the fundamental and the second harmonic is found at the same wall-normal

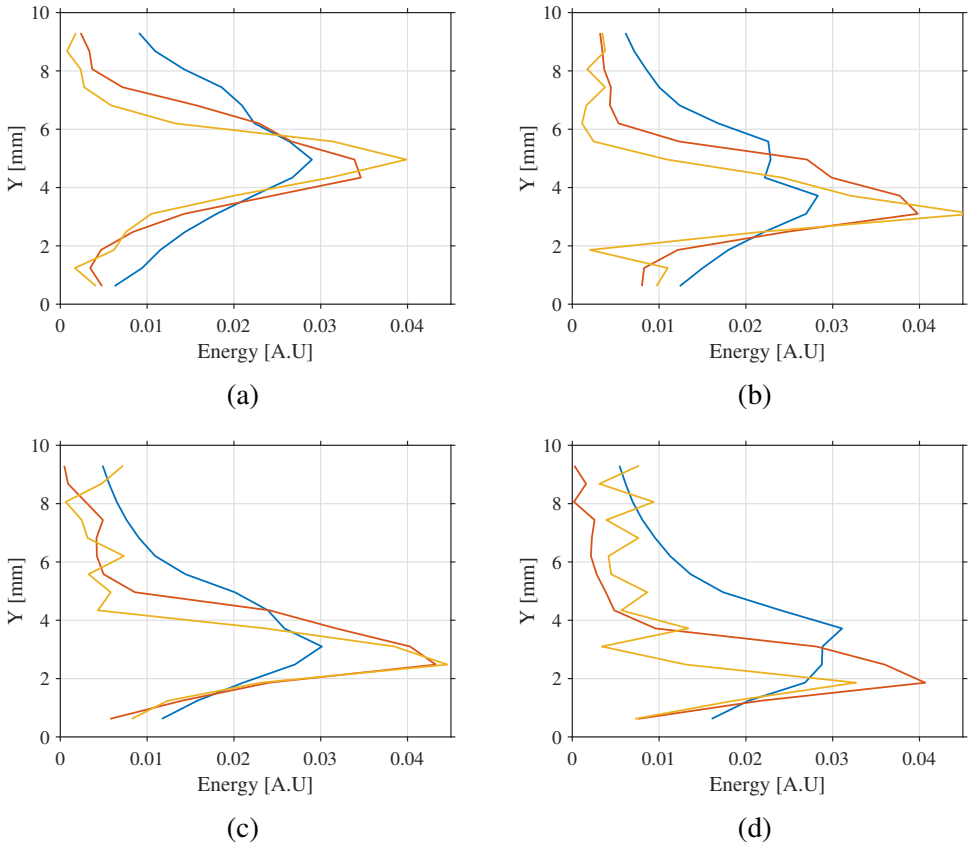

Figure 4.12: Wall-normal energy distribution of leading SPOD mode for the second-mode fundamental (blue), first-harmonic (red), and second-harmonic (yellow) structures at 0° (a), 1° (b), 2° (c), and 3° (d).

height as the fundamental, while at nonzero incidence, all harmonic content is found one pixel (0.62 mm) closer to the wall than the fundamental. At all angles of attack, there is an indication of increased energy at a wall-normal height slightly above the primary peak found within the boundary layer. At 1° and 3°, this appears as secondary peak (at 3° this secondary peak exceeds that of the peak closest to the wall), while at 0° and 2° there is a definite steepening of the slope, but no physical peak is present. Notably, at nonzero incidence, the peak in second-mode energy found closest to the wall appears to shift closer to wall faster than the boundary layer shrinks. Between 0° and 3°, the boundary-layer thickness decreases by approximately 43% (based on boundary-layer edge estimates made directly from the schlieren images), but the wall-normal

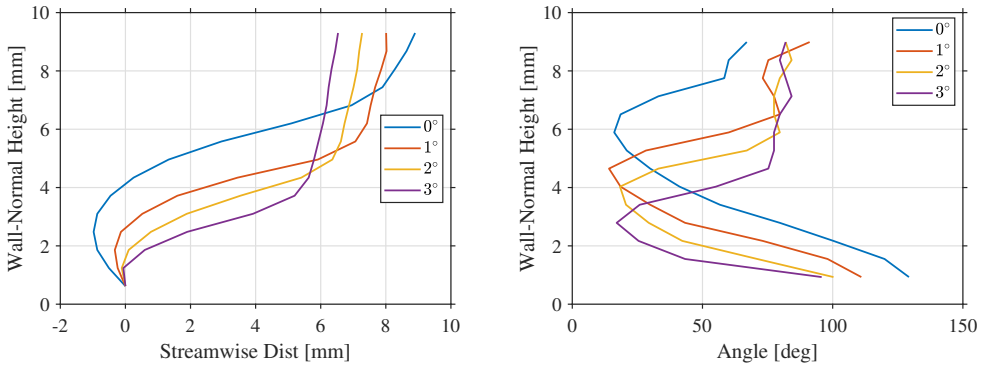

(a) Fundamental

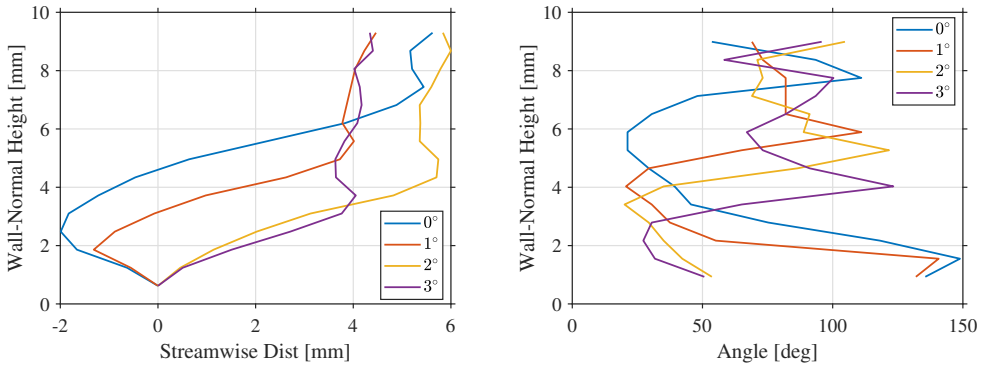

(b) First harmonic

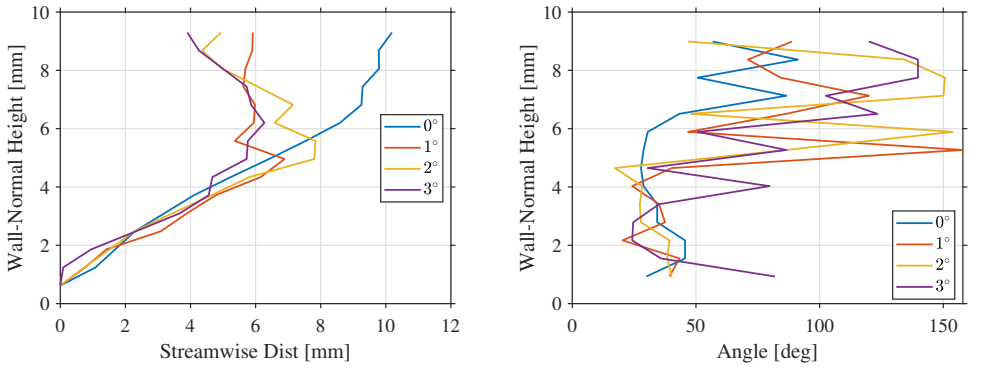

(c) Second harmonic

Figure 4.13: Wall-normal structure profiles (left) and angles (right) for the leading SPOD mode shape.

height of the peak in second-mode energy (again, considering the initial peak closest to the wall) decreases by approximately 60%.

In Figure 4.13, the wall-normal structure profiles and angles are plotted for each angle of attack, again using the leading SPOD mode shape at the fundamental, first-harmonic, and

second-harmonic peak frequencies. The profiles are determined by considering each individual row of pixels in the mode shape, starting at the wall, and performing a cross correlation with the row of pixels above it (see Laurence et al. 2016 for more details). The fundamental profiles appear to initially tilt upstream (structure angle > 90°) before turning around and reaching a fairly consistent angle within the boundary layer between 14°–18°. As the angle of attack is increased, the tendency for the structures to tilt upstream near the wall decreases. As the structures approach the boundary-layer edge, they straighten out and all end at an angle of approximately 90°. The wall-normal profiles of the first harmonic are roughly consistent with that of the fundamental, with structure angles dropping to 20°–21° within the boundary layer for 0°–2° angles of attack and 27° for 3° angle of attack. At 2° and 3° angle of attack, the first-harmonic structures no longer tilt upstream close to the wall, although they do start off at a steeper angle (~50°) than that which they take on near the center of the boundary layer. At all angles of attack shown, the second harmonic shows a fairly consistent structure angle throughout the boundary layer (between approximately 20°–30°), which roughly coincides with the structure angle found near the center of the boundary layer for the first-harmonic structures and is slightly higher than that of the fundamental structures.

4.6 Bispectral Mode Decomposition

The primary method for analyzing nonlinearity in fluid flows has been the use of higher-order spectra. In the particular cases where quadratic nonlinear terms are present in the governing equations, such as is the case in the Navier-Stokes equations, the bispectrum has been used for its capability of detecting three-wave coupling. In the present analysis, BMD is performed using

the same inputs and parameters as was done for SPOD. Figure 4.14a displays the mode bispectrum for the 0° angle-of-attack state. In these plots, f_1 and f_2 are the primary waves interacting to create content at $f_1 + f_2$ and λ_1 represents the strength of the nonlinear interaction. Clear peaks in the bispectrum can be observed involving the second-mode fundamental and harmonic content, indicating significant nonlinearity in the flow. Select mode shapes are shown in Figure 4.15 for the $85kHz + 85kHz \rightarrow 170kHz$ and $191kHz + 95kHz \rightarrow 286kHz$ sum interactions, approximately representing the interactions that generate the first and second harmonics. The particular frequencies chosen here result in the nearest frequency bins to the most amplified first- and second-harmonic frequencies found with SPOD. Excellent agreement in the mode shapes is observed between SPOD and BMD, confirming that the SPOD structures pertain to the nonlinearly generated second-mode harmonics.

BMD results for the 3° case are similarly shown in Figures 4.14b and 4.16. The mode bispectrum is qualitatively similar to that of the 0° case, with lobes of high λ_1 at the second-mode fundamental and harmonic frequencies now shifted to the most-amplified frequencies present at the 3° angle-of-attack state. Additionally, the strength of each nonlinear interaction has decreased relative to those of Figure 4.14a. Once again there is excellent agreement between the SPOD and BMD harmonic mode shapes. Note that the mode shapes of Figure 4.16 have a much better signal-to-noise ratio compared to the second-mode harmonic SPOD mode shapes in Figure 4.11b. This is due to the capability of BMD to reject content that is not quadratic phase-coupled. Table 4.3 summarizes the peak values of $|\log \lambda_1|$ for select nonlinear interactions for all angle-of-attack states. The left column of Table 4.3 indicates the frequency triad, with 0 representing the mean flow, 1 representing a frequency in the second-mode fundamental band, 2 representing a first-harmonic frequency, and so on. The values shown are the maximum values within the lobes

observed in Figure 4.14. In every instance the nonlinear interaction is found to be weaker at the 3° angle-of-attack state. For brevity, the mode bispectrum and second-mode harmonic mode shapes are omitted for the 1° and 2° angle-of-attack states; however, the peak values of $|\log \lambda_1|$ are included in Table 4.3. The trend of lower nonlinear interaction strength with increasing angle of attack is generally consistent. There is less separation in the peak values of the 1° and 2° angle-of-attack states; this may in part be due to insufficient convergence of the statistical data and partial contamination of the 2° BMD results by the artifacts mentioned in the previous section.

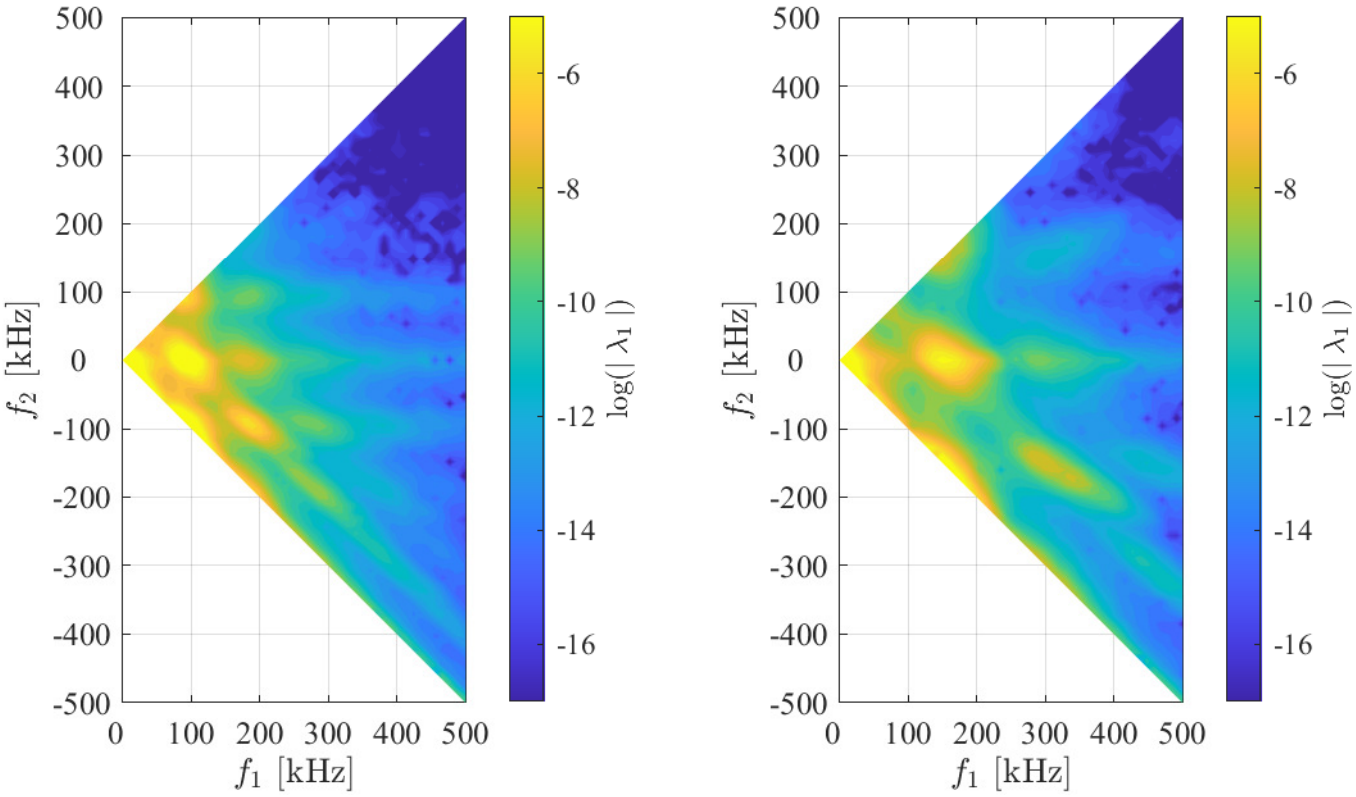

Figure 4.14: Mode bispectrum at (a) 0° angle of attack and (b) 3° angle of attack.

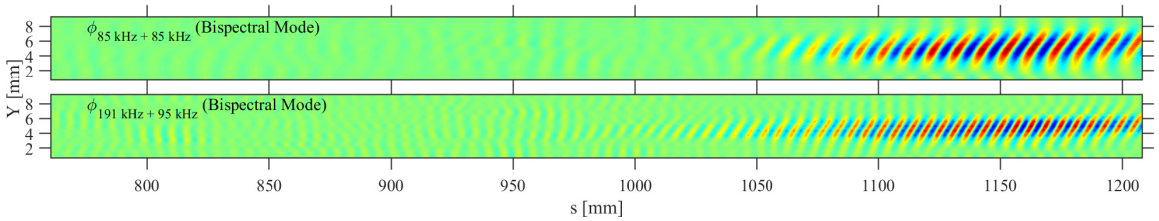

Figure 4.15: Bispectral mode shapes at 0° angle of attack resulting from triadic interactions $f_0 + f_0 \rightarrow 2f_0$ (top) and $2f_0 + f_0 \rightarrow 3f_0$ (bottom).

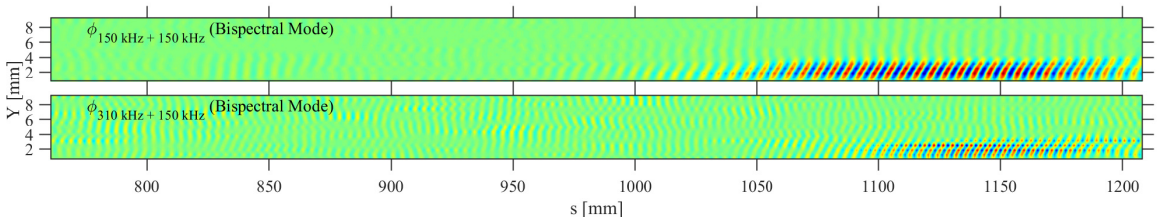

Figure 4.16: Bispectral mode shapes at 3° angle of attack resulting from triadic interactions $f_0 + f_0 \rightarrow 2f_0$ (top) and $2f_0 + f_0 \rightarrow 3f_0$ (bottom).

Table 4.3: $\log(|\ \lambda_1\ |)$.

Triad	0°	1°	2°	3°
(0,0,0)	-0.94	-0.91	-0.96	-1.41
(1,0,1)	-3.90	-4.18	-4.28	-4.91
(1,1,2)	-5.91	-6.63	-6.61	-7.59
(2,0,2)	-7.23	-7.85	-8.19	-8.75
(2,1,3)	-8.87	-9.84	-9.80	-11.27
(3,0,3)	-9.98	-10.5	-11.30	-11.91
(1,-1,0)	-3.00	-3.36	-3.48	-4.06
(2,-1,1)	-5.73	-6.53	-6.55	-7.53
(2,-2,0)	-6.07	-6.58	-6.75	-7.56
(3,-1,2)	-8.91	-9.83	-9.75	-11.16
(3,-2,1)	-8.47	-9.32	-9.30	-10.72
(3,-3,0)	-7.85	-8.73	-9.16	-9.53

4.7 Summary

The nonlinear development of the second mode was analyzed on a sharp 7° half-angle cone at Mach 14 at zero and nonzero angle of attack using high-speed calibrated schlieren imagery. Time-resolved pixel intensity signals were reconstructed from neighboring spatial data in sequen-

tial images and effective sampling rates greater than 2.5 MHz were attained. This technique was possible because the second mode and its harmonics, which were the dominant disturbances in the schlieren images, propagated at a near-constant phase speed over the field of view. Numerous spectral methods were performed to elucidate the growth of the second-mode fundamental and superharmonic content. These included an analysis of the pixelwise power spectral densities, spectral proper orthogonal decomposition, and bispectral modal decomposition.

N-factor growth over the schlieren field of view was calculated for each angle-of-attack state at the second-mode fundamental, first-harmonic, and second-harmonic peak frequencies. The fundamental growth rates decreased near the field of view for each angle-of-attack state, showing evidence of nonlinear saturation. Little variation in the growth rates with angle of attack was observed. However, since the model was continuously pitched, fewer images were available for the nonzero angle-of-attack states than for the zero angle-of-attack state, resulting in more noise in the spectra. These measurements could be made more accurately by using a lower pitch-rate and a focused-schlieren apparatus to improve the signal-to-noise ratio. The growth rate of the first harmonic exceeded that of the fundamental instability for each angle-of-attack state, with a slight decrease in the growth rate at 3° angle of attack. The growth rate of the second harmonic at zero angle of attack was approximately double of that found at the nonzero angles-of-attack. It is unclear if this is noise-related and better signal-to-noise would provide more confidence on the disparity.

Leading SPOD mode shapes clearly depicted the rope-like structure of the second-mode. Coherent first- and second- harmonic structures at the peak frequencies of the SPOD eigenspectrum were located at the same streamwise locations as the peak fundamental content. With increasing harmonic order, the lateral width of the coherent structure narrowed but remained ap-

proximately centered within the fundamental wave-packet. BMD bispectral modes generated from $f_0 + f_0$ and $2f_0 + f_0$ sum interactions were in excellent agreement with the leading SPOD mode shapes of the first and second harmonics, confirming their nonlinear origin. The mode shapes educed by BMD provided better clarity of harmonic structures due to the rejection of phase-incoherent disturbances. The strength of nonlinear interactions found in the BMD mode bispectrum decreased with increasing angle of attack. As BMD is nonnormalized, this is likely a result of the decreased power spectral density found at the peak second-mode frequencies at increased angle of attack.

Chapter 5: Cone-flare at zero incidence at Mach 14

In this chapter, a series of experiments on the naturally occurring laminar-to-turbulent transition process on cone-flare geometries was performed at a nominal Mach number of 14. A 5° half-angle cone frustum was combined with various flare compression angles, including +5°, +10°, and +15°, to evaluate the propagation of boundary-layer disturbances through both attached and separated shock wave-boundary-layer interactions. Experiments were conducted in the Longshot Hypersonic Gun Tunnel at the von Karman Institute for Fluid Dynamics. High-speed calibrated schlieren imagery was performed as the primary diagnostic with flush-mounted high-frequency pressure sensors providing additional point-wise measurements. The modified reconstruction technique described in section 2.2.2 is applied to the schlieren data to recover an effective sampling rate over 4 MHz. The Nyquist limit of the camera frame rate is thus bypassed, and spectral analysis of high-frequency fundamental and harmonic instability mechanisms is enabled.

5.1 Facility Overview

The experiments in the current investigation were conducted in the Longshot facility at the von Karman Institute for Fluid Dynamics, in Belgium. The Longshot operates on the gun tunnel principle, whereby moderate freestream enthalpies are produced via an isentropic compression of

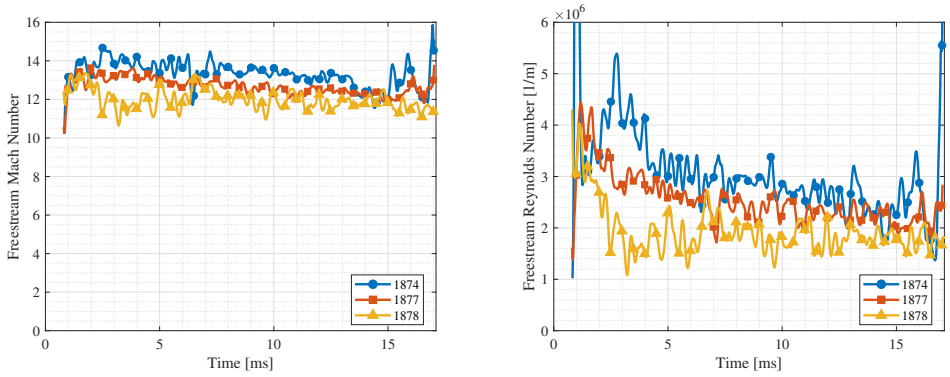

(a) Mach Number (b) Unit Reynolds Number

Figure 5.1: Freestream Mach number (left) and unit Reynolds number (right) during the approximate useful test time of shots 1874 (blue ○), 1877 (red □) and 1878, (yellow △).

the driven gas (here pure nitrogen) by an inertial piston. A collection of check valves at the end of the driven tube are used to trap the gas in the downstream reservoir at peak stagnation conditions. This mechanism extends the useful test time but results in a finite amount of compressed gas in a constant volume reservoir, leading to a temporal decay of stagnation conditions during the run. A contoured Mach 14 nozzle then expands the test gas to the desired conditions. Detailed descriptions of the tunnel compression process can be reviewed in detail in Grossir et al. (2017).

Three shots performed in the current campaign are reported here, each at the same nominal test conditions. The calculated freestream Mach number and unit Reynolds number [1/m] are shown in Figure 5.1 for each shot during the useful test time of approximately 16 ms. Further details of the freestream flow quantities during each shot can be found in Appendix B. The determination of freestream flow properties relies on measurements taken with three intrusive probes inside of the test section during each shot. These are a freestream static pressure probe, a Pitot pressure probe, and a stagnation point heat-flux probe. A full description of these probes as well as the modelling and numerical methods used to estimate the freestream properties from their measurements can be found in Grossir and Dias (2018).

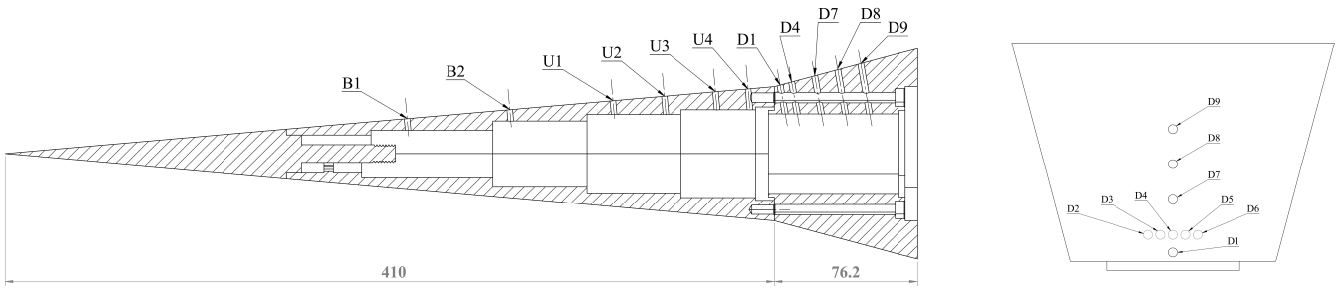

Figure 5.2: PCB® 132-B38 sensor layout. Lateral array (D2, D3, D5, D6) is exclusive to the +10° flare. Dimensions are in millimeters.

5.2 Model and Instrumentation

A 486.2 mm long cone-flare geometry was employed as the test article for this campaign. The model is composed of a sharp stainless steel conical nose tip followed by a primary 5° half-angle stainless steel conical frustum and an interchangeable secondary polyetheretherketone (PEEK) conical frustum of increased half-angle (to be henceforth referred to as the "flare" section). The nose-tip radius was measured to be 0.10 mm (Butler and Laurence 2022). Flare half-angles of 10°, 15°, and 20° were used in shots 1878, 1874, and 1877, respectively, corresponding to axisymmetric compression angles of +5°, +10°, and +15° (henceforth, the individual shots will be referred to by their compression angles). Two coplanar streamwise arrays of flush-mounted PCB® 132-B38 fast-response pressure transducers were installed on the top-facing sides of the cone and flare sections of the model. An additional lateral array of five PCB® sensors were installed at the D4 station of the +10° flare; these are separated by 6.5° (or, equivalently, an arclength of 4.32 mm), measured in the circular plane that cuts the flare at the D4 station. Figure 5.2 displays the +10° model configuration and sensor layout and Table 5.1 gives the corresponding sensor coordinates, measured along the model surface.

Table 5.1: Surface coordinates of PCB® 132-B38 sensors.

Station	B1	B2	U1	U2	U3	U4	D1	D4	D7	D8	D9
s [mm]	215	270	325	353	380	398	415	421	434	446	459

5.3 Schlieren Specifications

High-speed flow visualization was performed using a three-mirror schlieren setup, close in configuration to the conventional "Z"-type system. Light emitted from a Cavilux HF laser operating at 640 nm with a 30 ns pulse-width was first collimated by a 450 mm diameter parabolic mirror with a focal length of 3000 mm. The light path following this first mirror is parallel to the tunnel flow direction. Along the light path, there is an intermediate large planar mirror (610mm diameter) inclined by 45° to angle the light beam 90° before entering the test section side window. Light leaving the test section was focused using a 420 mm diameter parabolic mirror, also with a focal length of 3000 mm, and captured with a Phantom v2012 high-speed camera with a 12-bit depth. The camera alignment was modified for each run such that the compression corner was located at approximately the bottom center of the camera field of view. The camera roll angle was set at an intermediate value between the primary and secondary frustum half-angles to maximize the streamwise view of the model boundary layer. A horizontal knife-edge cutoff was used to visualize the density gradients approximately normal to the model surface. A nominal frame rate of 250 kHz with an image resolution of 1280x64 and image scale of 0.108 mm/pixel was used for the +10° configuration. For the +5° and +15° configurations, the camera settings were changed to a nominal frame rate of 500 kHz, 640x48 image resolution, and 0.200 mm/pixel image scale.

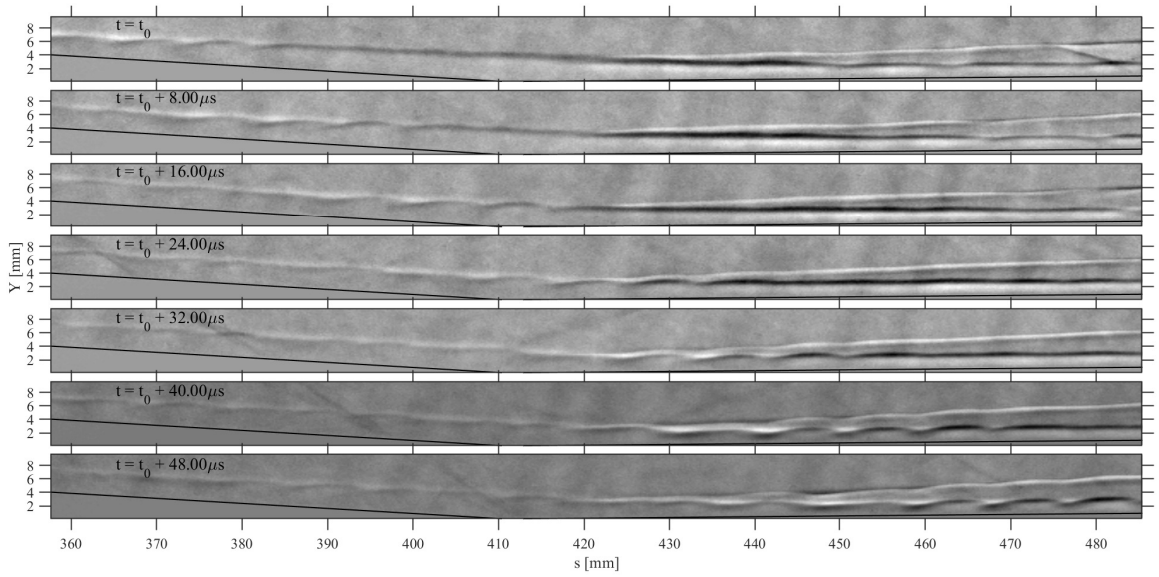

Figure 5.3: Schlieren image sequence at +5°.

5.4 General Behavior

As was done in the previous chapters, we begin by presenting image sequences from each shot to give the reader a visual representation of the general flow behavior. These are presented in Figures 5.3–5.7, which depict reference-subtracted images taken within the useful test time. For shots +5° and +15°, every fourth image is shown, resulting in time intervals of 8.00μs. For shot +10°, every second image is shown, resulting in time intervals of 7.86μs (note that the nominal frame rate was 250 kHz, but the real frame rate was 254.5 kHz). In each image, flow is moving left to right and solid black lines indicate the model surface.

Starting with the +5° shot (Figure 5.3), a second-mode wave packet can be seen entering the schlieren field of view in the first image with a leading wave located at approximately s = 385 mm. This wave packet propagates downstream and reaches the corner approximately 16μs later. Note that the corner is located at approximately s = 410 mm (to be precise, it is located at s =

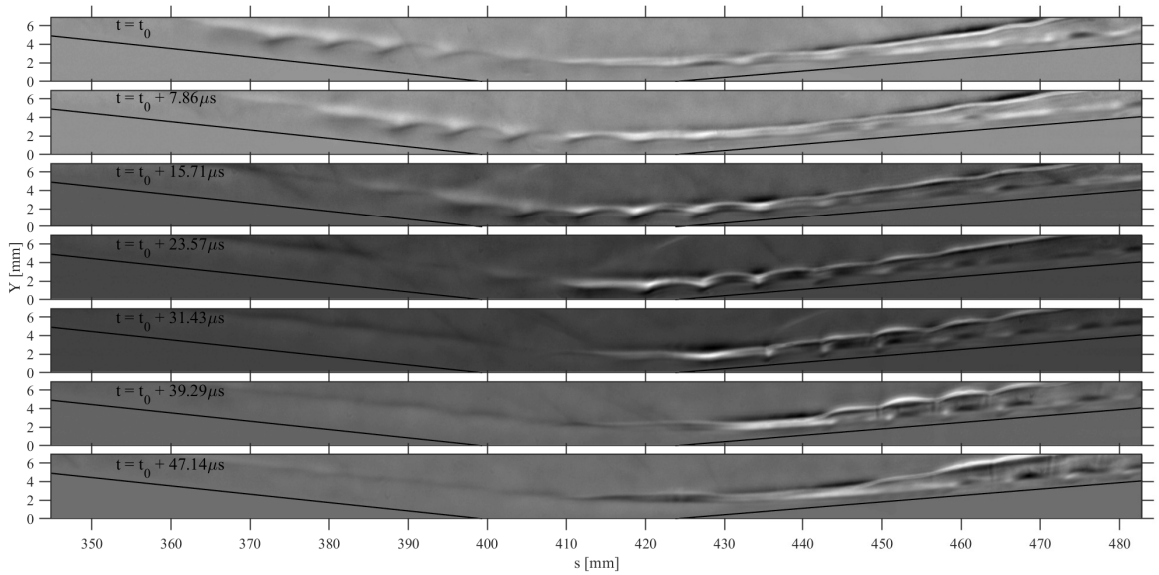

Figure 5.4: Schlieren image sequence at +10°.

$410/cos(5°) \approx 411.5$ mm). The corresponding attached shock wave can be seen to impinge the incoming boundary-layer edge near $s = 420$ mm. As the second-mode wave packet propagates through this shock, the density fluctuations (i.e., pixel intensity fluctuations) of the wave packet can be seen to grow in amplitude. The second-mode wave packet can be seen to continue to propagate within the boundary layer of the flare and does not appear to experience breakdown before leaving the schlieren field of view. Additionally, the wave packet perturbs the attached shock as it propagates through it. In the final images of the sequence, waves with approximately the same wavelength of the second mode can be seen propagating downstream along the shock wave, although these are relatively smaller in amplitude compared to the second-mode waves found within the flare boundary layer.

In Figure 5.4 a similar sequence is shown for the +10° configuration. First note that, near the corner, the incoming boundary layer seems to experience modulation further upstream than was just observed in the +5° case. This is most discernible in the first and final two images

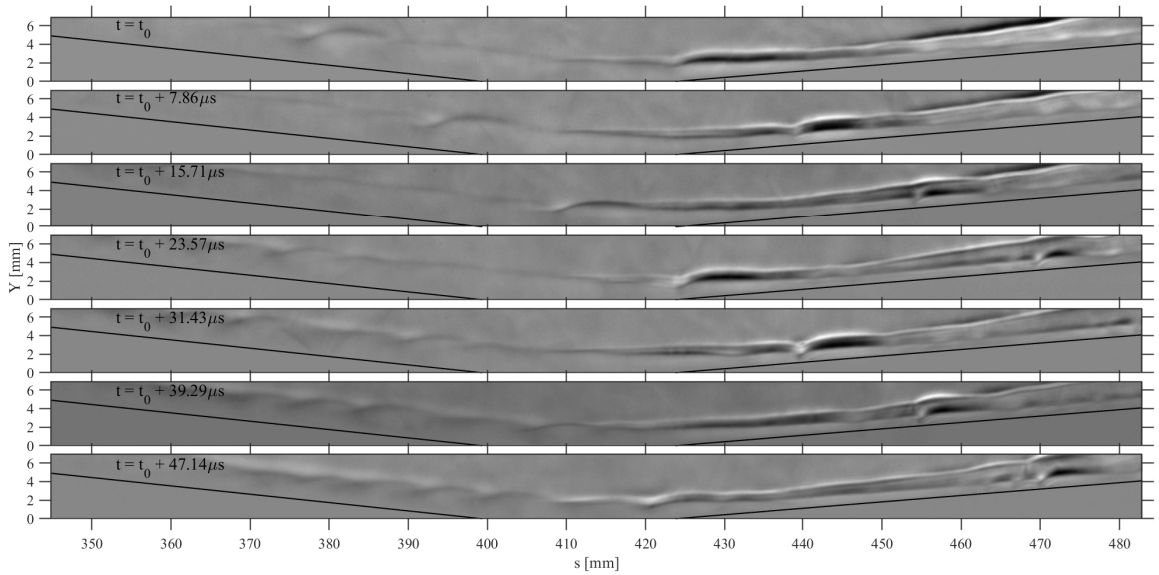

Figure 5.5: Schlieren image sequence at +10°.

of the sequence, when there appears to be a shallow shock present that impinges the incoming boundary layer at approximately $s = 410$ mm. A steeper shock wave can be observed further downstream. It is therefore believed that at this condition the corner flow contains a very small separated region between approximately $s = 410 - 430$ mm (though, due to the limited extent of the separation, the precise location of reattachment is difficult to discern). The incoming wave packet is amplified first near separation. A strong interaction with the steeper (reattachment) shock is observed, with second-mode radiation along the shock now seen to be of equal or greater magnitude than the wave packet contained within the flare boundary layer. Again, as was seen for the +5° case, the waves within the flare boundary layer do not experience breakdown. An additional sequence for this condition is shown in Figure 5.5. One of the waves in the incoming second-mode wave packet, centered at approximately $s = 380$ mm in the first image of the sequence, is significantly stronger than the rest of the wave packet. An interesting phenomenon occurs as this wave propagates through the shocks at the corner: A strong interaction is again

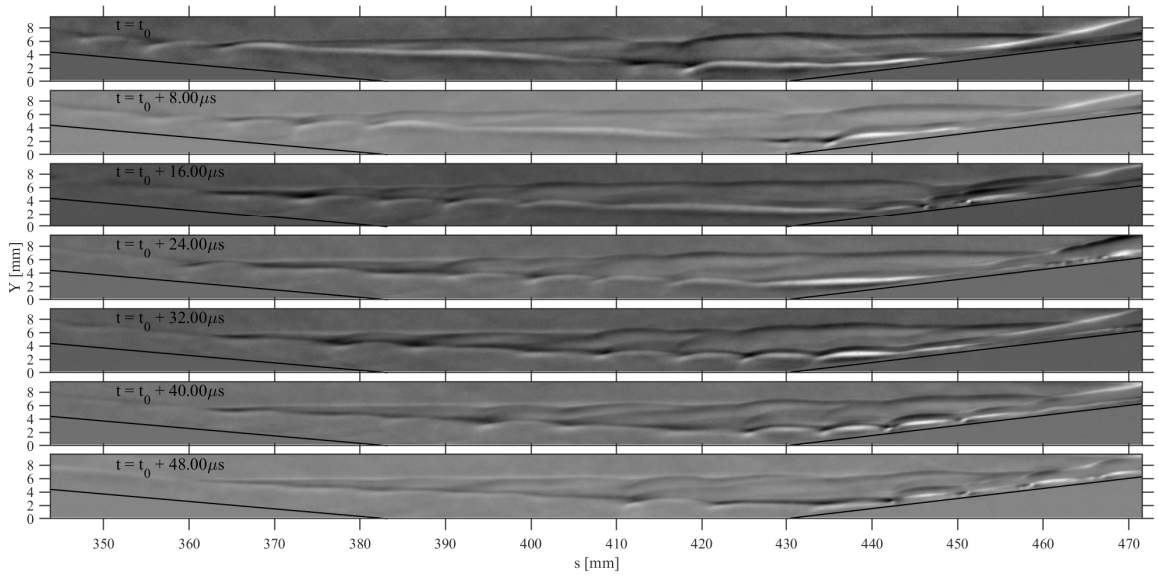

Figure 5.6: Schlieren image sequence at +15°.

observed between the reattachment shock and passing wave. Then, in the wake of the interaction, a "tail" with higher-wavenumber fluctuations appears on the strong wave inside the flare boundary layer. This higher-wavenumber tail can best be seen in the final image of the sequence between approximately $s = 460-470$ mm, with the parent wave located between approximately $s = 470-477$ mm. This behavior is consistently observed at this configuration when stronger amplitude second-mode waves encounter the corner.

Two image sequences are presented for the +15° shot in Figures 5.6 and 5.7. It is clear from these images that this model configuration produces a relatively large separation region, which is bounded by separation and reattachment shocks that impinge the relevant boundary layers at approximately $s = 355$ mm and $s = 337$ mm (note that there is slight unsteadiness in these locations, which is commonly observed in such flows but is further exacerbated in this case by the temporal decay of stagnation conditions). In Figure 5.6, the propagation of a second-mode wave packet through the corner is shown, which possesses a leading wave located at approxi-

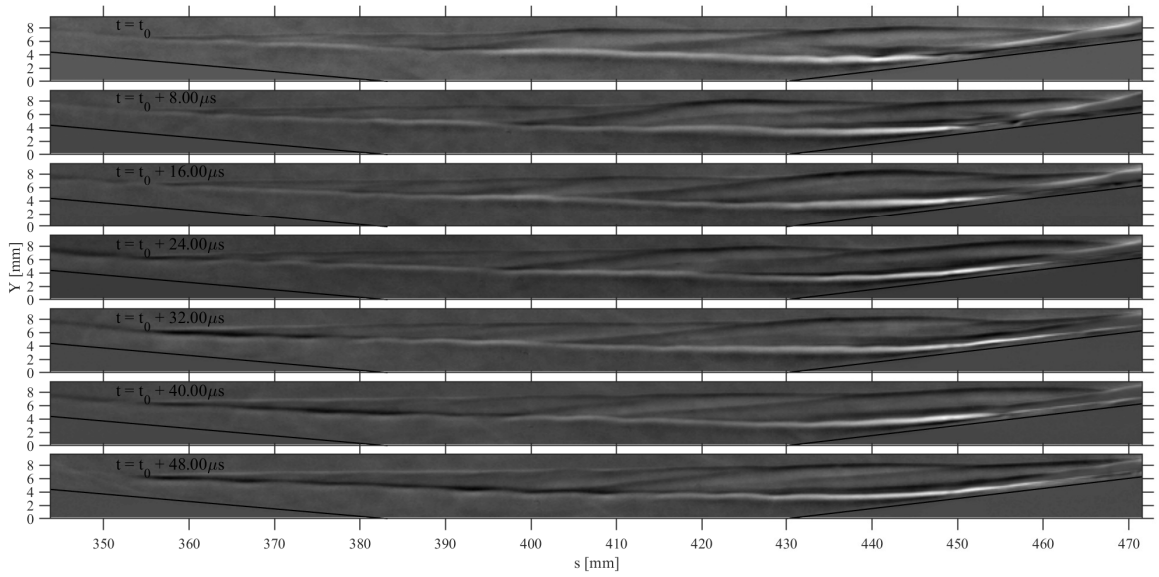

Figure 5.7: Schlieren image sequence at +15°.

mately $s = 368$ mm in the first image of the sequence. The wave packet propagates through the separation shock and is seen to traverse the separation bubble along the shear layer. Slight radiation of second-mode energy can be seen between the shear layer and separation shock, which originates at the separation point. Significant amplification of the wave packet is observed near reattachment. Thereafter, the wave packet continues to propagate within the thinner boundary layer on the flare, and some energy is again seen to radiate along the reattachment shock, though this radiation appears slightly weaker than in the +10° case. Figure 5.7 depicts the propagation of longer-wavelength structures that appear to originate along the shear layer. Two such waves can be along the shear layer in the first image, with crests (i.e., high pixel intensities) located at approximately $s = 375$ mm and $s = 405$ mm. Long streaks can be observed to emanate from these shear-layer waves and extend out towards the freestream, which then flatten out as they reach the separation shock.

5.5 Propagation Speeds

5.5.1 PCB® Sensors

In order to validate the second-mode propagation speed results computed directly from the schlieren images, the propagation speeds are also computed using pairs of PCB® sensors. This is done via computing the cross-correlation coefficients between segments of the first (upstream) PCB® sensor signal and shifted (lagged) segments of the second (downstream) sensor signal. Prior to this, the signals are band-pass filtered with a passband of 175-250 kHz using a zero-phase filter to attenuate content outside the second-mode band. The first signal is broken into 299 segments with 50% overlap, corresponding to segment lengths of 317 data points. For each segment, an array of normalized cross-correlation coefficient is computed with forward-shifted signals (i.e., forward in time) of the same length taken from the second PCB® sensor. The lag corresponding to the peak correlation coefficient is identified and a Gaussian curve is fitted using the coefficient values neighboring the peak. The location of the peak on this fitted curve is then recorded as the lag between the signals during this segment of the test time. This is repeated for all segments, and lags are converted to propagation speeds via the relation $U_{prop} = \frac{\Delta s}{k\Delta t}$, where U_{prop} is the propagation speed, Δs the distance between the sensors, k the lag (in units of data samples), and Δt the temporal resolution of the signals. An example of the results for this process is shown in Figure 5.8, which displays the calculated propagation speeds between sensors U3 and D4 during the +15° shot. Note that the majority of the results are clustered around a line beginning at approximately 2250 m/s at the start of the test time and ending at 1900 m/s. There are ordered outliers in the results located at approximately $\pm 400 - 700$ m/s away from this cluster.

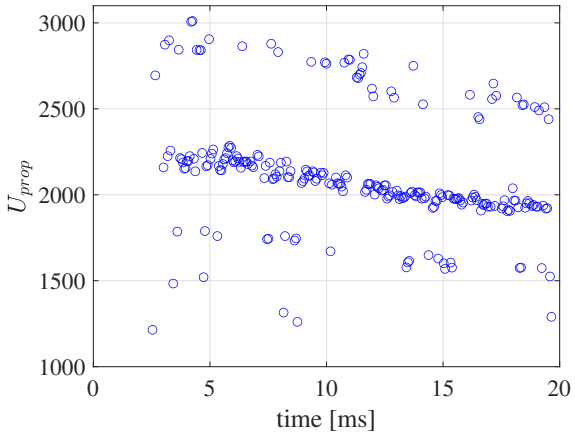

Figure 5.8: Calculated second-mode propagation speeds during the test time of the +15° shot between PCB® sensors U3 and D4.

The arrays of correlation coefficients calculated for each segment are periodic with respect to lag due to second-mode waves in the two signals moving in and out of phase. The peak correlation coefficient value may occasionally be located when the signals are in-phase but ±1 wavelength away from the true lag, resulting in the observed outliers. The mean and standard deviations of the propagation speeds calculated for each sensor pair for each shot are shown in Table 5.2; these statistics omit the aforementioned outliers as they can reasonably be deduced as incorrect peaks in the correlation coefficients. In addition to the overall mean propagation speed and standard deviation for each PCB® pair, the slope of a linear regression line fitted to the data is included as well as the residual standard deviation. The equation for the linear regression has the form $U_{prop} = \alpha t + b$, where t is the temporal coordinate and b is the y-intercept. Propagation speed averages are found to be 1771-2399 m/s. The averages with the largest standard deviations tend to be on either end of this range, indicating that an intermediate propagation speed in this range is more likely to be true.

Table 5.2: Propagation speeds between PCB® sensor pairs.

Shot	+5°				+10°				+15°			
PCB® pair	U_{prop} [m/s]	σ [m/s]	α [m/s^2]	σ_{res} [m/s]	U_{prop} [m/s]	σ [m/s]	α [m/s^2]	σ_{res} [m/s]	U_{prop} [m/s]	σ [m/s]	α [m/s^2]	σ_{res} [m/s]
B1/U1	2011	74	-15.6	16	-	-	-	-	2015	84	-18.8	15
U1/U3	2022	73	-14.8	21	1896	106	-22.5	41	1818	76	-14.4	38
U3/D4	2089	143	-21.3	94	1947	112	-23.2	37	2063	103	-20.6	35
D4/D7	2335	151	-29.4	52	2326	157	-27.4	94	1771	100	-15.0	74
D7/D8	2174	89	-17.5	27	1970	90	-16.8	50	2399	153	-10.1	146
D8/D9	2181	86	-17.1	21	1880	95	-8.6	86	1885	99	-4.4	97

5.5.2 Schlieren Imagery

As mentioned in section 2.2.2.1, disturbance velocities may also be measured directly from the schlieren images. A brief presentation of these results is given here to compare with the results found from the PCB® sensors. Figure 5.9 shows the second-mode propagation speeds plotted against $s-s_c$, where s_c is the streamwise location of the corner, for each shot. These are computed from image pairs using the methodology described in section 2.2.2.1, averaging over many image pairs inside the test time window. Due to the computational cost of the algorithm, only 200 images of the total available were used to compute the average speeds. This subset of images was taken in the 10-15 ms range of the useful test time, although the exact time window varied slightly between tests to ensure a window with densely populated wave packets was used. The results shown in Figure 5.9 were taken at wall-normal heights equal to the approximate boundary-layer edge. These edges (as well as edges corresponding to compression shocks generated by the flare and separation bubble) are identified by using a canny edge-detection operation on each image and averaging over all images captured during the useful test time. An example of the average detected edges for the +5° configuration is shown in Figure 5.10. The boundary-layer edges and

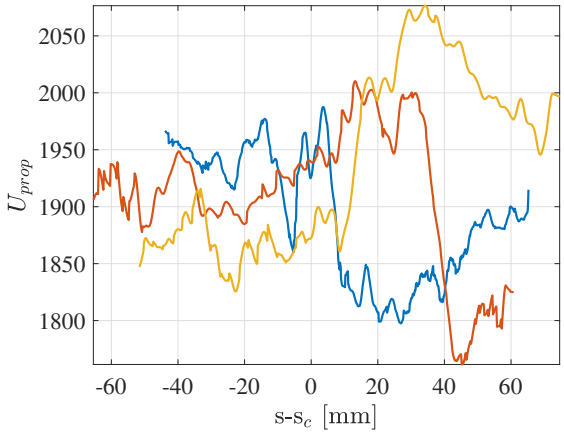

Figure 5.9: Calculated second-mode propagation speeds across the schlieren field of view for the +5° (yellow), +10° (blue), and +15° (red) configurations.

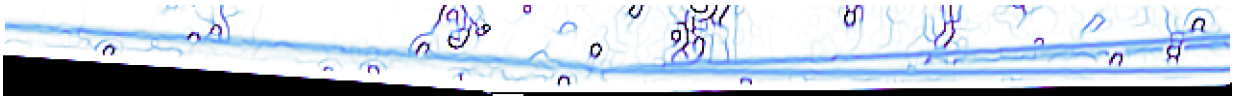

Figure 5.10: Average edges detected in Shot +5°

shock are readily apparent; the extraneous, more circular edges that are visible in Figure 5.10 represent tunnel window blemishes and can easily be disregarded. The wall-normal heights used in Figure 5.9 are the intersections of these edges with vertical lines in the images originating from the image horizontal coordinates given on the abscissa of Figure 5.9. The identified boundary-layer edge and shock locations will be used in later sections to probe the disturbance spectra along these features.

The propagation speeds derived from the schlieren images are in rough agreement with the results found with PCB® sensors, but they are, on average, slightly lower; however, this may be partly due to the image windows used being taken in the latter portions of the test time. Larger variations in the propagation speeds are observed in all shots after approximately 0 mm from the start of the image field of view. This coincides with the location of the compression corner, where the presence of the compression shocks and bifurcation of second-mode content along

these shocks leads to greater error in the algorithm.

5.6 PCB® Lateral Array

A lateral array of PCB® 132-B38 sensors were installed on the +10 deg flare to characterize the instability waves in the lateral direction. In particular, we are interested in measuring the width of second-mode wave packets. Since the reservoir conditions are unsteady, and therefore the pressure signals are non-stationary, the primary analysis technique chosen to investigate the auto- and cross-spectrum of the signals is the continuous wavelet transform using a Morlet wavelet. The Fourier analyses used in the previous chapters is useful for extracting the frequency content over the entire time series but does not distinguish which frequencies are present at a given time instant. On the other hand, wavelet analysis is particularly well-suited for this application. This is a necessary capability in the current context as the second-mode wave packets are intermittent.

The spectra for select PCB signals from the +10° shot are shown in Figure 5.11, obtained with both Welch's method for PSD estimation and also with the continuous wavelet transform. Pressure fluctuations have been normalized by time-resolved estimations of the wall pressure on the conical forebody of the model using the Taylor-Maccoll solution. The PSDs, which are plotted for the U3, D4, D7, and D8 PCB stations for $t = 8.5 - 13.0$ ms, show a peak between approximately 100-300 kHz, corresponding to the fundamental second mode. The wavelet transforms are computed for $t = 5.0 - 20.0$ ms (the first ~5 ms are dominated by transients associated with tunnel start-up) for PCB stations D3 and U4. The fundamental second-mode is again observed between approximately 100-300 kHz, with frequencies shown to slightly decrease throughout the test time.

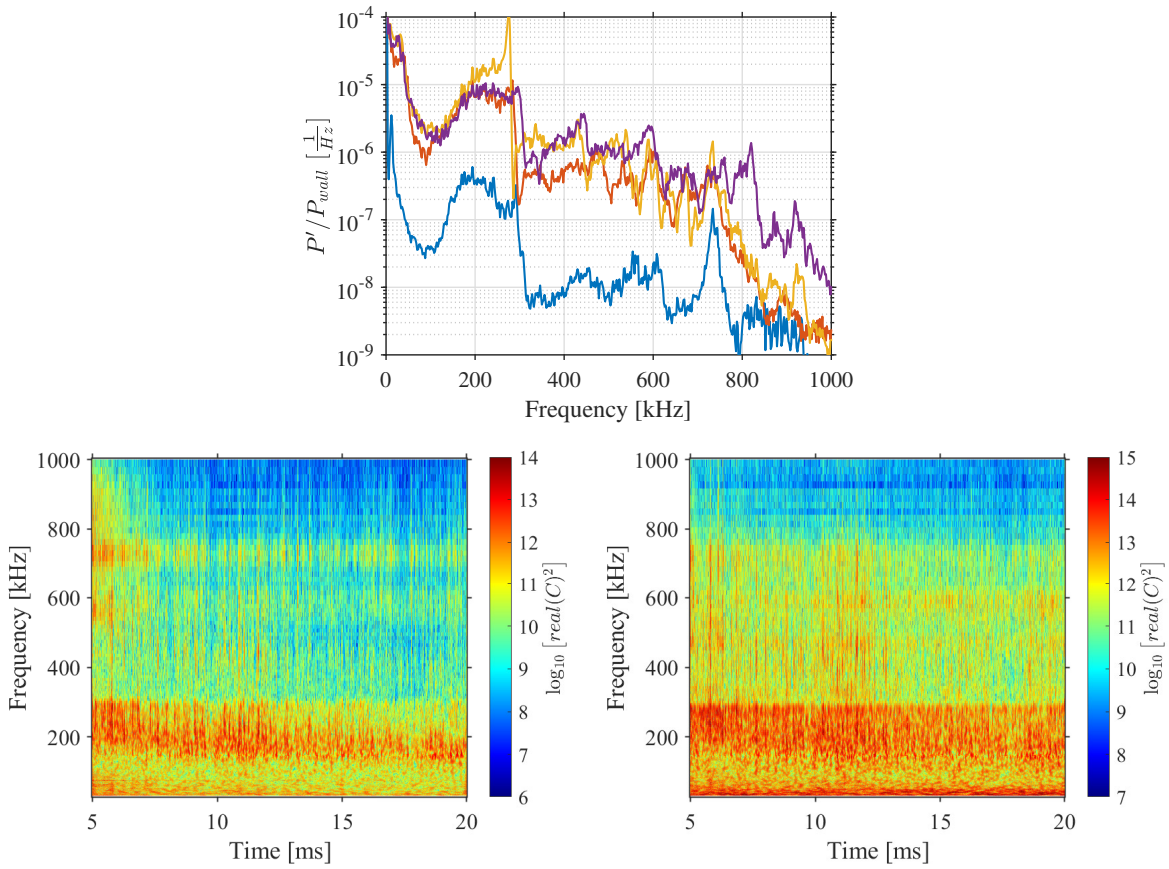

Figure 5.11: Power-Spectral-Densities at U3 (blue), D4 (red), D7 (yellow), and D8 (purple) PCB stations at +10° (top). Real part of the continuous wavelet transform for U3 (bottom left) and D4 (bottom right) PCB stations.

We first look at the magnitude-squared coherence (MSC) between neighboring PCB® sensor signals. This is a measurement, in the time-frequency plane, of the correlation between two signals, with a value of 1 corresponding to a constant phase difference and amplitude ratio. The MSC between two signals x and y is defined as

$$MSC = \frac{|(G_x^*(f,t)G_y(f,t)|^2}{|(G_x(f,t)|^2|G_y(f,t)|^2}, \tag{5.1}$$

where G is the continuous-wavelet transform operator, f and t are frequency and temporal coordinates, and * denotes the complex conjugate. The MSC is computed for sensor pairs in the

lateral and streamwise arrays. An example of the output from equation 5.1 is shown in the left plot of Figure 5.12 for the D2 and D3 sensor pair. After the initial period of transience observed in the first ~5 ms of the test, a substantial increase in the MSC is observed in the 125-400 kHz frequency range, which roughly corresponds to the fundamental second-mode frequency range (and, possibly, the first harmonic). For each sensor pair, the mean MSC value is computed in the frequency range of 150-250 kHz, neglecting the initial transient period, and plotted in the right of Figure 5.12. The selected frequency range was chosen to prevent any influence from lower frequency shear-layer disturbances as well as from the PCB® structural resonance located at approximately 300 kHz.

The right plot of Figure 5.12 depicts the drop in MSC with increasing distance between sensor pairs, with blue circles indicating lateral pairs (+10°) and purple diamonds (+5°), red squares (+10°), and yellow triangles (+15°) indicating streamwise pairs. Solid lines indicate the best exponential fit in the form $(1 - a)e^{-bx} + a$, where a is the approximate noise floor, b the exponential rate of decay, and x the distance between sensor pairs. The black exponential fit is taken using the MSC data from streamwise pairs across all shots. The value for the noise for, a, is approximated by taking all streamwise pair MSC values and solving for the value of a that minimizes the L2 norm of the regression error. Lateral pairs were excluded in estimating a because (1) their MSC values exhibit significantly faster exponential decay compared to streamwise pairs and thus cannot be grouped together, and (2) there is insufficient data at far distances to accurately estimate the noise floor. The noise floor is determined to be approximately 0.319, and this value is subsequently used in all exponential fits (including for the lateral array).

The MSC will change if the downstream PCB® of any particular pair experiences a lag (e.g., if a circular shift of the sensor signal is performed before the MSC is computed). The MSC within

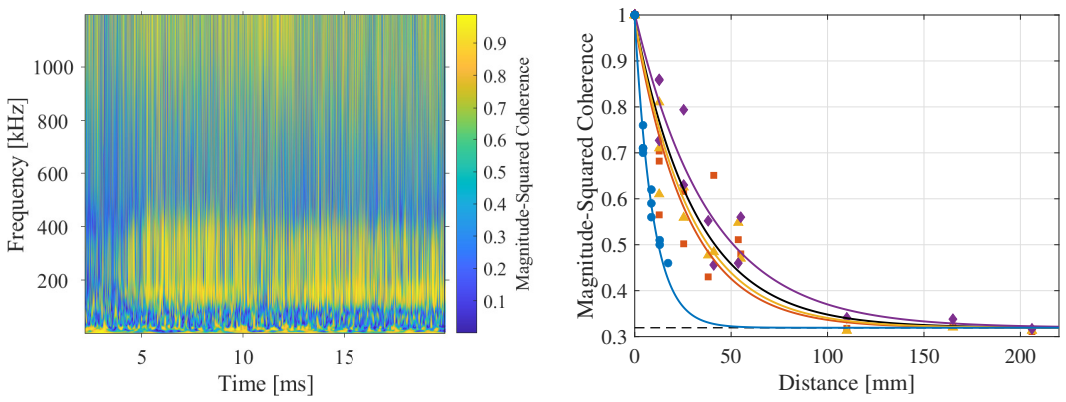

Figure 5.12: Magnitude Squared Wavelet Coherence between PCB® sensors D2 and D3 (left). Mean Magnitude Squared Wavelet Coherence identified between all PCB® sensor pairs. Pairs taken along lateral array is indicated in blue and streamwise array pairs are indicated in purple (+5°), red (+10°), and yellow (+15°). The mean exponential fit for all streamwise pairs is shown in black. (right).

the second-mode frequency range will be maximal when this lag is equal to the time it takes a second-mode wave packet to traverse the distance between the sensor pair. The lags are set for each sensor pair such that this maximum is achieved, and the resulting averages are those plotted in Figure 5.12. Note that this is an alternative method for calculating the mean propagation speed of second-mode disturbances. While this fit dies not provide a direct measurement of the width of the second-mode wave packets, we can show that the coherence between signals drops off much more quickly in the lateral direction due to the limited width of the wave packets. Following the exponential curve fit of the MSC data of the lateral PCB® pairs, 95% of the distance to the noise floor (i.e., a MSC value of 0.353) will be reached at a lateral distance 27.9 mm away.

5.7 Pixelwise Power Spectral Densities

In this section, a select few results of the pixelwise power spectral densities are presented to provide the reader with a general idea of the frequency content of the flow. Three locations

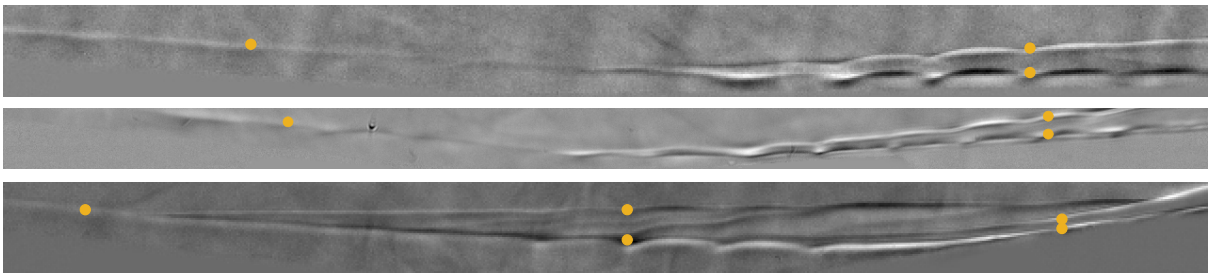

Figure 5.13: Locations of selected pixelwise PSDs for the +5° (top) , +10° (middle) , and +15° (bottom), overlaid on a reference-subtracted image during the useful test time of each shot.

Table 5.3: Surface coordinates of pixelwise PSDs shown for each test case.

Shot	Cone BL [mm]	Flare/Reattachment Shock [mm]	Flare BL [mm]	Separation Shock [mm]	Shear Layer [mm]
+5°	384	467	467	-	-
+10°	378	466	466	-	-
+15°	353	458	458	412	412

are chosen: (1) at the boundary-layer edge of the primary frustum, upstream of any influence from the compression corner, (2) at the boundary-layer edge of the flare, and (3) along either the attached shock generated by the flare or the reattachment shock. For the +15° configuration (the only configuration which experienced significant separation at the compression corner), two additional pixel locations were probed, along the separation shock and the shear layer of the separation bubble. The surface coordinates for each of these locations for each configuration, as measured from the cone nose tip, are shown in Table 5.3 and their locations within the schlieren field of view are displayed in Figure 5.13 as yellow markers. The locations of the boundary-layer edge and shocks were identified by using the canny edge-detection methodology described in section 5.5.2.

In Figure 5.14, the PSDs for all probe locations are shown together for each model configuration. The PSD in the freestream (taken at a pixel in the top-center portion of the field of view, above any prominent flow features) is also included as a baseline for comparison. Due to the

temporal decay of stagnation conditions during the test time, the pixelwise signals are cropped such that only the data in the range of 3.5 - 8 ms after flow arrival are used for Fourier analyses, thereby neglecting initial transients and minimizing long-term temporal variations in the instabilities while maintaining a large enough data set to adequately resolve them (note that the time-stamps of PCB® signals are not synchronized with the schlieren camera and the temporal range used here for the schlieren analysis roughly corresponds to 8.5 - 13 ms in the PCB® time axis, shown in Figure 5.12). Welch's method is used to compute the PSDs of each signal, using segments of length 1080 with 50% overlap (totaling 49 averaged segments) and a Blackman window function. In each case, there is a clear elevation in the spectra centered at approximately 225 kHz, corresponding to the second mode. Recall that the schlieren videos of the +5°, +10°, and +15° configurations had been captured at nominal frame rates of 500 kHz, 250 kHz, and 500 kHz, respectively. Using the original (without reconstruction) pixelwise time signals would therefore preclude the spectral analysis of any content above 250 kHz, 125 kHz, and 250 kHz, respectively, which includes either all or a majority of the fundamental second-mode content and any higher harmonics of the second mode.

Note that there exists a significant spike in the spectra at approximately 430 kHz, which is most prominent in the freestream PSD for the +5° and +15° shots, but also appears in the PSDs of most of the probes of those shots. This is an artifact generated by the reconstruction procedure due to the presence of a fringe-like pattern observable in the raw schlieren videos. The fringe patterns, whose origins are unknown but suspected to be related to the Cavilux HF laser light source, appear to propagate simultaneously in the left and right directions at a slower speed than the second-mode waves. Because the propagation speed of these fringe-patterns is significantly different than the propagation speeds used in the reconstruction process, they generate artifacts

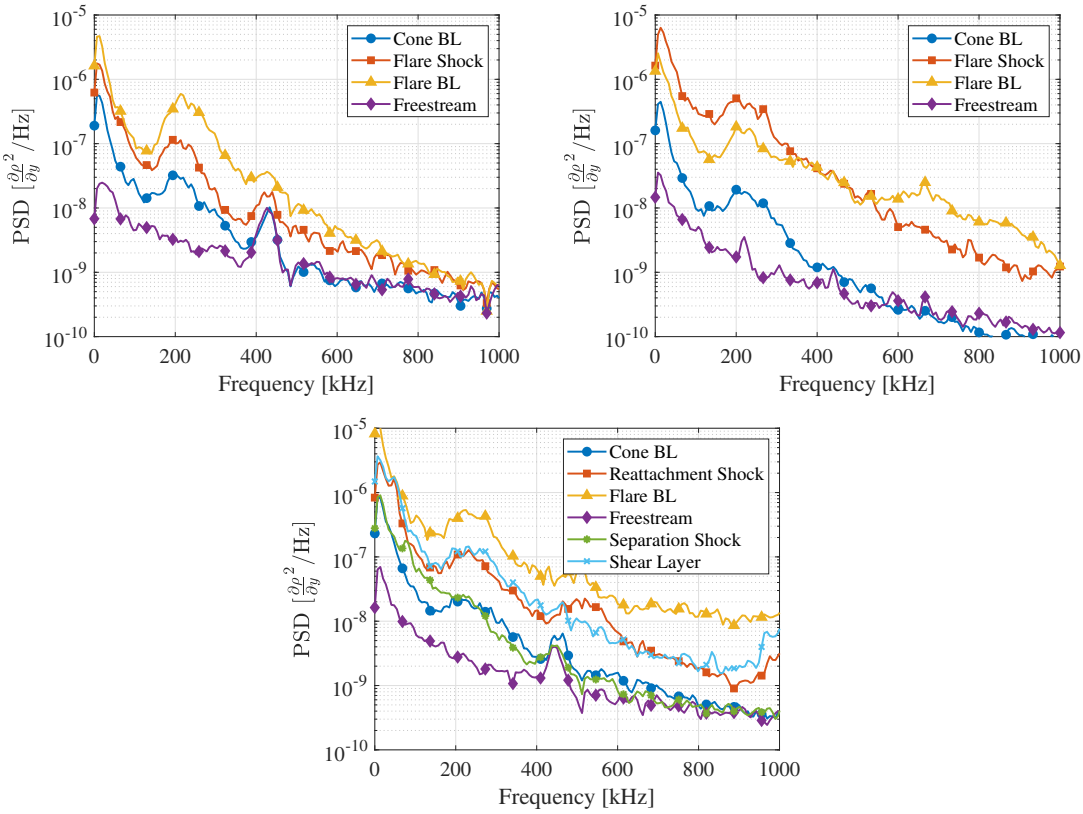

Figure 5.14: Power-Spectral-Densities at select pixels for compression angles of +5° (left), +10° (right), and +15° (bottom).

in the spectra of the reconstructed signals. The mechanism for how incorrect propagation speeds of features in the videos produce artifacts in the reconstructed signals is discussed at length in Appendix A.

Note also in Figure 5.14 the significant elevation in the PSD at the reattachment shock probe of the +15° shot centered at 500 kHz and again at 1000 kHz. The content at 500 kHz is slightly too high to be considered the first harmonic of the second mode, which would be centered at 450 kHz. In addition, the spectrum at this probe exhibits an additional elevation for frequencies under approximately 75 kHz, indicating that there is more prominent low-frequency content compared to other probes. This is unsurprising, as there exists a separation bubble at this configuration. Low-frequency oscillations within the separation bubble will transfer into

low-frequency displacements of the reattachment shock (see, for example, Butler and Laurence 2022). This content is unlikely to propagate at the same speeds as the second mode, and therefore we can expect artifacts associated with this low-frequency content to arise at frequencies between $nF_s \pm 75$ kHz, where n is an integer and F_s is the camera frame rate (here 500 kHz). These artifacts are suspected to be responsible for the elevations observed near 500 kHz and 1000 kHz and will be further investigated in subsequent sections.

The second-mode energy in the +5° configuration is seen to significantly increase between the cone and flare boundary layer probe locations. The second-mode peak remains well defined and amplification at higher frequencies is modest compared to the other configurations. This indicates the flow on the flare remained laminar and second-mode dominated, which is consistent with schlieren video observations. There is also a clear second-mode peak located at the flare shock probe location with a peak power that is in between those found on the cone and flare boundary layer probe locations. This demonstrates the tendency for energy of incoming disturbances to be radiated along shock features, which was also observed at Mach 6 (see Butler and Laurence 2021).

At +10°, the increase in second-mode energy within the boundary layer across the shock appears to be comparable to that seen at +5° (note that the incoming second-mode energy appears slightly lower in this case compared to +5°); however, the second-mode content located on the shock exceeds that found in the flare boundary layer at the same streamwise position, and is also significantly higher than that located on the shock in the other configurations. Additionally, there are minor peaks in the spectra centered at frequencies of approximately 400 kHz, 625 kHz, and 850 kHz. These may correspond to superharmonics of the second mode and will be further investigated using a bispectral analysis. There is significant broadband elevation in the PSD of

the flare probe compared to that of the +5° configuration, indicating the flow is closer to transition to turbulence.

The spectra of the +15° probes again exhibit strong second-mode content, with the second-mode center frequencies at the shear layer, reattachment shock, and flare boundary layer probes appearing at slightly higher frequencies. The spectrum of the additional probe located along the separation shock appears to lie very closely to that of the cone boundary layer. The peak fundamental second mode is located at approximately the same frequency and power; however, energies on the upper side band of the fundamental second mode are slightly decreased. Notably, frequencies between approximately 50-200 kHz are the only frequencies with elevated power compared to those at the flare boundary layer probe, indicating possible instabilities within this range. The spectrum at the shear layer probe within the separation bubble exhibits broadband elevations in power compared to the spectrum of the cone flare boundary layer probe. The spectra of the shear layer and reattachment shock probe locations are very similar. Both exhibit an additional peak at approximately 50 kHz, possible related to a shear-layer instability. The second-mode content is also nearly identical, suggesting that second-mode waves encountering reattachment are radiated along the shock but are not amplified along this path (as was observed in the other configurations, where the energy along the shock was always greater than that found upstream of the corner). As can be seen by the spectrum of the flare boundary layer probe, reattachment does amplify the second mode, as well as nearly all other frequencies, but the amplification is confined to the content that remains within the boundary layer. Notably, the 50 kHz peak found along the shear layer and reattachment shocks is not amplified in the flare boundary layer. Similar to the +10° case, there is broadband elevation in the PSD of the flare probe, indicating an acceleration towards transition to turbulence. The spectral broadening at high frequencies above 500 kHz is

even more prominent for the +15° configuration.

5.8 Global Power Spectral Densities

The figures of this section represent the spatial distributions of disturbance power integrated over select frequency bands of interest. Figure 5.15 first displays the integrated PSD in the band 200 kHz to 250 kHz, encompassing approximately ±25 kHz from the peak fundamental second-mode power identified in Figure 5.14. Dashed lines indicate the wall-normal height within the boundary layer of the most-amplified content at each streamwise position (i.e., pseudo-streamline of maximum second-mode power). Note that the +10° shot was captured at a different resolution than for the +5° and +15° shots and therefore the spatial stretching of vertical axis is different. The increased image resolution and magnification during this shot may also be responsible for the difference in the noise floor, which is lower than the other two shots. In all cases, there is a band of higher amplitude disturbances located within the boundary layer of the primary cone frustum leading into the compression corner. The disturbance power at the +5° and +10° configurations is rapidly amplified at the corner and bifurcates into two prominent branches along the flare boundary layer and shock. For the +5° configuration, the flare branch experiences slight spatial amplification, and the shock branch experiences slight decay. For the +10° configuration, both branches experience peak amplitude at the corner before briefly decaying between approximately $s = 440 - 450$ mm and then reamplifying. In the separated case of the +15°, there exists a large separation bubble beginning upstream of the corner at approximately $s = 355$ mm, with flow reattaching to the flare surface at approximately $s = 437$ mm. The incoming second-mode waves experience minor transmission along the separation shock; however, the majority of the

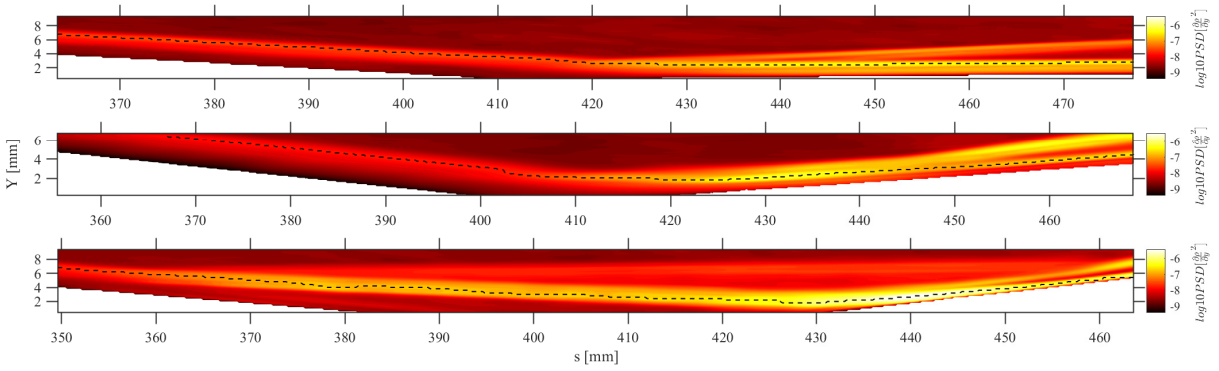

Figure 5.15: Spatial distribution of the integrated power spectral density over the 200-250 kHz band for compression angles of +5° (top), +10° (middle), and +15° (bottom).

energy remains located within the separated boundary layer (or shear layer) upstream of the corner. The second-mode energy is slightly amplified within the separation bubble. Upon reaching the corner, the second-mode power is again strongly amplified and bifurcates, with peak power occurring at approximately s = 440 mm, shortly downstream of the corner. Energy content propagating along the reattachment shock then experiences more rapid decay but is reamplified at the point of intersection with the separation shock (this intersection occurs at a mean location of approximately s = 460 mm and Y = 7.5 mm). Content propagating within the reattached boundary layer experiences decay following its peak at the corner and then seems to plateau, possibly caused by induced transition.

Figure 5.16 displays the integrated power in the band 30 kHz to 80 kHz, representing the approximate frequency range of shear-layer disturbances observed on this geometry at Mach 6 by **?**. Note that these disturbances may be propagating at a significantly different speed than that used for the reconstruction of temporal signals; therefore, we must be wary of making any quantitative conclusions. However, as discussed in Appendix A, we may still make remarks regarding the qualitative behavior of these disturbances. For the +5° and +10° cases, the distributions of

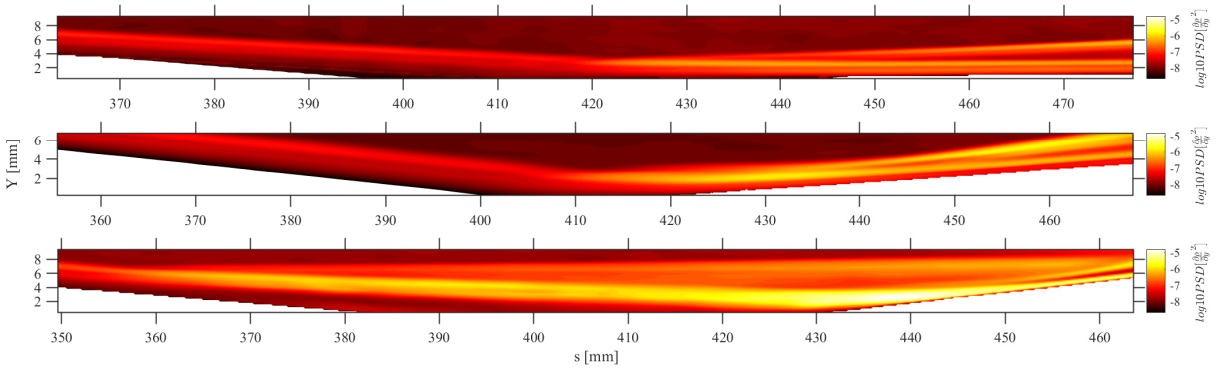

Figure 5.16: Spatial distribution of the integrated power spectral density over the 30-80 kHz band for compression angles of +5° (top), +10° (middle), and +15° (bottom).

these disturbances are similar to those of the second-mode disturbances, with bifurcation occurring at the compression corner. Notably, however, propagation through the shock produces only minor amplification of disturbance power in this frequency range, particularly in the +5° configuration. The low-frequency behavior in the +15° configuration shows greater amplification within the shear layer and between the shear layer and separation shock. The bifurcation of energy along the boundary layer and separation shock is initially similar to that observed for the second-mode disturbances. However, the separation shock branch has clear spatial amplification leading towards its intersection with the reattachment shock. The disturbances are also significantly amplified at the corner, with the strongest regions of amplification located again near approximately $s = 440$ mm on the flare surface.

The spatial distributions of the integrated PSD within the first, second, and third second-mode superharmonic frequency bands are plotted in Figures 5.17-5.19. In each case, the power located upstream of the corner is significantly lower than the fundamental disturbance. The +5° configuration shows the weakest presence of superharmonic content, with the only discernible content located downstream of the corner in the flare boundary layer and flare shock branches.

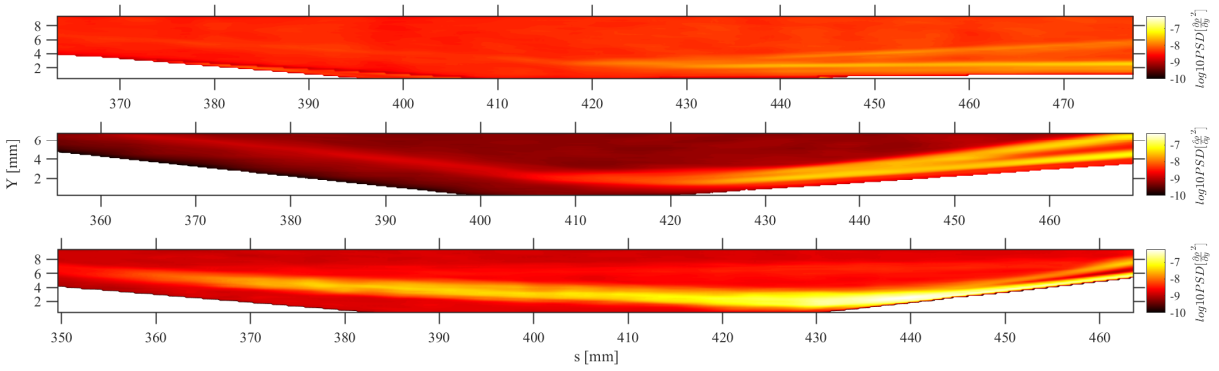

Figure 5.17: Spatial distribution of the integrated power spectral density over the 375-425 kHz band for compression angles of +5° (top), +10° (middle), and +15° (bottom).

The second and third superharmonics are noticeably weaker than the first. The same observations are true for the +10°, though here some content is present upstream of the corner, particularly for the first harmonic. Since the conditions and geometry are nominally the same upstream of the corner for each of these two cases, this discrepancy may only be due to the reduced noise floor of the +10° case. In the separated case of the +15° configuration, there is significantly stronger superharmonic content observed, which becomes amplified as the disturbances traverse the separation bubble. Note that there is little content observed along the separation shock, however, except for a minimal elevation in power for the first harmonic. In a similar fashion as observed for the fundamental disturbance, the superharmonic is most amplified just downstream of the reattachment shock, thereafter decaying slightly. There remains a slight radiation of energy along the flare shock, but this is less substantial than that observed for the fundamental instability and decreases in prominence with increasing frequency.

As mentioned previously, the low-frequency disturbances generated by the shear layer may not be propagating at the same velocity as the second mode, thereby invalidating quantitative conclusions regarding these disturbances from the reconstructed signals. However, the camera

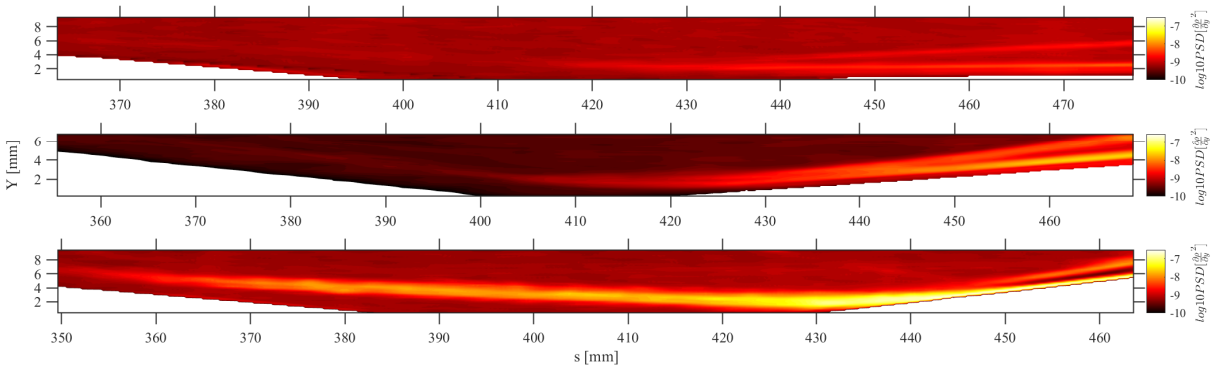

Figure 5.18: Spatial distribution of the integrated power spectral density over the 600-650 kHz band for compression angles of +5° (top), +10° (middle), and +15° (bottom).

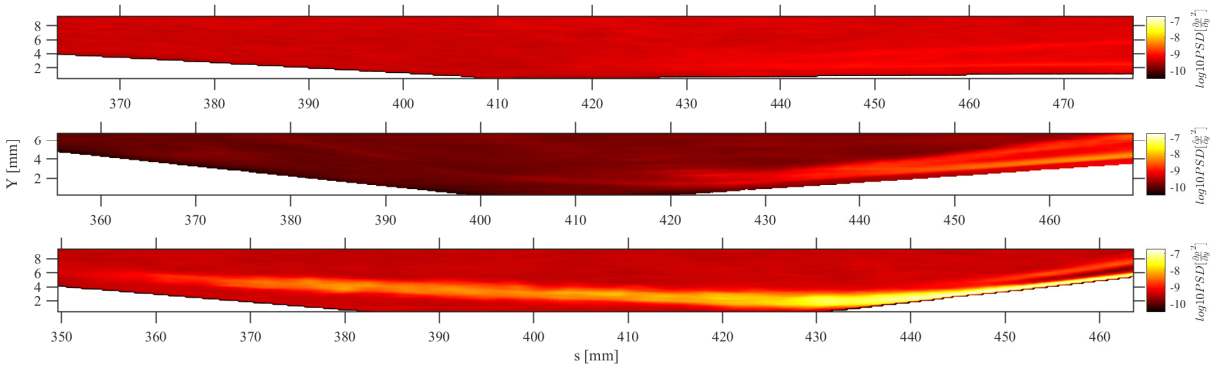

Figure 5.19: Spatial distribution of the integrated power spectral density over the 825-875 kHz band for compression angles of +5° (top), +10° (middle), and +15° (bottom).

frame rate for the +15° configuration was 500 kHz, sufficient to resolve and analyze the low-frequency content present within the separation region. The spatial distributions of integrated PSD over the 30-80 kHz frequency band was thus computed directly from the calibrated video data without performing the reconstruction technique; this is shown in Figure 5.20. The PSD power is seen to closely align with that observed in Figure 5.16. The bifurcation of energy at the start of the separation is further highlighted in this figure, with two pseudo-streamlines marking the pathways of most-amplified content along the shock and shear-layer branches. In the left figure of Figure 5.21, the N-Factors along each of these pathways is plotted, using the formula,

$$\Delta N(s) = \frac{1}{2} \ln \frac{PSD(f_{max}, s)}{PSD(f_{max}, s_0)}, \tag{5.2}$$

where $PSD(f_{max}, s)$ denotes the power of the most-amplified frequency (between the range 30-120 kHz, which has been extended compared to the 30-80 kHz range due to additional content along the separation shock at slightly higher frequencies observed in Figure 5.14) at a particular streamwise position along the pseudo-streamline and s_0 is the most-upstream position visible in the field of view. Following the pseudo-streamline through the separation bubble (i.e., the blue line in Figure 5.21), there is a sharp rise in N-Factor to a value of approximately 1 due to the interaction with the separation shock. After the shock, there is a brief region of approximately 20 mm where the low-frequencies appear to by neutrally stable, followed by a region of 30-40 mm where the disturbances appear linearly unstable. Near the corner (s = 410 mm), the growth rate of the disturbances begins to gradually increase as the separation bubble compression towards the reattachment shock. The N-Factor peaks at a value of approximately 2.5 at the reattachment point, sharply decaying thereafter and then flattening again, likely caused by spectral broadening

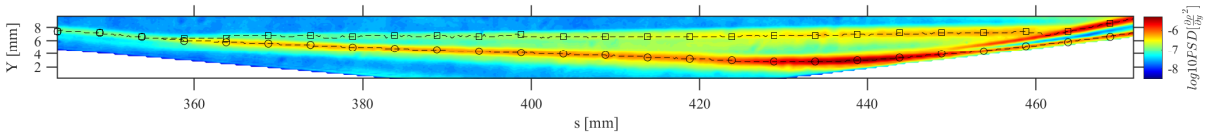

Figure 5.20: Spatial distribution of the integrated power spectral density over the 30-80 kHz band, computed from the raw video data of the +15° configuration.

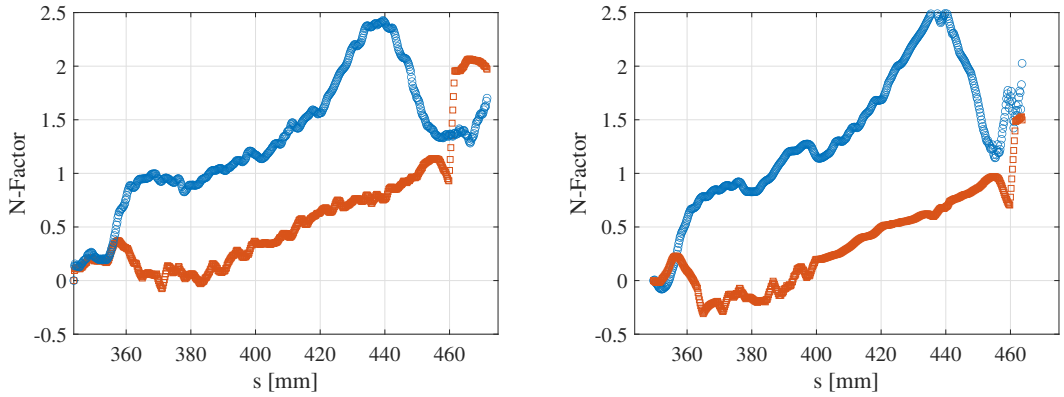

Figure 5.21: N-Factors along pseudo-streamlines of the shear layer (blue) and separation shock (red), computed with raw time-series data (left) and reconstructed data (right) for the +15° case.

and transition. If instead we follow the pseudo-streamline along the separation shock, there is a brief drop in N-factor associated with the interaction with the separation shock, perhaps indicating only a fraction of the power of a passing disturbance is transmitted along this pathway. However, thereafter the disturbance appears to grow linearly along the entire separation shock until its intersection with the reattachment shock.

On the right plot of Figure 5.21, the N-factors along these same pseudo-streamlines are shown using the reconstructed signals. Overall, the curves are remarkably similar to those computed with the raw data, indicating the reconstruction procedure is not appreciably altering the amplitudes of low-frequency disturbances (note the reconstructed data is plotted over a more limited range, because of the need of data both upstream and downstream of the relevant pixel). One notable difference, however, is that the growth rates in the reconstructed curves, particularly those along the shear-layer pseudo-streamline, appear ”smoothed” near the separation shock and cor-

ner. This is caused by the reconstruction procedure's reliance on spatial data away from a given pixel. It is generally advised that a sufficiently high frame rate is used such that the waveform of a propagating disturbance does not significantly evolve between successive images. A frame of half the disturbance frequency should suffice in most cases to ensure the interpolation remains accurate. In the vicinity of shocks, however, the waveform of disturbances will be rapidly altered. Since a point having its temporal signal reconstructed near the shock will rely on spatial data from before and after the shock, the result will be that the sharp alteration of the waveform (e.g., the wave amplitude) will be captured by a wider range of pixels. For these reasons, the neutrally stable region found after the separation shock is less apparent and the concavity of the N-factor curve at the corner has a larger radius of curvature.

In a similar manner, the N-factor growth for the second-mode disturbances are plotted in Figure 5.22 using the reconstructed signals for each of the flare configurations. These are again computed using equation 5.2, now with the frequency range shifted to 180-300 kHz. The pseudo-streamlines correspond to the height of maximum second-mode power at each streamwise position (these are plotted in Figure 5.15 as dashed lines). For the +5° and +10° cases, these are confined within the boundary layers upstream and downstream of the corner (though the second-mode power along the flare shock temporarily exceeds that found in the flare boundary layer for the +10° configuration, the pseudo-streamline for the current analysis follows the path along the boundary layer). In the separated case of the +15° configuration, the pseudo-streamline follows the shear layer and then extend along the flare boundary layer. The N-factors plotted in Figure 5.22 show that, for +5° and +10°, the second mode is linearly growing ahead of the flare shock and then undergoes strong amplification. This amplification occurs nearly linearly at +5° between approximately $s = 415 - 435$ mm, reaching a maximum N-factor of 1.5 before decaying

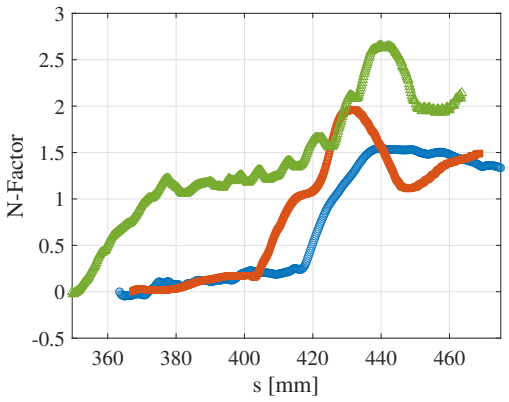

Figure 5.22: N-Factors along pseudo-streamlines of maximum second-mode power for the +5° (blue), +10° (red), and +15° (green) configurations.

slightly thereafter. For the +10° configuration, this amplification occurs over two steps, with the first occurring slightly upstream of the corner and the second step occurring at approximately the same location as that seen for the +5° configuration. This indicates that the stronger SWBLI is affecting the state of the incoming boundary layer upstream of the corner and supports the characterization that there is a small separation region at this condition. For the fully separated +15° case, there is first strong amplification of the second-mode disturbances through the separation shock. Notably, the streamwise width of this region of enhanced growth is larger than that seen for the low-frequency content, suggesting an extended interaction between the second-mode waves and shock. After this interaction, the N-factors appear to grow linearly again at a rate comparable to that observed at +5° and +10° upstream of the corner. This is followed by strong amplification again near reattachment before a post-shock decay and (possibly temporary) plateau.

To further illustrate the growth along the pseudo-streamlines, the full spectra along these paths are shown in Figure 5.23. Here, both main pseudo-streamlines of the +15° configuration are included (as shown in Figure 5.20). In each case, the left column shows the PSD, and the

right column shows the frequency-resolved N-factor growth, i.e.,

$$\Delta N(f, s) = \frac{1}{2} \ln \frac{PSD(f, s)}{PSD(f, s_0)}. \tag{5.3}$$

Note that, in equation 5.3, the power at each frequency is normalized by the upstream power of at the same frequency, rather than by the maximum within a certain band (as is the case in equation 5.2).

In the top row of images, corresponding to the pseudo-streamline through the shear layer, a second-mode band is present in the PSD spectra along with low-frequency content. The associated plot to the right depicts weak broadband amplification of the second mode between the separation and reattachment shocks. More unstable disturbances appear at lower frequencies (<100 kHz), with a clear band of moderate N-factors (up to ~1.2) within the separation bubble. The frequencies associated with the peak N-factor in this low-frequency range decrease with increasing streamwise position. The streak first becomes prominent at a frequency of approximately 80 kHz and a streamwise position of $s = 365$ mm and ends at a frequency of approximately 45 kHz at the reattachment shock. Note that, although the peak ΔN shows a decreasing frequency trend, the power at 45 kHz actually remains higher than that at frequencies between 50-100 kHz throughout the bubble, and therefore Figure 5.20 is effectively depicting the N-factors at 45 kHz.

The N-factors along the separation shock pseudo-streamline (lower row of images) show significant growth of low frequencies between 40-160 kHz. The strongest amplification occurs for 75 kHz, reaching an N-factor of approximately 1.1 before the pseudo-streamline's intersection with the reattachment shock. This region of heightened N-factors in the spectra appears to have two distinct lobes, one with a base of 45-90 kHz and the other with a base of 95-160 kHz.

Given the signal-to-noise, it is difficult to conclude if these two bands are physically different disturbance types or an anomaly caused by poor convergence. However, it may be significant that the second lobe is at approximately twice the frequency of the first. The experiments of Butler and Laurence (2021) on the same geometry at Mach 6 identified nonlinear self-resonance of low-frequency (~50 kHz) disturbances along the shear layer and additional resonances at 95 kHz further downstream along the shear layer. They suggested that these resonance interactions were responsible for the radiation of energy that was seen to emanate from the shear layer and propagate out into the freestream. The field of view of their schlieren, however, did not extend much higher than the shear layer and, therefore, they did not capture how these disturbances were amplified closer to the separation shock. Figure 5.23 demonstrates that the disturbance behavior is significantly different along the separation shock than observed for the shear-layer pseudo-streamline. This suggests that the growth of the disturbances along the separation shock is not only from radiation from the shear layer.

5.9 Spectral Proper Orthogonal Decomposition

In this section we employ spectral proper orthogonal decomposition (SPOD) to educe coherent flow structures associated with frequencies of elevated power identified in the previous section. The algorithm employed in this analysis can be found in detail in section 2.3.1 and in Towne et al. (2018). Again, we are primarily concerned with the leading SPOD modes (i.e., those that exhibit the highest energy at each frequency) since these typically contain the most relevant content. Given the additional flow complexity of the cone-flare compared with a straight cone (see Chapters 3 and 4), more than one SPOD mode may be required to represent the major-

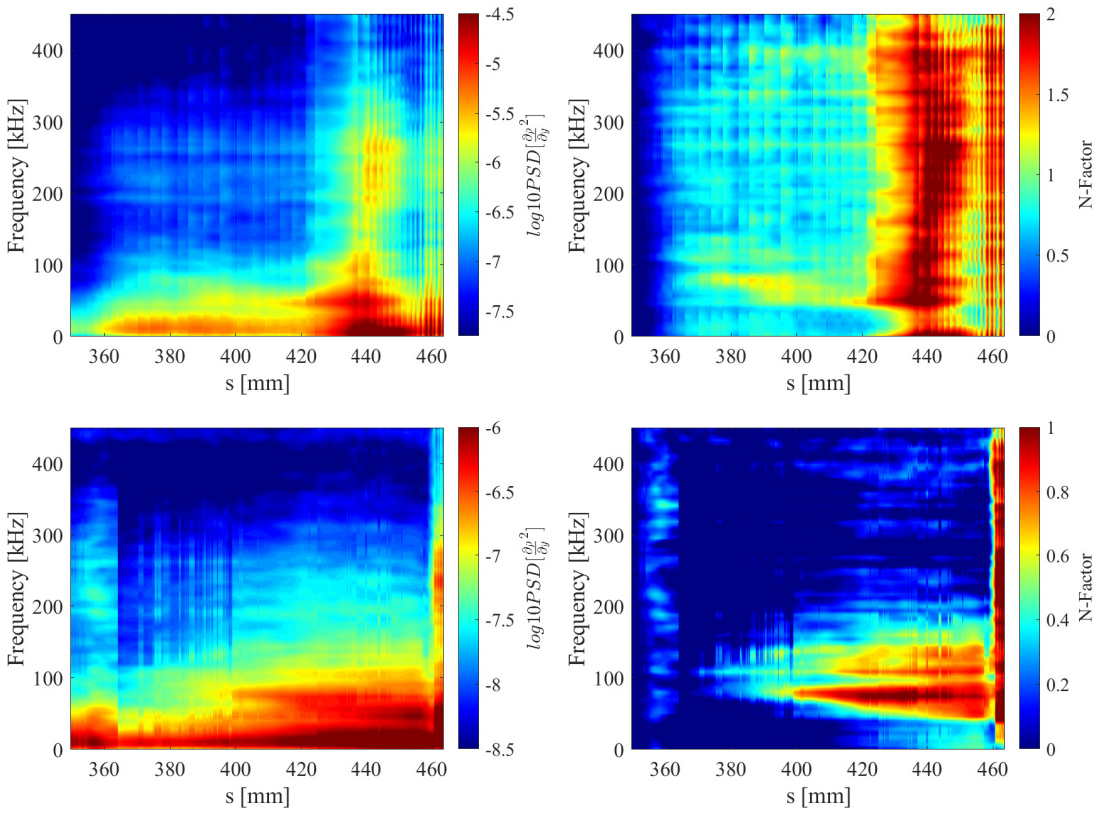

Figure 5.23: PSDs (left) and N-Factors (right) along pseudo-streamlines of the shear layer (top) and separation shock (bottom).

Table 5.4: SPOD Specifications.

Shot	Snapshots	Blocks	Block Length	Frequency Resolution [kHz]	F_{max} [MHz]
+5°	29238	113	512	12.31	3.15
+10°	16020	61	512	6.96	1.78
+15°	26989	104	512	12.00	3.07

ity of the energy at any given frequency. The SPOD modes are computed using the method of "snapshots", where each snapshot is represented by a single image from the time-resolved reconstructed signal. The SPOD spectra is estimated using Welch's method with block sizes of length 512 and 50% overlap, and a Hamming windowing function. The total number of snapshots used for each case, along with the total number of averaged blocks and resulting frequency resolution, are presented in Table 5.4.

5.9.1 +5° Configuration

The SPOD eigenvalue spectrum for the +5° configuration is shown in Figure 5.24. The left plot displays the eigenvalues while the right plot displays the modal energy percentage, i.e.,

$$\text{Modal Energy Percentage} = \frac{\lambda_i}{\sum_{j=1}^{N_b} \lambda_j}. \tag{5.4}$$

Only the five leading modes for each frequency are included; while the fifth of these modes still clearly depicts the second-mode peak at approximately 210 kHz, the modal energy contribution becomes diminishingly small and is therefore considered insignificant.

Note that there are spikes in the SPOD eigenvalue spectrum corresponding to artifacts of the reconstruction procedure. The strongest of these is again at approximately 430 kHz, which is observed to affect all five leading SPOD modes. A second, weaker artifact is observed at ap-

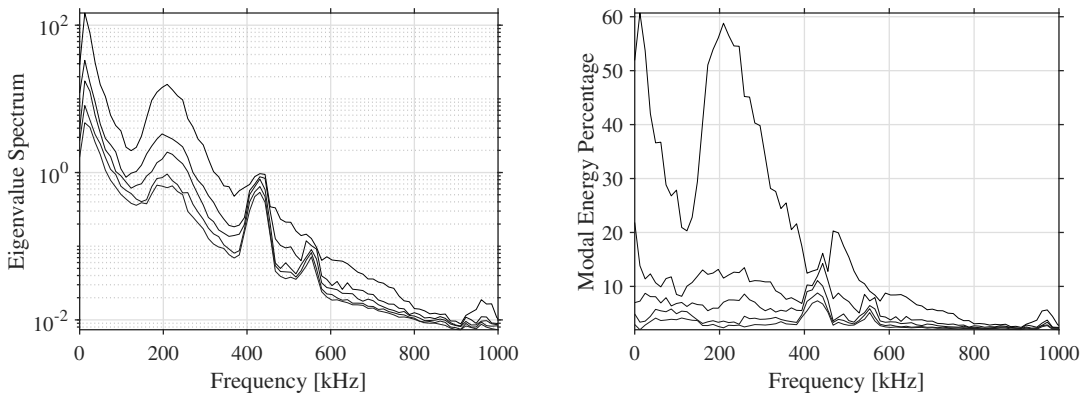

Figure 5.24: SPOD eigenvalue spectrum (left) and the modal energy percentages (right) for the five leading SPOD modes for the +5° shot.

proximately 540 kHz; this corresponds to the same artifact as that of 430 kHz (see Appendix A) appearing at another aliased frequency. The classification of spectral anomalies in the reconstructed signals as artifacts can usually be confirmed by using the combined characteristics of high energy and high-rank behavior as a criterion. There is significantly less separation in the eigenvalues of the first five leading SPOD modes at 430 kHz and 540 kHz than at other frequencies, which is typical of these artifacts. In addition, the eigenvectors of these modes, the first two of which are shown in Figure 5.25 for each frequency, clearly depict the fringe-like patterns mentioned previously. There are other underlying wave structures visible along the boundary layer and flare shock in these eigenvectors. They are in the frequency range of the fist superharmonic of the second mode but are obscured by the fringe-like artifacts.

The eigenvalue spectrum shows a fairly constant decline in energy with increasing frequency for frequencies below 100 kHz, typical of hypersonic facility freestream disturbances (Duan et al. 2018), indicating that these oscillations do not play a significant role in the dynamics of the flow. In Figure 5.26, the first two leading SPOD mode shapes of three frequencies within the span of the fundamental second-mode band are displayed, encompassing the peak fundamen-

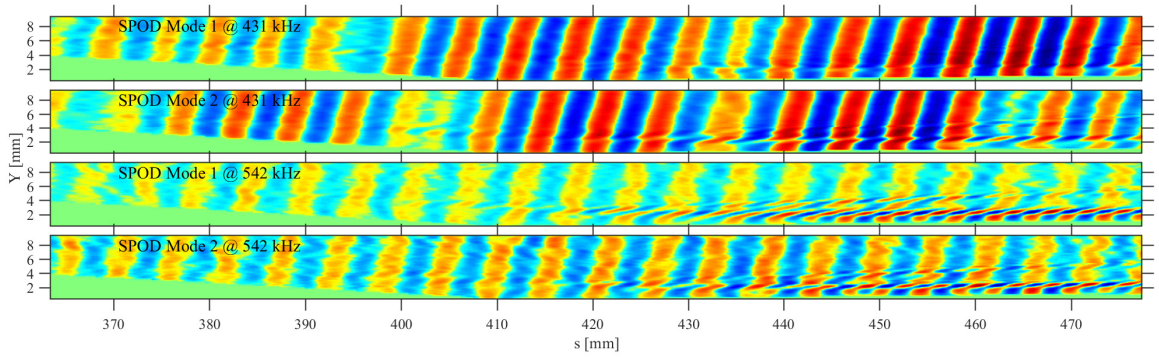

Figure 5.25: First two leading SPOD mode shapes for frequencies 431 kHz and 542 kHz for the +5° shot (frequencies of artificial spikes in SPOD eigenvalue spectrum).

tal frequency and the upper and lower sidebands. The eigenvalue of the first SPOD mode for the fundamental second mode peaks at 209 kHz, coinciding with the peak in the modal energy percentages with a value of 58%. While this is a significant portion of the total energy, the second SPOD modes nevertheless contain meaningful flow features that represent over 10% of the total energy.

In each set of modes shown in Figure 5.26, the energy distribution of the mode 1 shapes are heavily weighted toward the structures following the compression corner, while the mode 2 shapes contain more energy inside the structures upstream of the corner. One reason why these areas appear to be somewhat separated by the SPOD method may be because the second-mode waveform is distorted during its propagation through the flare shock. Note that, upstream of the corner, the second mode maintains its characteristic rope-like structure but, following the corner, the waves are substantially flatter in their top and bottom portions. This waveform is consistent with that seen directly in the schlieren, for example in the top image of Figure 5.13. This is further explored in Figure 5.26, where the third leading SPOD mode shape is included for a frequency of 209 kHz. In mode 3, the energy is even more heavily concentrated upstream of the boundary layer, with the mode structure become significantly distorted after the shock, particularly in the

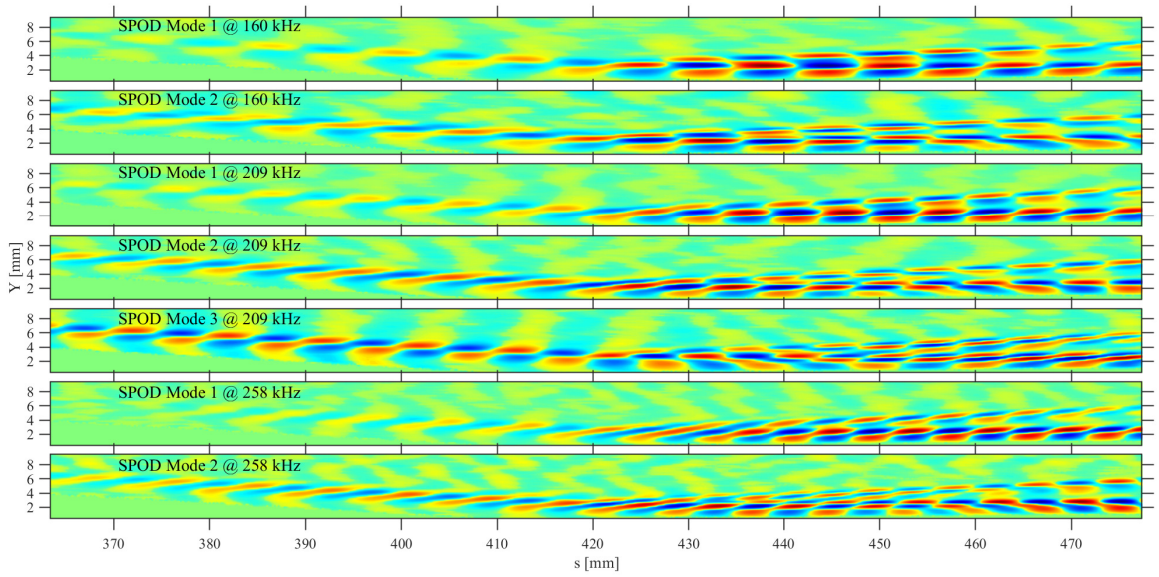

Figure 5.26: Leading SPOD mode shapes for frequencies 160 kHz, 209 kHz, and 258 kHz for the +5° shot.

range of $s = 430 - 450$ mm. At all frequencies shown in Figure 5.26, the radiation of energy along the flare shock appears to decay slightly in mode 1 near the end of the field of view and grow slightly in mode 2.

As the frequency increases in the SPOD eigenspectrum, the modal energy percentage of mode 1 generally decreases. There are two notable instances where the modal energy percentage increases at high frequencies (see Figure 5.24), indicating possible second-mode superharmonic content. These elevations in the spectrum are centered at approximately 475 kHz and 625 kHz. The latter of these is consistent with the second superharmonic observed in the pixelwise PSDs shown in section 5.7. The former is slightly higher than that observed for the first superharmonic; however, the artifact centered at 430 kHz may be obscuring the true peak of the first superharmonic in the SPOD eigenspectrum. The first and second leading mode shapes at frequencies of 468 kHz and 628 kHz (the closest frequency bins to the identified center frequencies of the first

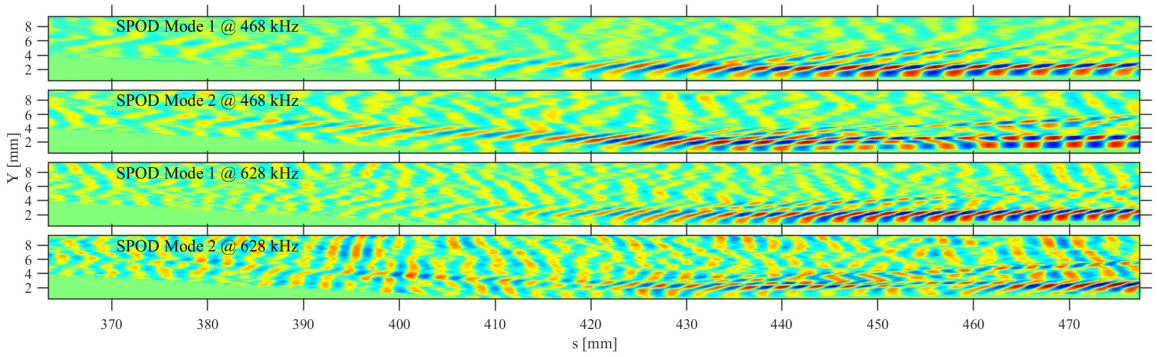

Figure 5.27: First two leading SPOD mode shapes for frequencies 468 kHz and 628 kHz for the +5° shot.

and second superharmonics), are shown in Figure 5.27. The first superharmonic exhibits similar behavior to the fundamental disturbance, with SPOD mode 1 depicting structured modal content within the flare boundary layer and SPOD mode 2 exhibiting stronger content upstream of the corner. The second superharmonic shows only coherent structures for the mode 1 shape, with the mode 2 shape reaching exhibiting primarily random and seemingly incoherent features. The upstream content is notably less prevalent for the first harmonic than the fundamental and is not present at all for the second superharmonic. Both superharmonics show only limited energy radiated along the flare shock, which rapidly decays at mode 1 but appears to grow for mode 2 at 468 kHz.

5.9.2 +10° Configuration

The SPOD eigenvalue spectrum and modal energy percentages for the +10° configuration are displayed in the left and right plots of Figure 5.28, respectively. Similar to that observed in the +5° configuration, there is no obvious elevation in the eigenvalue spectrum that suggests the existence of a shear-layer instability. The fundamental second-mode peak frequency is located at

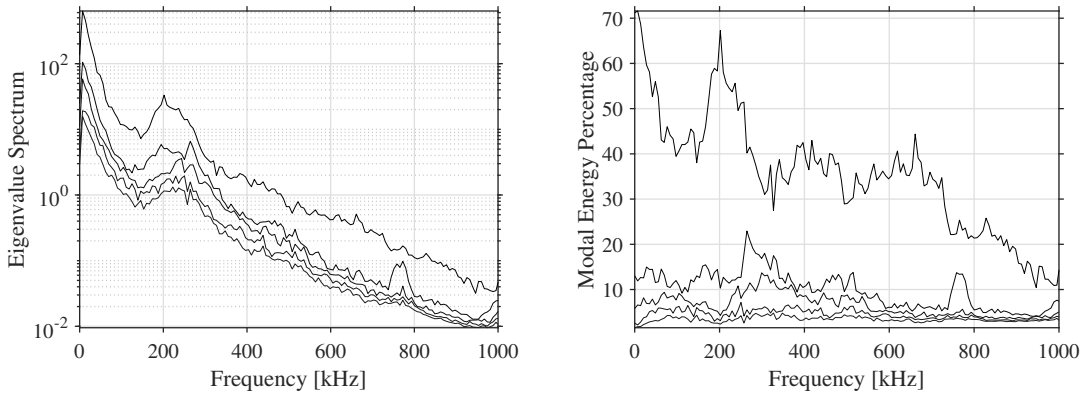

Figure 5.28: SPOD eigenvalue spectrum (left) and the modal energy percentages (right) for the five leading SPOD modes for the +10° shot.

202 kHz for the first SPOD mode, approximately equal to that found for the +5° configuration. Note that for the other four SPOD modes shown, the center frequency of the fundamental second-mode band shifts slightly to the right. This behavior was not observed for the +5° configuration and may be due to the stronger compression, and thus thinner boundary layer, of the +10° flare. The leading two SPOD mode shapes for the fundamental second mode for three frequencies are shown in Figure 5.29, comprising the peak frequency of SPOD mode 1 (202 kHz) and two side-band frequencies approximately 40 kHz away from this peak. The incoming second-mode waves again experience significant amplification at the compression corner for all three frequencies. For this configuration, there is very strong radiation of second-mode energy along the flare shock resulting in second-mode structures that are comparable in strength to the structures found in the flare boundary layer. This radiated energy also does not appear to decay in either mode 1 or 2 at the displayed frequencies, as was observed for mode 1 at +5°, but persists at a roughly constant amplitude for the entire field of view. The leading SPOD mode also shows a relatively constant amplitude of the second-mode energy located in the flare boundary layer after the initial amplification at these frequencies. SPOD mode 2, however, does show some decay of second-mode

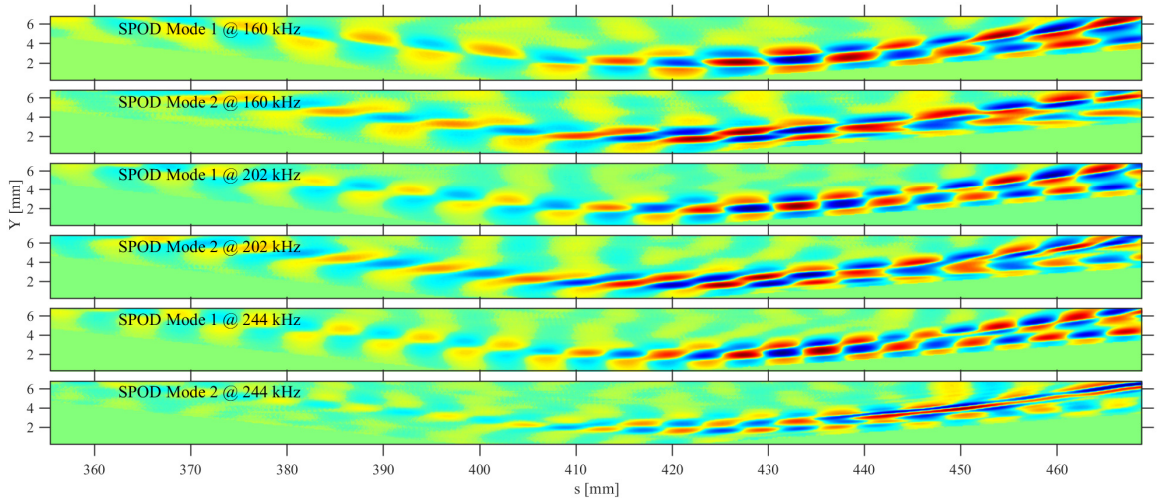

Figure 5.29: First two leading SPOD mode shapes for frequencies 160 kHz, 202 kHz, and 244 kHz for the +10° shot.

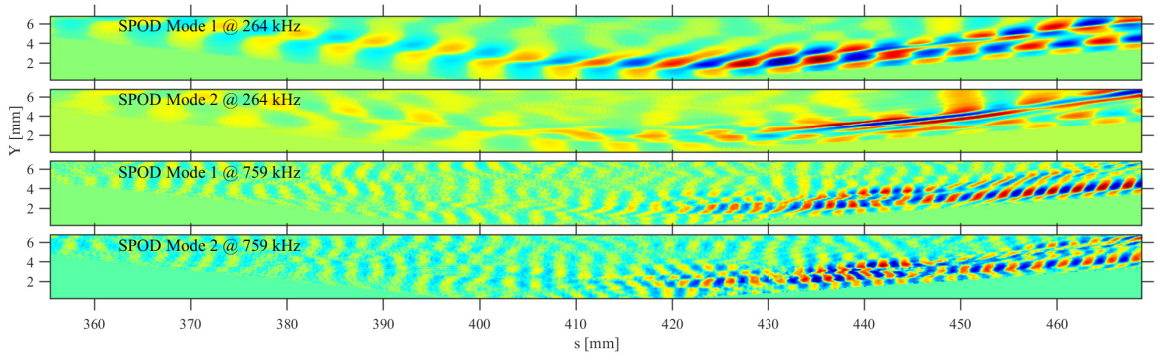

Figure 5.30: First two leading SPOD mode shapes for frequencies 264 kHz and 759 kHz for the +10° shot (frequencies of artificial spikes in SPOD eigenvalue spectrum).

structures in the flare boundary layer for all three frequencies. At frequencies of 160 kHz and 202 kHz, the SPOD mode 2 also depicts more slanted features in the upstream region, which are stretched significantly at the corner, a mechanic likely associated with the bifurcation of waves along the shock. Note that the SPOD mode shapes at 244 kHz show significantly less content upstream of the corner, which supports our earlier remark regarding the center frequency shift found at higher-order SPOD modes.

The SPOD mode 2 at 244 kHz shows an elongated structure that is approximately aligned

with the flare shock and propagates in the direction normal to the shock. To investigate the origin of this feature, note that this frequency is on the lower sideband of a sharp spike found in the eigenvalue spectrum of SPOD mode 2 (see Figure 5.28). The peak frequency of this artifact is at 264 kHz and the first two SPOD modes at this frequency are shown in Figure 5.30. Similarly to that seen for 244 kHz, the leading SPOD mode shows coherent content, but the second mode depicts a strong artificial structure aligned with the flare shock. This is an artifact that arises from errors in the disturbance propagation velocities found in that vicinity, due to limitations in the current algorithm in resolving the sharp deflections found at the flare shock. There is a second artificial spike observed in the eigenvalue spectrum of SPOD mode 2 that has its peak energy at 759 kHz. The first two SPOD mode shapes at this frequency are also displayed in Figure 5.30. While there appear to be coherent structures located in the downstream portions of the flare boundary layer for these mode shapes, there are incoherent structures with high energy levels between $s = 435 - 445$ mm. This region is close to the origin of the reattachment shock at the corner and may again be caused by slight errors in the propagation velocities computed at those locations. These particular artifacts are likely more prominent at this condition because the frame rate is 250 kHz rather than 500 kHz and sharp deflections are especially difficult to resolve if the time interval between frames leads to large displacements of features between images.

At frequencies greater than the fundamental second mode (i.e., above 300 kHz), the eigenvalue spectrum of the leading SPOD mode shows a relatively constant logarithmic decay in the eigenvalue magnitude with increasing frequency (see Figure 5.28). However, there is significant separation between the first and second SPOD eigenvalues at these higher frequencies, which is indicative of low-rank behavior. Indeed, when examining these eigenvalues instead by their individual percentages of the total aggregated modal energy found at each frequency (right plot), clear

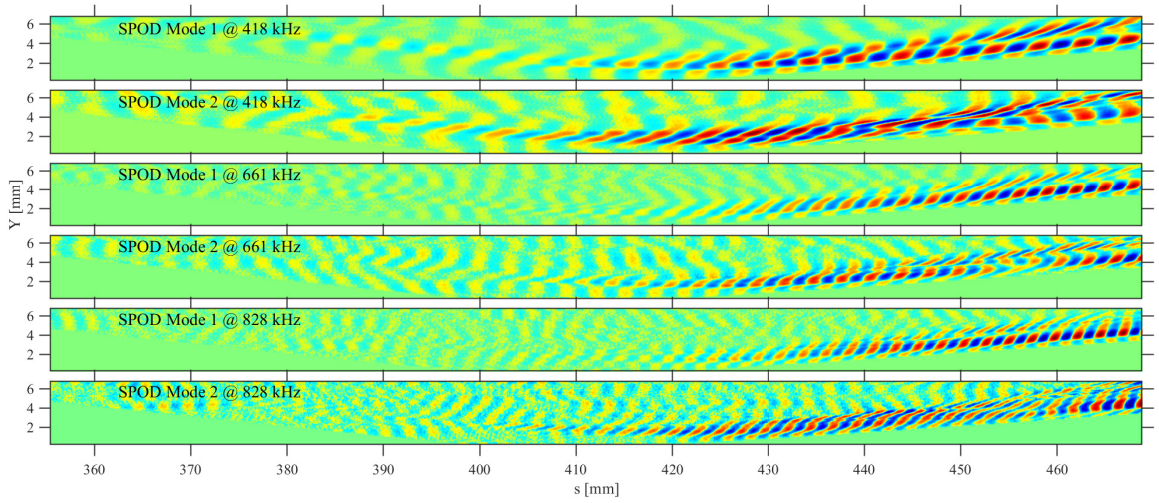

Figure 5.31: First two leading SPOD mode shapes for frequencies 418 kHz, 661 kHz, and 828 kHz for the +10° shot.

bumps in the spectrum arise at approximately integer multiples of the fundamental second-mode frequencies. The peaks of each of these elevations, again according to modal energy percentage, are located at approximately 418 kHz, 661 kHz, and 828 kHz. The corresponding SPOD eigenvectors for the leading two modes are shown for each of these frequencies in Figure 5.31. Coherent oscillatory structures are observed in each mode shape located within the flare boundary layer, but there is little evidence that the structures exist at any significant energy level prior to their amplification at the compression corner. The second SPOD mode at 418 kHz does exhibit rope-like structures that are just becoming discernible upstream of the corner, which indicates that there is some growth in the first harmonic range occurring within the downstream regions of the primary frustum. This lack of substantial higher-harmonic content upstream of the corner is relatively consistent with that observed for the +5° configuration. At 418 kHz there is also strong radiation of coherent content along the flare shock for both leading modes that persists at an approximately constant amplitude throughout the field of view. The radiation found here is much

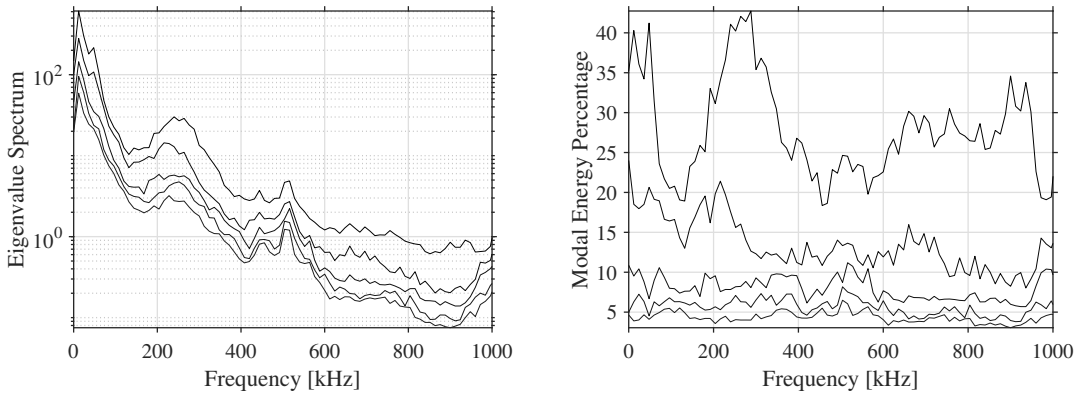

Figure 5.32: SPOD eigenvalue spectrum (left) and the modal energy percentages (right) for the five leading SPOD modes for the +15° shot.

greater than that observed for the +5° configuration at similar frequencies. At the higher frequencies of 661 kHz and 828 kHz, the radiated energy is significantly reduced relative to the energy found within the flare boundary layer. The waves found within the flare boundary layer at mode 1 are significantly more coherent than those identified at +5°, particularly for the higher-harmonic content. Note that this shot was taken with superior spatial resolution (0.108 mm/pixel instead of 0.200 mm/pixel), and this may, to some extent, improve the coherence of higher wavenumber features. At SPOD mode 1, these high-frequency waves grow as they move downstream on the flare within the boundary layer. The structures of mode 2 appear to amplify closer to the corner, between approximately $s = 405 - 430$ mm, and this may be associated with their interaction with the separation and reattachment shocks bounding the small separation region at the corner.

5.9.3 +15° Configuration

The SPOD eigenvalue spectrum and modal energy percentages for the +15° configuration are displayed in the left and right plots of Figure 5.32. Again there is a clear elevation corresponding to the fundamental second mode, which here has its peak frequency shifted to approximately

240 kHz. Note that a stronger compression at the corner results in a thinner boundary layer, which will lead to amplifications of higher second-mode frequencies compared to the previous configurations. The second SPOD mode has its peak closer to 200 kHz, which is in better agreement with the +5° and +10° cases and likely corresponds to the second-mode content upstream of the corner. Figure 5.33 displays the first two SPOD modes for the peak fundamental second-mode frequency as well as for two sideband frequencies. The leading SPOD mode at 240 kHz shows significant amplification of waves upon passing through the separation shock. Synchronized waves can be seen bifurcating along the separation shock, where they remain at a relatively constant amplitude. The reattachment shock generates further transitory amplification of the second mode; this is followed by a rapid decay on the flare surface, particularly for SPOD mode 1 at all three frequencies. The SPOD mode 2 at each frequency exhibits the most radiation of energy along the reattachment shock. Note that the SPOD mode 1 of the fundamental second mode retains its characteristic rope-like structure for the majority of the field of view, particularly for 240 kHz and 288 kHz. Along the shear layer and at reattachment, the wave structures of SPOD mode 2 at these two frequencies contain waves that have additional oscillatory features in the direction normal to the cone surface. This may be related to the distortion of the second-mode waveform upon reattachment (or passage through the separation shock).

Additionally, the eigenspectrum for this configuration in Figure 5.32 is not monotonically decreasing in energy for low frequencies under 100 kHz (as was the case for +5° and +10°). There is an additional peak in the spectra, centered at approximately 50 kHz, indicating an additional disturbance likely corresponding to a shear-layer instability. The most dominant mode shapes identified by SPOD for a series of low frequencies are shown in Figure 5.34. The strongest is that at 48 kHz, which shows a disturbance which is most-amplified just upstream of reattachment,

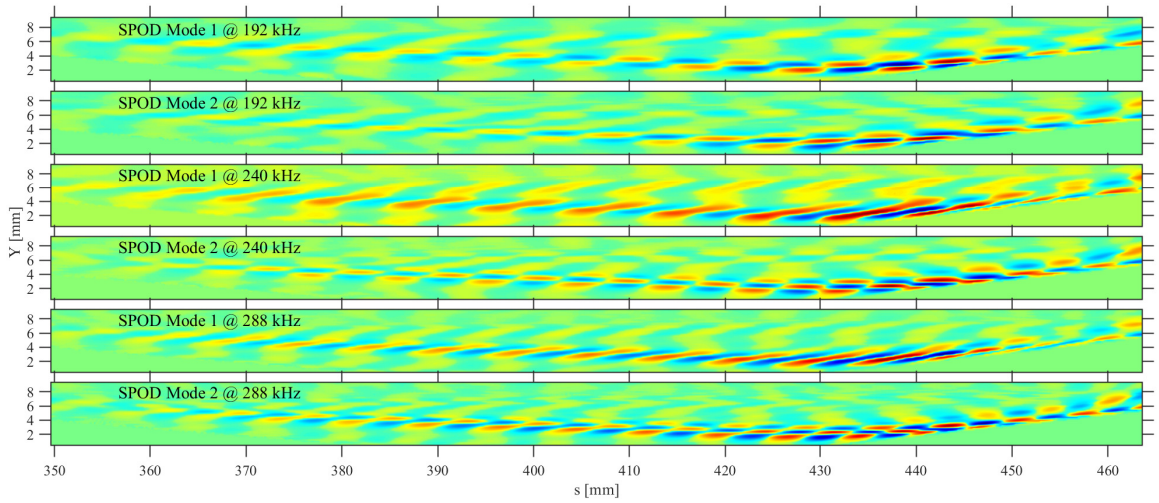

Figure 5.33: First two leading SPOD mode shapes for frequencies 192 kHz, 240 kHz, and 288 kHz for the +15° shot.

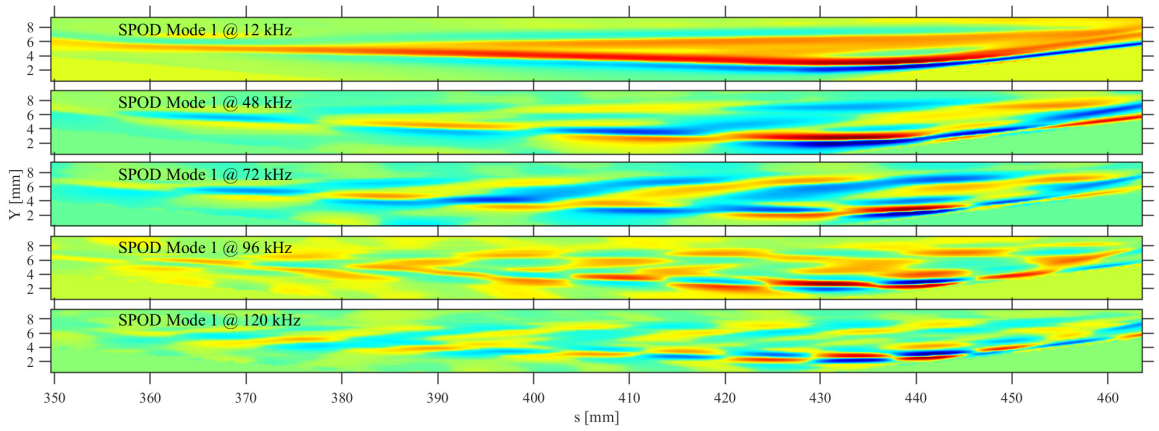

Figure 5.34: First leading SPOD mode shapes for frequencies 12 kHz, 48 kHz, 72 kHz, 96 kHz, and 120 kHz for the +15° shot.

closely resembling that found at Mach 6 by Butler and Laurence (2021) at similar frequencies. The energy of the mode shape is primarily concentrated along the shear layer. At a slightly higher frequency of 72 kHz, the mode shape now depicts structures that have a more consistent energy level between the shear layer and separation shock, with waves appearing to radiate from the shear layer and terminate at the shock. Similar structures were observed at Mach 6 by Butler and Laurence (2021) in the upstream portion of the shear layer at 60 kHz, though the limited vertical extent of their schlieren precluded the identification of the additional peak in the structures near the separation shock. The amplitude of these structures grow as they propagate downstream, indicating they are the content responsible for the growth identified along the separation shock pseudo-streamline in section 5.8. As the frequencies increases to 96 kHz and 120 kHz, the regions of activity in the mode shapes shift away from the separation bubble and into localized excitation of boundary layer disturbances near reattachment.

Butler and Laurence (2021) suggested that radiated energy from the shear layer found on this geometry at Mach 6 was caused by self-resonance of low-frequency shear-layer disturbances. If this were true, then we would expect to find a strong correlation between regions of high energy along the shear layer in low-frequency disturbance SPOD modes with regions of large amounts of radiation found in the SPOD modes at frequency doubles of the relevant frequencies. For example, in Figure 5.34, we would expect the mode at 96 kHz to possess radiated structures similar to those found at 72 kHz if there is self-resonance of the 48 kHz mode along the shear layer. However, this does not appear to be the case for mode 1. To investigate this further, the first three SPOD modes are shown in Figures 5.35–5.38 for frequencies of 36 kHz, 48 kHz, 72 kHz, and 96 kHz, respectively. In addition to the mode shapes, the spatial distribution of energy for each mode is also plotted. Note that the SPOD modes are complex and, therefore,

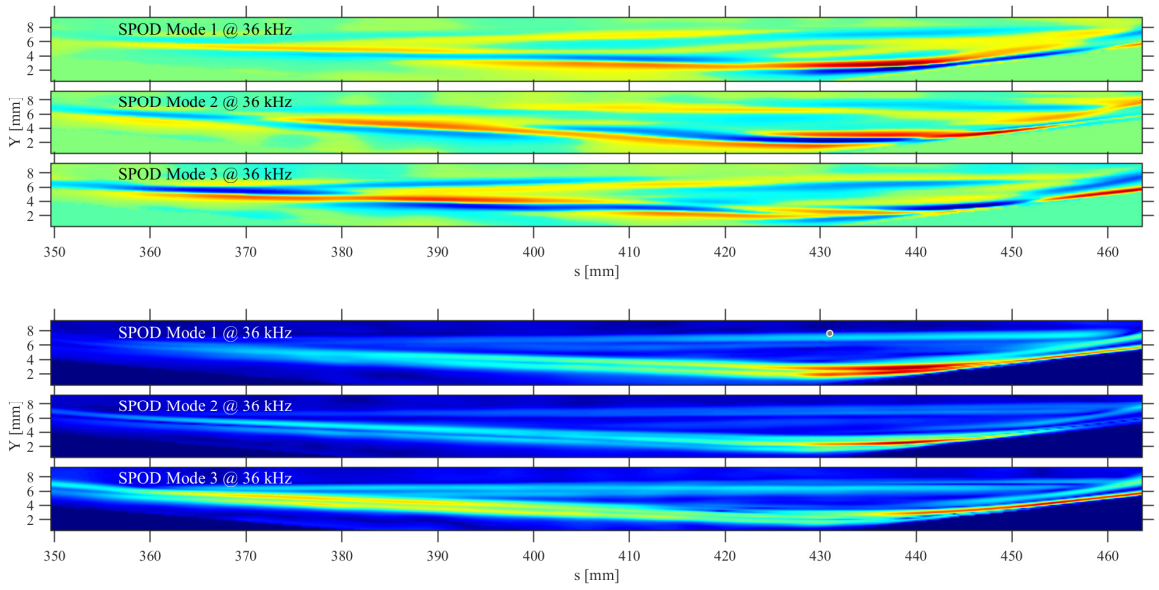

Figure 5.35: First three leading SPOD mode shapes at 36 kHz (top) and the spatial distribution of energy for each mode (bottom) for the +15° shot.

the mode shapes (i.e., wave structures) are generated by plotting the real part (or, alternatively, the imaginary part) of the mode and the spatial distributions of energy are generated by plotting the absolute value of the mode. The frequencies chosen for these figures represent low-frequency disturbances (36 kHz and 48 kHz) found to be dominant along the shear layer and their frequency doubles (72 kHz and 96 kHz).

Note that, in Figures 5.35 and 5.36, modes 1 and 2 at the low frequencies show high-energy content that is quite localized near reattachment. However, mode 3 at these frequencies shows much stronger waves in the upstream portions of the shear layer, between approximately $s = 360 - 400$ mm. Conversely, mode 3 at 72 kHz (Figure 5.37) and 96 kHz (Figure 5.38) shows strong radiated structures emanating from the upstream portions of the shear layer (again between approximately $s = 360 - 400$ mm) and extending upwards towards the separation shock. For the case of 72 kHz, which was seen to have the largest N-factors along the separation shock (see Figure 5.23), these radiated structures are also observed in mode 1. The localized content

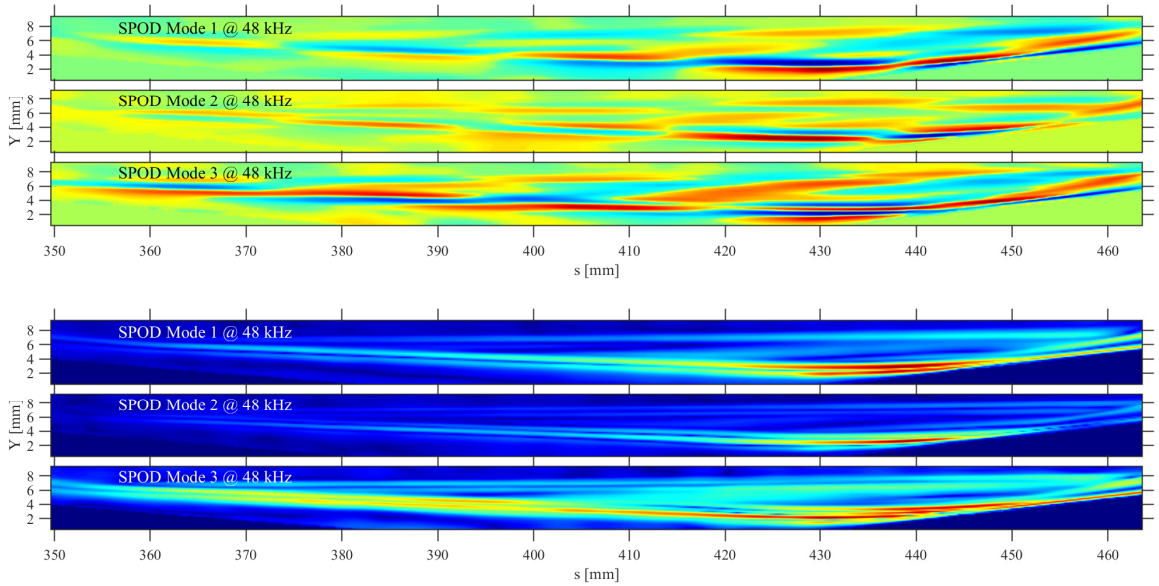

Figure 5.36: First three leading SPOD mode shapes at 48 kHz (top) and the spatial distribution of energy for each mode (bottom) for the +15° shot.

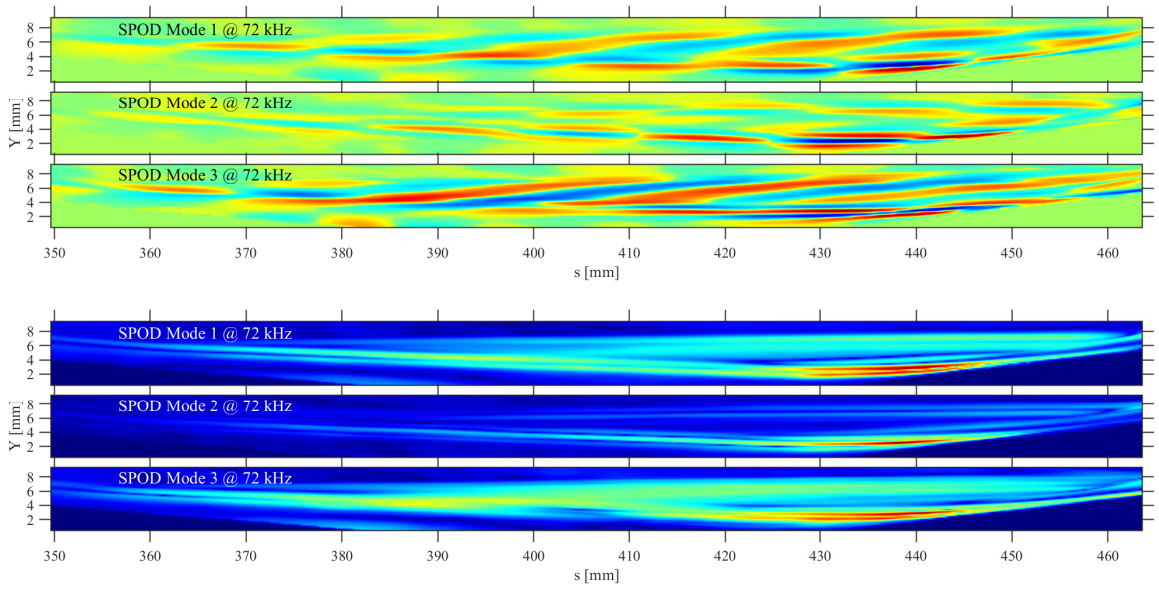

Figure 5.37: First three leading SPOD mode shapes at 72 kHz (top) and the spatial distribution of energy for each mode (bottom) for the +15° shot.

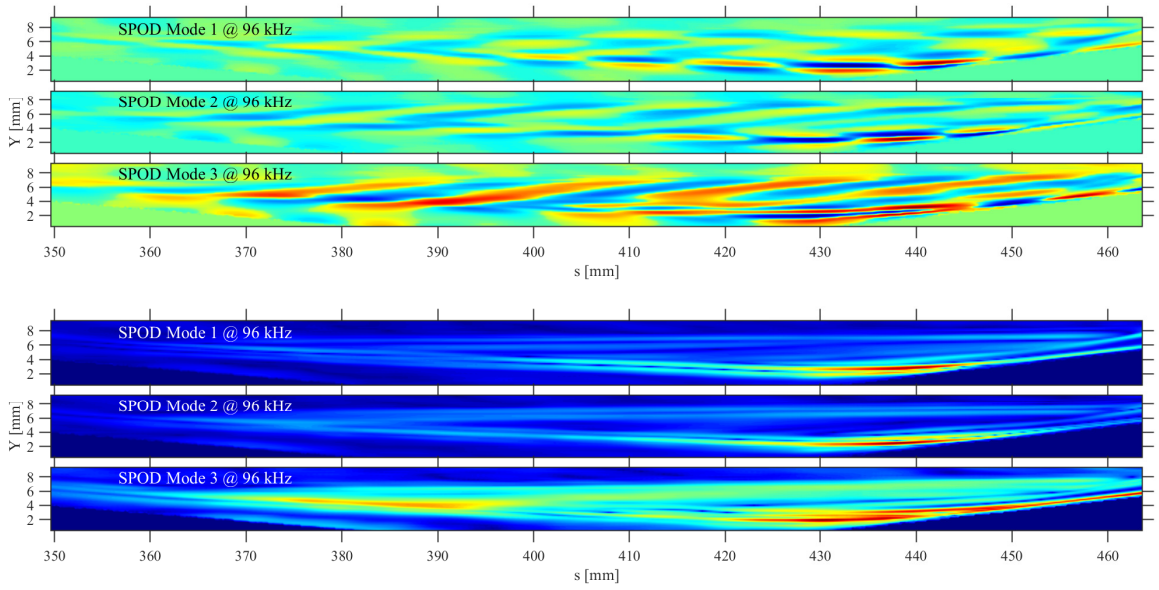

Figure 5.38: First three leading SPOD mode shapes at 96 kHz (top) and the spatial distribution of energy for each mode (bottom) for the +15° shot.

near reattachment found in many of these low-frequency SPOD modes is likely caused by the broadband amplification of disturbances there by the intense compression (see Figure 5.23). As we saw for the second mode, the distortion of waves experienced near reattachment can lead to a separation of upstream and downstream content in the SPOD modes, and that behavior seems consistent for the low-frequency modes as well. It is the upstream portion of the shear layer disturbances, found in mode 3 at 36 kHz and 48 kHz, that appears to be experiencing self-resonance. This will be further investigated in the following section with a BMD analysis.

The high-frequency content is also markedly different for this configuration, exhibiting low rank behavior evident by the higher modal energy percentages for frequencies greater than 450 kHz in the right part of Figure 5.32. This may be an indication of stronger superharmonics, which are visualized at frequencies of 420 kHz, 660 kHz, and 900 kHz in Figure 5.39. The mode shapes at these frequencies show clearer elevation of coherent structures above surrounding noise than the high-frequency structures observed for the previous configurations. For example,

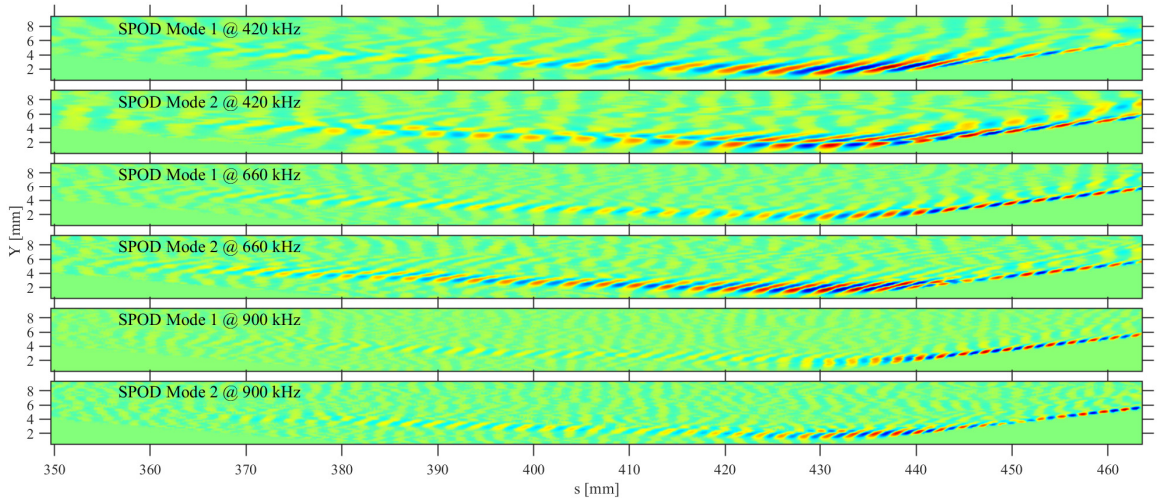

Figure 5.39: First two leading SPOD mode shapes for frequencies 420 kHz, 660 kHz, and 900 kHz for the +15° shot.

for the +5° configuration, by SPOD mode 2 at 628 kHz (Figure 5.27) the coherent structures in the flare boundary layer were only marginally distinguishable from surrounding noise. The high-frequency structures for the +15° configuration are coherent not only for content amplified downstream of the corner, but also within the separation bubble, where weak but coherent waves can be observed. Though the field of view upstream of the separation shock is limited, there is a lack of coherent structures prior to $s = 360$ mm. Growth of content in the frequency range of the second-mode superharmonics may possibly be facilitated by the strong SWBLIs. Notably, there is significantly less content radiated along the separation and reattachment shocks than observed at the previous configurations. Therefore, while a stronger shock may excite stronger harmonics, the steeper shock-wave angle may inhibit radiation of modal energy away from the boundary layer.

The sharp peaks in the eigenvalue spectrum of Figure 5.32 located at approximately 444 kHz and 516 kHz are believed to be artificial. The leading two SPOD mode shapes located at

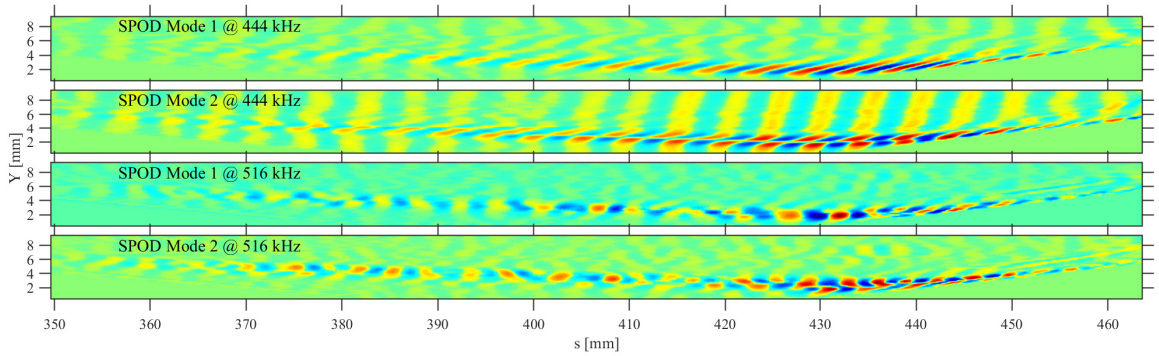

Figure 5.40: First two leading SPOD mode shapes for frequencies 444 kHz and 516 kHz for the +15° shot (frequencies of artificial spikes in SPOD eigenvalue spectrum).

these frequencies are displayed in Figure 5.40. SPOD mode 1 at 444 kHz shows only a coherent wave structure akin to the first superharmonic. However, the second mode shape contains the same fringe-like structure observed in the previous configurations. The mode shapes of frequency 516 kHz show a heavily distorted structure in the expected regions of second-mode superharmonic activity. As was mentioned previously, there is a strong likelihood that low-frequency content that is not propagating at the second-mode propagation speed will be modulated by the reconstruction procedure, creating an artificial disturbance with harmonic frequencies between $nF_s \pm f$, where F_s is the camera frame rate and f the frequency of the original disturbance. These artifacts are the most likely culprits of the corrupted mode shapes located in the vicinity of nF_s, of which that of 516 kHz appears to be the most affected.

5.10 Bispectral Mode Decomposition

Following the identification of the coherent structures contributing the greatest energy at each frequency, we wish to quantify the levels of quadratic phase coupling for various frequency triads. This metric grants insight into the nonlinear behavior of the flow field, as there will exist a

Table 5.5: BMD Specifications.

Shot	Snapshots	Blocks	Block Length	Frequency Resolution [kHz]	F_{max} [MHz]
+5°	29238	113	512	12.31	3.15
+10°	13350	103	256	11.60	1.47
+15°	26989	104	512	12.00	3.07

statistical relationship between the phases of nonlinearly-coupled modes. In this section we will present the results of applying BMD to each of the cone-flare configurations. Like SPOD, BMD is computed using a method of snapshots with the principles of Welch's method implemented for spectral convergence. The specifications, including the number of snapshots, number of blocks (i.e., realizations), block length, frequency resolution, and Nyquist limit are displayed in Table 5.5. For all cases, Hamming windows were used with 50% overlap between blocks. For the +5° and +15° shots, these specifications are identical to those used for SPOD. Note that BMD is more memory intensive than SPOD as the decomposition is performed for every resolvable frequency triad rather than for each individual frequency. In the case of the +10° shot, the required memory demanded by the computations, using the specifications used for SPOD, exceeded the 32 GB RAM available for this analysis. This was encountered only for the +10° shot, where the image resolution is greater than the other two cases. To resolve this issue, the temporal signals were downsampled such that the total time spanned by the signals was kept constant but the number of snapshots was reduced. The block length was also reduced from 512 to 256 as this increases the frequency resolution and reduces the total number of resolvable triads.

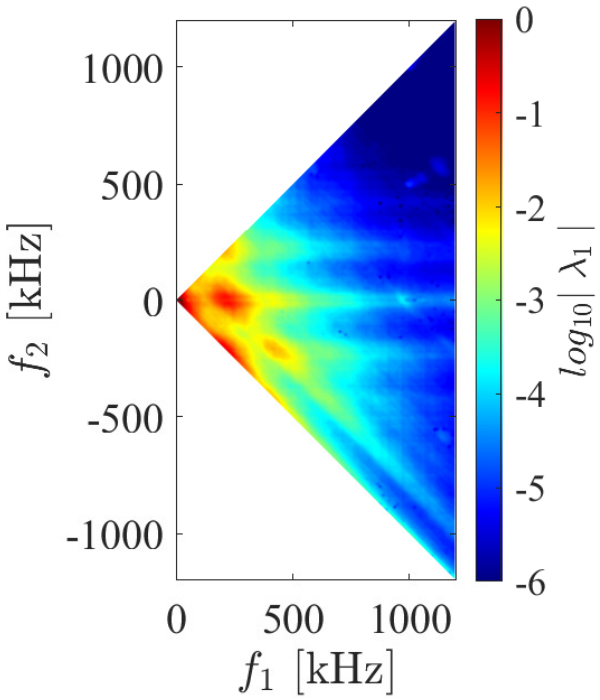

Figure 5.41: Magnitude mode bispectrum for the +5° configuration.

5.10.1 +5° and +10° Configurations

We first present the magnitude mode bispectrum for the +5° configuration, displayed in Figure 5.41, which plots the numerical radius for each frequency triad $(f_1, f_2, f_1 + f_2)$. Here the numerical radii are plotted using logarithmic color scaling for better visualization. Similar to the bispectral results of the straight cone discussed in earlier chapters, the most prominent regions of the spectrum, indicating the strongest nonlinear triadic interactions, are the sum and difference interactions involving the fundamental second-mode frequencies and integer multiples of the fundamental frequency range. This indicates that there is statistically significant quadratic phase coupling between the fundamental second-mode and the frequencies found in the superharmonic ranges, strongly suggesting that the high-frequency content identified by SPOD is indeed nonlinearly generated second-mode harmonic content.

Note that for every triadic interaction found in the bispectrum plot there is a corresponding bispectral mode, which indicates the structure produced by the nonlinear interaction. Similar to SPOD, these outputs are exhaustive, and only a select few of the bispectral modes are presented here, found in Figure 5.42 for the +5° configuration. These pertain to the strongest peaks found in the bispectrum plot, located at $(f_1, f_2, f_1 + f_2)$ positions of $(f_0, -f_0, 0)$, $(f_0, 0, f_0)$, $(2f_0, -f_0, f_0)$, $(f_0, f_0, 2f_0)$, $(2f_0, 0, 2f_0)$, $(2f_0, f_0, 2f_0)$, and $(3f_0, f_0, 4f_0)$, where f_0 indicates the approximate second-mode fundamental peak frequency (~209 kHz) and 0 includes ± 12 kHz. Interactions involving very low frequencies may either be (1) difference self-interactions causing mean flow deformation, which would involve exactly the zero-frequency, (2) difference interactions between f_1 and f_2 producing nonzero low-frequency content (e.g., ± 12 kHz), (3) sum interactions involving a nonzero f_1 with the mean flow (i.e., zero-frequency), leading to a nonlinear mean flow reinforcement of f_1, and (4) sum or difference interactions between a nonzero f_1 with a nonzero low-frequency, leading to a broadening of the sidebands of f_1. Given that the frequency resolution is approximately 12 kHz, and additionally given that the reconstruction procedure is not strictly valid for low-frequencies propagating at substantially different velocities from the second mode (more on this can be found in Appendix A), it is difficult to precisely differentiate between interactions that either involve the zero-frequency or nonzero low frequencies. Therefore, the second and fifth top-most bispectral modes shown in Figure 5.42 could be either option 3 or 4. The top-most bispectral mode in Figure 5.42 depicts option 1, but slightly varying either of the interacting frequencies, which is limited by the current frequency resolution, would produce option 2. Given the breadth of the lobes of heightened λ_1 values seen in Figure 5.41 (e.g., the lobe centered at $(f_0, 0, f_0)$ extends away from the abscissa), interactions between the second mode (including harmonics) and both the mean flow and low frequencies are occurring at

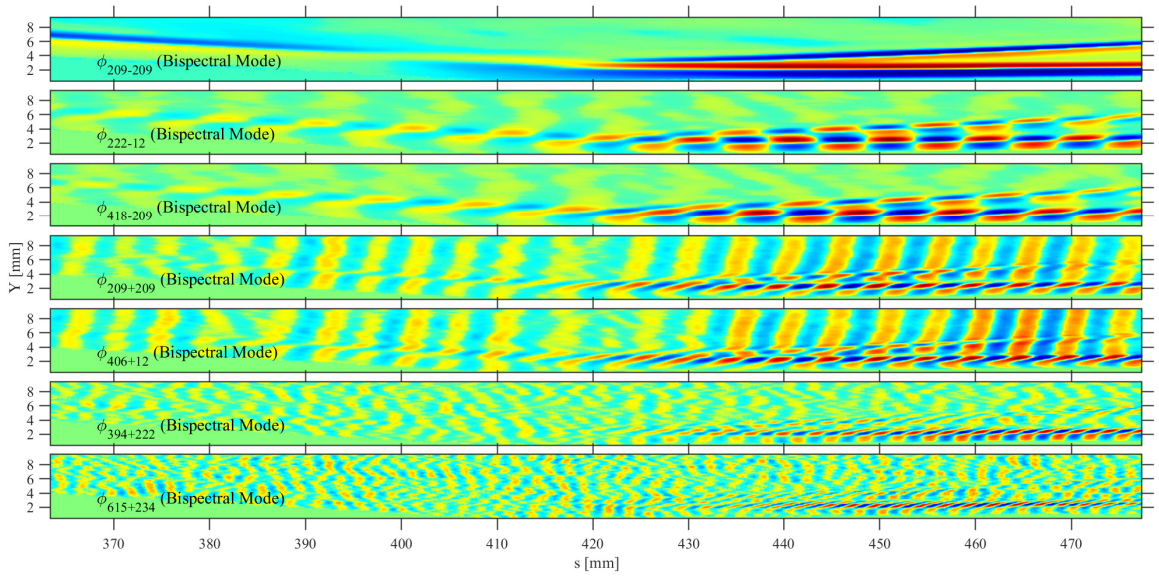

Figure 5.42: Bispectral modes for the +5° configuration

similar strengths.

For the harmonic modes at frequencies of 418 kHz and 616 kHz, the bispectral modes are very similar to the leading SPOD modes at these frequencies, suggesting these modes are generated by fundamental self-resonance $(f_0, f_0, 2f_0)$ and fundamental resonance with the first harmonic $(2f_0, f_0, 3f_0)$. Again, the harmonic content is primarily concentrated on the flare after amplification at the corner, with radiation of energy along the flare shock diminishing with increasing frequency. A notable advantage of BMD is its ability to reject noise: While SPOD is already useful for dimensionality reduction, with leading modes representing physical coherent structures and higher modes associated with energy variance that is unimportant to the fluid dynamic processes (i.e., noise), BMD has superior noise rejection due to the additional consideration of phase relationships between harmonically-related frequencies. For this reason, the artifacts discussed previously at 431 kHz (shown in Figure 5.25), are severely reduced in the bispectral modes found at 418 kHz. Note that we have shown the modes producing 418 kHz because

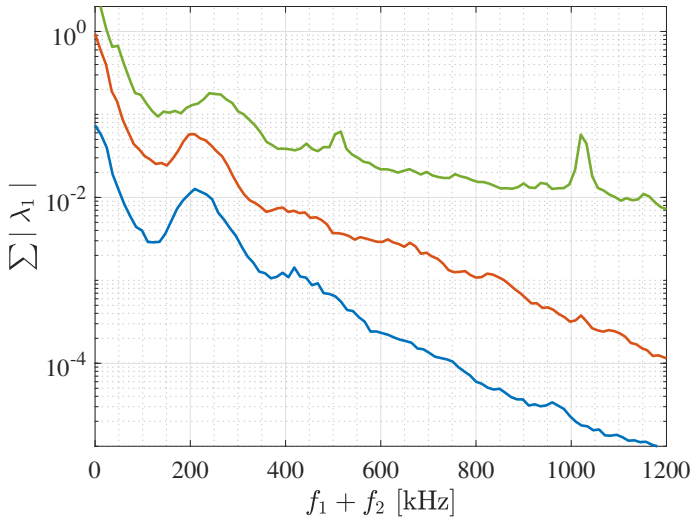

Figure 5.43: Summed mode spectra for configurations +5° (blue), +10° (red), and +15° (green.

that is where the peaks in the bispectrum are located; slightly shifting the interacting frequencies to produce 431 kHz (e.g., (222 kHz, 209 kHz, 431 kHz) rather than (209 kHz, 209 kHz, 418 kHz)) produces nearly identical mode shapes with a similarly reduced power of the artifacts. As was demonstrated in the previous chapters, it is possible to educe higher frequency content with BMD than SPOD due to the superior noise-rejection. In Figure 5.42, we can observe a coherent third harmonic of the second-mode at 849 kHz, whereas with SPOD we could only observe up to the second harmonic for this configuration.

In Figure 5.43, the summed mode spectrum for the +5° configuration is plotted alongside the summed mode spectrum for the +10° and +15° configurations, in each case defined as

$$\sum | \lambda_1(f) | = \frac{1}{N_f(f)} \sum_{f=f_1+f_2} | \lambda_1(f_1, f_2) | . \tag{5.5}$$

This quantity sums the numerical radius of each triad producing content at $f = f_1 + f_2$, where N_f is the total number of triads contributing to the sum. Equation 5.2 is graphically represented

by summing diagonals with a slope of -1 in the magnitude mode bispectrum plots. The result quantifies the extent to which each individual frequency is involved in quadratic phase coupling (Schmidt 2020). The greatest elevation in the summed mode spectrum for the +5° configuration is located at the second-mode fundamental frequencies with minor broadband elevations between approximately 375-550 kHz and 575-750 kHz. The latter elevation is very slight, but there is a definite increase in the slope at 575 kHz that indicates nonlinear activity over this frequency range.

The magnitude mode bispectrum for the +10° configuration is displayed in Figure 5.44. In general, the areas of increased nonlinear activity align very closely with that observed at the +5° configuration, but at a higher magnitude. This is best demonstrated when comparing the summed mode spectra for these two cases (Figure 5.43), where regions of second-mode harmonic activity are more clearly elevated in the regions 350-500 kHz, 550-750 kHz, and 800-900 kHz from surrounding noise. The bispectral modes for the peak triadic interactions in the elevated regions of the magnitude mode bispectrum are displayed in Figure 5.45. These represent the same interaction types observed in Figure 5.45 for the +5° configuration. The mode shapes depicting second-mode harmonic structures are considerably more coherent than those observed in Figure 5.45 and almost identical to the leading SPOD modes found at the same frequencies (see Figure 5.31). One notable difference, however, is that Figure 5.45 demonstrates that with interactions involving increasingly higher harmonic content, the amplification of the resulting bispectral modes moves further downstream. This agrees with the bispectral results of the previous chapters, suggesting that a cascade of nonlinear interactions is occurring in the order listed (from top to bottom) in Figure 5.45.

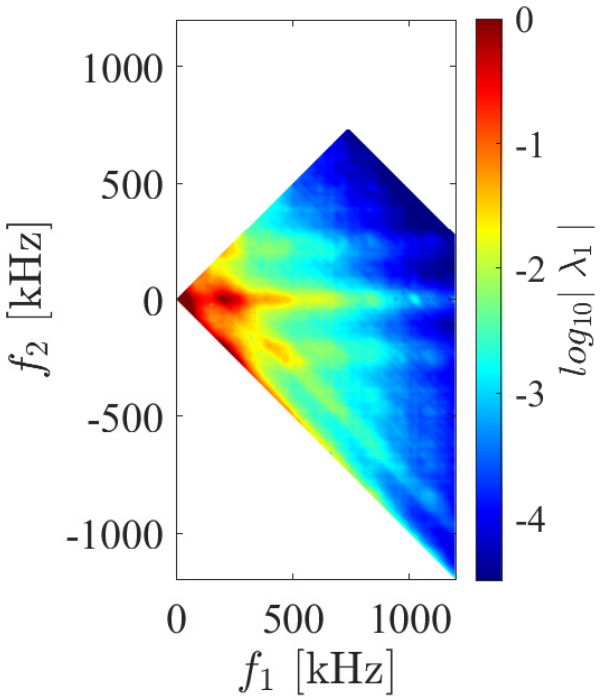

Figure 5.44: Magnitude mode bispectrum for the +10° configuration.

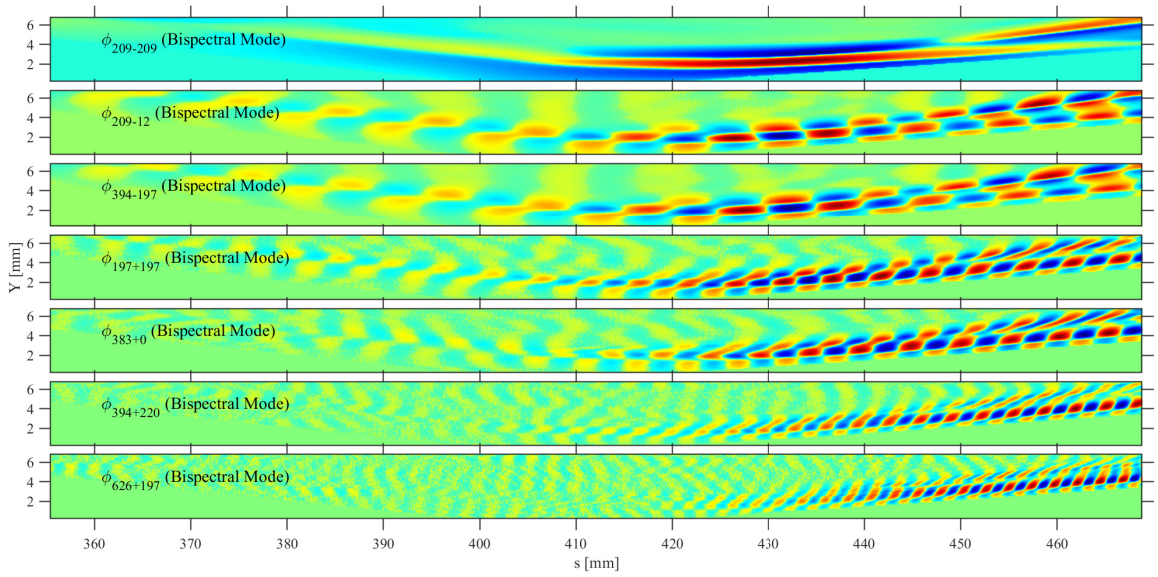

Figure 5.45: Bispectral modes for the +10° configuration

5.10.2 +15° Configuration

In the case of the +15° flare, the presence of a separation bubble in addition to a stronger compression at the flare considerably advances the nonlinear behavior of the disturbances. As can be seen in the magnitude mode bispectrum plot of Figure 5.46, not only are the aforementioned interactions stronger, but there are now many additional elevated lobes throughout the spectrum corresponding to nonlinear interactions involving higher second-mode harmonics. Note there remains some influence in the bispectrum from artifacts. One is along the diagonal of -1 slope producing content at 500 kHz (i.e., (f_1, f_2, 500 kHz)); this is most prominent at the abscissa. Two additional diagonals producing content at 1.0 MHz and 1.5 MHz show narrow-banded elevations caused by the artifacts. Outside of these, the new elevations in the spectrum have frequency ranges approximately consistent with that of the fundamental second mode at integer multiples of the fundamental frequency range. Note that the sum self-interactions of frequencies in the fundamental second-mode frequency range, i.e., ($f_0 \pm \delta f$, $f_0 \pm \delta f$, $2f_0 \pm 2\delta f$), produce first-harmonic content with twice the bandwidth (see Khan et al. 2022). Here f_0 refers to the fundamental second-mode peak frequency and δf refers to the width of either fundamental sideband. This effect compounds for higher harmonics. Though, graphically, the higher-harmonic lobes appear to have the same bandwidth as the fundamental second mode, the noise floor has considerably increased compared to the previous configurations. This is likely due to the spectral broadening caused by the gradual increasing of harmonic bandwidths. In the summed mode spectra shown in Figure 5.43, the slope of the +15° at higher frequencies is considerably flatter compared to those of +5° and +10°, again owing to spectral broadening. The summed mode spectra also shows a slight peak at 48 kHz, suggesting that the shear-layer instability contributes to the nonlinear

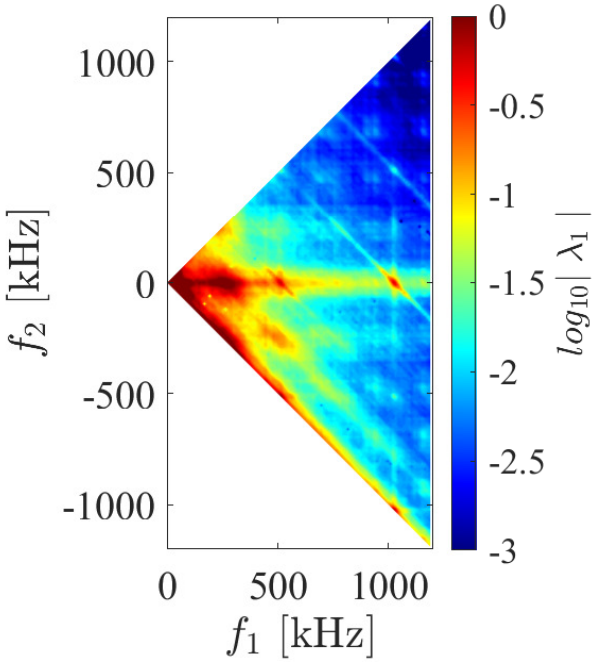

Figure 5.46: Magnitude mode bispectrum for the +15° configuration.

activity in the separated case.

In Figure 5.47, bispectral modes for the +15° configuration, analogous to those of Figures 5.42 and 5.45, show the structures produced by the most prominent triadic interactions involving the second mode (including harmonics). The mode shapes of 240 kHz and 444 kHz are again almost identical to the leading SPOD modes at the same frequencies. The bispectral modes of 672 kHz and 900 kHz have the same structures of the leading SPOD modes, but with elevated content extending further upstream of the corner. At these high frequencies, content on the flare and content upstream of the corner was divided between the first and second SPOD modes. Therefore the bispectral modes appear to combine the leading two SPOD modes. While the structures associated with the second and third second-mode harmonics experience the greatest amplification just upstream of reattachment at approximately $s = 430-440$ mm, the coherent structures extend much further upstream at a weaker amplitude to approximately $s = 370$ mm and $s = 380$ mm,

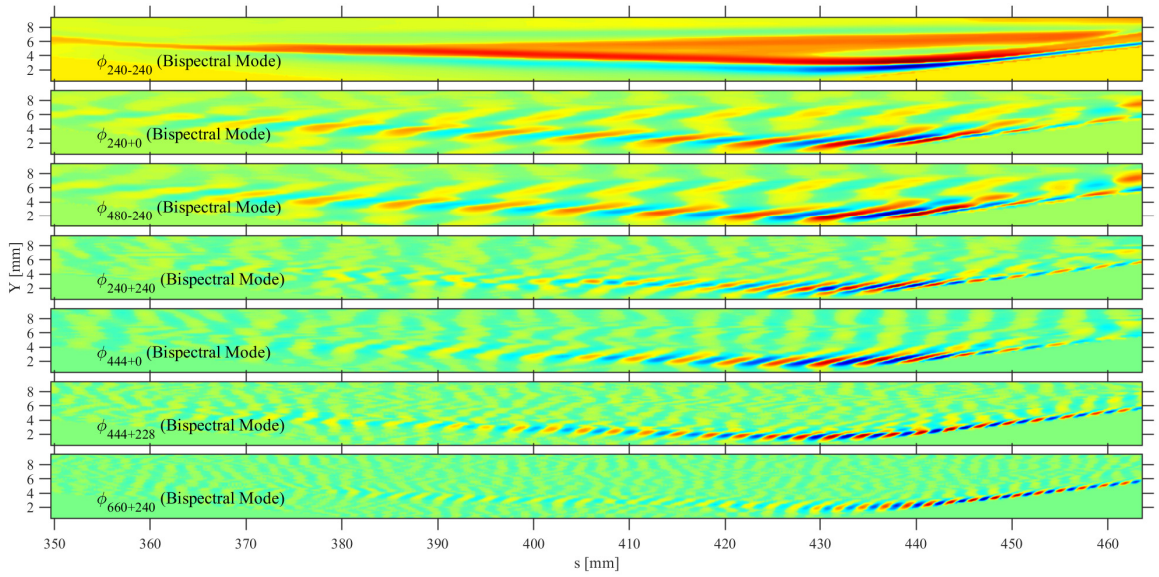

Figure 5.47: Bispectral modes for the +15° configuration

respectively. This was not observed at +5° and +10°, where coherent structures at these harmonics appeared only after the corner, located at $s > 410$ mm. Since the freestream conditions are nominally the same (see Figure 5.1; at the least, the measured unit Reynolds of shot 1877 does not exceed that of shot 1874), this further suggests the separation bubble induces nonlinearity by considerably amplifying the fundamental instability (see Figure 5.15).

The bispectral modes generated by the self-resonance interactions of 36 kHz (36 kHz, 36 kHz, 72 kHz) and 48 kHz (48 kHz, 48 kHz, 96 kHz) are shown in Figure 5.48. The first and third top-most figures here are the bispectral modes computed with the full schlieren field of view using the specifications shown in Table 5.5. Note that, unlike SPOD, BMD only outputs one mode (or eigenvector) per triadic interaction. There are strong nonlinear interactions in general at reattachment due to the broadband amplification of disturbances there (see Figure 5.23). The BMD results, when using the full field of view, therefore opt to generate a mode shape that is biased towards the content near reattachment (though, some weaker radiated structures can be

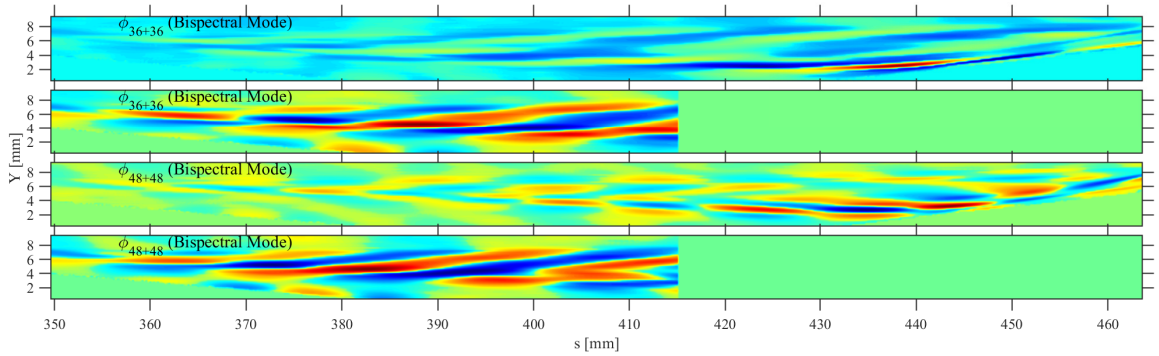

Figure 5.48: Bispectral modes generated by self-resonance interactions of low-frequency disturbances for the +15° configuration

seen for the self-resonance interaction of 36 kHz in addition to the content near reattachment). If instead the BMD is computed using only the region of the flow upstream of reattachment (here, for $s < 415$ mm), then the expected radiated structures become the dominant features of the bispectral modes generated by self-resonance. These are shown in the second and fourth top-most figures of Figure 5.48.

5.11 Summary

A novel technique was developed to transform spatially available data in schlieren cinematography into upsampled pixelwise temporal signals by utilizing the local velocity of propagating disturbances. The spatially-varying velocity field was computed by tracking the local displacements of disturbances in image pairs and averaging over many such pairs. The process enables the reconstruction of temporal signals in a two-dimensional flow field, a capability that is original to this study.

The reconstruction technique was applied to an experimental study of boundary-layer disturbances propagating through the axisymmetric compression corner of a cone-flare geometry at

Mach 14. Upsampled pixelwise temporal signals were computed over the entirety of the field of view, enabling the application of global analysis techniques. These included examinations of the global spatial distributions of pixelwise power spectral densities within specific frequency ranges, as well as the spectral proper orthogonal decomposition and bispectral mode decomposition of the complete spatiotemporal data set. These granted important insights into the dominant dynamical processes at the compression corner, including novel measurements of nonlinear interactions involving higher second-mode harmonics.

Due to the high Mach number of the freestream flow, narrow compression shock angles were generated at the flare. This led to strong bifurcations of second-mode waves along the flare/reattachment shocks and flare boundary layer. The radiation along the flare/reattachment shock was maximal for the fundamental second-mode instability and at the +10° flare configuration, with weaker radiation occurring at higher second-mode harmonics.

The SPOD and BMD analyses identified the dominant flow structures associated with specific discrete frequencies and frequency triads, respectively. In general, the bispectral modes were closely related to the leading SPOD modes, indicating that the dominant structures are heavily involved in nonlinear triadic interactions. The +10° and +15° configurations exhibited greater nonlinearity. Substantially lower-rank behavior at frequencies greater than the fundamental second-mode frequency range than measured at the +5° configuration indicated that harmonic flow structures were significant to the dynamical processes.

The presence of the separation bubble in the +15° configuration coincided with the emergence of a shear-layer instability at approximately 48 kHz. Additional unstable disturbances were identified along the separation shock, ranging in frequency from 40-160 kHz. The most unstable of these was a disturbance at approximately 75 kHz, which appeared linearly unstable along the

separation shock and whose mode shape consisted of waves spanning from the shear layer to the separation shock. Second-mode waves were considerably amplified by the SWBLI at the separation shock and appeared weakly unstable while traversing the separation bubble. The increase in second-mode amplitudes upstream of the corner ultimately resulted in earlier development of harmonic content.

Chapter 6: Conclusion

6.1 Summary

Accurate laminar-to-turbulent prediction of the boundary layer remains one of the leading hindrances for efficient hypersonic vehicle design. Great strides have been made to better our understanding of the transition process on simple geometries that are dominated by single-mode systems, such as the second-mode-dominated slender straight cone. Yet, realistic vehicles will experience a variety of instability types in the hypersonic flow regime, and multi-mode interaction and competition is a necessary research challenge that we must investigate to improve our prediction capabilities. One of the logical geometrical progressions from the straight cone configuration is to add an axisymmetric compression corner to a conical forebody. This induces a SWBLI that not only interacts with incoming second-mode waves but may also produce a separation bubble at the corner, introducing additional instabilities associated with the shear layer. Thus far, instability mechanisms on this geometry have been investigated at Mach numbers of 6 and below. This study has sought to characterize them at Mach 14, granting insight into the instability mechanisms in a high Mach number limit.

The current experimental methodology primarily relied on high-speed calibrated schlieren cinematography, allowing quantitative measurements of off-body disturbances and interactions. In order to resolve the high-frequency disturbances associated with nonlinear development of

the second mode without severe limitations on the field of view, a procedure was employed to reconstruct pointwise temporal signals with enhanced sampling rates. This technique leverages the spatial descriptions of disturbance waveforms present in the images, as well as the computed propagation velocities of these disturbances, to effectively produce artificial schlieren images at intermediate times between two real images.

The reconstruction technique was first applied to two experimental campaigns previously performed on a sharp, 7° half-angle cone to prove its effectiveness. The first of these was conducted in the NASA Langley 20-Inch Mach 6 Wind Tunnel at zero incidence. Time-resolved pixel intensity signals with sampling rates over 10 MHz were recovered, enabling the nonlinear analysis of the second-mode instability. Three Reynolds number conditions were explored, resulting in laminar to transitional boundary layers in the camera field of view. Flush-mounted PCB® sensors were also installed in the model to offer comparisons with the schlieren measurements. Excellent agreement was observed with regard to the measured fundamental and first-harmonic second-mode frequencies, providing confidence that the reconstruction technique was producing valid results.

Following this confirmation, a global analysis was performed on the second-mode nonlinear development to provide descriptions of the second-mode fundamental and harmonic growth throughout the boundary layer. The analysis identified that the most-amplified second-mode energy was found at the critical layer with a secondary peak at the boundary-layer edge. Nonlinear energy exchange among the fundamental and harmonic components of the second mode was found to be strongest along the critical layer, indicating nonlinear breakdown of wave packets was likely initiated there. Fundamental resonance was the strongest nonlinear interaction at all boundary-layer states, though higher-harmonic producing interactions were also present, in-

volving up to the 4th harmonic ($5f_0$). The results of an autobicoherence analysis identified that three-wave quadratic phase coupling was strongest upstream of the peak harmonic power produced by the interaction and was thus linked to harmonic growth rates, whereas a BMD analysis revealed the maximal energy exchange involved in the interaction was found where the PSDs of the interacting components was highest. These findings are in good agreement with previous studies on similar geometries. The additional application of SPOD and BMD provided the coherent structures associated with the fundamental and harmonic second-mode instabilities at specific frequencies, which are scarcer in experimental studies.

Additional experiments on the straight cone model were conducted at Mach 14 at zero and low-nonzero incidence in the AEDC Wind Tunnel 9 facility. Increasing the angle of attack resulted in a reduction in the boundary-layer thickness. This effect was responsible for a shift in the second-mode instability to higher frequencies, both for the fundamental and harmonic disturbances. N-factors were computed for the fundamental, first harmonic, and second harmonic. The growth rates of the first harmonic slightly exceeded that of the fundamental. However, there was no appreciable variation in the growth rate with angle of attack. The power of the second mode decreased with increasing angle of attack, and this is suspected to have been caused by a decrease in the amplitude of tunnel freestream noise at higher frequencies (this also prevented the second harmonic from reaching energy levels significantly higher than the noise floor, precluding accurate measurements of its growth rate at nonzero angles of attack). Despite this, the second-mode fundamental and harmonic structures (including the second harmonic), could be effectively educed from SPOD and BMD analyses. These depicted the slanted rope-like waves typical of the second mode, with peaks in the wall-normal eigenstructure moving closer to the model surface with increasing angle of attack, caused by the shrinking boundary-layer.

These straight cone investigations effectively replicated known second-mode characteristics with the pixelwise temporal signal reconstruction technique and expanded our global understanding of second-mode nonlinear development. An error analysis was also performed to investigate the effect of erroneously changing the propagation speed used in the reconstruction procedure (Appendix A). The reconstruction technique was found to be robust to variations in propagation speeds of up to ±10% of the second-mode propagation speed. It was identified that changing the propagation speed introduces amplitude and phase modulation of disturbances, the magnitude of which increases as the disturbance wavenumber is increased. Nonetheless, these errors remained small for second-mode content, particularly with regard to power spectral densities. Differences in the power spectral density and autobicoherence at second-mode fundamental and lower-harmonic frequencies were negligible, with errors marginally increasing for higher second-mode harmonics.

The aforementioned analyses gave assurance that the basic reconstruction technique is a viable approach to analyzing hypersonic boundary-layer transition on simple geometries. It was then modified such that its applicability was extended to two-dimensional flows with a spatially-variant disturbance velocity, as is the case of the corner flow on a cone-flare. This modified technique was applied to data collected in an experimental campaign performed in the Mach 10-20 Longshot Hypersonic Gun Tunnel located at the von Karman Institute for Fluid Dynamics in Belgium. The test article consisted of a sharp 5° half-angle conical forebody followed by an interchangeable secondary conical frustum of increased half-angle. Three different flare angles were employed, producing +5°, +10°, and +15° axisymmetric compression corners. A Mach-14 contoured nozzle and the same nominal freestream conditions were used for each model configuration.

The +5° and +10° configurations produced an attached oblique shock and small-scale separation region at the corner, respectively, resulting in second-mode dominated flows. In neither configuration was transition was not observed on the flare. The second-mode waves were found to be linearly unstable upstream of the corner, then, upon encountering the shock, the amplitudes were significantly amplified, peaking just downstream of the corner. This peak occurred slightly further downstream in the +5° configuration. The shock rested closer to the body in this case, and thus this delayed peak may have been caused by an extended interaction between the passing second-mode waves with the shock. However, the second mode reached higher N-factors for the +10° configuration due to the stronger compression. Additionally, for the +10° configuration, the strong amplification of the second-mode waves by the SWBLI transpired over two closely adjacent, but distinct, segments, likely corresponding to interactions with the separation and reattachment shocks. After a peak in the N-factor was achieved, it steadily decreased at a slow rate for the +5° configuration. For the +10° configuration, a sharp decrease in N-factor followed by another increase was observed. At the end of the field of view, the N-factors were approximately equal for both configurations.

Upon increasing the deflection angle to +15°, the flow separated well upstream of the corner, producing a separation bubble that was bounded upstream of the corner by a separation shock and downstream of the corner by a reattachment shock. The incoming second-mode waves were slightly deflected at the separation shock such that they appeared to traverse over the recirculating flow of the separation bubble. Transition to turbulence was again not observed on the flare immediately following reattachment; however, some breakdown of wave packets was observed on the flare, primarily at streamwise positions following the point where the separation shock impinged with the reattachment shock. These streamwise positions were near the end of the schlieren field

of view and could not be observed by the reconstruction procedure due to the technique's reliance on downstream data in the image. The initial SWBLI at separation produced broadband amplification of disturbances, including for propagating second-mode waves. The wave packets remained intact and appeared to undergo weak linear amplification as they traversed through the separation region. Very near the streamwise position of the corner, but upstream of reattachment, the growth rate gradually increased, with second-mode N-Factors peaking just downstream of the reattachment shock. These effects appear to be relatively broadband and may not indicate an intrinsic instability of the second mode through the separation region. After reattachment, the second mode exhibited similar behavior to that observed in the +10° configuration, sharply decreasing in amplitude and then slightly increasing thereafter.

The generation of the separation bubble coincided with the emergence of multiple unstable low-frequency disturbances. The first of these was located at approximately 48 kHz and whose eigenstructure was heavily concentrated along the top of the separation region, indicating it was a shear-layer instability. This mode had higher growth rates within this region than the second mode. However, it appeared to be less amplified by the SWBLIs at separation and reattachment and therefore reached comparable peak N-factors to the second mode. This peak was similarly located at the reattachment point. Following the peak, the mode was heavily damped, with N-factors dropping roughly twice as much after reattachment as the second mode. There was evidence that the most-unstable (but not most-amplified) frequencies of this mode decrease as it progresses through the separation region, with most-unstable frequencies initially around 80 kHz and ending at approximately 48 kHz.

An additional instability that exhibited different behavior than the aforementioned shear-layer instability was found to produce most-unstable frequencies of approximately 72 kHz through-

out the separation bubble. This instability was identified by following the spectral development along the separation shock. Frequencies between 40-160 kHz were found to be unstable, with the frequencies between 95-160 kHz possibly belonging to a different disturbance-type, as there appeared a meaningful separation between this band and the amplified band centered at 72 kHz. The growth rate of this disturbance appeared to be remarkably linear along the entirety of the separation shock until its impingement with the reattachment shock. The growth rate was close to that seen for the 48 kHz shear-layer disturbance in approximately the first half of the separation bubble. However, as the 48 kHz shear-layer disturbance approached the corner and experienced further compression upstream of reattachment, the growth rate gradually increased, similar to what was observed for the second-mode disturbances, and exceeded that of the 72 kHz disturbance. Using SPOD, the eigenstructure of the 72 kHz disturbance was determined to contain elongated structures extending from the shear layer to the separation shock, with local peaks in amplitude at either end. These structures, as well as similar structures found at 95 kHz, emanated from the upstream portions of the shear layer; localized peaks in energy were found in the same regions of the shear layer in the SPOD modes at 36 kHz and 48 kHz, suggesting that the radiated structures may be produced by self-resonance of low frequency shear-layer disturbances.

A nonlinear analysis using the bispectral mode decomposition revealed the dominant triadic interactions in each flow field and the structures produced by these interactions. At the +5° configuration, the strongest interactions were the commonly observed second-mode resonance interactions responsible for producing second-mode harmonic content. Unsurprisingly, the fundamental second-mode was the dominant player among these interactions, with its sum and difference self-interactions the most prominent among the group, along with its interactions with the mean flow and with low-frequency oscillations. Other interactions involving the first,

second, and third harmonic were observed in the bispectrum, growing weaker with increasing harmonic. Each of these interactions was predominantly excited after the compression corner. Nonlinearly-generated waves were observed primarily within the flare boundary layer, but also existed along the flare shock wave, appearing as radiated energy. For increasingly higher harmonics, the extent of nonlinear activity along the shock steadily decreased, with the second and third harmonics appearing to be completed isolated within the flare boundary layer.

The nonlinear behavior for the +10° configuration was qualitatively very similar to that observed in the +5° configuration. The main quantitative difference observed was an increase in the magnitudes of all nonlinear interactions. The first-harmonic structures generated from fundamental resonance were observed to amplify just upstream of the compression corner, rather than being isolated to the flare. As was mentioned previously, a small separation region at the corner caused amplification of the second mode slightly upstream of the shock; this was accompanied by an increase in the strength of fundamental resonance. Additionally, the increased strength of the nonlinear interactions led to increased radiation of harmonic energy along the shock, though the trend of decreasing radiation with increasing harmonic was still observed.

In the separated case of the +15° configuration, the extent of nonlinearity was further increased from the attached cases. The broadband amplification of disturbances by the separation shock appeared to play an important role here, as it excited the second-mode disturbance to a sufficient amplitude to nonlinearly generate first, second, and third harmonic content well upstream of the corner. The nonlinear interactions were further amplified just upstream of the reattachment shock and persisted within the flare boundary layer downstream of reattachment. Notably, little to none of the nonlinear activity was found along the separation and reattachment shocks other than the fundamental interaction with the mean flow (reinforcing either the fundamental or its

sidebands) and the difference interaction between the first harmonic and fundamental (depositing energy from the first harmonic back into the fundamental). The nonlinear behavior of the low frequency shear-layer disturbances was strongest near reattachment due to broadband excitation of disturbances near reattachment. Limiting the field of view of the BMD analysis to the flow upstream of reattachment confirmed that the elongated structures found radiating from the shear layer at slightly higher frequencies ($\sim$ 75 – 95 kHz) were generated by self-resonance of the low-frequency shear-layer disturbances.

6.2 Future Work

The most straight-forward continuation of this work would be to expand the parameter space of the cone-flare investigations. In fact, this is quite a necessary future task as the current experiments have served as only a limited introduction into the transition mechanisms on this geometry at high Mach numbers. Additionally, the temporal decay of stagnation conditions within the Longshot facility have precluded effectively characterizing the instability mechanisms with respect to freestream unit Reynolds number. Though few high Mach number facilities exist today, it would be beneficial to reproduce these experiments in a facility that can create similar, steady stagnation conditions (e.g., AEDC Wind Tunnel 9). Investigations at higher freestream unit Reynolds number are also needed to fully induce turbulence on the model, thereby permitting the determination of which mechanism is ultimately responsible for transition. Other parameters which are of interest include the effects of nose bluntness, angle of attack, and wall-to-edge temperature ratio. A degree of nose bluntness is expected on realistic vehicles and produces additional wisp-like disturbances within the entropy layer. An investigation of how these disturbances

interact with the SWBLI would be of practical importance.

With regards to the reconstruction technique, improvements may be made by optimizing the schlieren system. The use of a rectangular light source would create a linear calibration as well improve the signal-to-noise ratio for deflection angles near the limits of the observable range of the system. Signal-to-noise may also be improved by utilizing a focusing schlieren, which has become easier to install in recent years due to systematic improvements. The disturbance measurements may be further extended by introducing simultaneous global, time-resolved heat-transfer measurements provided by fast-response temperature-sensitive paint (TSP). Of particular interest is determining whether transition induced by different instability mechanisms will result in varying degrees of augmentation of the heat flux at the surface: the time-resolved nature of the schlieren and TSP measurements, together with feature-identification techniques, such as those based on Multiple Signal Classification (MUSIC), short-time Fourier-transform, and wavelet-transform algorithms, would enable this in multi-mode scenarios.

Appendix A: Effect of Propagation Speed on Reconstructed Signal

The application of the reconstruction technique in the present global analysis approach requires the assumption that all content passing through a given pixel has the same propagation speed. This is adequate for analysis of the second-mode fundamental and harmonics (see Laurence et al. 2014a; Unnikrishnan and Gaitonde 2020) but will not be true in general, especially if other disturbance types (e.g., first-mode waves, shear-layer waves, etc.) are present in the boundary layer. In this section, we briefly analyze the effect of changing the propagation speed used in the reconstruction technique on the pixelwise power spectral density and autobicoherence computed from the data of Chapter 3. The error analysis will pertain specifically to the original procedure applied to flows with quasi-parallel disturbance streamlines and a universal propagation speed. However, it is expected to be relevant for the modified technique applied to two-dimensional flow fields as well.

As mentioned in section 2.3, the reconstruction technique computes the linearly-weighted average of the backward and forward spatial signals around the pixel of interest from images taken at times t_1 and $t_1 + \Delta t$, where the width of spatial signals used in each image is equal to $U_p \Delta t$. The linearly-weighted average of the spatial signals are then concatenated sequentially over all images, creating a temporal signal. An error in the propagation speed of the disturbance changes the width $U_p \Delta t$, resulting in a phase-shift between the backward and forward spatial

signals used in the linearly-weighted averaging. We will refer to this phase-shift between the spatial signals as ϕ.

Suppose first that equal averaging (i.e., constant weights of $1/2$) was used on the backward and forward spatial signals of images at t_1 and $t_1 + \Delta t$ and an error in the propagation speed of a disturbance wave exists. The computed average wave will have a reduced amplitude (with complete destructive interference at $\phi = 180°$) and a phase equal to the average phase of the two parent waves (representing a phase error from the true physical wave of $\phi/2$). Additionally, at the point of concatenation with the subsequent averaged wave, taken from times $t_1 + \Delta t$ and $t_1 + 2\Delta t$, there will be a discrete phase-shift in the reconstructed signal equal to ϕ, which occurs because the spatial signal at time $t_1 + \Delta t$ goes from leading the signal at time t_1 to lagging the signal at $t_1 + 2\Delta t$. This error creates a "ringing" in the spectrum of the reconstructed signal, with artifactual spikes arising at $nf_s + f$ and $nf_s - f$, where n is an integer, f_s the original sampling rate (i.e., the camera frame rate), and f the disturbance frequency. This is the same mechanism that produces the spikes shown in Figure 3.4, which originate from stationary irregularities in the images (e.g., window blemishes) and result in artifacts at nf_s because f is 0. In addition, spatial changes in the mean flow (e.g., the boundary-layer height) over the propagation distance used in the reconstruction will produce narrow-banded artifacts at nf_s. A sufficiently high frame rate ensures that this effect is small, as changes in the mean flow state will become negligible. In these experiments of Chapter 3, the boundary-layer growth over the schlieren field of view was estimated to lie between 2.25 and 2.75 pixels for all conditions. With an average propagation distance of approximately 38 pixels, and twice the distance used in each reconstruction procedure (incorporating forward and backward signals), this results in a minimal boundary-layer growth of 0.108 to 0.144 pixels over the spatial length used in reconstruction. Using instead a linearly-weighted averaging of

the backward and forward spatial signals (as is done in the present implementation) assures the averaged wave is exact at either end. This removes the discrete phase-shift at concatenation and the phase error, ϕ, is gradually covered over the distance $U_p \Delta t$. The artifacts remain but at a significantly decreased power.

If such errors in propagation speed exist, the reconstruction technique will therefore still correctly measure the disturbance frequency, but with amplitude and phase error. At $\phi = 180°$, the weighted averaging prevents complete destructive interference (as would be the case with equal averaging), but the artifact power is at a maximum. Past 180° phase error, the artifact power decreases but the disturbance begins to be aliased to $f + f_s$, with complete aliasing (and complete artifact removal) occurring when an entire wavelength has been either added or removed from the spatial distance $U_p \Delta t$. This occurs when the error in propagation speed is equal to $\pm f_s/\kappa$, where κ is the disturbance longitudinal wavenumber. For this reason, higher-wavenumber disturbances will experience greater amplitude and phase error from errors in their propagation speeds.

In Figure A.1, PSD and autobicoherence results (plotted with the same color scale) are presented using three different propagation speeds. The signal used is taken from condition Re97 at $s = 330$ mm and a vertical height corresponding to the maximum second-mode disturbance (approximately 0.91 mm above the cone surface). Condition Re97 was chosen for this analysis due the higher amplitudes of second-mode harmonics. The propagation speeds used in the reconstruction were $0.9U_{p_0}$, U_{p_0}, and $1.1U_{p_0}$, where U_{p_0} is the calculated propagation speed shown in Table 2. A 10% error encompasses the majority of variability in the propagation speed of the disturbances of current interest. Adopting $1.1U_{p_0}$ more accurately reconstructs disturbances propagating at the edge velocity, such as entropic and vortical disturbances. A propagation speed of $0.9U_{p_0}$ encompasses first-mode waves (on similar geometries at Mach 6, the first-mode has

been measured to have a longitudinal phase velocity of 89% of the edge velocity (Maslov et al. 2006)) and, to some degree, free-stream disturbances (which have been shown to possess propagation speeds in the range of 63-81% of the free-stream velocity in this facility (Chou et al. 2018)). Additionally, nonlinear interactions between the second-mode fundamental or harmonics with disturbances of other families, which propagate at different speeds, will produce content that propagates at an intermediate speed, $(f_1 + f_2)/(\kappa_1 + \kappa_2)$ (Ball 1963). Disturbances of other families that are likely to be interacting in this case (e.g., first-mode waves and low-frequency disturbances) will be of lower frequency and wavenumber than the second mode. Therefore, $(f_1 + f_2)/(\kappa_1 + \kappa_2)$ will be more heavily weighted towards the second-mode propagation speed and likely to fall into the range of 10% deviation from U_{p_0}.

In either case of error (±10%), there are minimal differences compared to the original results. The PSD (Figure 20a) in the range of the fundamental second mode remains nearly unchanged in amplitude and frequency. However, the error in the PSD gets progressively worse at higher second-mode harmonics. This is expected, as the same error in propagation speed will produce larger phase errors during the signal reconstruction for higher-wavenumber disturbances. For this same reason, errors in the propagation speed also have the largest effect on higher-harmonic-producing nonlinear interactions observed in the autobicoherence. The quantitative error remains small for interactions involving the second-mode fundamental and the lower harmonics. For example, the $f_0 + f_0 \rightarrow 2f_0$ interaction has peak b^2 values of 0.84, 0.81, and 0.81 in Figures 20b through 20d, respectively, and the $2f_0 + f_0 \rightarrow 3f_0$ interaction has peak b^2 values of 0.60, 0.57, and 0.53. The quantitative error increases for triadic interactions involving higher harmonics, however the lobes of all notable interactions remain qualitatively consistent.

Finally, one may be concerned that, because the second-mode fundamental consists of an

approximately 150 kHz band centered near the camera frame rate (286 kHz), the harmonics may instead themselves only be artifacts occurring at frequencies $nf_s + f$ and $nf_s - f$, where f is a fundamental frequency. Performing a quick spatial Fourier transformation of the rows of pixels in the raw images discredits this, as the resulting spectra (not shown) clearly show harmonic content at the expected wavenumbers.

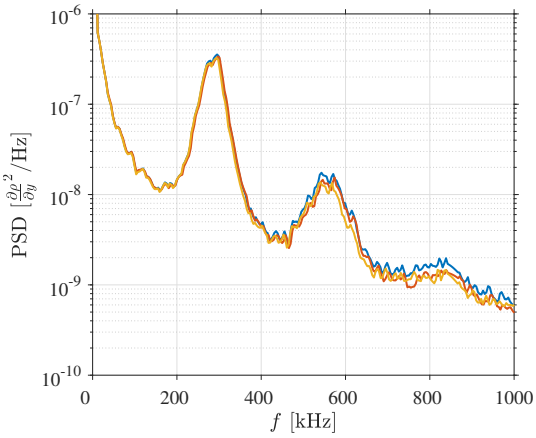

(a) Power-spectral-densities

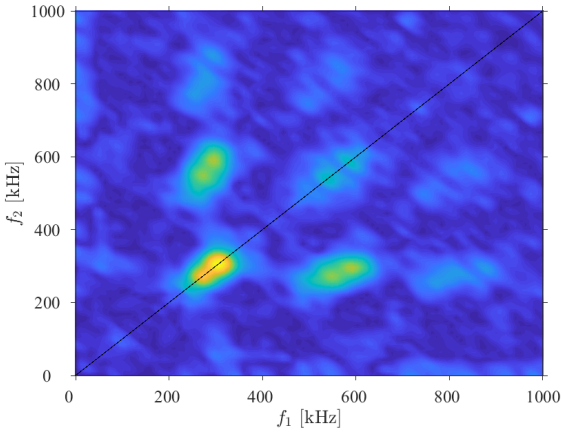

(b) Autobicoherence using original propagation speed, U_{p_0}.

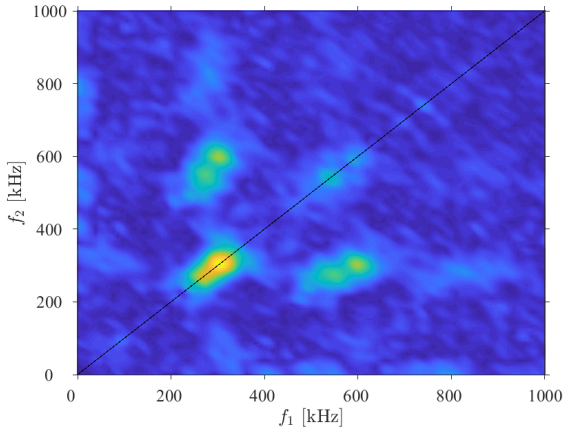

(c) Autobicoherence using $U_p = 0.9U_{p_0}$.

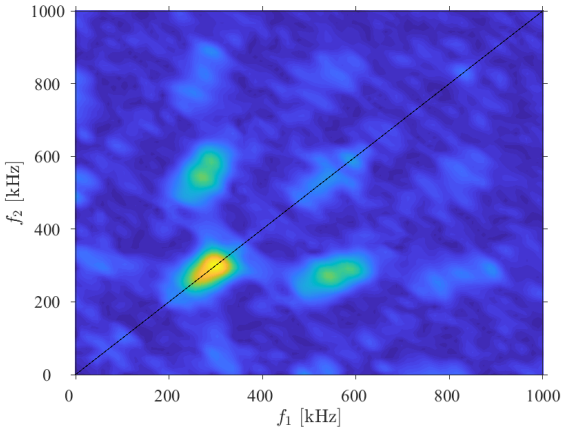

(d) Autobicoherence using $U_p = 1.1U_{p_0}$.

Figure A.1: (a) PSDs using prorogation speeds of U_{p_0} (blue), $0.9U_{p_0}$ (red), and $1.1U_{p_0}$ (yellow). (b-d) Autobicoherence using propagation speeds of U_{p_0} (b), $0.9U_{p_0}$ (c), and $1.1U_{p_0}$ (d).

Appendix B: Unsteady Freestream Flow Conditions

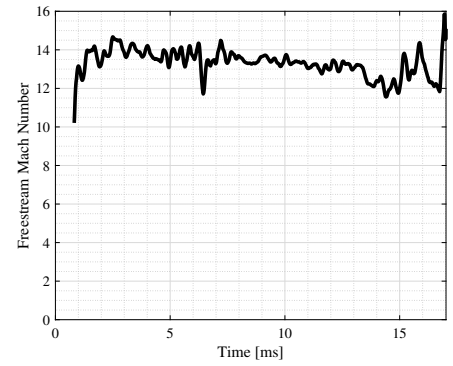

(a) Mach Number

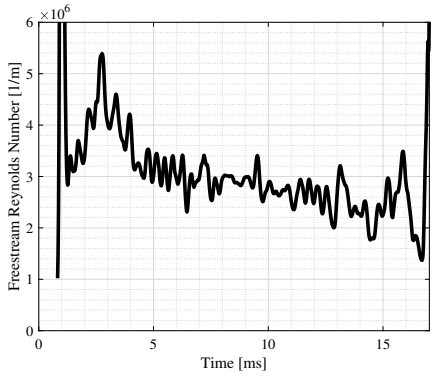

(b) Unit Reynolds Number

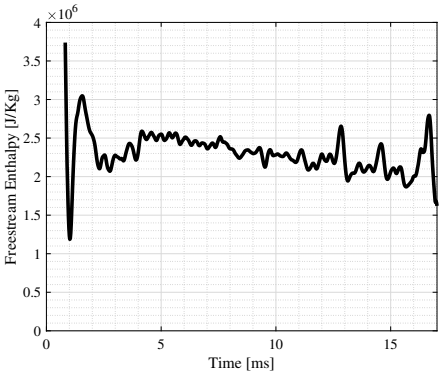

(c) Enthalpy

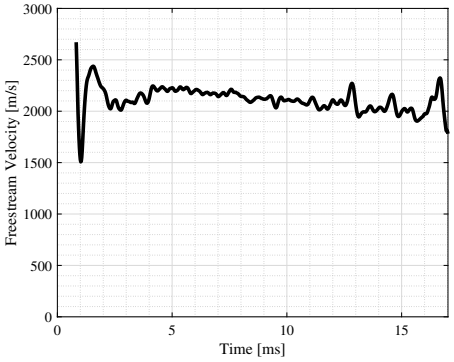

(d) Velocity

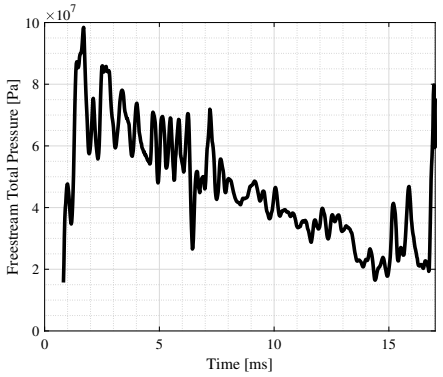

(e) Total Pressure

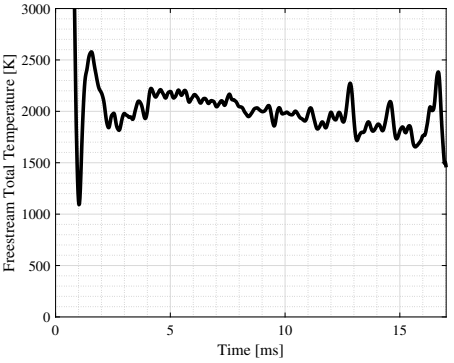

(f) Total Temperature

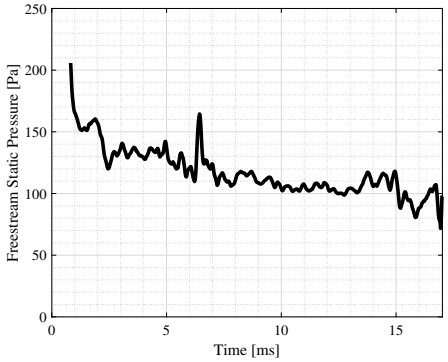

(g) Static Pressure

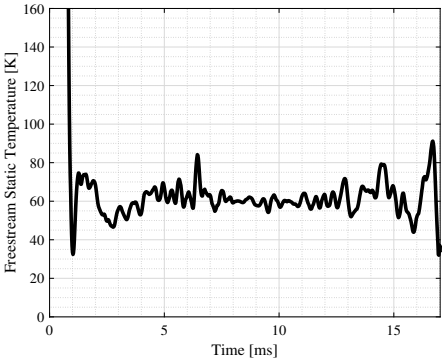

(h) Static Temperature

Figure B.1: Shot 1874 Freestream Test Conditions

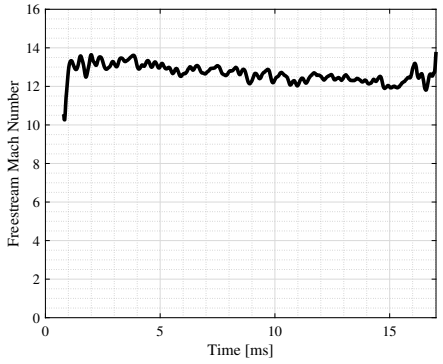

(a) Mach Number

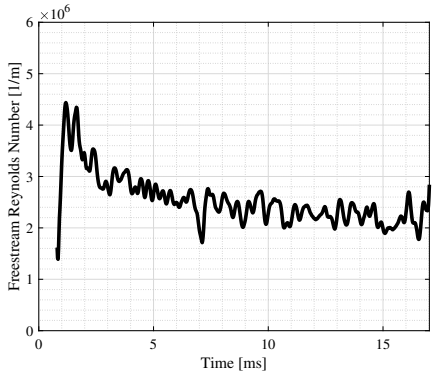

(b) Unit Reynolds Number

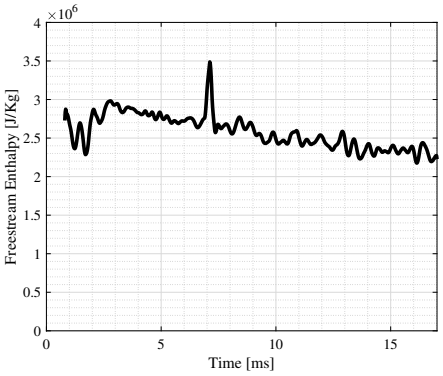

(c) Enthalpy

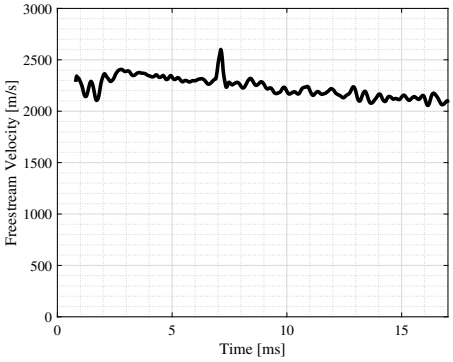

(d) Velocity

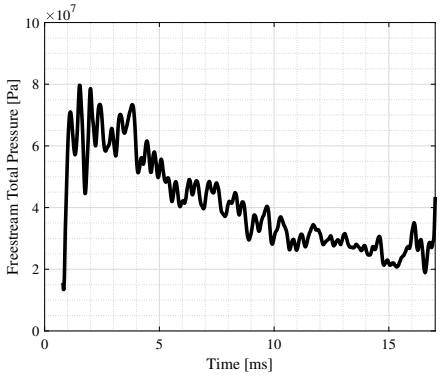

(e) Total Pressure

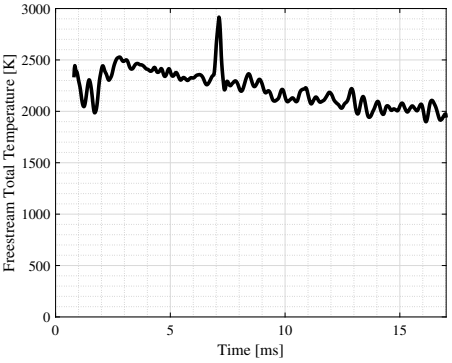

(f) Total Temperature

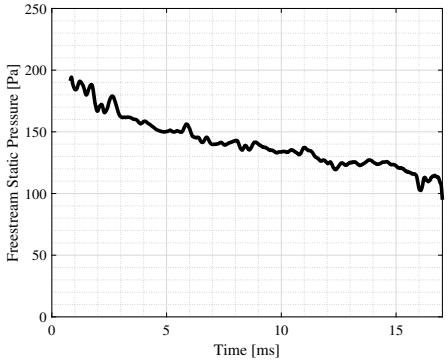

(g) Static Pressure

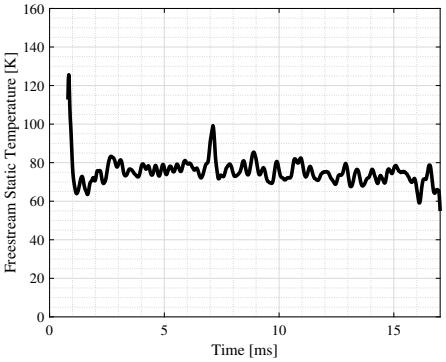

(h) Static Temperature

Figure B.2: Shot 1877 Freestream Test Conditions

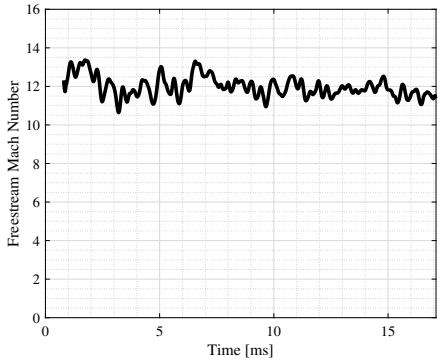

(a) Mach Number

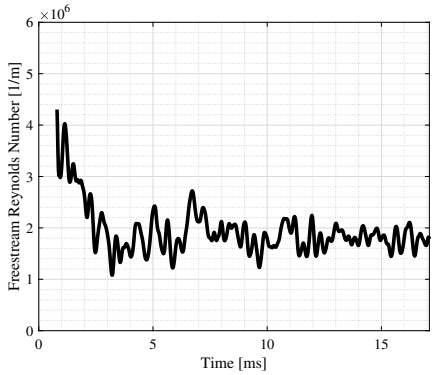

(b) Unit Reynolds Number

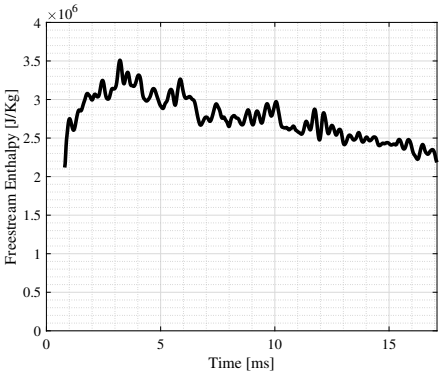

(c) Enthalpy

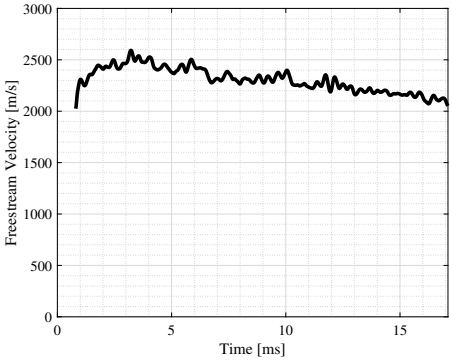

(d) Velocity

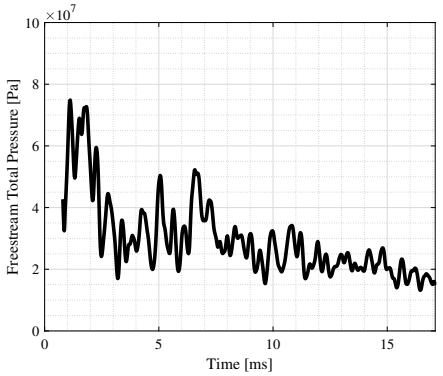

(e) Total Pressure

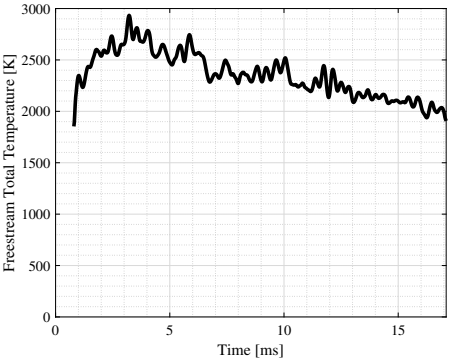

(f) Total Temperature

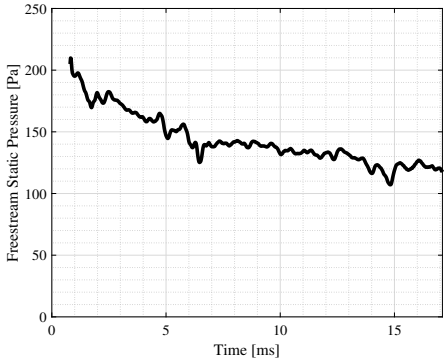

(g) Static Pressure

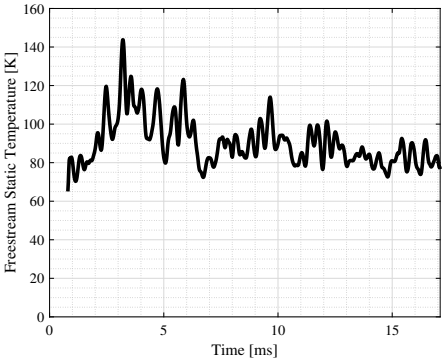

(h) Static Temperature

Figure B.3: Shot 1878 Freestream Test Conditions

Bibliography

P. Balakumar, H. Zhao, and H. Atkins. *Stability of Hypersonic Boundary-Layers over a Compression Corner*. 2002. doi: 10.2514/6.2002-2848.

P. Balakumar, H. Zhao, and H. Atkins. Stability of hypersonic boundary layers over a compression corner. *AIAA Journal*, 43(4):760–767, 2005. doi: 10.2514/1.3479.

F. Ball. Energy transfer between external and internal gravity waves. *J. Fluid Mechanics*, 19(3): 465–478, 1963.

E. K. Benitez, S. Esquieu, J. S. Jewell, and S. P. Schneider. Instability measurements on an axisymmetric separation bubble at Mach 6. AIAA Paper 2020-3072, 2020.

K. Berger, S. Rufer, K. Hollingsworth, and S. Wright. NASA Langley Aerothermodynamics Laboratory: Hypersonic testing capabilities. AIAA Paper 2015-1337, 2015.

D. Bountin, A. Shiplyuk, and A. Maslov. Evolution of nonlinear processes in a hypersonic boundary layer on a sharp cone. *J. Fluid Mechanics*, 61:427–442, 2008.

D. R. Brillinger. An introduction to polyspectra. *The Annals of Mathematical Statistics*, 36(5): 1351–1374, 1965.

C. Butler and S. Laurence. Interaction of second-mode wave packets with an axisymmetric expansion corner. *Experiments in Fluids*, 62:140, 2021.

C. Butler and S. Laurence. Transitional hypersonic flow over slender cone/flare geometries. *J. Fluid Mechanics*, 949:A37, 2022.

K. Casper, S. Beresh, J. Henfling, R. Spillers, B. Pruett, and S. Schneider. Hypersonic wind tunnel measurements of boundary layer pressure fluctuation. AIAA Paper 2009-4054, 2009.

K. Casper, S. Beresh, J. Henfling, R. Spillers, and B. Pruett. High-speed schlieren of disturbances in a transitional hypersonic boundary-layer. AIAA Paper 2013-0376, 2013.

K. Casper, S. Beresch, and S. Schneider. Pressure fluctuations beneath instability wavepackets and turbulent spots in a hypersonic boundary layer. *J. Fluid Mechanics*, 756:1058–1091, 2014.

N. Chokani. Nonlinear spectral dynamics of hypersonic laminar boundary layer flow. *Physics of Fluids*, 11:3846–3851, 1999.

N. Chokani. Nonlinear evolution of Mack modes in a hypersonic boundary layer. *Physics of Fluids*, 17:014102, 2005.

A. Chou, A. Leidy, B. Bathel, R. King, and G. Herring. Measurements of freestream fluctuations in the NASA Langley 20-Inch Mach 6 tunnel. AIAA Paper 2018-3073, 2018.

S. Craig, R. Humble, J. Hofferth, and W. Saric. Nonlinear behavior of the Mack modes in a hypersonic boundary layer. *J. Fluid Mechanics*, 872:74–99, 2019.

A. Craik. Non-linear resonant instability in boundary layers. *J. Fluid Mechanics*, 50(2):393–413, 1971.

A. Demetriades. Hypersonic viscous flow over a slender cone, part iii: Laminar instability and transition. AIAA Paper 1974-0535, 1974.

A. Demetriades. Boundary layer instability observations at Mach number 7. *J. Applied Mechanics*, 99:No. 1, 1977.

A. Demetriades. New experiments on hypersonic boundary laver stability including wall temperature effects. pages 39–54, 1978.

L. Duan, M. Choudhari, A. Chou, F. Munoz, S. Ali, R. Radespiel, T. Schilden, W. Schroder, E. Marineau, K. Casper, and et al. Characterization of freestream disturbances in conventional hypersonic wind tunnels. 2018.

M. Estorf, R. Radespiel, S. Schneider, H. Johnson, and S. Hein. Surface-pressure measurements of second-mode instability in quiet hypersonic flow. AIAA Paper 2008-1153, 2008.

M. Fischer and R. Wagner. Transition and hot-wire measurements in hypersonic helium flow. *AIAA Journal*, 10(10):1326–1332, 1972.

K. Fuji. Experiment of two-dimensional roughness effect on hypersonic boundary-layer transition. *J. Spacecraft and Rockets*, 43:731–738, 2006.

K. Fuji, H. Noriaki, K. Tadao, T. Shoichi, N. Muneyoshi, I. Yukihiro, N. Akihiro, and O. Hiroshi. A measurement of instability wave in the hypersonic boundary layer on a sharp cone. AIAA Paper 1991-1639, 2011.

M. Gragston, F. Siddiqui, and J. Schmisseur. Detection of second-mode instabilities on a flared cone in Mach 6 quiet flow with linear array focused laser differential interferometry. *Experiments in Fluids*, 62:81, 2021.

G. Grossir and B. Dias. Flow characterization of the VKI longshot wind tunnel. *North Atlantic Treaty Organization Science and Technology Organization*, STO-EN-AVT-325, 2018.

G. Grossir, Z. Ilich, and O. Chazot. Modeling of the VKI Longshot Gun Tunnel compression process using a quasi-1D approach. AIAA Paper 2017-3985, 2017.

A. Hameed, N. Parziale, L. Paquin, C. Butler, and S. Laurence. Spectral analysis of a hypersonic boundary layer on a right, circular cone. AIAA Paper 2020-362, 2020.

M. Hargather and G. Settles. A comparison of three quantitative schlieren techniques. *Optics and Lasers in Engineering*, 50:8–17, 2012.

K. Heffner, A. Chpoun, and J. Lengrand. *Experimental study of transitional axisymmetric shock-boundary layer interactions at Mach 5*. 1993. doi: 10.2514/6.1993-3131.

T. Herbert. Parabolized stability equations. *Annual Review of Fluid Mechanics*, 29(Volume 29, 1997):245–283, 1997. ISSN 1545-4479. doi: https://doi.org/10.1146/annurev.fluid.29.1.245.

J. L. Hill, M. P. Borg, and M. F. Reeder. Global mode reconstruction using phase-consistent spod. AIAA Paper 2023-1985, 2023.

J. Hofferth, R. A. Humble, and D. Floryan. High-bandwidth optical measurements of the second-mode instability in a Mach 6 quiet tunnel. AIAA Paper 2013-0378, 2013.

B. Hollis. Real-gas flow properties for NASA Langley Research Center Aerothermodynamic Facilities Complex wind tunnels. No. NASA-CR-4755, 1996.

C. Illingworth. Unsteady laminar flow of gas near an infinite flat plate. *Mathematical Proceedings of the Cambridge Philosophical Society*, 46:603–613, 1950.

T. Jackson and C. Grosch. Inviscid spatial stability of a compressible mixing layer. *Journal of Fluid Mechanics*, 208:609–637, 1989. doi: 10.1017/S002211208900296X.

T. Jackson and C. Grosch. Absolute/convective instabilities and the convective mach number in a compressible mixing layer. *Physics of Fluids A: Fluid Dynamics*, 2(6):949–954, 06 1990.

Y. Kachanov and V. Levchenko. The resonant interaction of disturbances at laminar-turbulent transition in a boundary layer. *J. Fluid Mechanics*, 138:209–247, 1984.

J. Kendall. Supersonic boundary layer stability experiments. 1967.

J. Kendall. Wind tunnel experiments relating to supersonic and hypersonic boundary-layer transition. *AIAA Journal*, 13:290–299, 1975.

R. Kennedy. *An experimental investigation of hypersonic boundary-layer transition on sharp and blunt slender cones*. PhD thesis, University of Maryland, College Park, 2019.

R. Kennedy, S. Laurence, M. Smith, and E. Marineau. Hypersonic boundary-layer transition features from high-speed schlieren images. AIAA Paper 2017-1683, 2017.

R. Kennedy, S. Laurence, M. Smith, and E. Marineau. Visualization of the second-mode instability on a sharp cone at Mach 14. AIAA Paper 2018-2083, 2018a.

R. Kennedy, S. Laurence, M. Smith, and E. Marineau. Investigation of the second-mode instability at Mach 14 using calibrated schlieren. *J. Fluid Mechanics*, 845:R2, 2018b.

R. Kennedy, J. Jewell, P. Paredes, and S. Laurence. Characterization of instability mechanisms on sharp and blunt slender cones at Mach 6. *J. Fluid Mechanics*, 936:A39, 2022.

A. A. Khan, T. Liang, A. Batista, and J. Kuehl. On energy redistribution for the nonlinear parabolized stability equations method. *Fluids*, 7(8), 2022. ISSN 2311-5521. doi: 10.3390/fluids7080264. URL https://www.mdpi.com/2311-5521/7/8/264.

R. Kimmell and J. Kendall. Nonlinear disturbances in a hypersonic laminar boundary layer. AIAA Paper 1991-320, 1991.

J. T. Lachowicz, N. Chokani, and S. P. Wilkinson. Boundary-layer stability measurements in a hypersonic quiet tunnel. *AIAA Journal*, 34(12):2496–2500, 1996. doi: 10.2514/3.13430.

J. Lafferty and J. Norris. Measurements of fluctuating pitot pressure, "tunnel noise," in the AEDC Hypervelocity Wind Tunnel No. 9. AIAA Paper 2007-1678, 2007.

S. Laurence, A. Wagner, K. Hannermann, V. Wartemann, H. Lüdeke, H. Tanno, and K. Itoh. Time-resolved visualization of instability waves in a hypersonic boundary layer. *AIAA Journal*, 50(1):243–246, 2012.

S. Laurence, A. Wagner, and K. Hannermann. Schlieren-based techniques for investigating instability development and transition in a hypersonic boundary layer. *Experiments in Fluids*, 55: 1–17, 2014a.

S. Laurence, A. Wagner, and K. Hannermann. Schlieren-based techniques for investigating instability development and transition in a hypersonic boundary layer. *Experiments in Fluids*, 55: 1782, 2014b.

S. Laurence, A. Wagner, and K. Hannermann. Experimental study of second-mode instability growth and breakdown in a hypersonic boundary layer using high-speed schlieren visualization. *J. Fluid Mechanics*, 797:471–503, 2016.

L. Lees and C. Lin. Investigation of the stability of the laminar boundary layer in a compressible fluid. NACA TN 1115, 1946.

A. Leidy, R. King, M. Choudhari, and P. Paredes. Hypersonic second-mode instability response to shaped roughness. AIAA Paper 2021-0149, 2021.

J. Li. The cut-off frequency of constant temperature hot-wire systems in turbulent velocity measurements. 2004.

M. Lugrin, S. Beneddine, C. Leclercq, E. Garnier, and R. Bur. Transition scenario in hypersonic axisymmetrical compression ramp flow. *Journal of Fluid Mechanics*, 907:A6, 2021. doi: 10.1017/jfm.2020.833.

L. Mack. Linear stability theory and the problem of the supersonic boundary-layer transition. *AIAA Journal*, 13:278–289, 1975.

E. Marineau, C. Moraru, and D. Daniel. Sharp cone boundary-layer transition and stability at Mach 14. AIAA Paper 2017-0766, 2017.

E. Marineau, G. Grossir, A. Wagner, M. Leinemann, R. Radespiel, H. Tanno, R. Wagnild, and K. Casper. Analysis of second-mode amplitudes on sharp cones in hypersonic wind tunnels. *J. Spacecraft and Rockets*, 56:307–318, 2019.

D. Marren, J. Coblish, E. Marineau, J. Norris, I. Kurits, D. Lewis, M. Smith, and M. Marana. The Hypervelocity Wind Tunnel No. 9 - continued excellence through improvement and modernization. AIAA Paper 2015-1340, 2015.

A. Maslov, A. Shiplyuk, D. Bountin, and A. Sidorenko. Mach 6 boundary-layer stability experiments on sharp and blunted cones. *J. Spacecraft and Rockets*, 43:71–76, 2006.

D. Miller, R. Hijman, and M. Childs. Mach 8 to 22 studies of flow separations due to deflected control surfaces. *AIAA Journal*, 2(2):312–321, 1964. doi: 10.2514/3.2289.

A. Nayfeh and A. Bozatli. Nonlinear wave interactions in boundary layers. AIAA Paper 1979-1496, 1971.

A. Novikov, I. Egorov, and A. Fedorov. Direct numerical simulation of wave packets in hypersonic compression-corner flow. *AIAA Journal*, 54(7):2034–2050, 2016. doi: 10.2514/1.J054665.

N. Parziale, J. Shepherd, and H. Hornung. Differential interferometric measurement of instability in a hypersonic boundary layer. *AIAA Journal*, 51:750–754, 2013.

J. Potter and J. Whitfield. Boundary-layer transition under hypersonic conditions. *AGARDograph*, pages No. 97, Part III, 1965.

A. Roghelia, H. Olivier, I. Egorov, and P. Chuvakhov. Experimental investigation of Görtler vortices in hypersonic ramp flows. *Experiments in Fluids*, 58(139), 2017.

C. Running, T. Juliano, J. Jewell, M. Borg, and R. Kimmel. Hypersonic shock-wave/boundary-layer interactions on a cone/flare. *Experimental Thermal and Fluid Science*, 109:109911, 2019. ISSN 0894-1777. doi: https://doi.org/10.1016/j.expthermflusci.2019.109911.

C. Running, T. Juliano, M. Borg, and R. Kimmel. Characterization of post-shock thermal striations on a cone/flare. *AIAA Journal*, 58(5):2352–2358, 2020. doi: 10.2514/1.J059095.

H. Schardin. *Die Schlierenverfahren und ihre Anwendungen*, pages 303–439. Springer Berlin Heidelberg, Berlin, Heidelberg, 1942. ISBN 978-3-540-77207-1. doi: 10.1007/BFb0111981. URL https://doi.org/10.1007/BFb0111981.

O. Schmidt. Bispectral mode decomposition of nonlinear flows. *Nonlinear Dynamics*, 102: 2479–2501, 2020.

O. T. Schmidt and T. Colonius. Guide to spectral proper orthogonal decomposition. *AIAA Journal*, 58(3):1023–1033, 2020. doi: 10.2514/1.J058809. URL https://doi.org/10.2514/1.J058809.

S. Schneider. Hypersonic laminar-turbulent transition on circular cones and scramjet forebodies. *Progress in Aerospace Sciences*, 40:1–50, 2004.

G. Settles. *Schlieren and shadowgraph techniques : visualizing phenomena in transparent media*. Springer, 2001.

N. Shumway and S. Laurence. Methods for identifying key features in schlieren images from hypersonic boundary-layer instability experiments. AIAA Paper 2015-1787, 2015.

J. Sivasubramanian and H. Fasel. Numerical investigation of the development of three-dimensional wavepackets in a sharp cone boundary layer at Mach 6. *J. Fluid Mechanics*, 756:600–649, 2014.

J. Sivasubramanian and H. Fasel. Direct numerical simulation of transition in a sharp cone boundary layer at Mach 6: fundamental breakdown. *J. Fluid Mechanics*, 768:175–218, 2015.

G. Speak and D. Walters. *Optical Considerations and Limitations of the Schlieren Method*. H.M. Stationery Office, 1954.

K. Stetson and R. Kimmel. On hypersonic boundary-layer stability. AIAA Paper 1992-737, 1992.

K. Stetson, E. Thompson, J. Donaldson, and L. Siler. Laminar boundary layer stability experiments on a cone at Mach 8, Part I: Sharp cone. AIAA Paper 1983-1761, 1983.

K. Taira, S. L. Brunton, S. T. M. Dawson, C. W. Rowley, T. Colonius, B. J. McKeon, O. T. Schmidt, S. Gordeyev, V. Theofilis, and L. S. Ukeiley. Modal analysis of fluid flows: An overview. *AIAA Journal*, 55(12):4013–4041, 2017. doi: 10.2514/1.J056060. URL https://doi.org/10.2514/1.J056060.

V. Theofilis. Global linear instability. *Annual Review of Fluid Mechanics*, 43(1):319–352, 2011. doi: 10.1146/annurev-fluid-122109-160705. URL https://doi.org/10.1146/annurev-fluid-122109-160705.

A. Towne, O. Schmidt, and T. Colonius. Spectral proper orthogonal decomposition and its relationship to dynamic mode decomposition and resolvent analysis. *J. Fluid Mechanics*, 847: 821–867, 2018.

S. Unnikrishnan and D. Gaitonde. Linear, nonlinear and transitional regimes of second-mode instability. *J. Fluid Mechanics*, 905:A25, 2020.

C. VanDercreek, M. Smith, and K. Yu. Focusing schlieren and deflectometry at AEDC Hypervelocity Wind Tunnel No. 9. AIAA Paper 2010-4209, 2010.

J. Weisberger, B. Bathel, G. Herring, G. Buck, S. Jones, and A. Cavone. Multi-point line focused laser differential interferometer for high-speed flow fluctuation measurements. *Applied Optics*, 59:11180–11195, 2020.

J. Weisberger, B. Bathel, J. Lee, and A. Cavone. Linear array photodiode and data acquisition system development for multi-point line FLDI measurements. AIAA Paper 2022-1796, 2022.

V. Zakkay, A. Bos, and P. Jensen. Laminar, transitional, and turbulent flow with adverse pressure gradient on a cone-flare at Mach 10. *AIAA Journal*, 5(2):201–207, 1967. doi: 10.2514/3.3943.

M. Zhuang, T. Kubota, and P. Dimotakis. Instability of inviscid, compressible free shear layers. *AIAA Journal*, 28(10):1728–1733, 1990. doi: 10.2514/3.10466.